université PARIS-SACLAY

NNT: 2018SACLS122

Thèse de doctorat

Optics optimization of longer L* Beam Delivery System designs for CLIC and tuning of the ATF2 final focus system at ultra-low β* using octupoles

Thèse de doctorat de l'Université Paris-Saclay
préparée à l'**Université Paris-Sud**

École doctorale n°576 : particules hadrons énergie et noyau : instrumentation, image, cosmos et simulation (PHENIICS)

Spécialité de doctorat: *Physique des accélérateurs*

Thèse présentée et soutenue à Orsay, le 6 Juillet 2018, par

Fabien Plassard

Composition du Jury :

ACHILLE STOCCHI Professeur, Université Paris-Sud (LAL)	Président
FRANK ZIMMERMANN Physicien Sénior (CERN)	Rapporteur
ANDREA JEREMIE Ingénieure de recherche (LAPP)	Rapporteur
ANGELES FAUS-GAULFE Ingénieure de recherche (LAL)	Examinateur
PHILIP BAMBADE Directeur de recherche (LAL)	Directeur de thèse
ROGELIO TOMAS Physicien Sénior (CERN)	Co-Directeur de thèse

Résumé

Titre: Optimisation de la ligne de faisceau du système de focalisation finale à long L* du collisionneur linéaire CLIC et étude des optiques de focalisation de l'ATF2 à ultra-bas β_y^* avec utilisation d'octupôles.

Mots clés : Collisionneur de leptons, accélérateur linéaire, Section Finale de Focalisation (FFS), dynamique du faisceau, optimisation de la ligne optique, luminosité, chromaticité, correction des aberrations linéaires et non-linéaires, octupôles, ATF2, CLIC, distance focale finale L^*, interface détecteur-machine

Afin de compléter les résultats du *Large Hadron Collider* (LHC), la communauté internationale de physique des particules et des accélérateurs envisagent la construction d'un collisionneur de leptons opérant à des énergies de l'ordre du Tera-électron-Volt (TeV). Les futures machines envisagées pour obtenir des mesures de haute précision à l'échelle du TeV sont des collisionneurs linéaires électron-positron (e^-e^+) fournissant une haute luminosité de quelques $10^{34}\mathrm{cm}^{-2}\mathrm{s}^{-1}$. Un défi important pour ces machines est de pouvoir focaliser le faisceau à des tailles transverses de l'ordre du nanomètre au point d'intéraction (IP), permettant d'atteindre la luminosité de conception.
Le système délivrant les faisceaux d'e^- et de e^+ de la sortie du Linac principal vers le point d'intéraction, le *Beam Delivery System* (BDS), réalise les fonctions critiques requises pour atteindre l'objectif de luminosité, tel que la collimation et la focalisation du faisceau. Le faisceau est focalisé par le système de focalisation finale (FFS) tout en corrigeant les aberrations d'ordre supérieur propagées le long du système. Les effets chromatiques contribuant à l'élargissement de la taille du faisceau, sont amplifiés par la force de focalisation des deux derniers quadripôles QF1 et QD0, ou doublet final (FD), et par la longueur de la distance focale finale L* entre QD0 et l'IP. L'approche de correction de la chromaticité retenue pour les deux grands projets actuels de collisionneurs linéaires, CLIC et ILC, est fondée sur la correction locale de la chromaticité générée par le doublet final. Ce shéma est actuellement testé à l'ATF2 au KEK (Japon).
Ce travail de thèse se concentre sur les problématiques liées au système de focalisation finale du projet CLIC, dans le cadre de la simplification de l'interface machine-détecteur (MDI), ainsi que sur le travail expérimental conduit à l'ATF2 pour l'optimisation et l'étude des optiques du système de focalisation finale à ultra-bas β_y^*.

Dans le Rapport d'études conceptuelles (CDR) du CLIC, le dernier quadripôle de l'accélérateur QD0 est intégré dans le détecteur. Ce choix a été imposé pour permettre de maximiser la luminosité, après optimisation de la distance L*. Un certain nombre de problèmes lié a cette configuration pour la zone d'expérimentation du CLIC résultent de l'interaction des champs magnétiques du QD0 et du détecteur, de la stabilisation de QD0, de la perte de luminosité due aux interventions plus longues nécessaire pour extraire QD0 du detéc-

teur, et de la perte d'espace à l'intérieur de l'expérience pour la détection calorimètrique de hadrons. Afin de pallier ces problèmes, un nouveau concept de détecteur, permettant de déplacer QD0 à l'extérieur du détecteur avec un L^* de 6 mètres a été proposé. Le récent scénario de construction du CLIC prévoit une énergie au centre de masse à 380 GeV pour la première phase d'opération et à 3 TeV pour la phase finale. Dans cette thèse, de nouveaux designs pour le système de focalisation finale avec $L^* = 6$ m ont été optimisés pour la première et dernière phases d'énergie du CLIC. Il a été mis en évidence que les performances de ces systèmes liées à la luminosité ainsi que la capacité de la machine à corriger la perte de luminosité dues aux inévitable imperfections de la ligne optique répondent aux éxigences de luminosité du CLIC pour chaque option de L^*. Par ailleurs, la capacité de ces systèmes à rétablir les performances nominales en corrigeant les aberrations linéaires et non-linéaires générées par les imperfections statiques de la machine en condition réelle à été étudiée. Les performances comparables, en terme de luminosité et de réglage de la machine, entre les différentes options de L^* pour chaque phase d'énergie, ont fait du design avec $L^* = 6$ m, un candidat sérieux pour devenir la nouvelle conception de référence pour le CLIC.

La ligne optique nominale ($\beta_y^* = 100\mu$m) et à ultra-bas β_y^* ($\beta_y^* = 25\mu$m) de l'ATF2 ont été conçues à la fois pour tester la faisabilité du FFS de l'ILC et pour étudier les capacités et limitations lorsque l'ATF2 opère avec un niveau de chromaticité comparable à celui du CLIC. La taille verticale du faisceau au point d'intéraction virtuel de l'ATF2 pour l'optique à ultra-bas β_y^* est de 20 nm, lorsqu'une paire d'octupôles est ajoutée à la ligne de faisceau pour la correction des aberrations chromatiques et géometriques de troisième ordre. Dans cette thèse, différentes configurations de β_x^* pour l'optique à ultra-bas β_y^* ont été ré-optimisées, en y incluant les nouvelles spécifications des octupôles ainsi que les récentes mesures d'erreurs de champs magnétiques d'ordre supérieur. Les aberrations non-linéaires dominantes contribuant à l'accroissement de la taille verticale du faisceau ont été identifiées et des simulations de corrections sous des conditions réalistes d'imperfections de la machine ont été éffectuées pour préparer la première implémentation expérimentale de l'optique à ultra-bas β_y^* ainsi que les premiers tests *in situ* des octupôles à l'ATF2. L'alignement de l'octupôle possédant la tolérance la plus faible aux désalignments transversaux a été effectué. Pendant les opérations de Juin et Novembre 2017, les octupôles ont permis d'identifier et corriger certaines aberrations résiduelles de second ordre. En Décembre 2017, l'optique à ultra-bas β_y^* à été implémentée et testée pour la première fois. Les multiples corrections apportées au faisceau ont permis d'obtenir une taille verticale moyenne de 97±6 nm. L'exploitation des résultats de Décembre 2017 ont permis d'améliorer le modèle optique de la ligne du faisceau et de pouvoir le tester à nouveau à l'ATF2 en Février 2018. Les améliorations de l'optique à ultra-bas β_y^* ont permis de réduire la taille moyenne du faisceau vertical à 70±6 nm en appliquant uniquement des corrections aux aberrations linéaires. Les leçons tirées de ces opérations et les actions requises pour les futures études expérimentales de l'optique à ultra-bas β_y^* sont également abordées dans cette thèse.

Abstract

Keywords : Lepton collider, linear accelerators, Final Focus System (FFS), beam dynamics, optics optimization, luminosity, chromaticity, linear and nonlinear aberration corrections, octupole magnets, ATF2, CLIC, final focal length L^*, machine-detector interface

The high energy physics community worldwide envisage to complement the results of the Large Hadron Collider (LHC) by experiments at a lepton collider where the collisions are of order tera-electron-volts (TeV). The future machines considered to carry out high precision physics in the TeV energy regime are electron-positron (e^+e^-) linear colliders, providing high luminosities to increase the potential of discoveries.
In order to achieve the design luminosity $\mathcal{L}$ above $10^{34}\text{cm}^{-2}\text{s}^{-1}$, linear colliders feature nanometer beam spot sizes at the Interaction Point (IP). The Beam Delivery System (BDS) transports the e^+ and e^- beams from the exit of the linacs to the IP by performing the critical functions required to meet the CLIC luminosity goal such as beam collimation and focusing. The beam is focused through the Final Focus System (FFS) while correcting higher order transport aberrations in order to deliver the design IP beam sizes. The chromatic contributions are amplified by the focusing strength of the two last quadrupoles named QD0 and QF1, reffered to as the Final Doublet (FD), and by the length of the final focal distance L^* between QD0 and the IP. The chromaticity correction approach chosen for the CLIC FFS is based on the Local chromaticity correction scheme which uses interleaved pairs of sextupole magnets in the FD region in order to locally and simultaneously correct horizontal and vertical chromaticity.
The current linear collider projects, the Compact Linear Collider (CLIC) and the International Linear Collider (ILC) have FFS lattices based on the Local Chromaticity correction scheme. This scheme is being tested in the Accelerator Test Facility 2 (ATF2) at KEK (Japan). This thesis concentrates on problems related to the optimization of BDS lattices for the simplification of the CLIC Machine Detector Interface (MDI) and on the experimental work for the implementation and study of a CLIC-like FFS optics for the ATF2, referred to as ultra-low β_y^* optics.

In the Conceptual Design Report (CDR) for CLIC, the last quadrupole magnet of the accelerator, QD0, was embedded in the detector. This layout choice was enforced to allow for the highest possible luminosities, obtained with a short distance L^*. There were a number of issues concerning the layout of the CLIC experimental area, including the magnetic field interplays between QD0 and the detector, QD0 stabilization, integrated luminosity loss due to longer interventions, and loss of coverage in the forward region of the detector. In order to alleviate these issues, a new detector concept has been proposed, moving QD0 to an L^* of 6 meters, outside of the detector. As recent implementation studies for CLIC have converged towards a new staged construction approach, CLIC would provide e^+e^- collisions covering a centre-of-mass energy range from 380 GeV to

3 TeV. In this thesis, new FFS designs with $L^* = 6$ m were optimized for the first and final energy stages of CLIC. The luminosity performance and the capacity of the machine to recover the luminosity loss due to realistic lattice imperfections have been studied for the short (nominal) and the longer L^* options. The luminosity performances of these new lattices meet the CLIC design requirements. Important steps towards showing the tunability of the nominal and long L^* FFS designs has been achieved. The close luminosity and tuning performances between both L^* options at both energy stages show that the $L^* = 6$ m design is a feasible candidate for being the new baseline for CLIC.

The ATF2 Nominal ($\beta_y^* = 100\mu$m) and ultra-low β_y^* ($\beta_y^* = 25\mu$m) lattices are designed to test the feasibility of the FFS of ILC and to study the possible performance limitations when operating the FFS with a chromaticity level comparable to the one of CLIC. The design IP vertical beam sizes for the ultra-low β_y^* optics of 20 nm is achieved when a pair of octupoles is optimized in the lattice to correct 3^{rd} chromatic and geometric vertical aberrations. In this thesis, different β_x^* configurations for the ultra-low β_y^* optics have been re-optimized, including updated specifications of the octupoles and their measured magnetic multipole errors. The dominant higher order contributions to the vertical beam size, σ_y^*, have been identified and tuning simulations have been performed to prepare the first experimental implementation of ultra-low β_y^*, as well as first tests *in situ* of the octupoles at ATF2. The goals were to apply the optics with β_y^* reduced to 25μm, prepare the octupoles for operation and address the main limitations when tuning the machine using the octupoles. The beam based alignment of the octupole with the tightest misalignment tolerance has been performed. In June and November 2017, the octupoles were shown to be helpful in identifying and correcting residual 2nd order aberrations through the transverse displacement of the octupoles during nominal optics tuning operations. In December 2017, ultra-low β_y^* optics have been implemented and tuned for the first time at ATF2. The long machine tuning converged to an average beam size of 97±6 nm. From the observations made during December operation, the optics model have been improved and tested once again at ATF2 during February 2018 operation. The improved ultra-low β_y^* have allowed to bring down the average vertical beam size to 70±6 nm with only linear knobs applied. The lessons learnt from these tuning operations and the required actions for the future ultra-low β_y^* lattice tuning sessions are also adressed in this thesis.

Acknowledgments

I am very grateful to all of those with whom I have had the great pleasure de collaborate on this PhD project.

My foremost thanks go to my thesis supervisor Rogelio Tomàs for whom I am considerably grateful, for his constant and very enthusiastic support towards the successful completion of this project. I wish to thank him for his invaluable help, for the trust he placed in me and for the rich scientific experience I gained throughout my time at CERN and KEK as a Technical student and as a PhD student.
I am deeply grateful to my University supervisor, Philip Bambade, for the help, for the interesting and motivating discussions during workshops and ATF2 operations at KEK, and for the support during the last 3 years despite the distance from Paris.

My sincere gratitude to Eduardo Marin Lacoma, Hector Garcia Morales, Oscar Blanco, Daniel Schulte, Andrea Latina and Marcin Patecki (CERN) for transmiting their knowledge on CLIC and ATF2 that I extensively benefited. I wish to thanks all the CLIC Beam Physics, MDI and Detector working groups, especially Lau Gatignon, Michele Modena, Elsener Konrad and Dominik Arominski for the fruitful discussions during meetings and workshops.

I would like to thanks the ATF and KEK staff for their help and hospitality. Special thanks to Toshiyuki Okugi, Kiyoshi Kubo, Nobuhiro Terunuma, Takashi Naito, Shigeru Kuroda, Toshiaki Tauchi (KEK), Glen White (SLAC), Douglas Bett and Marcin Patecki (CERN) who taught me so much about the ATF2 machine operation and also Jonas Breunlin, Eduardo Marin, Vera Cilento and Pierre Korysko (CERN) who gave me precious help during low-β_y^* operations. Many thanks to the FONT group, Philip Burrows, Neven Blaskovic Kraljevic, Talitha Bromwitch, Douglas Bett and Rebecca Ramjiawan (Oxford university) for their invaluable help on using the IPBPMs and also Michele Bergamaschi and Renjun Yang for the very helpful discussions and help in the ATF2 control room.
Many thanks to the European Commission's Horizon 2020 Programme through the Marie S. Curie RISE project E-JADE, who financially supported my work performed at KEK in Japan.

Special thanks to Felix Carlier, Lee Carver and Michael Schenk for the help, the support and for making the office a enjoyable and motivating workplace.
Finally, I would like to deeply thanks my parents, sister and brothers, friends and La Montagne, for the endless support and encouragement despite the distance from Réunion Island. Most importantly, I would like to express my profound gratitude to my beloved girlfriend Tiphaine, who was always by my side to help, encourage and inspire me during my PhD.

Contents

1 Introduction **1**
- 1.1 Motivations for e^+e^- linear colliders . . . 1
- 1.2 Overview of the current projects and test facilities . . . 2
  - 1.2.1 The proposed future linear colliders . . . 2
  - 1.2.2 Test facilities . . . 3
- 1.3 CLIC baseline-staging scenario . . . 6
- 1.4 The CLIC Beam Delivery System . . . 6
  - 1.4.1 Collimation Section . . . 8
  - 1.4.2 Final Focus System . . . 9

2 Beam Dynamics in FFS **11**
- 2.1 Basic concept of linear transverse beam optics . . . 11
- 2.2 Nonlinear magnetic multipoles . . . 15
- 2.3 Chromaticity and correction concept . . . 17
- 2.4 Synchrotron radiation . . . 19
- 2.5 Oide effect . . . 20
- 2.6 Luminosity . . . 20
- 2.7 Effects of the detector solenoid . . . 22
- 2.8 Tuning the FFS . . . 23
  - 2.8.1 Beam Based Alignment . . . 24
  - 2.8.2 Linear and Nonlinear aberration correction techniques . . . 24

3 CLIC 3 TeV BDS optics optimization with $L^* = 6$ m **29**
- 3.1 Impact of the L^* on the CLIC MDI . . . 29
  - 3.1.1 MDI with the CLIC CDR FFS design . . . 29
  - 3.1.2 Motivations for a long L^* FFS . . . 30
- 3.2 High order optimization of the FFS with $L^* = 6$ m . . . 32
  - 3.2.1 Optics design procedure . . . 32
- 3.3 Higher order optimization of the BDS . . . 37
- 3.4 Optics comparison with CDR FFS design . . . 40
  - 3.4.1 Parameters . . . 40
- 3.5 Quadrupole stabilization tolerances . . . 42
  - 3.5.1 Multipolar tolerances . . . 42
- 3.6 Collimation depth . . . 44
- 3.7 Tuning of the FFS . . . 46
  - 3.7.1 Tuning under transverse misalignment . . . 47
  - 3.7.2 Tuning results of the optimized lattice . . . 50
  - 3.7.3 Tuning under realistic static imperfections . . . 51
  - 3.7.4 Executive summary . . . 54

4 Alternative FFS length optimization with L* = 6 m and L* = 3.5 m for CLIC 3 TeV **57**
4.1 Shorter FFS with L* = 6 m for tunnel cost reduction . . . 57
4.1.1 Chromaticity correction preservation for shorter designs . . . 57
4.1.2 Luminosity performances . . . 61
4.1.3 Impact on tuning efficiency . . . 62
4.2 Longer FFS with L* = 3.5 m to ease the tuning . . . 65
4.2.1 Chromaticity correction preservation for longer designs . . . 66
4.2.2 Luminosity performances . . . 67
4.2.3 Impact on tuning efficiency . . . 69
4.2.4 Executive summary . . . 70

5 CLIC BDS optimization at $\sqrt{s}$ = 380 GeV: L* = 4.3 m vs L* = 6 m **73**
5.1 BDS optics design optimization . . . 73
5.2 Design optimization for the CLIC energy upgrade . . . 82
5.3 Tuning of the Final Focus System . . . 83
5.4 Dispersion impact on tuning under transverse misalignment . . . 86
5.5 Alternative optics for beamstrahlung minimization . . . 89
5.6 Executive summary . . . 91

6 The Accelerator Test Facility 2 (ATF2) **93**
6.1 Motivations for ultra-low β_y^* study at ATF2 . . . 93
6.2 Simulation studies of the ATF2 ultra-low β_y^* optics . . . 95
6.2.1 Optics design and higher order correction . . . 95
6.2.2 Tuning of the FFS for lower β_y^* optics . . . 99
6.3 Experimental study of the ultra-low β_y^* optics tuning . . . 102
6.3.1 Diagnostics and correction techniques used for beam size tuning . . . 102
6.3.2 The ATF2 octupoles . . . 107
6.3.3 $25\beta_x^* \times 0.25\beta_y^*$ optics tuning measurements at ATF2 . . . 111
6.3.4 Discussion on the measurements of February 2018 . . . 122

7 Conclusions **127**

Bibliography **143**

Chapter 1

Introduction

This chapter gives a brief overview of the major physics challenges and opportunities of future e^+e^- linear colliders in the 380 GeV - 3 TeV center of mass energy region. The two proposals for the next generation of linear colliders with their current associated accelerator test facilities are decribed, with special emphasis on the Beam Delivery System of the Compact Linear Collider (CLIC).

1.1 Motivations for e^+e^- linear colliders

The Large Hadron Collider (LHC) is currently exploring physics in the energy regime of 13 -14 TeV center-of-mass energy since the start of its Run 2 (2015), delivering luminosity above $10^{34}\text{cm}^{-2}\text{s}^1$ [1]. An upgrade of the LHC is forseen, the High Luminosity LHC (HL-LHC) [2], delivering luminosity up to a factor 5 larger than the LHC nominal value and enabling to operate the collider beyond 2025 with extanded exploitation of the LHC physics potential. The future of high-energy accelerators will depend on the results and eventual discoveries given by the LHC. e^+e^- colliders are the best candidates to determine accurately the properties of new particles discovered by the LHC [3]. The unique feature of linear colliders is the low backgrounds arising from the elementary e^+ and e^- particle collisions which can be orders of magnitude lower than the backgrounds faced by hadron collider experiments. Linear colliders preserve polarization to a very high degree which provides crucial informations about the spin orientations of the interacting particles. The clean experimental environment and the well-specified center-of-mass energy and initial state, allows precise and unbiased measurements of the standard model. The background can be further reduced and the initial state can be more precisely known by the possibility of higher polarization of the e^+ and e^- beams. Moreover, as the e^+e^- initial state is electrically neutral, the leptons and hadrons events may be studied with comparable statistics [4]. More details about the physics potential of linear colliders as well as interesting opportunities for e^-e^-, $e^-\gamma$ or $\gamma\gamma$ colliders to probe new physics can be found in [3, 5].
The choice of linear rather than circular e^+e^- colliders to study the particle physics at the TeV energy regime was driven by the amount of radiated energy of the charged particles moving in the accelerator, called synchrotron radiation. This radiation causes important energy loss in the required bending magnets for electrons and positrons with sufficiently high energy. The radiated power emitted during transverse acceleration of relativistic charged particles is given by:

$$P_s = \frac{e^2 c}{6\pi\varepsilon_0}\frac{E^4}{(m_0c^2)^4\rho_r^2} \tag{1.1}$$

where e is the electron charge, ε_0 is the electric permittivity of vacuum, c the speed of light, E is the partcile energy, m_0 is the rest mass and ρ_r is the bending radius of the particle trajectory. The power emitted by syncrotron radiation is inversely proportional to the fourth power of the energy at rest, where for electrons $m_e c^2 = 0.511$ MeV and for protons $m_p c^2 = 938.19$ MeV. The energy loss increases the cost of running the machine during its operation and thus e^+e^- circular colliders are economically less interesting than linear colliders, especially at the TeV energy range. However, one can limit the radiated energy of e^+e^- circular collider by increasing the machine radius as shown in Eq.(1.1). Such a collider is under design study, the Future Circular Collider for e^+e^- collisions (FCC-ee), which will be constructed in a 80-100 km tunnel in the Geneva area and envisages centre-of-mass energy from 90 to 400 GeV [6]. The FCC-ee would be the first step towards the long-term goal of a 100 TeV proton-proton collider (FCC-hh). The energy loss due to synchrotron radiation is negligeable in e^+e^- linear colliders allowing them to reach multi-TeV center-of-mass energy as detailed in Section 1.2.

1.2 Overview of the current projects and test facilities

Two e^+e^- linear colliders are proposed to complement the LHC physics study, the International Linear Collider (ILC) [7] and the Compact Linear Collider (CLIC) [8]. Both proposals are studied by an international collaboration with different laboratories and universities worldwide. Although the technology used for particle acceleration is different between CLIC and ILC, they are both composed of the similar main subsystems:
Sources of e^- and e^+ : Electrons are produced by the interaction of an intense laser beam and a semiconductor cathode which causes the production of electron bunches. Positrons production is based on the interation of gamma photons, resulting from the radiation of an electron beam passing through undulators, with a target producing pairs of longitudinally polarized electrons and positrons [9]. Particles coming from the source are pre-accelerated and transported towards the Damping Ring.
Damping Ring : The beams transverse emittances are reduced by several orders of magnitude in a few hundreds of milliseconds using the synchrotron radiation caused by superconducting wigglers [10].
Main Linac : The beam energy is increased up to its design value while preserving small emittance.
Beam Delivery System (BDS): Is responsible for transporting the beams from the exit of the high energy linacs, focusing them to the sizes required to meet the luminosity goals. the BDS must perform several critical functions as performing the beam diagnostics, collimation, transport and match the beam into the Final Focus System. More details are given in Section 1.4.

1.2.1 The proposed future linear colliders

ILC The International Linear Collider is based on 1.3 GHz superconducting radio frequency accelerating cavities with gradient of 31.5 MV/m each. The same cavitites are being used by the European XFEL facility at Desy [11]. The ILC is designed to achieve

Table 1.1: CLIC and ILC design parameters

	ILC 500 GeV	CLIC 380 GeV	CLIC 3 TeV
Luminosity $\mathcal{L}_{\text{total}}$ [$10^{34}\text{cm}^{-2}\text{s}^{-1}$]	1.8	1.5	5.9
Peak luminosity $\mathcal{L}_{1\%}$ [$10^{34}\text{cm}^{-2}\text{s}^{-1}$]	1.05	0.9	2
Repetition rate f_{rep} [Hz]	5	50	50
Bunch length σ_z [μm]	300	70	44
Bunch population N_e [$\times 10^9$]	2.0	5.2	3.72
Number of bunches n_{b}	1312	352	312
Bunch separation [ns]	554	0.5	0.5
Accelerating gradient [MV/m]	31.5	72	72 / 100
Estimated power consumption [MW]	163	252	589
Proposed site length [km]	31	11.4	50.1

center-of-mass energy range between 200 MeV and 500 GeV in the first four years of operation. The machine could be upgraded to a center-of-mass of 1 TeV. The Beam Delivery System design and the Machine Detector Interface are comparable for ILC and CLIC, and will be described in Sections 1.4 and 3.2. The main beam parameters are summarized in Table 1.1.

CLIC The Compact Linear Collider is a project led by CERN that aims to collide e^+e^- beams with center of mass up to 3 TeV delivering a total luminosity $\mathcal{L}_{\text{total}}$ of $5.9\times10^{34}\text{cm}^{-2}\text{s}^{-1}$ and a peak luminosity $\mathcal{L}_{1\%}$, coming from the collisions with energy larger than 99% of the maximum energy, of $2\times10^{34}\text{cm}^{-2}\text{s}^{-1}$. The nanometer level beam spot size at the Interaction Point (IP), required to reach the design luminosity is achieved through the Beam Delivery System (BDS) detailed in Section 1.4.The high beam energy is achieved by an innovative two-beam acceleration design, using accelerating cavitites made of copper, delivering an accelerating gradient of 100 MV/m [12]. The CLIC accelerating scheme allows to increase the beam energy from 9 GeV, coming from the Damping Rings, to 1.5 TeV in a single pass. Beam power is extracted from the drive beam and converted to RF power in special RF devices called PETS (Power Extraction and Transfer Structures) and it is then transported to the accelerating structures in the Main Beam. The high current drive beam is obtained by recombining the bunches coming from the drive beam accelerator. This recombination is done in the delay loop and the combiner rings CR1 and CR2 [13, 14]. The main parameters are summarized in Table 1.1.

1.2.2 Test facilities

CTF3 The CLIC Test Facility has been built at CERN and has demonstrated the feasibility of the high-current Drive Beam production by means of the bunch recombination. It has also demonstrated the possibility to efficiently extract the power from the Drive Beam, and to validate the two-beam acceleration scheme by accelerating a witness electron beam provided by a dedicated injector. The beam parameters have been scaled

with respect to the CLIC design [15].

FFTB The Final Focus Test Beam was located at the end of the SLAC linac (SLC), which was delivering an electron beam with an energy of about 46.6 GeV. The goal was to reduce the beam size following the non-local chromaticity correction, called "Traditional" Final Focus System scheme (see Section 1.4.2). The smallest vertical beam size measured was 70±7 nm [16].

ATF2 The Accelerator Test Facility 2 [17,18], based at KEK (Japan), was constructed in 2008. It is a scaled down implementation of the linear collider beam delivery system, which serves for demonstrating the feasibility of final focus systems for ILC and CLIC. The main purpose of the ATF2 beam line is to demonstrate beam focusing with a novel final focus system scheme called local chromaticity correction [19], and to establish a beam tuning method for linear collider final focus systems (see Section 2.8).
The electron bunches are produced by an RF gun and accelerated by an s-band linear accelerator up to 1.3 GeV before entering the damping ring. The damping ring has a 140 m circumference and delivers vertical beam emittance below 10 pm [20, 21]. The beam is extracted from the ATF Damping Ring (DR) to perform the nanometer beam size focusing and stabilisation. The total length of the ATF2 beam line is 90 m, with 52 m long extraction line (EXT) and 38 m long final focus (FF) line. The EXT line is used for the extraction and manipulation of the beam out of the DR and preparing it for injection into the FF. The beam is focalized to the required size using the two last quadrupoles QF1FF and QD0FF where the chromaticity is locally corrected by means of 5 normal sextupole magnets. The beam size is measured at the IP using the Shintake monitor which can measure the beam vertical beam size down to 20 nm [22, 23]. The ATF DR and ATF2 beamline is illustrated in Figure 1.1.
The chromaticity of the ATF2 beam line is designed to be comparable to the ILC final focus system with a resulting design IP vertical beam size of 37 nm (see Table 1.2). In 2016, the vertical beam size was focused to less than 41 nm at the bunch population of 0.7×10^9 at the IP using optics referred to as 10×1 optics because of the 10 times larger than design β_x^* [24].
CLIC FFS tuning feasibility study is also being carried out at ATF2. The aim is to demonstrate the small beam tuning feasiblity at the CLIC chromaticity level, expected to be 5 times larger than ILC. The chromaticity approximately scales as $\xi_y \propto \frac{L^*}{\beta_y^*}$ and therefore β_y^* is decreased by a factor 4 in order to bring the chromaticity close CLIC as shown in Table 1.2. The optics used for CLIC study is referred as ultra-low β_y^* optics or 1×0.25 optics. The design beam size achievable with the ultra-low β_y^* optics is limited to 29 nm due mainly to amplified higher order aberrations and magnetic imperfections such as multipolar errors. However the beam size can be reduced in design to 20 nm if a pair of octupoles is introduce in the final focus line [25]. This pair of octupoles have been designed at CERN and installed in ATF2 beamline in November 2016 [26]. Optics optimization, tuning simulations and experimental results on the ultra-low β_y^* optics study at ATF2 using octupoles are detailed in Chapter 6.

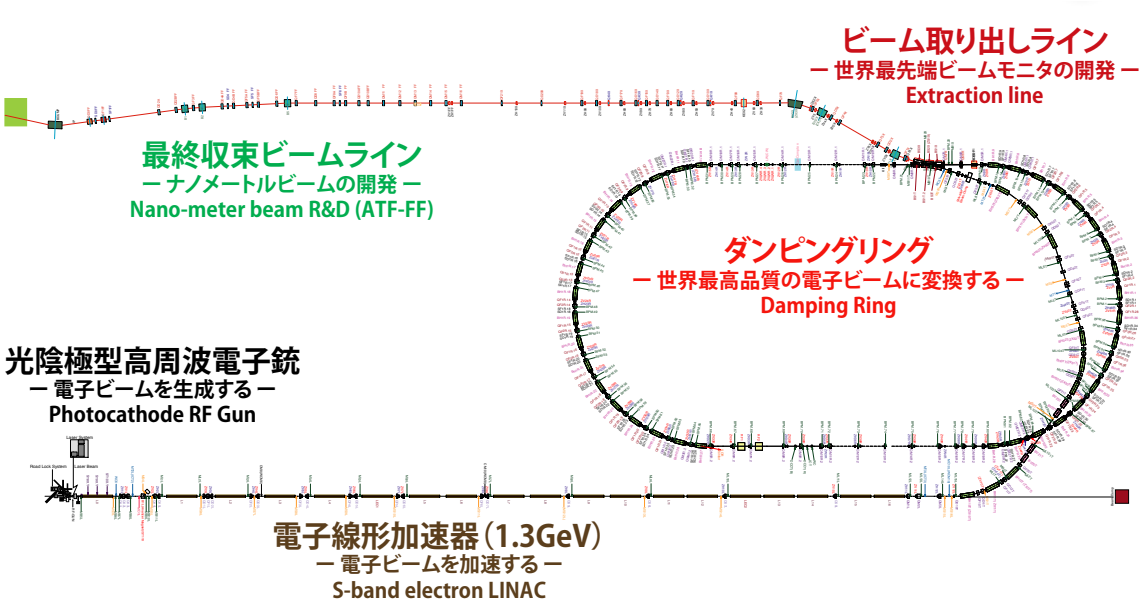

Figure 1.1: General scheme of the Accelerator Test Facility

Table 1.2: Beam and optics parameters for the ILC, CLIC and ATF2 Final Focus

	ILC	CLIC	ATF2 ($10\beta_x^* \times 1\beta_y^*$)	($10\beta_x^* \times 0.25\beta_y^*$)
Beam energy [GeV]	500	3000	1.3	1.3
L^* [m]	4.1	6	1	1
ε_y [pm]	0.07	0.003	12	12
β_x^* / β_y^* [mm]	11 / 0.48	4 / 0.07	40 / 0.1	40 / 0.025
σ_x^* [μm] / σ_y^* [nm]	0.47 / 5.9	0.04 / 1	8.9 / 37	8.9 / 20
Chromaticity ($\frac{L^*}{\beta_y^*}$)	8542	50000	10000	40000
QD0 length [m]	2.2	4.7	0.475	0.475
QF1 length [m]	2.0	5.6	0.4441	0.4441
Length between the FD [m]	3.9	6.83	0.905	0.905

1.3 CLIC baseline-staging scenario

The optimised staging scenario foresees three main centre-of-mass energy stages at 380 GeV, 1.5 TeV and 3 TeV for a full CLIC programme. The Conceptual Design Report (CDR) [8] published in 2012, projected collisions at 500 GeV c.o.m energy for the first energy stage. Recent studies for CLIC have converged towards a staged approach offering a more suitable physics programme for the post-LHC era. The first stage is proposed to be at 380 GeV [27]. At this energy, precision Higgs physics will be one of the main focuses of the CLIC programme with particular emphasis on the Higgsstrahlung process which dominates Higgs production at this energy. More details about physics potential at CLIC 380 GeV can be found in [28]. The implementation scenario CLIC energy stages

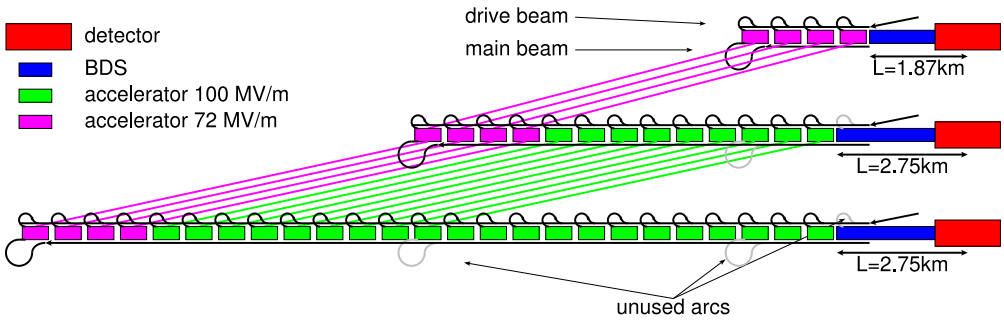

Figure 1.2: CLIC potential energy staging concepts for 380 GeV, 1.5 TeV and 3 TeV c.o.m. In this solution, the modules at the beginning of the previous main linac are moved to the new beginning during the upgrade.(Figure taken from [8])

is shown in Figure 1.2. The first energy stage requires four decelerator structures in order to increase each beam energy to 190 GeV while an additional 21 decelerator are needed for the final energy stage. The CLIC 380 GeV uses a single drive-beam generation complex to feed both linacs while two are needed for CLIC 3 TeV as illustrated in Figures 1.3 and 1.4. The optics optimization of the Beam Delivery Systems taking into account the energy staging strategy in the CLIC tunnel, where the Linacs are aligned, is detailed in Chapter 5.

1.4 The CLIC Beam Delivery System

The Beam Delivery System (BDS) transports the e^+ and e^- beams from the exit of the linacs to the IP by performing the critical functions required to meet the CLIC luminosity goal [29]. The optical functions and layout of the entire BDS is shown in Figure 1.5. The beam properties are measured in the Diagnostic section at the exit of the linacs and corrected before entering the Collimation system. There, the particles with transverse amplitude or energy deviations significantly larger than those of the reference particle, referred to as beam halo, are intercepted by the betatron and energy collimation system to protect the down-stream beam line and to minimize background in the detector. The

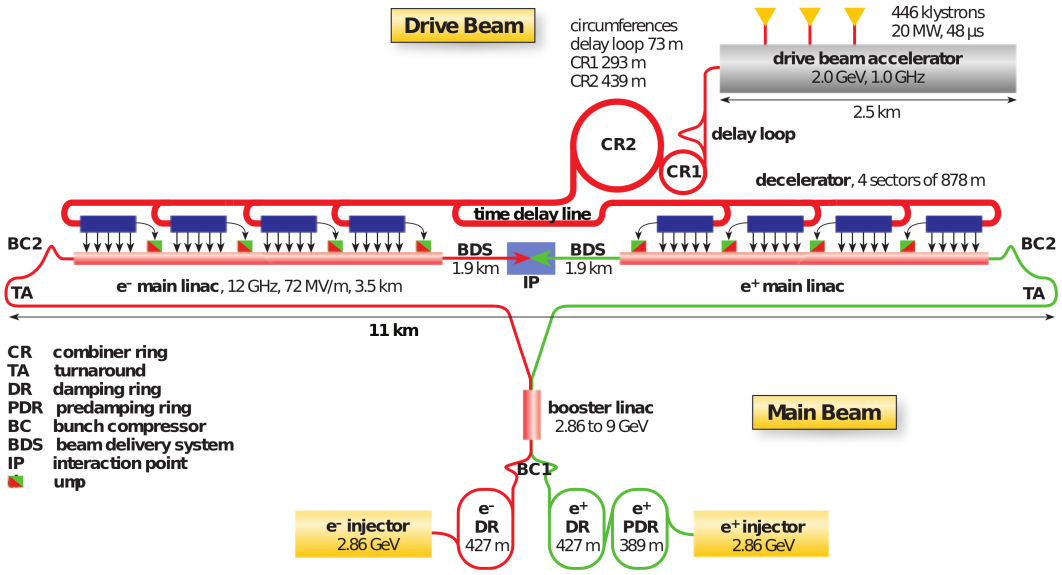

Figure 1.3: General scheme of the CLIC 380 GeV (Figure taken from [8])

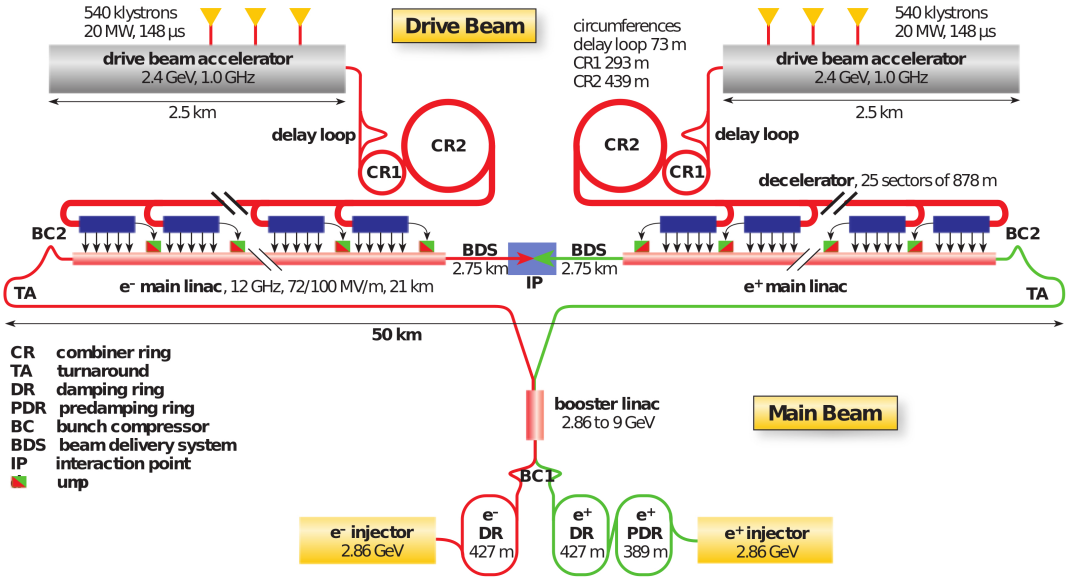

Figure 1.4: General scheme of the CLIC 3 TeV (Figure taken from [8])

beam is then focalized through the Final Focus System (FFS) while correcting higher order transport aberrations in order to deliver horizontal and vertical beam sizes close to the CLIC design requirements ($\sigma_x^* = 40$ nm and $\sigma_y^* = 1$ nm). A more detailed description of the main subsystems and key functions of the Collimation section and FFS are given

in the following Sections.

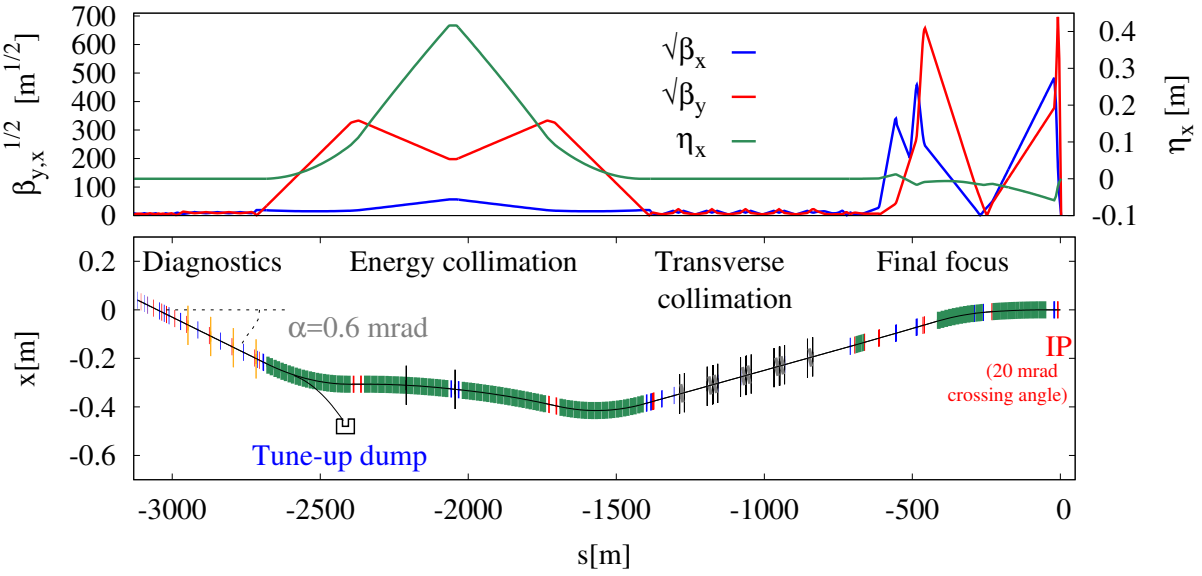

Figure 1.5: Optics (top) and layout (bottom) of the CLIC 3 TeV Beam Delivery System ($L^* = 6$ m FFS).

1.4.1 Collimation Section

The layout of the entire Collimation section is shown in Figure 1.5. The Diagnostic section is the initial part of the BDS. It includes 4 skew quadrupoles which independently correct the 4 transverse coupling parameters. It contains also 4 laser wires for the measurement of the beam size down to 1 μm, which allow to reconstruct the full 2D transverse phase space and thus determine the projected horizontal and vertical emittances. The energy collimation section is designed to intercept mis-steered or errant

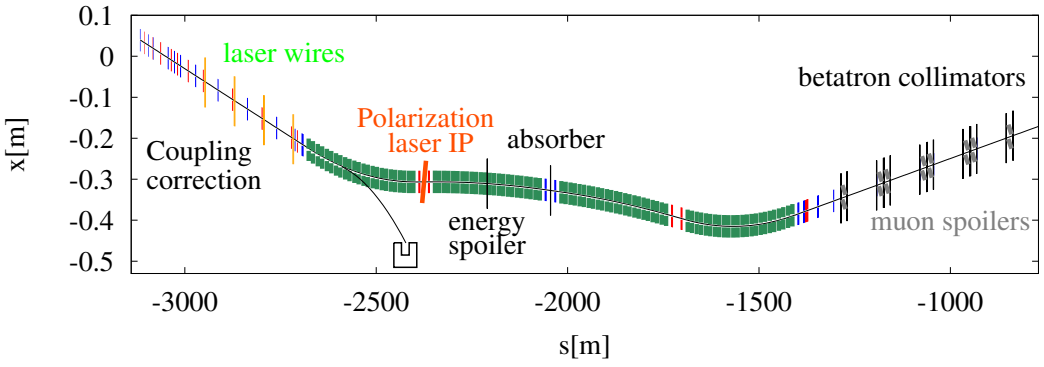

Figure 1.6: Layout of the CLIC 3 TeV collimation system.

beams with large energy deviation by means of an energy spoiler which can survive the

impact of a full bunch train [30]. The scattered particles from the energy spoiler are stopped downstream by a collimator absorber. The beam particles with large betatron amplitudes are removed by betatron collimators in the transverse collimation section in order to provide acceptable experimental background. The collimator gaps must ensure that neither beam particles nor synchrotron radiation photons emitted hits the final quadrupoles, the vertex detector or the extraction quadrupole. It was found in [31] that high energy secondary muons can be produced in the collimation section, creating undesired background in the detector. The muon rates are kept low in the experiment by means of muon spoilers in the transverse collimation section.

1.4.2 Final Focus System

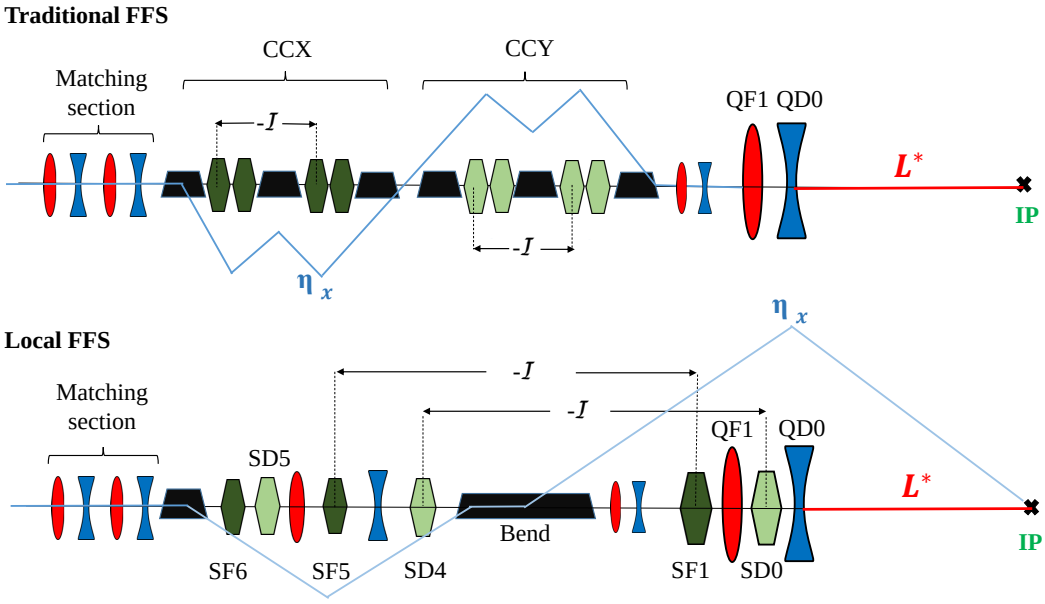

Figure 1.7: Simplified layout of the Traditional FFS scheme (upper plot) versus the Local chromaticity correction scheme (bottom plot). The blue lines represents the horizontal dispersion η_x along the system. The sextupoles are represented by green hexagons.

The strong focusing required to achieve the nanometer level beam size at the IP for CLIC is driven by the two last quadrupoles (QF1 anf QD0), referred to as Final Doublet (FD). The final focus forms an almost parallel beam at the entrance of the FD of several hundreds of nanometers which is then demagnified down to few nanometers at the IP. The beam coming from the main linac is not fully monochromatic and even a minor energy spread of a fraction of percent ($\approx$ 0.3 % for CLIC), will focalize particles with different energies at different points causing large dilution of the beam size at the IP. The chromaticity is amplified by the focusing strength of the FD and by the length of the focal distance between QD0 and the IP called L^*. The FFS design is thus driven by the compensation of these chromatic effects mainly generated by the FD. The chromaticity

is corrected using sextupoles in dispersive regions and located in a way to cancel the geometrical aberrations introduced as detailed in Section 2.3. There are two chromaticity correction approaches for future linear collider FFS: the non-local chromaticity correction scheme, referred to as Traditional scheme, and the Local scheme.
The Traditional design, experimentally validated at FFTB [16], consists in two dedicated sections for the horizontal and vertical chromaticity correction, called CCX and CCY respectively. The sextupoles are introduced in pairs in high horizontal dispersion η_x and high β values and separated by a π-phase advance, allowing a minus identity transformation matrix between them ($M = -\mathcal{I}$) for the cancellation of the second order geometrical aberrations introduced by these sextupoles. The chromaticity is fully compensated in CCX and CCY and thus the dispersion is zeroed downstream of the FD. The non-zero dispersion regions are introduced by the bending magnets, in both chromaticity correction sections as illustrated in Figure 1.7. In order to be applicable to multi-TeV scale e^+/e^- colliders, the traditional scheme must have long and weak bending magnets in order to minimize the synchrotron radiation emitted which can significantly degrade the luminosity. Therefore, the traditional FFS scheme optimized and proposed for CLIC 3 TeV is 1503 meters [32, 33]. The Local scheme uses interleaved pairs of sextupole magnets in the FD region in order to locally and simultaneously correct horizontal and vertical chromaticity. Upstream bending magnets generate dispersion throughout the FFS which is then zeroed at the IP. Sextupoles placed in FD region generate second order dispersion. However, it can be compensated simultaneously with x and y chromaticity provided that half of the total horizontal chromaticity of the whole FFS is generated upstream. Geometrical aberrations are cancelled by separating the sextupoles with a $-\mathcal{I}$ matrix transformation. Two more sextupoles (SF6 and SD5 shown in Figure 1.7) are used to correct higher order aberrations. More details are presented in Section 2.3. This scheme requires fewer bendings, making the FFS more compact than the traditional scheme with a total length of about 450 meters. It also shows larger momentum bandwidth, which represents the luminosity loss due to the possible energy mismatch coming from the linac, thanks to the locality of the correction [19]. This new scheme, is considered as baseline for CLIC and ILC FFS and it is currently being tested at ATF2.

Chapter 2

Beam Dynamics in FFS

This chapter aims to provide an overview of key concepts of transverse beam dynamics neeeded to apprehend the results, measurements and correction techniques which are extensively used throughout this thesis. A complete description of beam dynamics theory is comprehensively described in specialized books on accelerator physics, i.e [34–37]. First, we introduce the matrix formalism used in linear beam optics to describe the transport of the beam and the properties of the lattice. Then we describe the dynamics of the particles transported through multipolar elements such as sextupoles and octupoles, and the chromaticity correction theory applied to linear collider FFS. We then explore the dominant effects impacting the final performance of the collider and the optics design of the FFS, such as synchrotron radiation, Oide effect, beam-beam forces, impact of the detector solenoid and beamline imperfections. Finally, we present the concepts of linear and nonlinear beam tuning techniques which are applied for CLIC FFS simulations and experimentally at ATF2.

2.1 Basic concept of linear transverse beam optics

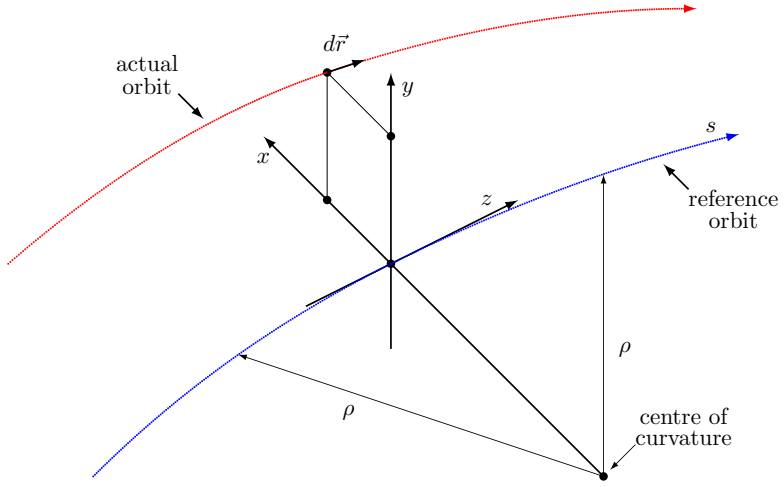

Figure 2.1: Coordinate system used to describe the motion of particles. Figure comes from [38]

The beam line is described as a sequence of magnetic elements placed along a reference orbit, such as dipole bending the particle trajectory and quadrupoles focalising the beam.

The reference orbit refers to the path of the charged particle traveling along the reference trajectory s with its ideal momentum p_0 through ideal magnets. The horizontal and vertical positions are given by the axis x and y, respectively. The longitudinal position within the bunch is denoted by z. Each particle at any location along the beam line can be represented in phase space by its canonical coordinates $\vec{u_{\mathrm{f}}} = (x,\, x',\, y,\, y',\, z,\, \delta_p)$. Where the x' and y' coordinates are the horizontal and vertical slopes defined as $x' = \frac{\mathrm{d}x}{\mathrm{d}s}$ and $y' = \frac{\mathrm{d}y}{\mathrm{d}s}$. The δ_p coordinate refers to the particle momentum deviation normalised to p_0. In linear transverse beam optics, the particles are transported through the sequence of magnetic elements by a linear map of the initial phase space coordinates:

$$\vec{u_{\mathrm{f}}} = \mathrm{R}\vec{u_0} = \begin{pmatrix} \mathrm{R}_{11} & \mathrm{R}_{12} & \mathrm{R}_{13} & \mathrm{R}_{14} & \mathrm{R}_{16} \\ \mathrm{R}_{21} & \mathrm{R}_{22} & \mathrm{R}_{23} & \mathrm{R}_{24} & \mathrm{R}_{26} \\ \mathrm{R}_{31} & \mathrm{R}_{32} & \mathrm{R}_{33} & \mathrm{R}_{34} & \mathrm{R}_{36} \\ \mathrm{R}_{41} & \mathrm{R}_{42} & \mathrm{R}_{43} & \mathrm{R}_{44} & \mathrm{R}_{46} \\ \mathrm{R}_{61} & \mathrm{R}_{62} & \mathrm{R}_{63} & \mathrm{R}_{64} & \mathrm{R}_{66} \end{pmatrix} \begin{pmatrix} x \\ x'_0 \\ y_0 \\ y'_0 \\ \delta_p \end{pmatrix}, \tag{2.1}$$

where $\vec{u_0}$ and $\vec{u_{\mathrm{f}}}$ are the initial and final coordinates, respectively. R is the square matrix that represents an ensemble of elements of the lattice from position $0 \to f$. Each element along the beamline, such as dipoles, quadrupoles or drifts, is represented by a matrix R_n, and one obtain the final transport matrix between any locations along the beamline by matrix multiplication:

$$\mathrm{R} = \mathrm{R}_n \mathrm{R}_{n-1} ... \mathrm{R}_2 \mathrm{R}_1. \tag{2.2}$$

The general differential equation for transverse on momentum linear uncoupled motion is described by the Hill's equation,

$$x'' + (\frac{1}{\rho^2} + k(s))x = 0 \tag{2.3}$$

$$y'' - k(s)y = 0, \tag{2.4}$$

where k is field strength. The equation of motion for the vertical plane are equivalent to the horizontal plane in the absence of dipole fields. The principal solutions of this differential equation are for $k > 0$

$$x(s) = \cos(\sqrt{k}L)x_0 + \frac{1}{\sqrt{k}}\sin(\sqrt{k}L)x'_0 \tag{2.5}$$

$$y(s) = \cosh(\sqrt{|k|}L)y_0 + \frac{1}{\sqrt{|k|}}\sinh(\sqrt{|k|}L)y'_0, \tag{2.6}$$

and for $k < 0$

$$x(s) = \cosh(\sqrt{|k|}L)x_0 + \frac{1}{\sqrt{|k|}}\sinh(\sqrt{|k|}L)x'_0 \tag{2.7}$$

$$y(s) = \cos(\sqrt{k}L)y_0 + \frac{1}{\sqrt{k}}\sin(\sqrt{k}L)y'_0, \tag{2.8}$$

assuming here only the pure quadrupole term ($\frac{1}{\rho^2} = 0$). A quadrupole focusing in the horizontal plane, defocuses in the vertical plane and vice versa. The solutions of Eq.(2.3)

allows to write the 2D transport matrix of the magnetic elements. The transport matrix of a quadrupole is given by:

$$\mathrm{R}_{\text{focusing quad}} = \begin{pmatrix} \cos\sqrt{k}L_\mathrm{q} & \frac{\sin\sqrt{k}L_\mathrm{q}}{\sqrt{k}} \\ -\sqrt{k}\sin\sqrt{k}L_\mathrm{q} & \cos\sqrt{k}L_\mathrm{q} \end{pmatrix}, \tag{2.9}$$

$$\mathrm{R}_{\text{defocusing quad}} = \begin{pmatrix} \cosh\sqrt{|k|}L_\mathrm{q} & \frac{\sinh\sqrt{|k|}L_\mathrm{q}}{\sqrt{|k|}} \\ \sqrt{|k|}\sinh\sqrt{|k|}L_\mathrm{q} & \cosh\sqrt{k}L_\mathrm{q} \end{pmatrix}. \tag{2.10}$$

The transport matrix of a drift space is obtain for $k = 0$ since no force is acting on the particle:

$$\mathrm{R}_{\text{drift}} = \begin{pmatrix} 1 & L \\ 0 & 1 \end{pmatrix}. \tag{2.11}$$

A rectangular dipole in a bending plane is described by:

$$\mathrm{R}_{\text{dipole}} = \begin{pmatrix} \cos(\frac{l_\mathrm{d}}{\rho_\mathrm{d}}) & \rho_\mathrm{d}\sin(\frac{l_\mathrm{d}}{\rho_\mathrm{d}}) \\ -\frac{1}{\rho_\mathrm{d}}\sin(\frac{l_\mathrm{d}}{\rho_\mathrm{d}}) & \cos(\frac{l_\mathrm{d}}{\rho_\mathrm{d}}) \end{pmatrix}, \tag{2.12}$$

where l_d and ρ_d are the length and the bending radius of the the dipole, respectively.
It is a good approximation to treat the quadrupole magnet as a thin lens ($L_q \to 0$) and for a constant integrated gradient $K = kL_q$, the quadrupole transport matrices simplify to:

$$\mathrm{R}_{\text{focusing quad}} = \begin{pmatrix} 1 & 0 \\ -K & 1 \end{pmatrix}, \tag{2.13}$$

$$\mathrm{R}_{\text{defocusing quad}} = \begin{pmatrix} 1 & 0 \\ K & 1 \end{pmatrix}. \tag{2.14}$$

Instead of tracking all the particles, one might want to track the overall behaviour or envelope of the beam, i.e mainly its size and divergence. This information can be represented by the covariance matrix of the beam:

$$\Sigma = \begin{pmatrix} \sigma(x,x) & \sigma(x,x') & \sigma(x,y) & \sigma(x,y') & \sigma(x,\delta_p) \\ \sigma(x',x) & \sigma(x',x') & \sigma(x',y) & \sigma(x',y') & \sigma(x',\delta_p) \\ \sigma(y,x) & \sigma(y,x') & \sigma(y,y) & \sigma(y,y') & \sigma(y,\delta_p) \\ \sigma(y',x) & \sigma(y',x') & \sigma(y',y) & \sigma(y',y') & \sigma(y',\delta_p) \\ \sigma(\delta_p,x) & \sigma(\delta_p,x') & \sigma(\delta_p,y) & \sigma(\delta_p,y') & \sigma(\delta_p,\delta_p) \end{pmatrix}, \tag{2.15}$$

where $\sigma(u_i, u_j)$ is the covariance of the coordinates u_i and u_j and with $u_1 = x$, $u_2 = x'$, $u_3 = y$, $u_4 = y'$, $u_5 = \delta_p$. From Eq.(2.1) and using the properties of the covariance matrix, the beam behavior at the position s in the lattice is given by:

$$\Sigma_s = \mathrm{R}\Sigma_0\mathrm{R}^T, \tag{2.16}$$

where Σ_0 is the initial beam covariance matrix. The motion of an ensemble of particles along the beam line is commonly described by the Twiss parameters α, β, γ and the

emittance ε. Such formalism is normally used to treat the special case of uncoupled, monochromatic ($\delta_p = 0$), gaussian beams. Under these additional assumptions one can study horizontal (x, x') and vertical (y, y') phase space independently. The phase space beam distribution at any location of the transport line is described by the phase ellipse (see Fig 2.2):

$$\varepsilon = \gamma(s)z^2 + 2\alpha(s)zz' + \beta(s)z'^2 \quad \text{where} \quad z \in x, y. \tag{2.17}$$

$\beta(s)$ is the beta-function of the accelerator, which describes the variation of the oscillation envelope along the beam line. The gamma-function, $\gamma(s)$, describes the envelope of oscillations in x' and y'. The beta and gamma functions are related by the alpha-function:

$$\alpha(s) = -\frac{1}{2}\frac{\partial\beta(s)}{\partial s} = \sqrt{\gamma(s)\beta(s) - 1}. \tag{2.18}$$

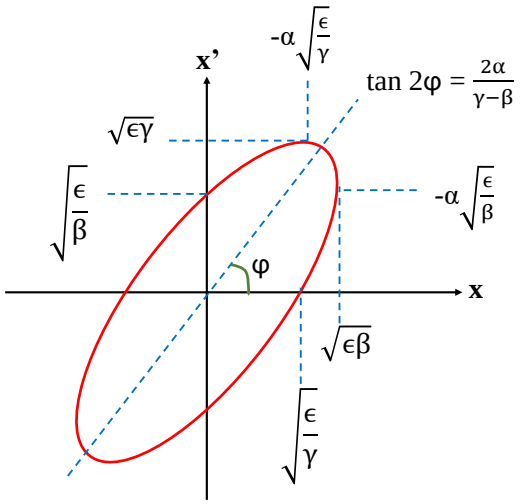

Figure 2.2: Graphical representation of the Twiss parameters

The location of a beam waist is defined by $\alpha = 0$. The emittance ε defines the area of phase space contained by the ellipse and varies when the beam energy changes. One can construct the normalized emittance ε_N, invariant under acceleration, defined as $\varepsilon_N = \gamma\varepsilon$, where $\gamma = \frac{E}{m_0c^2}$ is the relativistic factor.
The Twiss parameters determine the shape and orientation of the ellipse and are related to the beam covariance matrix by:

$$\Sigma = \begin{pmatrix} \sigma(z,z) & \sigma(z,z') \\ \sigma(z',z) & \sigma(z',z') \end{pmatrix} = \varepsilon \begin{pmatrix} \beta & -\alpha \\ -\alpha & \gamma \end{pmatrix}. \tag{2.19}$$

Liouville's theorem states that the phase space volume is conserved in a closed system. The determinant of the covariance matrix Σ is conserved along the beamline and so is the emittance:

$$\det(\Sigma) = \varepsilon^2(\beta\gamma - \alpha^2) = \varepsilon^2. \tag{2.20}$$

The evolution of the Twiss parameter along the beam line is given by:

$$\begin{pmatrix} \beta_s & -\alpha_s \\ -\alpha_s & -\gamma_s \end{pmatrix} = \mathrm{R} \begin{pmatrix} \beta_0 & -\alpha_0 \\ -\alpha_0 & -\gamma_0 \end{pmatrix} \mathrm{R}^T, \tag{2.21}$$

Given the initial Twiss parameters one can alternatively express the transport matrix from an initial location to a final location s using the betatron functions:

$$\mathrm{R} = \begin{pmatrix} \sqrt{\frac{\beta_s}{\beta_0}}(\cos\Delta\varphi_s + \alpha_0 \sin\Delta\varphi_s) & \sqrt{\beta_0\beta_s}\sin\Delta\varphi_s \\ -\frac{1+\alpha_0\alpha_s}{\sqrt{\beta_0\beta_s}}\sin\Delta\varphi_s + \frac{\alpha_0-\alpha_s}{\sqrt{\beta_0\beta_s}}\cos\Delta\varphi_s & \sqrt{\frac{\beta_0}{\beta_s}}(\cos\Delta\varphi_s + \alpha_s\sin\Delta\varphi_s) \end{pmatrix}, \tag{2.22}$$

where $\Delta\varphi_s$ is the phase advance defined as:

$$\Delta\varphi_s = \int_0^s \frac{1}{\beta(s)}\mathrm{ds}. \tag{2.23}$$

From Eq.(4.3), one can calculate the ideal beam size as:

$$\sigma_z(s) = \sqrt{\sigma(z,z)(s)} = \sqrt{\beta(s)\varepsilon_z} \tag{2.24}$$

In presence of energy spread δ_p, the particles trajectory deviates from their reference orbit by $\Delta z = \eta_z\delta_p$, where the dispersion function η_z is given by

$$\eta_z = \frac{\Delta z}{\delta_p}. \tag{2.25}$$

This contribution adds in quadrature to the beam size as:

$$\sigma_z(s) = \sqrt{\varepsilon_z(s)\beta_z(s) + \delta_p^2\eta_z^2(s)} \tag{2.26}$$

2.2 Nonlinear magnetic multipoles

Nonlinear magnetic fields produced by sextupoles, octupoles or higher order multipoles can be introduced by design in the beam line for correcting nonlinear aberrations. Multipolar fields can also be produced by the imperfections of the lattice elements. The magnetic field of a multipole of order n is given by:

$$B_y(x,y,s) + iB_x(x,y,s) = [b_n(s) + ia_n(s)](x+iy)^{n-1}, \tag{2.27}$$

where the normal and skew field component $b_n(s)$ and $a_n(s)$ are defined as:

$$b_n(s) = \frac{1}{(n-1)!}\frac{\partial^{n-1}B_y}{\partial x^{n-1}}\bigg|_{(0,0,s)}, \tag{2.28}$$

$$a_n(s) = \frac{1}{(n-1)!}\frac{\partial^{n-1}B_x}{\partial x^{n-1}}\bigg|_{(0,0,s)}. \tag{2.29}$$

The magnetic field can be derived by differentiating the vector potential $A_s(x,y)$:

$$\overrightarrow{B} = \nabla \times A_{s\ (x,y)}, \tag{2.30}$$

$$\text{with,} \qquad A_s(x,y) = \sum_{n=1} \frac{1}{n}[b_n(s) + ia_n(s)](x+iy)^n. \tag{2.31}$$

One can distinguish the normal and skew components by separating the real and imaginary parts of the vector potential:

$$\frac{1}{B_0\rho}A_{s,nS} = \mathrm{Im}\left[\frac{k_{(n-1)S}}{n!}(x+iy)^n\right], \tag{2.32}$$

$$\frac{1}{B_0\rho}A_{s,nN} = \mathrm{Re}\left[\frac{k_{(n-1)N}}{n!}(x+iy)^n\right], \tag{2.33}$$

where the magnetic rigidity $B_0\rho = \frac{p}{e}$ and the normal and skew field strengths are defined as:

$$k_{(n-1)N} = \frac{1}{B_0\rho}\frac{\partial^{(n-1)}B_y}{\partial x^{(n-1)}}, \tag{2.34}$$

$$k_{(n-1)S} = \frac{1}{B_0\rho}\frac{\partial^{(n-1)}B_x}{\partial x^{(n-1)}}. \tag{2.35}$$

The momentum kick received by a particle in the magnetic field of a multipole is obtained from Hamilton's equation:

$$\frac{\mathrm{d}p_z}{\mathrm{d}s} = -\frac{\mathrm{dH}}{\mathrm{d}z}, \tag{2.36}$$

where $z \in \{x,y\}$ and the contribution to the hamiltonian H_n of a multipole of order n is proportional to the real part of the magnetic vector potential $A_s(x,y)$ [39,40]:

$$\mathrm{H}_n = -\frac{1}{B_0\rho}\mathrm{Re}\left[\frac{1}{n}[b_n(s) + ia_n(s)](x+iy)^n\right]. \tag{2.37}$$

Let $K_n = \int k_n \mathrm{ds}$ be the integrated strength of the magnet. The changes of phase space coordinates through the normal and skew quadrupoles, sextupoles and octupoles, in the thin lens approximation, are:

- Normal n^{th} multipole:

  Quadrupole ($n = 2$):

  $$\Delta x' = -K_{1N}x, \tag{2.38}$$

  $$\Delta y' = K_{1N}y. \tag{2.39}$$

  Sextupole ($n = 3$):

  $$\Delta x' = -\frac{1}{2}K_{2N}(x^2 - y^2), \tag{2.40}$$

  $$\Delta y' = K_{2N}xy. \tag{2.41}$$

  Octupole ($n = 4$):

  $$\Delta x' = -\frac{1}{6}K_{3N}(x^3 - 3xy^2), \tag{2.42}$$

  $$\Delta y' = -\frac{1}{6}K_{3N}(y^3 - 3x^2y). \tag{2.43}$$

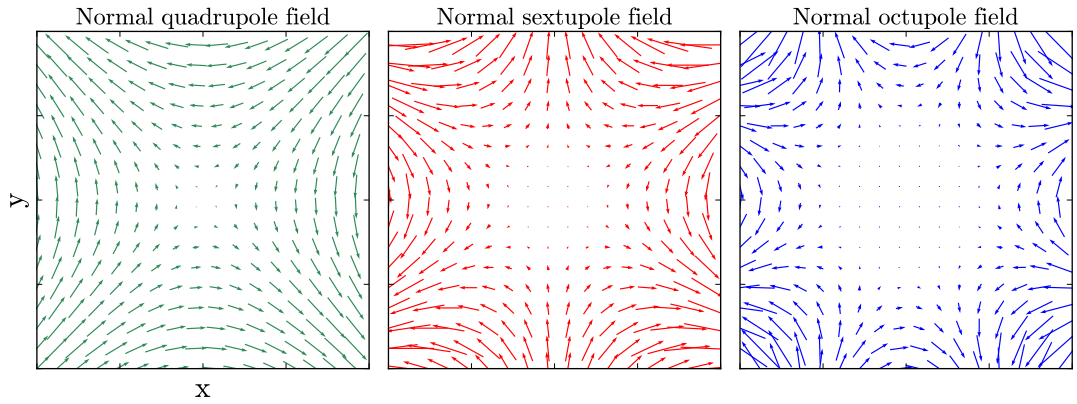

Figure 2.3: From left to right: magnetic fields of pure normal quadrupole, sextupole and octupole.

- Skew n^{th} multipole:

  Quadrupole ($n = 2$):

$$\Delta x' = K_{1S} y, \tag{2.44}$$

$$\Delta y' = K_{1S} x. \tag{2.45}$$

  Sextupole ($n = 3$):

$$\Delta x' = K_{2S} xy, \tag{2.46}$$

$$\Delta y' = \frac{1}{2} K_{2S} (x^2 - y^2). \tag{2.47}$$

  Octupole ($n = 4$):

$$\Delta x' = -\frac{1}{6} K_{3S} (y^3 - 3yx^2), \tag{2.48}$$

$$\Delta y' = \frac{1}{6} K_{3S} (x^3 - 3xy^2). \tag{2.49}$$

An illustration of pure normal quadrupole, sextupole and octupole fields are shown in Fig. 2.3.

2.3 Chromaticity and correction concept

Quadrupoles generate energy dependent aberrations, referred to as chromatic aberrations, for off momentum particles with relative momentum deviation $\delta_p = \frac{p - p_0}{p_0}$. The particles are focused at different longitudinal positions as illustrated in Figure 2.4 according to their momentum and if uncorrected the chromatic aberrations would dominate the IP spot size. In the FFS the chromaticity is mainly generated by the strong FD quadrupoles and it is dominant in the vertical plane due to the smaller vertical β function at the IP, referred to as β_y^*. The last quadrupole QD0 focalise the beam to the IP

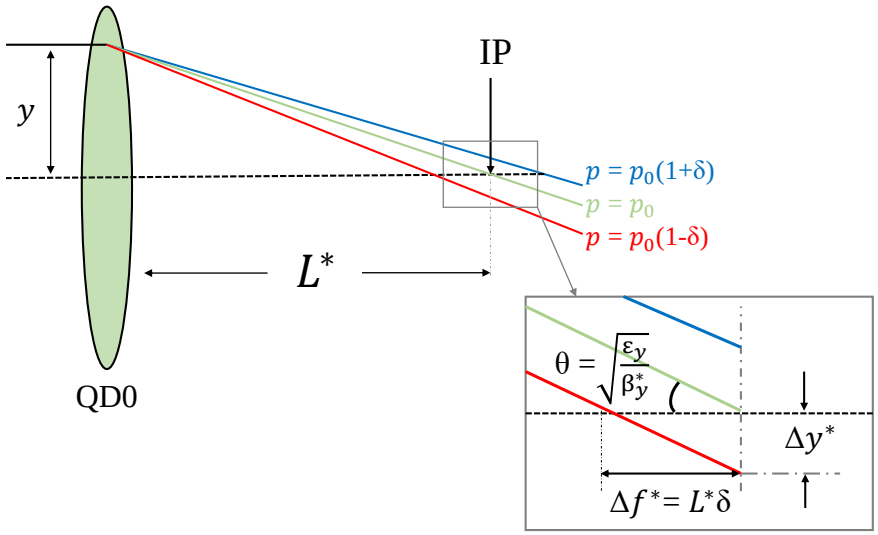

Figure 2.4: Scheme of the chromatic effect produced by the final quadrupole QD0 approximated as a thin lens of focal length L^*. The blue, green and red lines represent the trajectory of particles arriving at the quadrupole with the same y coordinate but with larger, equal and smaller momentum respectively than p_0.

with a focal distance f^*, which deviation is related to the distance L^* by:

$$\Delta f^* \approx L^* \delta_p. \tag{2.50}$$

The vertical position shift at the IP, neglecting the correlation between the energy and the beam divergence, is related to the distance L^* and the β function at the IP by:

$$\Delta y^* \approx \Delta f^* \sqrt{\frac{\varepsilon_y}{\beta_y^*}} \approx L^* \delta_p \sqrt{\frac{\varepsilon_y}{\beta_y^*}}. \tag{2.51}$$

For $\sigma_y^* = \sqrt{\varepsilon_y \beta_y^*}$, one can approximate the relative IP vertical beam size increase by:

$$\frac{\Delta_y^*}{\sigma_y^*} \approx \frac{L^*}{\beta_y^*} \delta_p \sim \xi_y \delta_p, \tag{2.52}$$

where ξ_y is the vertical chomaticity. Reducing β_y^* or increasing the distance L^* worsens the impact of the chromatic effects on the beam size and increases the β functions at the FD as:

$$L^* \sqrt{\frac{\varepsilon_y^*}{\beta_y^*}} = \sqrt{\varepsilon_y \beta_y^{QD0}} \Rightarrow \beta_y^{QD0} = \frac{L^{*2}}{\beta_y^*}. \tag{2.53}$$

The chromaticity generated between any location s along the system can be calculated using the matrix formalism applied to describe the higher order elements of the system such as sextupoles. The transport map is extended by additional matrices [41] relating the final coordinates $u_{f,i}$ with the initial ones by:

$$u_{f,i} = \sum_{j=1}^{5} \mathrm{R}_{i,j}\ u_{0,j} + \sum_{j,k=1}^{5} T_{i,jk}\ u_{0,j} u_{0,k} + \sum_{j,k,l=1}^{5} U_{i,jkl}\ u_{0,j} u_{0,k} u_{0,l} + O(\geq 4) \tag{2.54}$$

which is expressed in a more compact way as

$$\vec{u}_f = \sum_{jklmn} \vec{X}_{jklmn} \; x_0^j \; p_{x0}^k \; y_0^l \; p_{y0}^m \; \delta_0^n \tag{2.55}$$

where $\vec{X}_{jklmn}$ is the map coefficient between the initial and the final coordinates, represented by $\vec{u}_f = (x_f,\, p_{xf}, y_f,\, p_{yf},\, \delta_f)$. The natural vertical chromaticity generated can be expressed as [42]:

$$\xi_y^{*2} = (X_{00101}^2 \frac{\beta_{y0}}{\beta_y^*} + X_{00011}^2 \frac{1}{\beta_{y0}\beta_y^*}) \tag{2.56}$$

The correction of the chromaticity in the horizontal and vertical plane is performed using sextupoles in a dispersive region as introduced in Section 1.4.2. Considering only horizontal dispersion η_x produced by the upstream bending magnets, the horizontal position of the particle is deviated by $\eta_x\delta_p$. The horizontal and vertical kicks received from a focusing quadrupole under these conditions are given by:

$$\Delta x'_{\text{quad}} \approx -K_{1N}(x + \eta_x\delta_p - x\delta_p - \eta_x\delta_p^2) \tag{2.57}$$

$$\Delta y'_{\text{quad}} \approx K_{1N}(y - y\delta_p) \tag{2.58}$$

By adding the kick from a sextupole located in a dispersion region,

$$\Delta x'_{\text{sext}} = -K_{2N}(x\eta_x\delta_p + \frac{1}{2}\eta_x^2\delta_p^2 + \frac{1}{2}(x^2 - y^2)) \tag{2.59}$$

$$\Delta y'_{\text{sext}} = K_{2N}(yx + y\eta_x\delta_p) \tag{2.60}$$

One observes the cancellation of terms proportional to $x\delta_p$ and $y\delta_p$ if the strength of the sextupole $K_{2N}\eta_x = K_{1N}$ and assuming no variation of the β-functions between the quadrupole and the sextupole. However the second order dispersion term is only half compensated by the sextupole. The terms proportional to δ_p^2 can be vanished by increasing the sextupole strength by a factor 2 and generating the additional natural chromaticity upstream of the bending magnets in non-dispersive region. The sexupoles generate geometric aberrations, the terms proportional to $(x^2 - y^2)$ and xy, so another sextupole is introduced in the beamline, upstream of the bending magnets, with a π-phase separation ($-\mathcal{I}$ telescopic transformer) between them in order to cancel the geometrical terms at the exit of the second sextupole. As the sextupoles use the dispersion to compensate chromaticity, one can choose to run with higher dispersion (higher dipole strength) or higher sextupole strength. One has to find a compromise between synchrotron radiation generated in bending magnets and geometric aberrations generated by the sextupoles.

2.4 Synchrotron radiation

The electromagnetic radiation emitted from relativistic charged particles as they are accelerated is called synchrotron radiation. The IP beam size growth for the local chromaticity correction FFS is dominated by the energy loss due to synchrotron radiation in the bending magnets. If the energy loss occurs at a dispersive location, it causes a change

in the particle orbit, which leads to a statistical increase of the emittance and can also cause backgrounds in the detector. The impact of synchrotron radiation on beam size on various L_{FFS}, L^* and beam energy will be discussed in Chapter 3 and 5. Synchrotron radiation is emitted also through quadrupoles and becomes important especially at the Final Doublet QD0 and QF1 of the CLIC FFS. The limit of focusing due to synchrotron radiation is called Oide effect.

2.5 Oide effect

The Oide effect is caused by the radiation in a focusing magnet leading to changes in energy of the particles which ultimately modifies the focusing effect. The limit on the minimum beam size achievable is specially relevant in the vertical plane for CLIC. The beam size contribution due to the Oide effect is added in quadrature to the linear beam size and is given by [43, 44]. In Chapters 3 and 4, the calculated beam size contribution to the vertical beam size σ_y^* from Oide effect takes into account only radiation due to the vertical motion of the particles (see Eq. (2.61)) and not the radiation in the final quadrupoles due to the horizontal motion:

$$\sigma_y^{*2} = \beta_y^* \varepsilon_y + \frac{110}{3\sqrt{6\pi}} r_e \lambda_e \times F(\sqrt{k}L, \sqrt{k}L^*) \left(\frac{\gamma^2 \varepsilon_y}{\beta_y^*}\right)^{\frac{5}{2}} \tag{2.61}$$

where r_e is the classical electron radius, λ_e is the Compton wavelength and the dimensionless function F is defined as:

$$F(\sqrt{k}L, \sqrt{k}L^*) \equiv \int_0^{\sqrt{K}L} d\phi |\sin\phi + \sqrt{k}L^* \cos\phi|^3 \times \left[\int_0^{\phi} (\sin\phi' + \sqrt{k}L^* \cos\phi')^2 d\phi'\right]^2 \tag{2.62}$$

The vertical rms spot size becomes minimum for:

$$\sigma_{y,\mathrm{min}}^* = \sqrt{\frac{7}{5}} (\gamma\varepsilon_y)^{\frac{5}{7}} \times \left[\frac{275}{3\sqrt{6\pi}} r_e \lambda_e F(\sqrt{k}L, \sqrt{k}L^*)\right]^{\frac{1}{7}} \tag{2.63}$$

and it is achieved at:

$$\beta_y^* = \left[\frac{275}{3\sqrt{6\pi}} r_e \lambda_e F(\sqrt{k}L, \sqrt{k}L^*)\right]^{\frac{2}{7}} \gamma (\gamma\varepsilon_y)^{\frac{3}{7}} \tag{2.64}$$

For constant beam parameters, the contribution of the Oide beam size depends on k, L and L^* as discussed in [44] and Chapter 4.

2.6 Luminosity

The luminosity is defined as the number of events produced per second $\dot{N}_p$ per unit of interaction cross section σ_p of the physicsl process:

$$\dot{N}_p = \sigma_p \mathcal{L} \tag{2.65}$$

As the cross sections of the processes of interest are extremely small, high luminosities are required in order to keep a large enough event rate. Assuming head-on collisions of bunches with Gaussian distributions and no offset or crossing angle at the interaction point, the luminosity is given by:

$$\mathcal{L} = \mathcal{L}_0 \mathcal{H}_D = \frac{N_p^2 n_b f_{rep}}{4\pi \sigma_x^* \sigma_y^*} \mathcal{H}_D, \tag{2.66}$$

where $\mathcal{L}_0$ is the geometrical luminosity, $\sigma_{x,y}^*$ are the horizontal and vertical beam sizes at the IP, N_p is the number of particle per bunch, n_b is the number of bunches per train and f_{rep} is the repetition frequency of the trains. The parameter $\mathcal{H}_D$ is the enhancement factor that contains the impact of beam-beam forces. This factor is in the order of 1.5-2 for CLIC at 3 TeV. The beam current is represented by the term $N_p n_b f_{rep}$ and is limited by the power consumption of the collider and its transfer efficiency into beam power. The luminosity is therefore enhanced by minimizing the factor $\sigma_x^* \sigma_y^*$. However, beam-beam effects set a lower limit to the achievable horizontal beam size.
The beams generates strong electromagnetic fields at the collision point. In an e^+e^- collider, the beams focus each other, the so called pinch effect, which reduces the effective beam size and therefore increases the luminosity. The magnitude of the pinch effect is described by the disruption parameter $D_{x,y}$:

$$D_{x,y} = \frac{2N_p r_e \sigma_z}{\gamma \sigma_{x,y}^* (\sigma_x^* + \sigma_y^*)} \tag{2.67}$$

where σ_z is the longitudinal beam size. When the beams focus each other they emit radiation called Beamstrahlung. Due to this effect, particles lose energy and therefore collide with less than the initial energy. There are two relevant luminosity that figures in the total luminosity $\mathcal{L}_{\text{total}}$, taking into account the collisions of all particles with different energies, and the peak luminosity $\mathcal{L}_{1\%}$, taking into account collisions with energy larger than 99% of the maximum energy. The beamstrahlung impact on the luminosity spectrum is described by the parameter Υ defined as [45]:

$$\Upsilon = \frac{2}{3} \frac{\hbar \omega_c}{E}, \tag{2.68}$$

where $\hbar$ is the plack constant, ω_c is the critical frequency characterizing the synchrotron light spectrum and E is the particle energy. The factor $\hbar\omega_c$ is called the critical energy. The average value of the beamstrahlung parameter is estimated as:

$$\langle \Upsilon \rangle = \frac{5}{6} \frac{N_p r_e}{\alpha \sigma_z (\sigma_x^* + \sigma_y^*)}. \tag{2.69}$$

Here α is the fine structure constant. The number of photons emitted per beam particles N_γ depends on the bunch charge and transverse dimensions:

$$N_\gamma \propto \langle \Upsilon \rangle \frac{\sigma_z}{\gamma} \propto \frac{N_p}{\sigma_x^* + \sigma_y^*}, \tag{2.70}$$

and the average energy of each photon is proportional to:

$$E_\gamma \propto \langle \Upsilon \rangle \frac{1}{\gamma} \propto \frac{N_p}{(\sigma_x^* + \sigma_y^*)\sigma_z}. \tag{2.71}$$

In order to reduce the beamstrahlung while delivering maximum luminosity, the FFS aims to provide beams at the collision point with transverse sizes that maximize the sum $(\sigma_x^* + \sigma_y^*)$ and minimize the product $(\sigma_x^* \sigma_y^*)$. This can be achived by using flat beams $(\sigma_x^* >> \sigma_y^*)$. Under this condition one can approximate $\sigma_x^* + \sigma_y^* \approx \sigma_x^*$ and therfore the number of beamstrahlung photons emitted is proportional to the term $\frac{N_p}{\sigma_x^*}$. Beam-beam effects are crucial for the design the linear colliders, especially for the FFS. The beamstrahlung is one of the major limitations for the luminosity and also affects the performance of the experiments by producing backgrounds. In Chapter 5 alternative optics for the CLIC FFS at 380 GeV are proposed to reduce Beamstrahlung.
The luminosity is mainly maximized by the very low vertical beam size σ_y^*. However, because of the very high beam divergence in the low-β_y^* region near the IP, a geometrical effect, arised from the shape of $\beta_y(s)$ called Hourglass effect. This effect can cause luminosity reduction since not all particles collide at the waist position. The transverse beam size dependence with the longitudinal position s is given by:

$$\sigma_y(s) = \sigma_y^* \sqrt{1 + \left(\frac{s}{\beta_y^*}\right)^2}. \tag{2.72}$$

The beams of CLIC and ILC will cross with an angle in the horizontal plane θ_c for the extraction of the spent beams and to avoid parasitic interactions between the e^+ and e^- bunches. For CLIC 3 TeV, $\theta_c = 20$ mrad and would cause luminosity reduction to:

$$\mathcal{L} = \mathcal{H}_D \frac{N_p^2 n_b f_{rep}}{4\pi \sigma_x^* \sigma_y^*} \frac{1}{\sqrt{1 + (\frac{\sigma_z}{\sigma_x^*} \tan \frac{\theta_c}{2})^2}}. \tag{2.73}$$

In order to avoid such a large luminosity loss, crab cavities are used to rotate the bunches and deliver head-on collisions while keeping the crossing angle at the IP. The luminosities simulated and reported in this thesis, for the optics optimization and tuning simulations, include pinching of the beams and emission of beamstrahlung, assuming head-on collisions.

2.7 Effects of the detector solenoid

The CLIC experiment forsees a solenoid field of 4 T [8]. Due to the CLIC crossing angle discussed previously, the beams do not travel parallel to the solenoid field resulting in beam coupling, vertical offset and dispersion at the IP. If the FD quadrupoles are away from the influence of the solenoid field, the vertical offset at the IP is [46]:

$$\Delta y^* = \frac{B_s L^{*2}}{B\rho} \frac{\theta_c}{4}, \tag{2.74}$$

where B_s is the solenoid field. If QD0 and QF1 are outside of the detector, the e^+ and e^- beams will have zero vertical orbit deviation a the IP, as the radial and longitudinal fields have opposite effects on the beam orbit. In that case various coupling terms are also cancelled at the IP [47]. The vertical orbit deflection generates synchrotron radiation and the corresponding beam size contribution is [46]

$$(\Delta\sigma_y^{\mathrm{SR}})^2 = C_E\gamma^5 \int_0^\infty \frac{\mathrm{R}_{36}^2(z)}{|\rho(z)|^3}\mathrm{d}z, \tag{2.75}$$

with

$$C_E = \frac{55}{24\sqrt{3}} r_e \lambda_e. \tag{2.76}$$

In the CLIC CDR the proposed FFS foreseen $L^* = 4.3$ m and $L^* = 3.5$ m at 380 GeV and 3 TeV respectively. This implies to place the last quadrupole QD0 partially or entirely inside the experiment. The overlap of the detector field with the QD0 field gives rise to new coupling terms at the IP, in particular the $<y, x'>$ correlation term, and significantly increases the vertical beam size [47, 48]. These additional aberrations need to be minimized with an anti-solenoid in order to shield the QD0 field from the experiment. The impact on the luminosity using the anti-solenoid for CLIC 3 TeV has been studied in [49]. Throughout this thesis, FFS designs are optimized for CLIC 3 TeV and 380 GeV with $L^* = 6$ m in order to take advantage of having the FD entirely outside the detector. The luminosity was calculated in this thesis without taking into account the effect of the solenoid field of the detector.

2.8 Tuning the FFS

The tolerances of the CLIC FFS are too restrictive to neglect the manufacturing and alignment imperfections of the magnetic elements. The demonstration of a tuning procedure that mitigates the emittance growth through the FFS and recovers the design performance of the machine is crucial to validate the CLIC FFS feasibility. This procedure utilizes beam-based alignment techniques (BBA) [50], to correct the beam orbit throughout the system, and tuning knobs, to combat known linear and nonlinear aberrations at the IP. The dominant source of luminosity loss from static imperfections is the transverse misalignment of the optics. Dynamic imperfections, like ground motion, cause beam size growth from the post tune-up state of the BDS. The quadrupole position jitter causes change in the beam transverse position at the IP and may miss the opposing beam. The tolerances in the vertical orbit shifts are tighter due to the smaller σ_y^*. When a quadrupole is vertically moved by Δy, the change in the vertical position at the IP is [51]

$$\frac{\Delta y^*}{\sigma_y^*} = \Delta y K_1 \sqrt{\frac{\beta_y}{\varepsilon_y}} \sin\Delta\varphi_y. \tag{2.77}$$

The FD quadrupoles are the most sensitive to these vibrations, where an offset Δy causes approximately an offset at the IP of equal magnitude. The tolerance on the FD is of the order of the nanometer level and can be corrected by an intra-train orbit feedback [52].

Here a description of the tuning technique applied to correct the orbit changes, due to the static offset of the quadrupoles and the linear and nonlinear aberrations, generated by the transverse misalignment, roll and strength errors of the quadrupoles and sextupoles of the FFS, is detailed.

2.8.1 Beam Based Alignment

The Beam Based Alignment techniques use the beam position measurements by means of Beam Position Monitors (BPM) to infer and correct the orbit and dispersion along the beam line. The first alignment algorithm used during the CLIC FFS tuning simulations is called one-to-one correction. This technique aims to flattened the orbit by steering the beam through the centre of each BPM using transverse kickers. The one-to-one correction is efficient for keeping the beam orbit within the beam pipe aperture but the effectiveness of the orbit correction is compromised by the misaligned BPMs, leading to a dispersive orbit. The Dispersion Free Steering (DFS), applied after the one-to-one correction, that attemps simultaneously to steer the beam to its nomial ordit and to correct the beam dispersion. This is performed by minimizing the following merit function [50]:

$$\chi^2 = \sum_{\text{BPMs}} \mathrm{x}_i^2 + \omega^2 \sum_{\text{BPMs}} (\mathrm{x}_i^{'} - \mathrm{x}_i - \eta_i \delta p)^2 + \kappa^2 \sum_{\text{correctors}} \theta_m^2, \tag{2.78}$$

where i and m are the indices of the BPMs and correctors, respectively. The vectors $\vec{\mathrm{x}}$ and $\vec{\mathrm{x}^{'}}$ give the BPM readings for the nominal beam and for the off-momentum beam w.r.t the nominal one, respectively. The parameters ω and κ are free and need to be tuned to optimize the algorithm performance. ω is a weighting factor balancing between orbit and dispersion correction. κ is used to limit the amplitude of the corrections and θ is the corrector strengths. The least squares solution of Eq. 2.78 can be written as the following system of equations:

$$\begin{pmatrix} \vec{\mathrm{x}} \\ \omega(\vec{\mathrm{x}} - \vec{\mathrm{x}^{'}}) \\ \vec{0} \end{pmatrix} = \begin{pmatrix} \mathrm{R} \\ \omega(\mathrm{R} - \mathrm{R}') \\ \kappa\mathcal{I} \end{pmatrix} \vec{\theta}, \tag{2.79}$$

where R and $\mathrm{R}^{'}$ are the response matrices of the nominal and the test beams used to quantify the dispersion. $\mathcal{I}$ is the identity matrix. The dispersion is evaluated by collecting two orbit readings, $\vec{x}_{\Delta E_+}$ and $\vec{x}_{\Delta E_-}$, of two beams, with energy deviations of $\pm\Delta E$. The dispersion is obtained as:

$$\vec{\eta} = \frac{\vec{\mathrm{x}}_{\Delta E_+} - \vec{\mathrm{x}}_{\Delta E_-}}{2\Delta E}. \tag{2.80}$$

2.8.2 Linear and Nonlinear aberration correction techniques

Linear aberrations at the IP created by the misaligned elements are corrected using pre-computed combinations of sextupole displacements in the transverse plane [53]. When

the normal sextupoles are displaced horizontally, feed-down to normal quadrupole kicks are generated:

$$\Delta x'_{\text{sext}} = -\frac{1}{2}K_{2N}(x^2 - y^2) - \overbrace{K_{2N}x\Delta x}^{\text{Normal Quadrupole}} - \frac{1}{2}\overbrace{K_{2N}\Delta x^2}^{\text{Dipole kick}}, \tag{2.81}$$

$$\Delta y'_{\text{sext}} = K_{2N}xy + \overbrace{K_{2N}y\Delta x}^{\text{Normal quadrupole}}. \tag{2.82}$$

The normal quadrupole kick distords the $\beta_{x,y}$ and η_x functions. The change of $\beta_{x,y}$ results in a longitudinal shift of the horizontal and vertical waist approximated as [53]:

$$\Delta s_{x,y} \approx K_{2N}\Delta x\beta^s_{x,y}\beta^*_{x,y}\cos 2\Delta\varphi_{x,y}, \tag{2.83}$$

where $\beta^s_{x,y}$ are the β functions at the sextupole location. As the sextupoles in the FFS are located in dispersive regions, the offset Δx also generates horizontal dispersion at the IP [53]:

$$\Delta\eta^*_x = K_{2N}\Delta x\eta^s_x\sqrt{\beta^s_x\beta^*_x}\sin\Delta\varphi_x. \tag{2.84}$$

When the normal sextupoles are displaced vertically, feed-down to skew quadrupole kicks are generated:

$$\Delta x'_{\text{sext}} = -\frac{1}{2}K_{2N}(x^2 - y^2) + \overbrace{K_{2N}y\Delta y}^{\text{Skew quadrupole}} + \frac{1}{2}\overbrace{K_{2N}\Delta y^2}^{\text{Dipole kick}}, \tag{2.85}$$

$$\Delta y'_{\text{sext}} = K_{2N}xy + \overbrace{K_{2N}x\Delta y}^{\text{Skew quadrupole}}. \tag{2.86}$$

The skew quadrupole field generates betatron coupling at the IP and vertical dispersion given by [53]:

$$\Delta\eta^*_x = K_{2N}\Delta y\eta^s_x\sqrt{\beta^s_x\beta^*_x}\sin\Delta\varphi_y. \tag{2.87}$$

Each set of sextupole knobs is constructed to be orthogonal, so that the chosen aberrations are corrected independently. The correlations between the beam coordinates are the quantities used for the construction of the linear knobs. The correlations $X_{i,j}$ are placed in a correlation matrix X in response to the transverse sextupole displacements. The correlation response matrix X is factorized through the singular value decomposition (SVD):

$$X = UWV^T, \tag{2.88}$$

where the columns of U and V are orthonormal and the diagonal matrix W gives the singular values. The columns of V provides the orthogonal combination of sextupole displacements used in the tuning procedure to correct the linear aberrations. The knobs are designed to independently correct the linear aberrations: $\alpha^*_{x,y}$, $\beta^*_{x,y}$ and $\eta^*_{x,y}$, η'^*_y, $< x, y >$, $< p_x, y >$ and $< p_x, p_y >$.

The BBA and linear knob corrections may not be enough to fully regain the desired luminosity. The remaining 2^{nd} order aberrations can be corrected using combinations of strength variation of the normal and skew sextupoles [54] or transverse displacement of

the octupoles. The 3rd order knobs are constructed using strength variation of the octupoles. When there is a normal sextupole field error ΔK_{2N} in the presence of dispersion, the deflection of the particles is given by:

$$\Delta x'_{\text{sext}} = -\frac{1}{2}\Delta K_{2N}(x^2 + 2\eta_x\delta_p x + \eta_x^2, \delta_p^2 - y^2), \tag{2.89}$$

$$\Delta y'_{\text{sext}} = \Delta K_{2N}(xy + \eta_x\delta_p y). \tag{2.90}$$

The IP horizontal and vertical positions are changed as:

$$\Delta x^*_{\text{sext}} = -\frac{\mathrm{R}_{12}^{s\to *}\Delta K_{2N}}{2}(x^2 + 2\eta_x\delta_p x + \eta_x^2\delta_p^2 - y^2), \tag{2.91}$$

$$\Delta y^*_{\text{sext}} = \mathrm{R}_{34}^{s\to *}\Delta K_{2N}(xy + \eta_x\delta_p y). \tag{2.92}$$

When the sextupole error sources are located at betatron phase advances to the IP of $(n + \frac{1}{2})\pi$, the horizontal and vertical positions at the error sources are correlated to the horizontal and vertical angles at the IP, x'^* and y'^* by:

$$\begin{cases} x = -\mathrm{R}_{12}^{s\to *}x'^*, & (2.93) \\ y = -\mathrm{R}_{34}^{s\to *}y'^*. & (2.94) \end{cases}$$

Finally the position changes at the IP from one normal sextupole field error can be expressed as fucntion of the 2nd order aberrations generated:

$$\Delta x^* = \mathrm{T}_{122}^{s\to *}x'^{*2} + \mathrm{T}_{126}^{s\to *}x'^*\delta_p + \mathrm{T}_{166}^{s\to *}\delta_p^2 + \mathrm{T}_{144}^{s\to *}y'^{*2} \tag{2.95}$$

$$\Delta y^* = \mathrm{T}_{324}^{s\to *}x'^*y'^* + \mathrm{T}_{346}^{s\to *}y'^*\delta_p \tag{2.96}$$

With

$$\mathrm{T}_{122}^{s\to *} = -\frac{\mathrm{R}_{12}^{3,s\to *}\Delta K_{2N}}{2} = -\frac{\Delta K_{2N}(\beta_x^s\beta_x^*)^{\frac{3}{2}}}{2} \tag{2.97}$$

$$\mathrm{T}_{126}^{s\to *} = \eta_x\mathrm{R}_{12}^{2,s\to *}\Delta K_{2N} = \eta_x\beta_x^s\beta_x^*\Delta K_{2N} \tag{2.98}$$

$$\mathrm{T}_{166}^{s\to *} = -\frac{\eta_x^2\mathrm{R}_{12}^{s\to *}\Delta K_{2N}}{2} = -\frac{\eta_x^2\sqrt{\beta_x^s\beta_x^*}\Delta K_{2N}}{2} \tag{2.99}$$

$$\mathrm{T}_{144}^{s\to *} = \frac{\mathrm{R}_{12}^{s\to *}\mathrm{R}_{34}^{2,s\to *}\Delta K_{2N}}{2} = \frac{\sqrt{\beta_x^s\beta_x^*}\beta_y^s\beta_y^*\Delta K_{2N}}{2} \tag{2.100}$$

$$\mathrm{T}_{324}^{s\to *} = \mathrm{R}_{12}^{s\to *}\mathrm{R}_{34}^{2,s\to *}\Delta K_{2N} = \sqrt{\beta_x^s\beta_x^*}\beta_y^s\beta_y^*\Delta K_{2N} \tag{2.101}$$

$$\mathrm{T}_{346}^{s\to *} = -\eta_x\mathrm{R}_{34}^{2,s\to *}\Delta K_{2N} = -\eta_x\beta_y^s\beta_y^*\Delta K_{2N} \tag{2.102}$$

The 2nd order aberrations generated at the IP by strength variation ΔK_{2S} of skew

sextupoles causes IP position changes expressed as:

$$\Delta x^* = \overbrace{(\sqrt{\beta_y^s\beta_y^*}\beta_x^s\beta_x^*\Delta K_{2S})}^{\mathrm{T}_{124}^{s\to *}} x'^* y'^* + \overbrace{(\eta_x\sqrt{\beta_x^s\beta_x^*\beta_y^s\beta_y^*}\Delta K_{2S})}^{\mathrm{T}_{146}^{s\to *}} y'^*\delta_p \quad (2.103)$$

$$\Delta y^* = \overbrace{\frac{1}{2}(\beta_x^s\beta_x^*\sqrt{\beta_y^s\beta_y^*}\Delta K_{2S})}^{\mathrm{T}_{322}^{s\to *}} x'^{*2} + \overbrace{(-\eta_x\sqrt{\beta_x^s\beta_x^*\beta_y^s\beta_y^*}\Delta K_{2S})}^{\mathrm{T}_{326}^{s\to *}} x'^*\delta_p + \overbrace{(\frac{1}{2}\eta_x^2\sqrt{\beta_y^s\beta_y^*}\Delta K_{2S})}^{\mathrm{T}_{366}^{s\to *}}\delta_p^2 + \overbrace{(-\frac{1}{2}(\beta_y^s\beta_y^*)^{\frac{3}{2}}\Delta K_{2S})}^{\mathrm{T}_{344}^{s\to *}} y'^{*2} \quad (2.104)$$

It is also possible to construct 2nd order knobs using the feed-down from sextupoles generated by the horizontal and vertical offset of octupoles. The deflection of the particles from a horizontal displacement of a normal octupole is given by:

$$\Delta x' = \overbrace{\frac{K_{3N}}{6}(3xy^2 - x^3)}^{\text{Octupole}} - \overbrace{\frac{K_{3N}}{2}(x^2 - y^2)\Delta x}^{\text{Normal sextupole}} - \overbrace{\frac{K_{3N}}{2}x\Delta x^2}^{\text{Normal quadrupole}} - \overbrace{\frac{K_{3N}}{6}\Delta x^3}^{\text{Dipole}} \quad (2.105)$$

$$\Delta y' = \overbrace{\frac{K_{3N}}{6}(3x^2y - y^3)}^{\text{Octupole}} + \overbrace{K_{3N}xy\Delta x}^{\text{Normal sextupole}} + \overbrace{\frac{K_{3N}}{2}y\Delta x^2}^{\text{Normal quadrupole}} \quad (2.106)$$

The normal sextupole kick generated allows the correction of the 2nd order aberrations T_{122}, T_{126}, T_{166}, T_{144}, T_{324} and T_{346}. When the normal octupole is moved vertically:

$$\Delta x' = \overbrace{\frac{K_{3N}}{6}(3xy^2 - x^3)}^{\text{Octupole}} + \overbrace{K_{3N}xy\Delta y}^{\text{Skew sextupole}} + \overbrace{\frac{K_{3N}}{2}x\Delta y^2}^{\text{Normal quadrupole}} \quad (2.107)$$

$$\Delta y' = \overbrace{\frac{K_{3N}}{6}(3x^2y - y^3)}^{\text{Octupole}} + \overbrace{\frac{K_{3N}}{2}(x^2 - y^2)\Delta y}^{\text{Skew sextupole}} - \overbrace{\frac{K_{3N}}{2}y\Delta y^2}^{\text{Normal quadrupole}} - \overbrace{\frac{K_{3N}}{6}\Delta y^3}^{\text{Dipole}} \quad (2.108)$$

The skew sextupolar kicks produce the 2nd order aberrations $\mathrm{T}_{124}^{s\to *}$, $\mathrm{T}_{146}^{s\to *}$, $\mathrm{T}_{322}^{s\to *}$, $\mathrm{T}_{326}^{s\to *}$, $\mathrm{T}_{366}^{s\to *}$ and $\mathrm{T}_{344}^{s\to *}$. Finally, 3rd order knobs can be constructed by using the strength variation of the normal octupoles. The aberrations produced from the normal octupoles in presence of dispersion are listed below.

$$\Delta x^* = -\frac{\mathrm{R}_{12}^{s\to *}K_{3N}}{6}(3xy^2 - x^3 + 3\eta_x\delta_p y^2 - 3\eta_x\delta_p x^2 - 3\eta_x^2\delta_p^2 x - \eta_x^3\delta_p^3) \quad (2.109)$$

$$\Delta y^* = -\frac{\mathrm{R}_{34}^{s\to *}K_{3N}}{6}(3x^2y - y^3 + 6\eta_x\delta_p xy + 3\eta_x^2\delta_p^2 y) \quad (2.110)$$

The position change at the IP due to the strength variation of the normal octupoles can be written as:

$$\Delta x^* = \mathrm{U}_{1244}^{s\to *}x'^* y'^{*2} + \mathrm{U}_{1222}^{s\to *}x'^{*3} + \mathrm{U}_{1446}^{s\to *}y'^{*2}\delta_p + \mathrm{U}_{1226}^{s\to *}x'^{*2}\delta_p + \mathrm{U}_{1266}^{s\to *}x'^*\delta_p^2 + \mathrm{U}_{1666}^{s\to *}\delta_p^3$$

$$\Delta y^* = \mathrm{U}_{3224}^{s\to *}x'^{*2}y'^* + \mathrm{U}_{3444}^{s\to *}y'^{*3} + \mathrm{U}_{3246}^{s\to *}x'^* y'^*\delta_p + \mathrm{U}_{3466}^{s\to *}y'^*\delta_p \quad (2.111)$$

(2.112)

$$\mathrm{U}^{s\to *}_{1244} = -\frac{\mathrm{R}^{2,s\to *}_{12}\mathrm{R}^{2,s\to *}_{34}K_{3N}}{6} \quad (2.113)$$

$$\mathrm{U}^{s\to *}_{1222} = \frac{\mathrm{R}^{4,s\to *}_{12}K_{3N}}{6} \quad (2.114)$$

$$\mathrm{U}^{s\to *}_{1446} = -\frac{\eta_x\mathrm{R}^{s\to *}_{12}\mathrm{R}^{2,s\to *}_{34}K_{3N}}{2} \quad (2.115)$$

$$\mathrm{U}^{s\to *}_{1226} = \frac{\eta_x\mathrm{R}^{3,s\to *}_{12}K_{3N}}{2} \quad (2.116)$$

$$\mathrm{U}^{s\to *}_{1266} = \frac{\eta_x^2\mathrm{R}^{2,s\to *}_{12}K_{3N}}{2} \quad (2.117)$$

$$\mathrm{U}^{s\to *}_{1666} = \frac{\eta_x^3\mathrm{R}^{s\to *}_{12}K_{3N}}{6} \quad (2.118)$$

$$\mathrm{U}^{s\to *}_{3224} = \frac{\mathrm{R}^{2,s\to *}_{12}\mathrm{R}^{2,s\to *}_{34}K_{3N}}{2} \quad (2.119)$$

$$\mathrm{U}^{s\to *}_{3444} = -\frac{\mathrm{R}^{4,s\to *}_{34}K_{3N}}{6} \quad (2.120)$$

$$\mathrm{U}^{s\to *}_{3246} = -\eta_x\mathrm{R}^{s\to *}_{12}\mathrm{R}^{2,s\to *}_{34}K_{3N} \quad (2.121)$$

$$\mathrm{U}^{s\to *}_{3466} = \frac{\eta_x^2\mathrm{R}^{2,s\to *}_{34}K_{3N}}{2} \quad (2.122)$$

The construction of the linear and nonlinear knobs is limited by the number of multipoles present in the FFS. One has to identify the aberrations that contribute the most to the beam size growth, then compute the tuning knobs accordingly. More details about the knobs construction applied to the CLIC and ATF2 FFS will be presented in Chapters 3,4, 5 and 6

This Chapter has given an overview of the theories of beam dynamics which are relevant to the material presented in this thesis. Indeed, a description of the chromaticity correction concept of the Local scheme, the linear and nonlinear aberrations generated by the lattice imperfections through the FFS and the correction techniques applied to bring the imperfect system to its design performance, are the key ingredients to apprehend the studies performed on the CLIC and ATF2 FFS optics presented throughout this thesis.

Chapter 3

CLIC 3 TeV BDS optics optimization with $L^* = 6$ m

Aiming to simplify the CLIC Machine Detector Interface (MDI), a new detector model has been designed allowing the last quadrupole QD0 of the FFS to be located outside of the experiment with a distance L^* from the IP of 6 meters. In this Chapter one attempt to give a fair performance comparison between the CDR FFS (nominal) lattice and the optimized $L^* = 6$ m design for CLIC at 3 TeV c.o.m. The main operational aspects, impacting the luminosity performance, are presented and a simulation campaign has been carried out to establish the FFS tuning feasibility under realistic static error conditions of the beamline optics.

3.1 Impact of the L^* on the CLIC MDI

The Machine Detector Interface design has to satisfy requirements from both the FFS and the detector sides. It must ensure the optimum luminosity for the experiment with minimal backgrounds while meeting constraints from the infrastructure. The FFS L^* parameter can have a considerable impact on the design of the detector and MDI, if this implies the integration or not of the last quadrupole QD0 inside the experiment. The Sections 3.1.1 and 3.1.2 summarize the benefits and drawbacks of the nominal FFS lattice with a short L^* of 3.5 meters and the motivations toward optimizing a longer L^* design with QD0 outside of the experiment.

3.1.1 MDI with the CLIC CDR FFS design

The CLIC CDR was considering the construction of two complementary detectors, the International Large Detector (ILD) and the Silicon Detector (SiD), installed in a push-pull scheme as designed for the ILC [7]. The push-pull goal was to share the luminosity by the two detectors, to ensure a better yield of physics and allow confirming discoveries from independent groups. In order to avoid significant extra cost and loss of beam time during push-pull operations, and also because the physics reach was very similar for ILD [55] and SiD [56, 57], it was agreed to move toward a single detector. The single detector is based on the SiD model and produces a 5 T solenoid field. The FFS baseline for the CDR foresees a short L^* of 3.5 m leading to place the final quadrupole QD0 inside the experiment as illustrated in Fig. 3.1. This layout choice was enforced to allow for the highest possible instantaneous luminosity [58] generally obtained with a short L^*, assuming no external solenoid field or vibrations from the detector. As discussed in

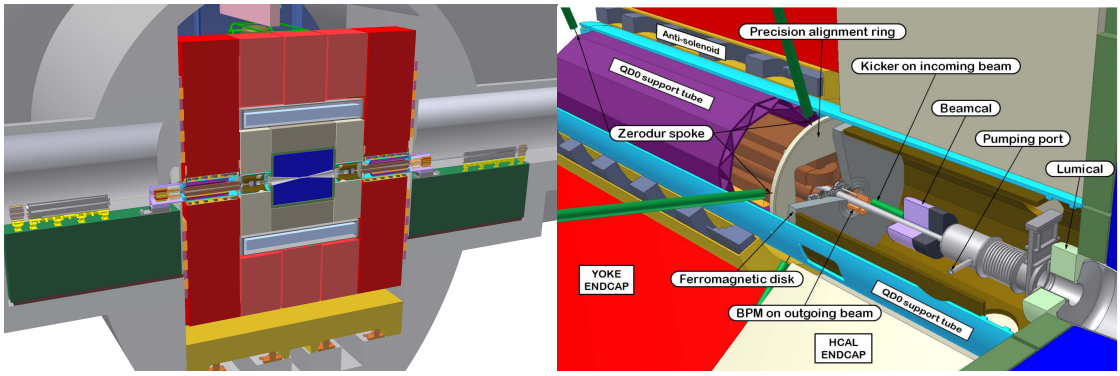

Figure 3.1: Left: Vertical cut through the SiD experiment. QD0 is located inside the detector and partially supported by the pre-insulator (green block) in the tunnel. Right: simplified MDI layout view showing a representation of part of the final-focus quadrupole, QD0, integrated into the CLIC SiD detector and shielded by an anti-solenoid. Figure comes from [8].

Section 2.8, any vertical motion of this quadrupole translates into an equivalent displacement of the beam at the IP. To maintain the beams in collision, the vertical position of the quadrupole must be stabilized to 0.15 nm at frequencies above 4 Hz [8]. Measurements on and near the CMS detector [59] indicate that ground motion and technical noise are much larger on the detector than at the ends of the tunnel. It imposes the integration of a pre-insulator system [8,60] and an active insulation to mitigate vibrations of QD0 inside the detector to the 0.1 nm level. This system still needs to be demonstrated in a detector-like environment. Due to the presence of a strong magnetic field, higher radiation, lack of space and access inside the detector, some critical components require longer interventions, leading to loss of integrated luminosity. Additionally, the QD0 being installed inside the detector takes away a significant fraction of the acceptance in the forward region. This is partially due to the need of shielding QD0 with an antisolenoid [48] in order to reduce the interplay between the detector and the QD0 fields, which would otherwise cause important quadrupole field deterioration and luminosity loss [61] (see Section 2.7). Beam dynamics simulations have shown that the anti-solenoid can cancel more than 90% of the beam distortions [62] at the IP introduced by the overlap between the QD0 and the detector fields. A schematic overview of the baseline interaction region design together with the simulated solenoid fields expected with the antisolenoid are shown in Fig. 3.2.

3.1.2 Motivations for a long L* FFS

In order to alleviate engineering and stabilization issues of the CDR MDI design, it has been proposed in [64, 65] to move out QD0 from the detector to the tunnel by increasing L*. This alternative design features a L* of 8 m giving 28% lower luminosity than the nominal design, due to the chromatic distorsion which increases with the distance L*.

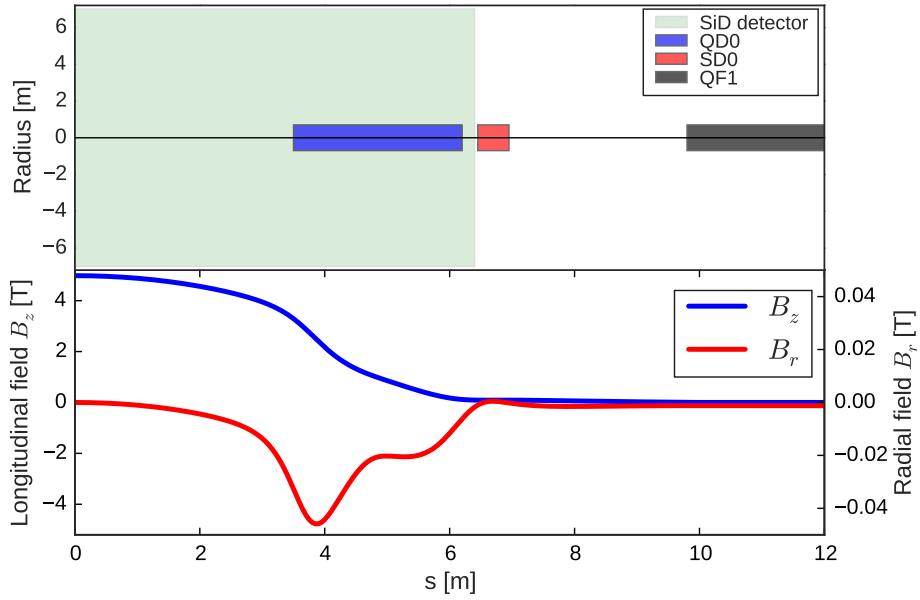

Figure 3.2: Schematic overview of the SiD interaction region layout from the last 12 meters of the FFS (upper plot). Simulation of the longitudinal and radial fields (bottom plot). QD0 overlaps with the SiD solenoid field for L* = 3.5 m.

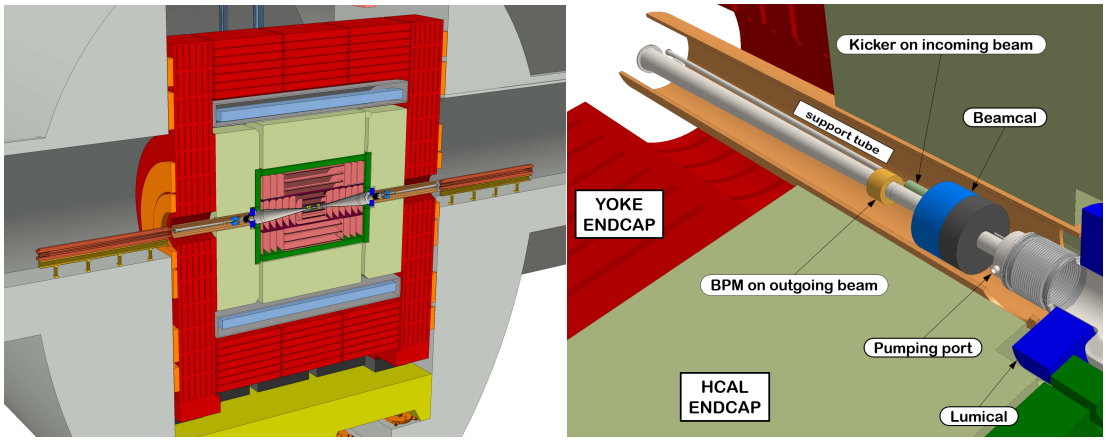

Figure 3.3: Left: Vertical cut through the new detector model CLICdet allowing QD0 to be located outside of the experiment. No pre-insulator or QD0 shielding are needed as opposed to the short L* design in Fig. 3.1 [63]. Right: Forward region of the CLICdet experiment [63].

Also, the sensitivity to transverse misalignments increased by a factor 5 [66]. It was then decided to focus the design optimization studies on a FFS with L* = 6 m which started in [42, 67], delivering luminosity close to the requirement but with more stringent tolerances against misalignment compared to the nominal design. The CLIC experiments

have proposed a new detector model named *CLICdet* [63], allowing to move out QD0 from the experiment to the tunnel with a minimum L* of 6 m. The novel interaction region layout is illustrated in Fig. 3.3. This new detector provides a 4 T solenoid field. The reduced end-cap and barrel yoke give a half length of the detector of 5918 mm which includes 4 ring coils used to remove the solenoid stray fields in the tunnel. The tunnel floor is much more stable than the detector which will significantly ease the QD0 stabilization [64,65]. The pre-insulator system is no longer needed and the access to the detector and QD0 is also simplified. The radial and longitudinal fields of the solenoid of the new detector have been computed along the first 12 meters from the IP and are shown in Fig. 3.4. The fields are zeroed at the QD0 entrance and thus no antisolenoid

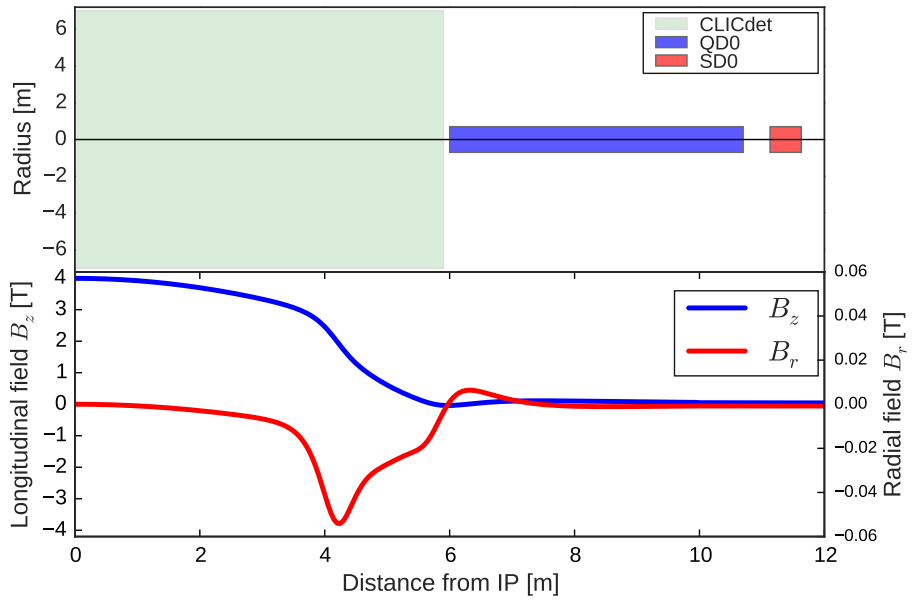

Figure 3.4: Schematic overview of the new detector (CLICdet) interaction region layout from the last 12 meters of the FFS (upper plot). Simulation of the longitudinal and radial fields (bottom plot). No overlapping between QD0 and the new detector field with L* = 6 m.

shielding is needed. The IP feedback position and latency are not affected by the change in L* [68]. The new detector and FFS layout should reduce the overall risk, improve the MDI feasibility and increase the detector acceptance.

3.2 High order optimization of the FFS with L* = 6 m

3.2.1 Optics design procedure

The design of the FFS is carried out using the MADX code [69]. The long L* design is based on the FFS scheme called Local chromaticity correction [19] starting from the nom-

Table 3.1: CLIC 3 TeV design parameters

L* [m]	3.5	6
FFS length [m]	450	770
Norm. emittance (IP) $\gamma\varepsilon_x/\gamma\varepsilon_y$ [nm]	660 / 20	660 / 20
Beta function (IP) β_x^*/β_y^* [mm]	7 / 0.068	7 / 0.12
IP beam size σ_x^*/σ_y^* [nm]	40 / 0.7	40 / 0.9
Bunch length σ_z [μm]	44	44
rms energy spread δ_p [%]	0.3	0.3
Bunch population N_e [$\times 10^9$]	3.72	3.72
Number of bunches n_b	312	312
Repetition rate f_rep [Hz]	50	50
Luminosity $\mathcal{L}_\mathrm{total}$ [$10^{34}\mathrm{cm}^{-2}\mathrm{s}^{-1}$]	5.9	5.9
Peak luminosity $\mathcal{L}_{1\%}$ [$10^{34}\mathrm{cm}^{-2}\mathrm{s}^{-1}$]	2	2

inal lattice [70] from which the final focal length L* has been increased from 3.5 meters to 6 meters. In order to preserve chromaticity compensation properties of the beamline, the drifts, dipole and quadrupole magnets have been scaled in length according to the increase of L*. Therefore, the total length of the system has been increased by 71.5%. The quadrupoles have been retuned in order to match the design optics parameters at the IP (see Table 3.1). The optical functions of the L* = 6 m lattice, compared with the nominal design, are shown in Fig. 3.5. The sextupole magnet gradients are tuned to minimize, order by order, the nonlinear contributions to the IP beam size using the MAPCLASS [71–73] code and the Polymorphic Tracking Code (PTC) [74]. The PTC code provides the map coefficients for a given beam line defined in the MADX environment. The PTC models the accelerator elements by the evaluation of their Hamiltonian. The accuracy of the model is determined by the maximum order used for the evaluation of the Hamiltonians. The MAPCLASS code profits from the calculation of the map coefficients by the PTC module of MADX to transport a distribution of particles.
For a given L*, lower β_y^* value reduces the beam size given by the linear Twiss functions, but increases the effect of chromatic aberrations. The optimum luminosity was found at $\beta_y^* = 0.068$ mm for the L* = 3.5 m design [58]. Longer L* implies larger chromatic distorsions (Eq.(2.51)) and thus β_y^* has to be re-optimized for this new design. The contributions to the IP vertical beam size σ_y^* from the higher order aberrations, after the sextupoles optimization for different β_y^* options, are shown in Fig. 3.6. The beam sizes were calculated for a monochromatic beam ($\delta_p = 0$) and for $\delta_p \neq 0$, showing the contribution from chromatic and geometric aberrations at each order. The 2$^{\mathrm{nd}}$ order chromatic aberrations as well as the 3$^{\mathrm{rd}}$ order chromatic and geometric aberrations contribute the most to the beam size growth and are amplified for lower β_y^* values. Longer L* leads to larger β functions along the FFS and the lengthening of the system gives higher dispersion level. Six normal sextupoles are used for chromaticity and higher order aberration corrections. The higher dispersion and β functions in the L* = 6 m design make its sextupoles weaker reducing the contribution from nonlinear aberrations to σ_x^*

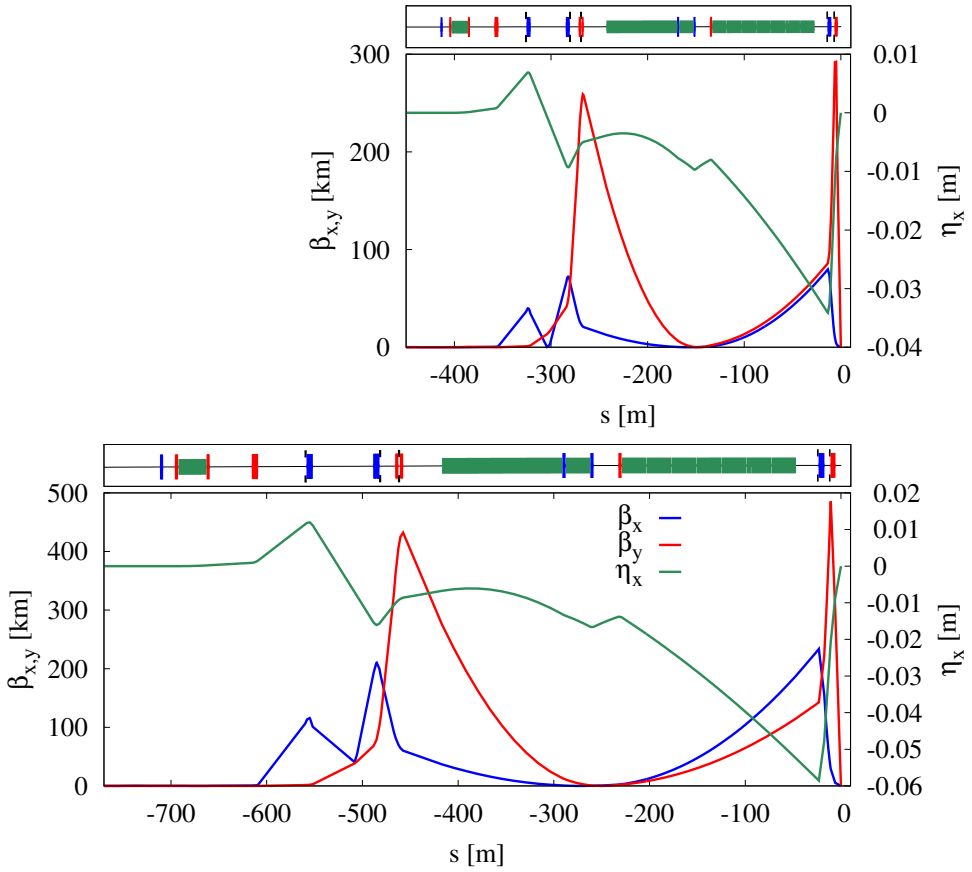

Figure 3.5: Optical functions through the Local correction scheme of the FFS for L* = 3.5 m (top plot) and L* = 6 m (bottom plot), where η_x is the dispersion function. The lattice for L* = 6 m has been lengthened with respect to the increase of L* from the nominal design.

and σ_y^*. However, at high energy, bending magnets introduce non-negligible growth of transverse emittance and energy spread due to synchrotron radiation. The angles of the bending magnets have been optimized for the L* = 6 m FFS in order to balance between these competing effects. This nonlinear optimization process has been repeated for several dispersion level options in the FFS. The bending magnet angles have been reduced in order to reduce the average dispersion η_x level at the sextupole locations up to 40% with steps of 5%. The beam was tracked through the BDS to the IP using the PLACET code [75] and the total luminosity ($\mathcal{L}_{\text{total}}$) and the peak luminosity ($\mathcal{L}_{1\%}$), coming from the collisions with energy larger than 99% of the maximum energy, were computed using the GUINEA-PIG code [76]. GUINEA-PIG simulates the interaction of two colliding beams including pinching of the beams and emission of beamstrahlung. The luminosity was calculated without taking into account the effect of the fringe fields or solenoid field of the detector, assuming head-on collisions and that the CLIC energy spread is expected to be 1%, full width of a uniform distribution $\Delta_{p,(\text{uniform})}$. This amounts to $\Delta_{p,(\text{RMS})}$

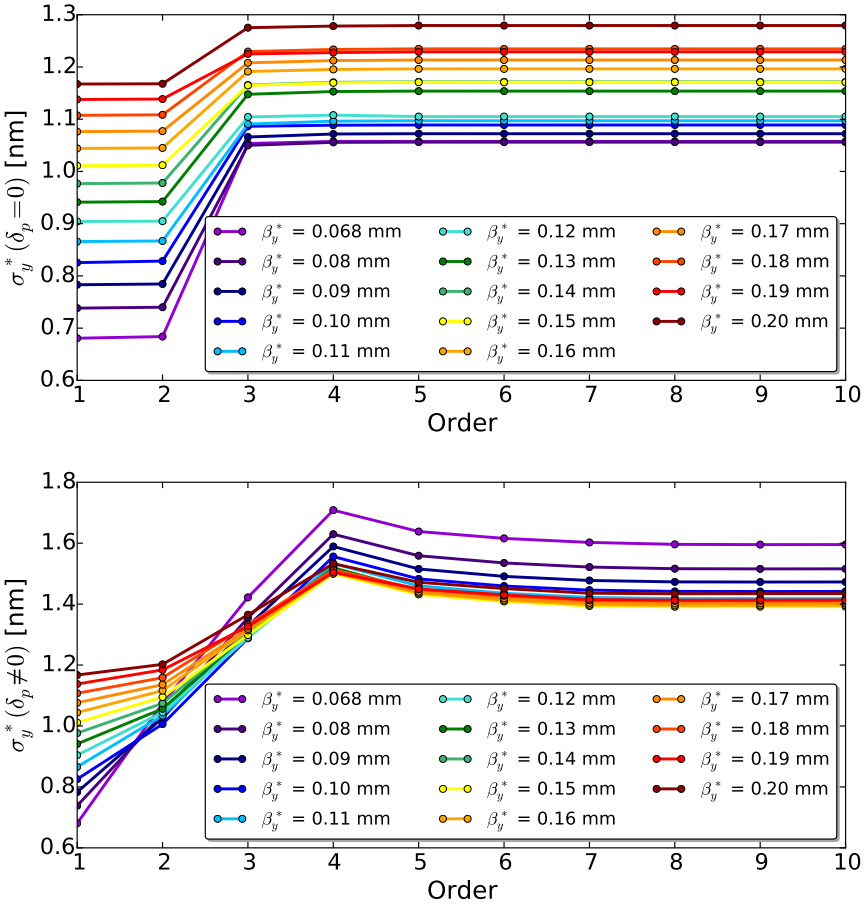

Figure 3.6: High order optimization of the vertical beam size for CLIC 3 TeV with L* = 6m and for different β_y^*. σ_y^* calculated for $\delta_p = 0$ (upper plot) and for $\delta_p \neq 0$ (lower plot).

$= \frac{\Delta_{p,(\text{uniform})}}{\sqrt{12}} \approx 0.3\%$. The results of the dispersion scan, are shown in Fig. 3.7. When lowering the dispersion while taking into account the effects of synchrotron radiation, σ_y^* slowly increases while σ_x^* decreases up to a dispersion reduction of 35%. The maximum total luminosity is reached for lower dispersion than the maximum peak luminosity. This is explained by the increase of beamstrahlung photons emitted for smaller horizontal beam size that deteriorates the luminosity spectrum in the peak while enhancing the total luminosity [77]. Finally a dispersion reduction of 15% has been applied to the FFS offering an increase of 11% and 3% in the total and peak luminosities, respectively. A scan of β_y^* has been performed in order to optimize the luminosity in the peak $\mathcal{L}_{1\%}$ as shown in Fig. 3.8. Unlike the nominal L* design [58], $\mathcal{L}_{1\%}$ reaches a maximum for $\beta_y^* = 0.10$ mm. However, $\beta_y^* = 0.12$ mm has been chosen as design parameter for tuning efficiency enhancement as described in Section 3.7.1.

The final performance of the long L* is computed for the full BDS and it is summarized in Table 3.2 and compared with the L* = 3.5 m design. As for the long L* option, the

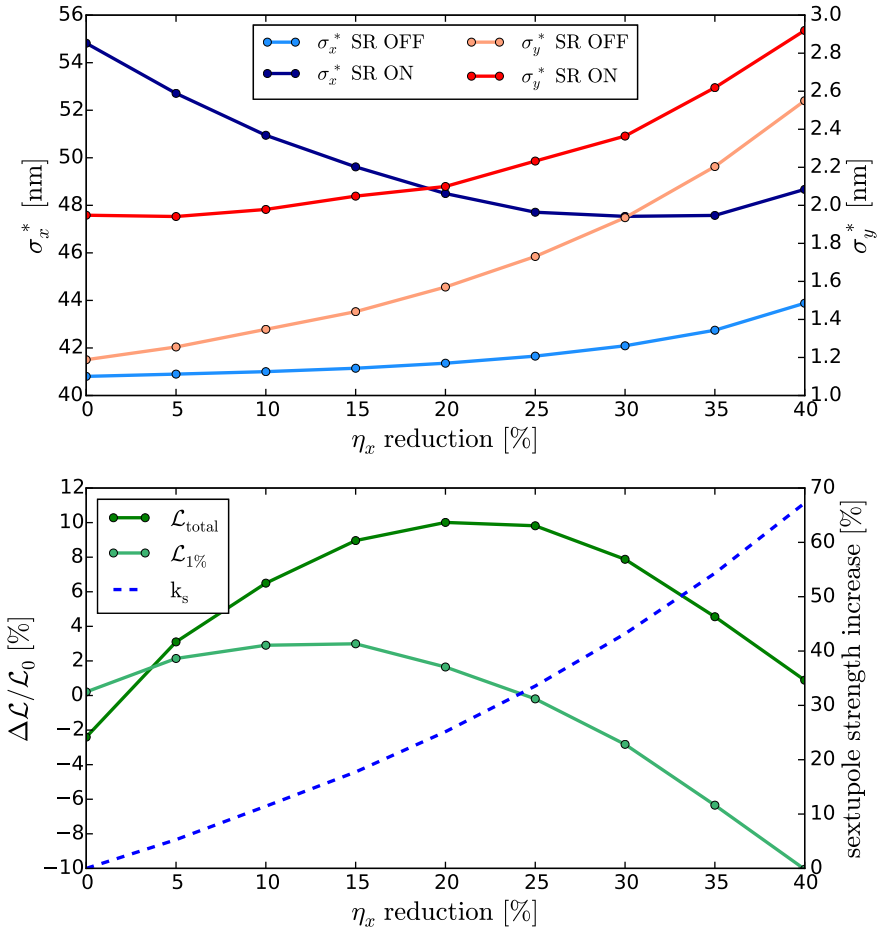

Figure 3.7: Impact of the dispersion level in the FFS on the horizontal and vertical beam sizes $\sigma^*_{x,y}$ (top plot), luminosity and sextupole strength k_2 (bottom plot) when η_x is reduced up to 40%.

nominal lattice optimized in this study does not include higher order multipoles, such as octupoles or decapoles, and differs therefore slightly from the performances exposed in [70]. The vertical chromaticity generated through the entire FFS, given in Table 3.2, was computed using the definition of the chromaticity given by Eq.(2.56). The vertical beam size contribution from the Oide effect $\sigma_{y,\text{Oide}}$, taking into account only radiation due to the vertical motion of the particles (see Eq. (2.61)), has been calculated using the MAPCLASS code (see Table 3.2). The total and peak luminosities of the optimized L* = 6 m design is reduced by 7.7% and 7% respectively compared to the nominal L* design, without higher order multipoles included in the beamline. However, when octupoles and decapoles are optimized in the L* = 3.5 m beamline [70], the difference in $\mathcal{L}_{\text{total}}$ and $\mathcal{L}_{1\%}$ between both L* options is 11.5% and 10.7% respectively. The luminosity loss due to the possible energy mismatch coming from the linac is shown in Fig. 3.9. The energy bandwidth is similar for both optimized L* options. The luminosity calculated

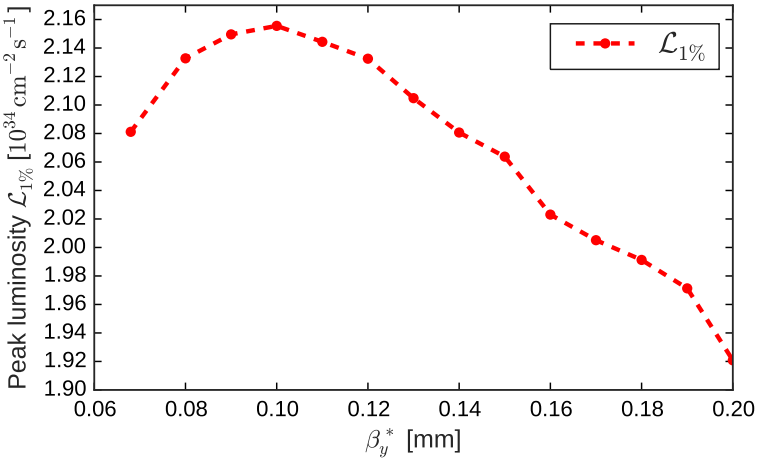

Figure 3.8: Peak luminosity maximization versus β_y^* for L* = 6 m.

Table 3.2: Simulated performance of both L* options when the beam is tracked through the entire BDS (for L* = 6 m, β_y^* = 0.12 mm). Comparison of vertical chromaticity, total and peak luminosities and impact of synchrotron radiation at the IP.

Design	ξ_y^*	$\frac{\sigma_x^*}{\sigma_x^{*\mathrm{noSR}}}$	$\frac{\sigma_y^*}{\sigma_y^{*\mathrm{noSR}}}$	$\mathcal{L}_{\mathrm{total}}$ [10^{34}cm^{-2}s^{-1}]	$\mathcal{L}_{1\%}$ [10^{34}cm^{-2}s^{-1}]	$\frac{\mathcal{L}_{1\%}}{\mathcal{L}_{1\%}^{\mathrm{noSR}}}$	$\sigma_{y,\mathrm{Oide}}$ [nm]
L* = 3.5 m	82027	1.18	1.86	7.04	2.3	0.81	0.92
L* = 6 m	79913	1.21	1.35	6.5	2.14	0.88	0.45

by tracking the beam from the entrance of the FFS to the IP is $\mathcal{L}_{\mathrm{total}} = 7{\times}10^{34}\mathrm{cm}^{-2}\mathrm{s}^{-1}$ and $\mathcal{L}_{1\%} = 2.25{\times}10^{34}\mathrm{cm}^{-2}\mathrm{s}^{-1}$ for L* = 6 m. For L* = 3.5 m [70] the corresponding luminosities are $\mathcal{L}_{\mathrm{total}}$ =7.8 $\times10^{34}\mathrm{cm}^{-2}\mathrm{s}^{-1}$ and $\mathcal{L}_{1\%} = 2.4{\times}10^{34}\mathrm{cm}^{-2}\mathrm{s}^{-1}$. It corresponds to approximately 10% of luminosity loss due to synchrotron radiation in the collimation section.

3.3 Higher order optimization of the BDS

In order to push up the luminosity and to fairly compare the performance of the nominal design optimized in [70] with the performance of the L* = 6 m, higher order corrections were performed on the long L* lattice with a pair of octupoles and a decapole, as included in the nominal L* design. Here, these corrections target only the vertical beam size σ_y^*. First, one has to identify the most dominant aberrations on σ_y^* in order to use the appropriate multipoles at the best locations along the FFS. By using the output map coefficients from MADX-PTC, the IP beam size contributions from each higher order aberrations were computed. This study revealed that the geometrical 3$^{\mathrm{rd}}$ order

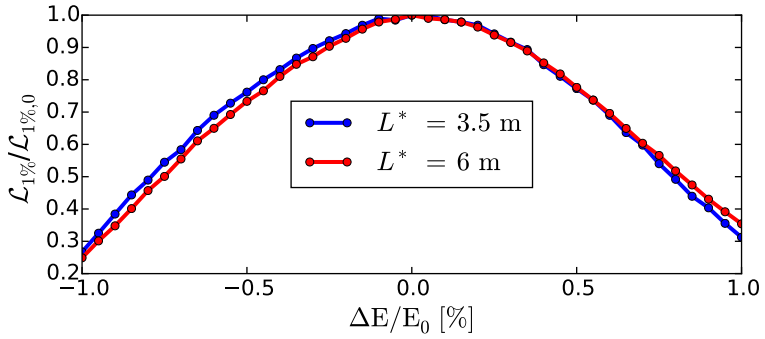

Figure 3.9: Energy bandwidth comparison between L* = 3.5 m and L* = 6 m. $\mathcal{L}_{1\%}$ is normalized to their respective maximum peak luminosity $\mathcal{L}_{1\%,0}$.

aberration U_{3224} contributes to approximately 0.2 nm in σ_y^* and the chromatic 3rd order aberration U_{3466} contributes to approximately 0.09 nm in σ_y^* as shown in Fig. 3.11. The residual 4th order chromatic aberration V_{32466} contributes to about 0.14 nm (Fig. **??**). The geometrical aberration U_{3224} has been efficiently corrected by using an octupole located in low-η_x and large β_y region. The chromatic aberrations U_{3466} and V_{32466} were corrected using respectively one octupole and one decapole located at the entrance of QD0, in high-η_x and large β_y region. The locations of these multipoles are shown in Fig. 3.12. After high order optimization of the FFS multipoles, the vertical beam size was reduced down to 1.07 nm (without taking into account synchrotron radiation) as shown in Fig. 3.13.

This reduction in the vertical beam size brings up the total and peak luminosities to

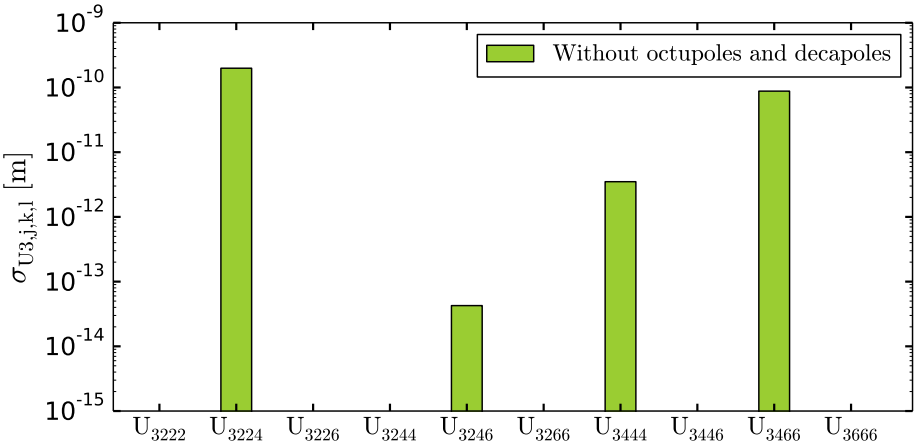

Figure 3.10: Main 3rd order contributions to the vertical beam size at the IP before the optimization of the octupoles and decapoles.

$\mathcal{L}_{\text{total}} = 7\times10^{34}\text{cm}^{-2}\text{s}^{-1}$ and $\mathcal{L}_{1\%} = 2.35\times10^{34}\text{cm}^{-2}\text{s}^{-1}$ when assuming a 1% full width energy spread at the entrance of the BDS. In Table 3.3 the luminosities were simulated

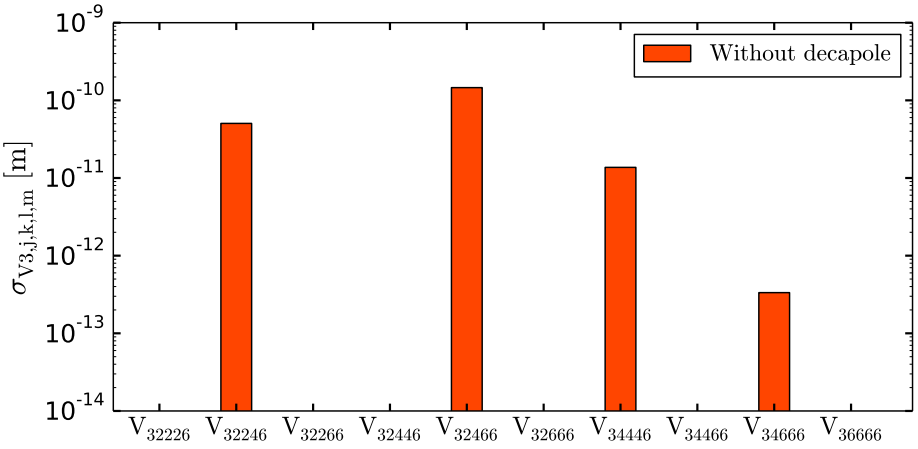

Figure 3.11: Main 4$^{\text{th}}$ order chromatic contributions to the vertical beam size at the IP before the optimization of the octupoles and decapoles.

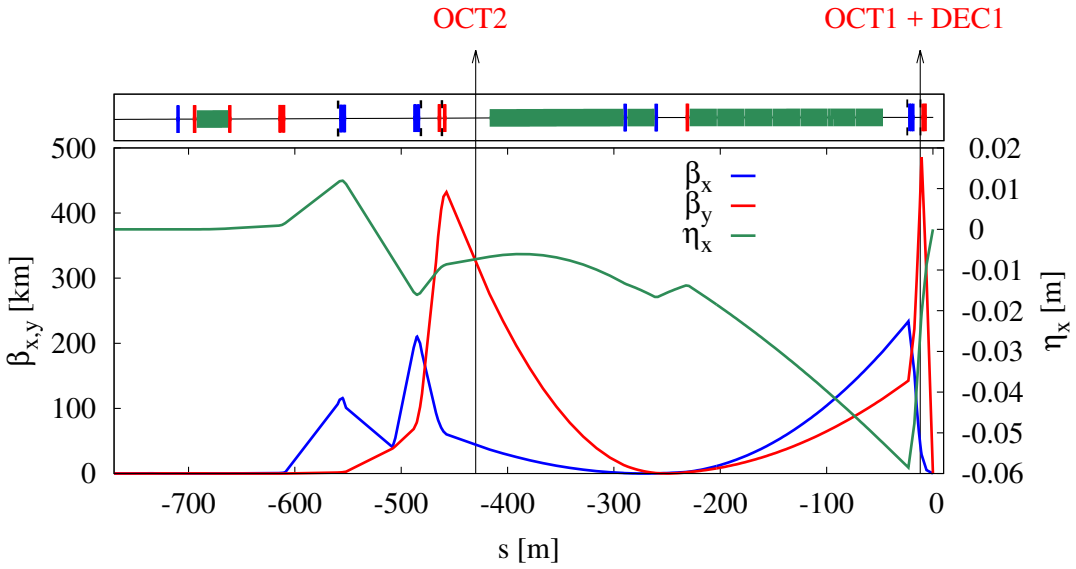

Figure 3.12: Locations along the FFS of the pair of octupoles (OCT1 and OCT2) and the decapole (DEC1).

assuming a more realistic energy spread shape coming from the main linac and taking into account uncorrelated energy spread of 1.6% of the pre-linac beam energy with a gaussian distribution. The energy distribution along the bunch is shown in Fig. 3.14. The energy spread shape coming from the main linac causes a luminosity loss of approximately 9% in $\mathcal{L}_{\text{total}}$ and 2% in $\mathcal{L}_{1\%}$ compared to the assumed 1% full width energy spread. Finally, the final peak luminosity of the CLIC 3 TeV BDS with L* = 6 m exceeds by 15% the design $\mathcal{L}_{1\%}$ and is approximately 5% lower than the $\mathcal{L}_{1\%}$ of the nominal L* = 3.5 m BDS design.

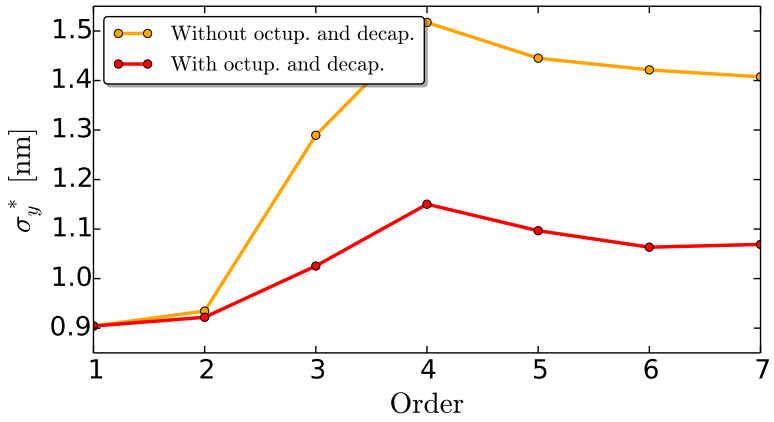

Figure 3.13: Vertical beam sizes at the IP calculated up to the 5$^{\text{th}}$ order, with and without octupoles and decapoles.

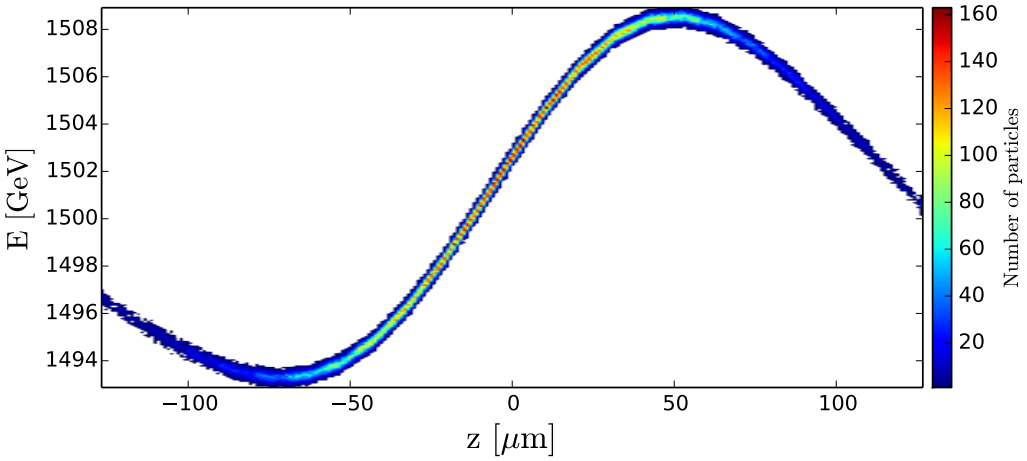

Figure 3.14: Energy distribution along the bunch at the entrance of the 3 TeV BDS assuming a realistic energy spread coming from the Main Linac.

3.4 Optics comparison with CDR FFS design

3.4.1 Parameters

The higher dispersion and β functions in the L* = 6 m design, compare with the nominal design (Fig. 3.5), make its sextupoles significantly weaker (see Table 3.4) reducing the contribution from nonlinear aberrations to σ_x^* and σ_y^*. The FD specification comparison between both L* options are summarized in Table 3.5. The maximum apertures of QF1 and QD0 are calculated according to their gradient G and by assuming a field limit at the pole-tip B_q of 1.5 T for L* = 6 m, in order to allow the use of normal conducting elec-

Table 3.3: Simulated performance of both L* options when the beam is tracked through the entire 3 TeV BDS assuming a realistic energy spread shape coming from the Main Linac.

Design	$\mathcal{L}_{\text{total}}$ [$10^{34}\text{cm}^{-2}\text{s}^{-1}$]	$\mathcal{L}_{1\%}$
L* = 3.5 m	7.6	2.4
L* = 6 m	6.4	2.3

Table 3.4: Integrated sextupole strengths k_2, dispersion η_x^s and horizontal β-function β_x^s at the sextupole locations of the FFS for both optimized L* options.

	L* = 3.5 m			L* = 6 m		
Magnet	k_2 [m^{-2}]	η_x^s [mm]	β_x^s [km]	k_2 [m^{-2}]	η_x^s [mm]	β_x^s [km]
SF6	10.5	6.5	38	3.4	12	112
SD5	19.1	-4.8	20	7.6	-8	55
SF5	-8.2	-8.4	63	-2.8	-15	185
SD4	16.6	-5	22.3	5.4	-9	66
SF1	-6.3	-33	79	-2.0	-58.4	233
SD0	22.5	-13	12	7.4	-22.3	34

tromagnets. The QD0 of the L* = 3.5 m design uses a compact hybrid quadrupole based on permanent magnet inserts and classical electro-magnetic coils, allowing a maximum field at the pole-tip of $B_q = 2.2$ T. The quadrupole aperture radius is given by:

$$\text{Ap} = \frac{B_q}{G}, \tag{3.1}$$

with $G = k_1 \times B\rho$ and k_1 is the normalized strength of the quadrupole. The reduced gradient of the FD for L* = 6 m, allows an aperture approximately twice larger for QD0 compared with the L* = 3.5 m design.

Table 3.5: Final Doublet gradient and aperture radius comparison.

FD parameters	L* = 3.5 m	L* = 6 m
G_{QF1} [T/m]	202.4	68.6
G_{QD0} [T/m]	-581.5	-197
Ap_{QF1} [mm]	7.4	22
Ap_{QD0} [mm]	3.8	8
l_{QF1} [m]	3.26	5.6
l_{QD0} [m]	2.73	4.7

Table 3.6: Vertical offset tolerances (in nanometer) for the last quadrupole magnets in the CLIC FFS for a relative peak luminosity loss of 2%

Magnet	L* = 3.5 m	L* = 6 m
QD0	0.2	0.25
QF1	0.8	1
QD2	8	9
QF3	16	19

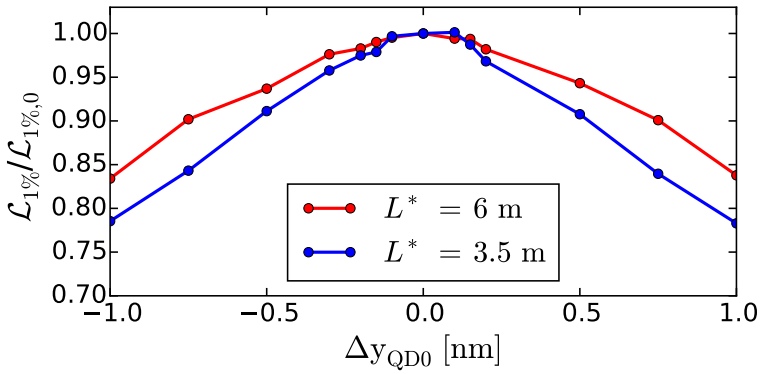

Figure 3.15: QD0 vertical offset scan as function of the relative peak luminosity loss for L* = 6 m and L* = 3.5 m designs.

3.5 Quadrupole stabilization tolerances

An important source of luminosity loss for CLIC is related to the change of the e^+ and e^- beam positions at the IP due to quadrupole position jitter. The vibration error tolerances are tigher in the vertical plane due to the smaller beam size. The tolerances in the FD are expected to be the tighest as a vertical displacement of the FD causes a displacement of the beam at the IP of the same magnitude. The vertical vibration tolerances have been quantified for the last four FFS quadrupoles QF3, QD2, QF1 and QD0 of the L* = 6 m lattice. The results are compared, in Table 3.6, with the nominal FFS design where the tolerances have been studied in [78]. The tolerances are defined as the offset required to induce a 2% peak luminosity loss and do not take into account the correction of the beam offset at the IP by the IP position feedback. A comparison of the vertical offset scan performed on QD0 for L* = 6 m and L* = 3.5 m is shown in Fig. 3.15. As the vertical beam size σ_y^* is larger for the L* = 6 m option, its tolerances to vibration errors in its final quadrupole magnets are therefore slightly larger.

3.5.1 Multipolar tolerances

The multipolar tolerances are defined as the error required to induce a 2% luminosity loss. The tolerances are evaluated for the FD, where they are the tightest, and compared

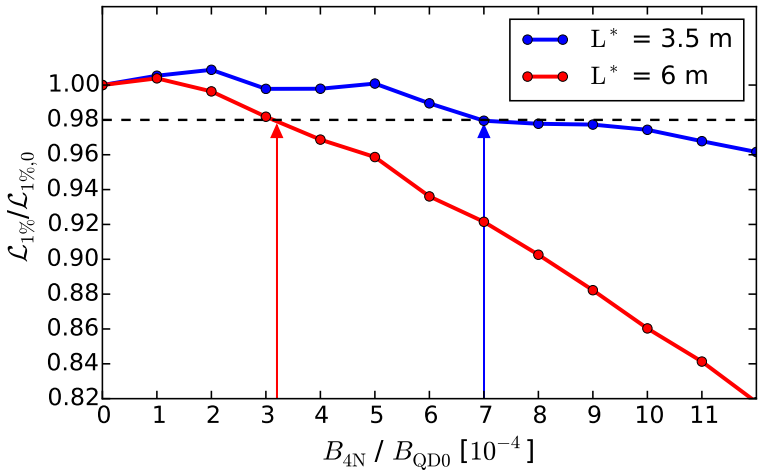

Figure 3.16: Scan of normal octupole field error applied on QD0 at R = 1 mm for L* = 3.5 m and L* = 6 m.

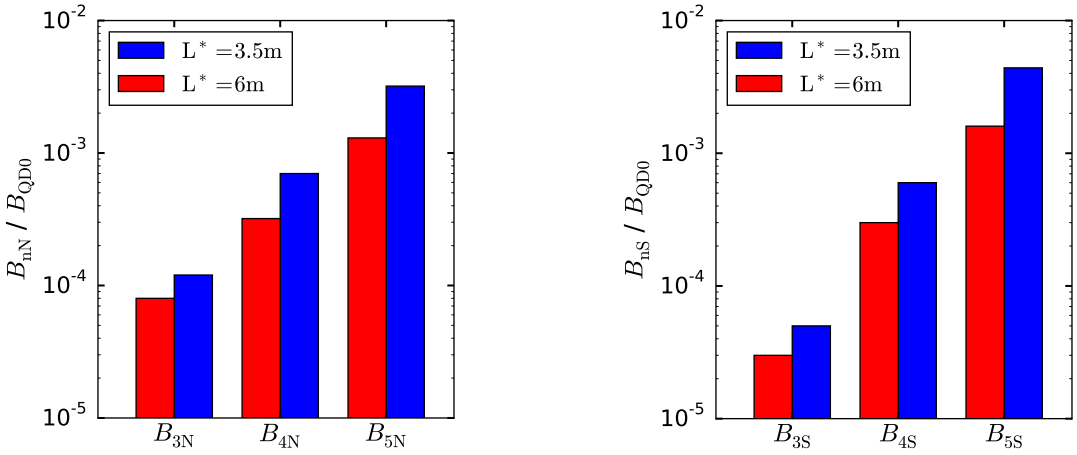

Figure 3.17: Normal (left) and skew (right) sextupole, octupole and decapole field error tolerances for QD0.

between the nominal and the long L* designs. The tolerances to normal and skew sextupole, octupole and decapole field errors, noted B_{3N}, B_{4N}, B_{5N}, B_{3S}, B_{4S} and B_{5S}, respectively, are calculated individually for QF1 and QD0 and defined as the ratio of the multipole field and the quadrupole field. An example of the scan of normal octupole field errors B_{4N} applied on QD0 at a raduis R = 1 mm, is shown in Fig. 3.16. The same study has been performed on the FD for the other multipolar field errors as shown in Figs. 3.17 and 3.18. The larger $\beta_{x,y}$ at the FD location for the L* = 6 m design makes the lattice more sensitive to higher multipole field errors compared to the nominal design.

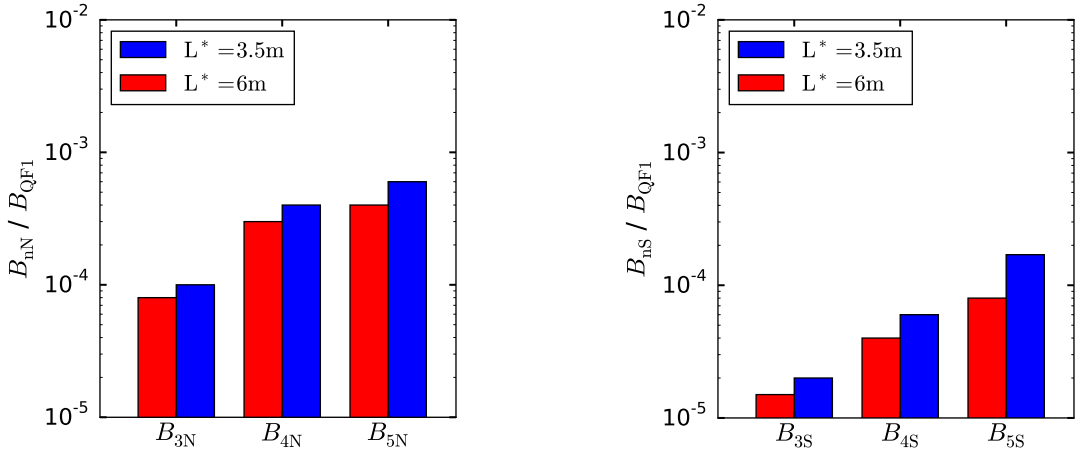

Figure 3.18: Normal (left) and skew (right) sextupole, octupole and decapole field error tolerances for QF1.

3.6 Collimation depth

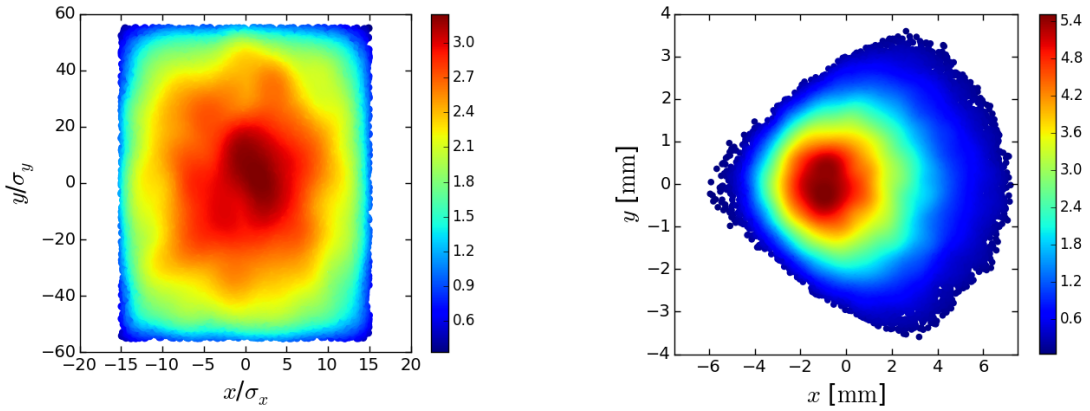

Figure 3.19: Left plot: Beam distribution at the entrance of the FFS collimated to $15\sigma_x$ and $55\sigma_y$. Right plot: resulting beam distribution at the entrance of QF1, when tracked with 1.4% flat distribution energy spread and synchrotron radiation for the L* = 6 m design.

The BDS collimator apertures were optimized for the CLIC FFS at 3 TeV with L* = 3.5 m with the aim of mitigating the wakefield effects on the luminosity performance while keeping a good efficiency in cleaning the undesired beam halo. The betatron collimation depths have to satisfy the condition that no beam particles or synchrotron radiation photons should hit either QF1, QD0, the vertex detector or the extraction quadrupole. For CLIC, the tight bore aperture of the final quadrupole QD0 determines the actual collimation depth. For the L* = 3.5 m FFS design, QD0 imposes an aperture of 3.8 mm. The optimum transverse collimation depths were found for $15\sigma_x$ and $55\sigma_y$ [30]. The

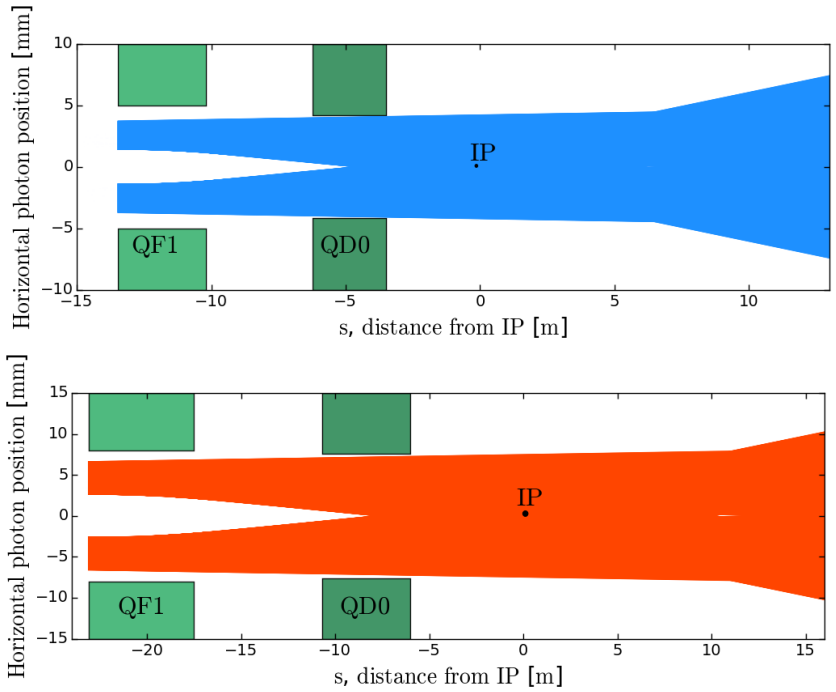

Figure 3.20: Horizontal position of the emitted photons through the FD and CLIC detector for $L^* = 3.5$ m (top plot) and $L^* = 6$ m (bottom plot).

beam size at the entrance of the FD for $L^* = 6$ m should be approximately 30% larger than the nominal design due to the increase of L^*. The lower field gradient of QD0 imposed by the longer focal length L^* and the longer magnet length l_{QD0} after the scaling of the FFS length with respect to the increase of L^* from 3.5 m to 6 m, allows an aperture for QD0 of 8 mm (see Table 3.5). The impact of the new $L^* = 6$ m design on the necessary collimator apertures compare to the nominal settings has been checked. The beam is assumed to be perfectly collimated at the entrance of the FFS with a phase space ellipse thickness of $15\sigma_x$, $15\sigma_{x'}$, $55\sigma_y$ and $55\sigma_{y'}$. The beam is then tracked through the FFS with a flat energy spread distribution of width 1.4% and by taking into account synchrotron radiation. The distribution of the beam particles at the entrance of the FFS and at the entrance of the QF1 is shown in Fig. 3.19. The transverse beam distributions were simulated at different locations through QF1 and QD0 and the photons emitted were tracked from the entrance of the FD to few meters along the post-collision line. The same simulation has been reproduced for the nominal design for comparison. The results are shown in Figs. 3.20 and 3.29 and show that the beam particles and emitted photons pass safely through the FD in both cases. The simulation results suggest that no tightening of the collimation depth is required for the scaled in length $L^* = 6$ m FFS design.

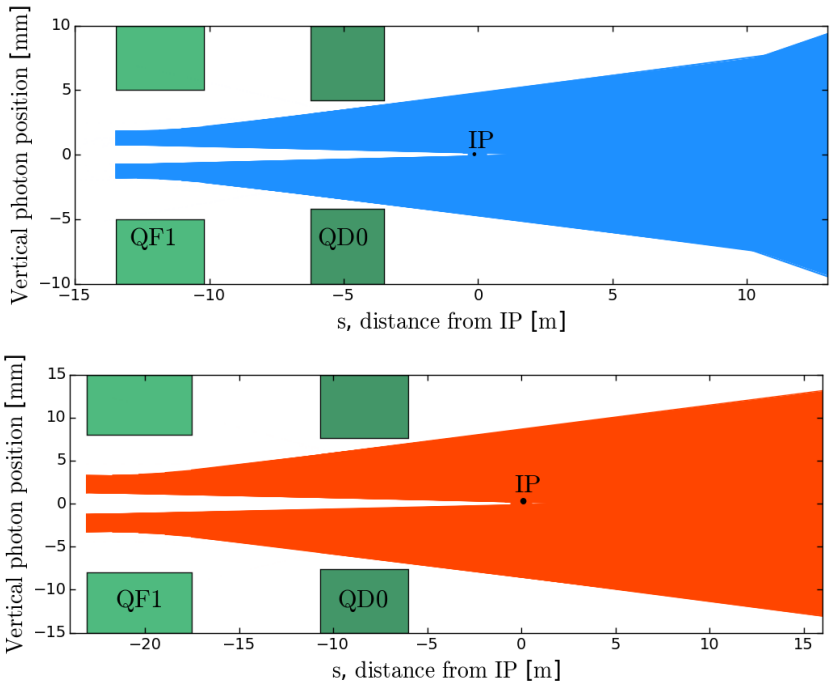

Figure 3.21: Vertical position of the emitted photons through the FD and CLIC detector for L* = 3.5 m (top plot) and L* = 6 m (bottom plot).

3.7 Tuning of the FFS

The tuning of the FFS consists of bringing the system to its design performance under realistic beam line imperfections. The tuning efficiency is of special importance as it determines the feasiblity of the lattice. As described in Section 2.8, the tuning procedure consists of beam based alignment techniques for the orbit correction and orthogonal sextupole knobs that aim to correct chosen aberrations at the IP, independently. The evaluation of the tuning efficiency is estimated over 100 randomly misaligned machines. The figure of merit of the tuning procedure is the luminosity. Since the effect of ground motion is not included into the simulations the target luminosity is 110% of the design luminosity $\mathcal{L}_0 = 5.9{\times}10^{34}\text{cm}^{-2}\text{s}^{-1}$, so that 10% budget for the luminosity loss due to dynamic imperfections is allowed. The tuning goal for the CLIC BDS is that 90% of the machines reach $\geq 110\%\mathcal{L}_0$. Tuning simulations, taking into account only the transverse misalignment of the FFS optics, were conducted on the nominal FFS design with L* = 3.5 m [79] and showed that 90% of the machines should reach $\geq$ 90% of the design luminosity in 18000 luminosity measurements, as reported in the CLIC CDR [8]. This Section reports from a tuning simulation campaign on the L* = 6 m FFS lattice. Section 3.7.1 shows the tuning simulation results by taking into account only the transverse misalignment of the FFS beam line optics as simulated in [79]. In Section 3.7.3, the tuning was performed under more realistic static error conditions by adding roll and strength errors to the FFS optics. The construction of the linear and 2$^{\text{nd}}$ order sextupole knobs needed to bring the L* = 6 m FFS lattice to its design performance is described

Table 3.7: Errors applied to the CLIC 3 TeV FFS lattice for the tuning simulations

σ_{offset} (Quadrupole, Sextupole and BPMs)	10 μm
BPM resolution	10 nm

here.

3.7.1 Tuning under transverse misalignment

3.7.1.1 Linear knobs construction

Linear aberrations at the IP created by the misaligned optics are corrected using pre-computed combinations of sextupole displacements (see Section 2.8). The knobs are orthogonal in order to correct independently the chosen set of beam aberrations. Each sextupole is displaced individually in the horizontal and vertical planes to build the corresponding aberration response matrices. The orthogonal knobs are constructed by inverting the aberration reponse matrices using the singular value decomposition method. Each knob vector gives the transverse sextupole displacements needed to correct the target aberration. The horizontal and vertical offsets of the 6 sextupoles present in the FFS allows to construct a total of 12 linear knobs. The orthogonality of the aberration response when scanning the α_x, α_y, η_x, η_y and $< p_x, y >$ coupling knobs, is shown in Fig. 3.22. The efficiency of the BBA techniques and linear knobs during the tuning procedure of the L* = 6 m FFS lattice with $\beta_y^* = 0.12$ mm, is shown in Fig. 3.23. The quadrupoles, sextupoles and BPMs were randomly misaligned according to a Gaussian distribution of width $\sigma_{\text{offset}} = 10\mu$m (see Table 3.7). Figure. 3.23 shows the average horizontal and vertical beam sizes $\sigma_{x,y}^*$ and total luminosity $\mathcal{L}_{\text{total}}$ of 100 machines, after the 1 - 1 correction, DFS and 1 iteration of linear knobs. Here one iteration of the linear knobs includes two optimizations of each knob.

3.7.1.2 Impact of β_y^* on tuning

The β_y^* scan performed on an error-free lattice has shown that the maximum luminosity is achieved for $\beta_y^* = 0.10$ mm for the L* = 6 m option (see Fig. 3.8). The tuning performance is also strongly impacted by the β^* value. As shown in Fig. 3.24, lower β_y^* values result in larger β_y along the FFS. When a sextupole is transversally misaligned, additional normal and skew quadrupole fields are introduced by the horizontal and vertical offsets, according to Eq. (2.81) and Eq. (2.85), respectively. Assuming a $(n + \frac{1}{2})\pi$ betatron phase advance between the sextupoles and the IP, the corresponding changes in the IP horizontal and vertical spot sizes due to the feed-down to normal quadrupole kicks are:

$$\Delta\sigma_x^* = K_{2N}\Delta x\beta_x^s\sigma_{x,0}^*, \tag{3.2}$$

$$\Delta\sigma_y^* = K_{2N}\Delta x\beta_y^s\sigma_{y,0}^*, \tag{3.3}$$

where K_{2N} is the integrated sextupole strength and $\beta_{x,y}^s$ is the betatron amplitude at the sextupole location. The change in beam sizes at the IP due to the feed-down skew

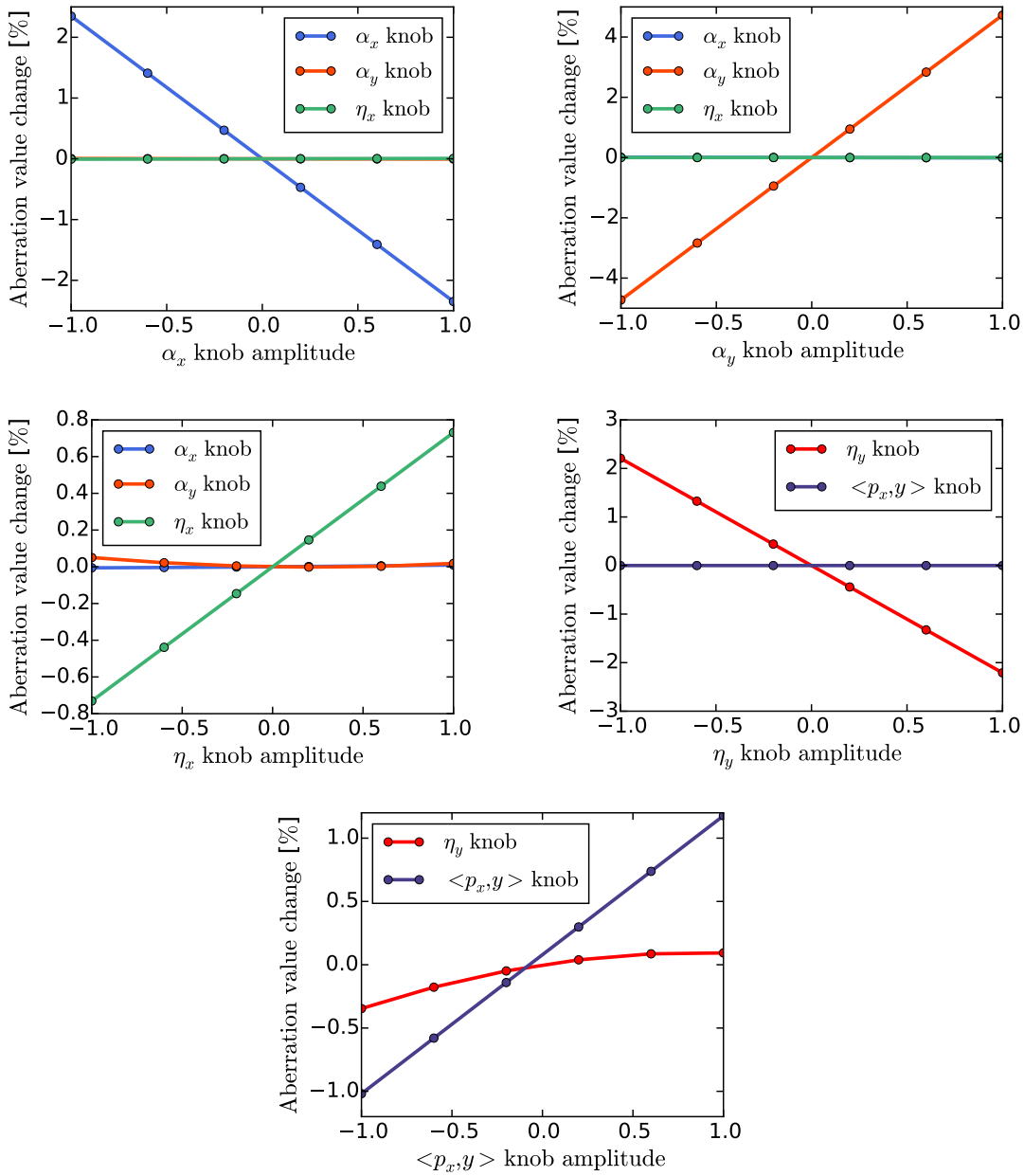

Figure 3.22: Simulation results showing the orthogonality of the linear knobs, constructed using transverse displacements of the normal sextupoles of the FFS. The plots shows the relative change of each aberration w.r.t the error-free lattice design value when the knobs are scanned.

quadrupole kicks arising from the vertical offset of a sextupole is given by:

$$\Delta\sigma_x^* = K_{2N}\Delta y\sqrt{\beta_x^s\beta_x^*}\sigma_y, \tag{3.4}$$

$$\Delta\sigma_y^* = K_{2N}\Delta y\sqrt{\beta_y^s\beta_y^*}\sigma_x. \tag{3.5}$$

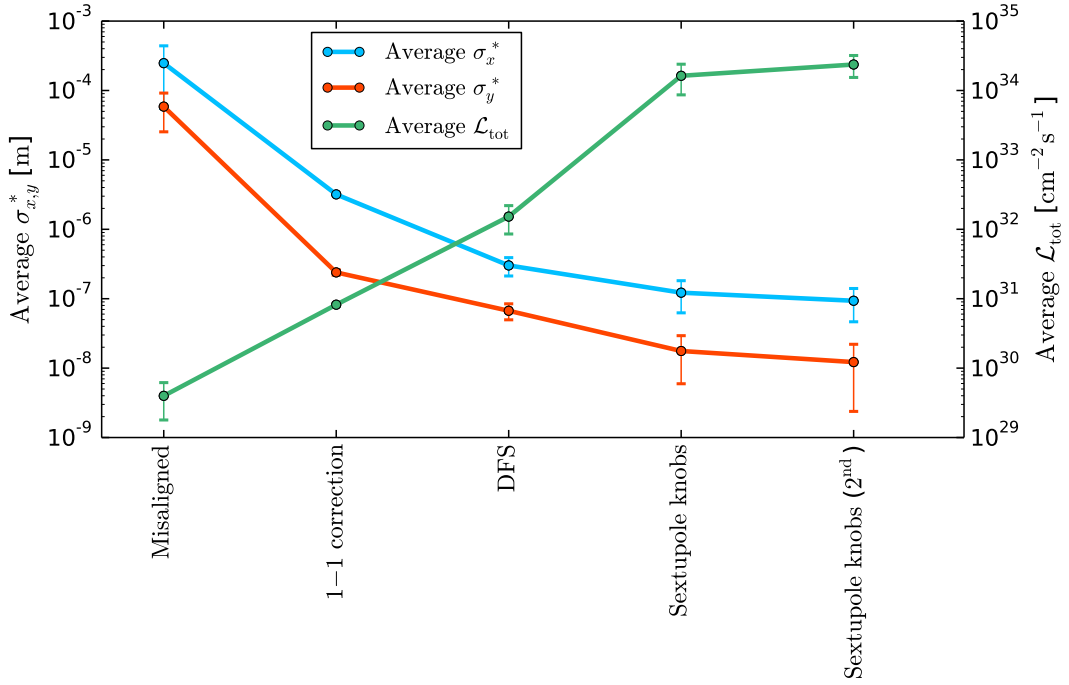

Figure 3.23: Example of the average beam sizes $\sigma^*_{x,y}$ and total luminosity $\mathcal{L}_{\rm total}$ after one iteration of BBA and 1 iteration of sextupole knobs (all linear knobs are scaned 2 times) applied on the L* = 6 m FFS lattice with β^*_y = 0.12 mm.

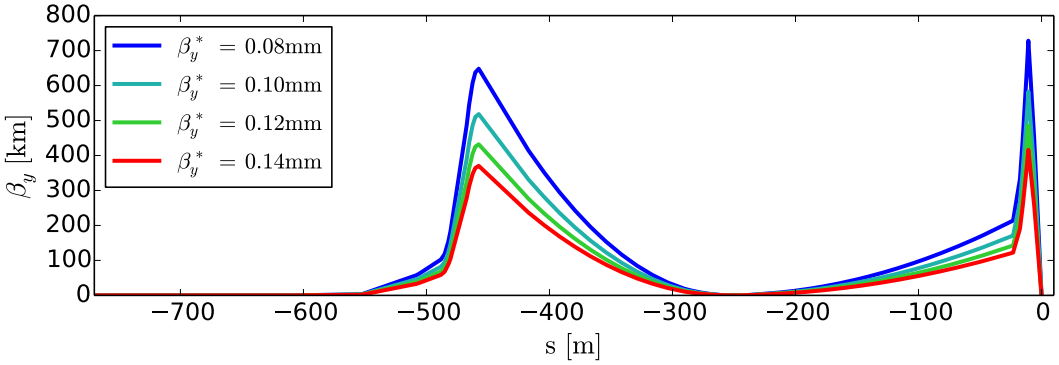

Figure 3.24: Vertical β-functions along the FFS for different β^*_y values.

The Eq. (3.2) and Eq. (3.4) shows the impact of the sextupole strength and $\beta^s_{x,y}$ values on the IP beam size when sextupoles are transversally misaligned. Lowering one of these values makes the lattice more tolerant to the transverse errors. Here, a scan of the β^*_y is performed by adding as figure of merit the tuning performance. The aim is to find a compromise between maximum luminosity achievable and tunability of the

lattice. The comparison of the tuning efficiency of 4 different lattices with $\beta_y^* = 0.08$, 0.10, 0.12 and 0.14 mm, after the BBA and one iteration of linear knobs, is shown in Fig. 3.25 (left plot). After one tuning iteration, a large difference in the average luminosity recovered by the 100 machines simulated is observed for larger β_y^* values, especially between $\beta_y^* = 0.10$ mm and $\beta_y^* = 0.12$ mm. When 5 iterations of linear knobs is applied to these lattices (Fig. 3.25 right plot), one can observe a clear improvement of the lattice tunability for $\beta_y^* = 0.12$ mm. The number of machines that reach 90% of $\mathcal{L}_0$ has been increased from 58% to 80% when β_y^* is increased from 0.10 mm to 0.12 mm while the luminosity loss is very small (< 1%) compared to the gain in tuning performance. These results justify the design β_y^* in Table 3.1 for L* = 6 m.

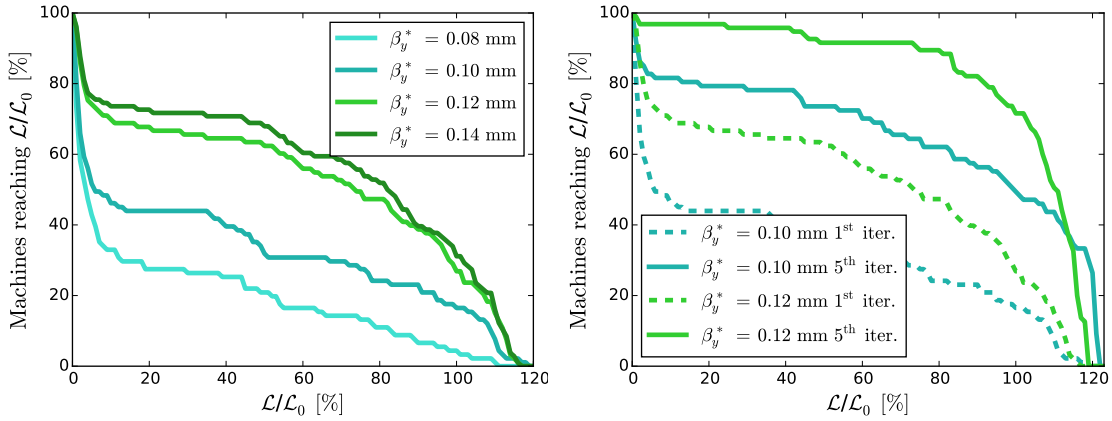

Figure 3.25: Left plot: tuning performance comparison for different β_y^* values after one iteration of BBA and 1 iteration of sextupole knobs. Right plot: tuning performance comparison between $\beta_y^* = 0.1$ mm and $\beta_y^* = 0.12$ mm, after one iteration of BBA and 5 iterations of sextupole knobs.

3.7.2 Tuning results of the optimized lattice

Only linear knobs are then applied iteratively to L* = 6 m FFS lattice with $\beta_y^* = 0.12$ mm, in order to maximize the luminosity of each machine. Figure 3.26 shows the evolution of the luminosity distribution after various iterations of knob scan. The increase of the average luminosity recovered is fast for the first iterations and starts to slowly converge for higher number of knob scans. After the 12^{th} iteration, which corresponds to ≈5000 luminosity measurements, 97% , 92% and 87% of the machines reach above 90%, 100% and 110% of $\mathcal{L}_0$, respectively. These results demonstrate the tuning feasibility of the L* = 6 m FFS design to be at the same level or better than the L* = 3.5 m design given in the CDR [8]. The tunability of the lattice under transverse misalignment is an important step towards demonstrating the feasiblity of the FFS design. In order to establish the tuning feasiblity of the design under realistic static error conditions, additional imperfections, roll and strength errors should be considered in the tuning simulations.

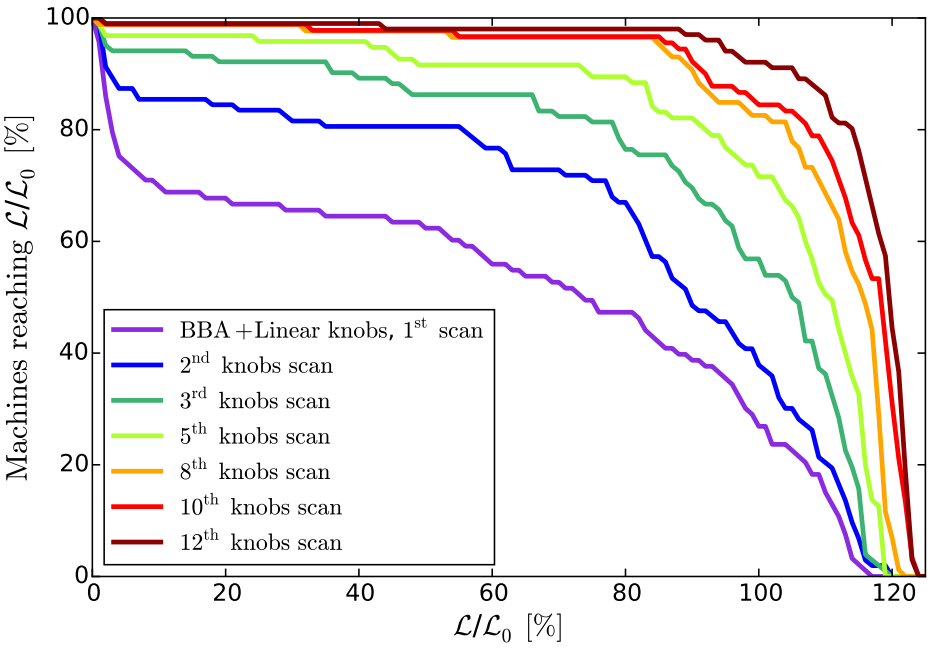

Figure 3.26: Tuning performance results for the optimized L* = 6 m design with $\beta_y^* = 0.12$ mm under transverse misalignment of the optics. 87% of the machines achieve at least 110% of the design luminosity after 12 iterations of linear knobs, corresponding to approximately 5000 luminosity measurements.

3.7.3 Tuning under realistic static imperfections

3.7.3.1 Nonlinear knobs construction

In the following tuning studies, the tuning of the lattice has been reproduced by taking into account more realistic static error conditions (see Table 3.8). This study goes a step beyond the tuning campaign performed on the nominal lattice of the CDR. By introducing these additional imperfections to the lattice the tuning performance is strongly impacted. The roll and strength errors of the quadrupoles generate additional linear contributions to the IP beam size. The roll and strength errors of the sextupoles produce additional 2nd order contributions to the IP beam size, that are not corrected by the linear knobs. The average contribution from the 2nd order aberrations over 100 machines simulated after applying the errors of Table 3.8, is shown in Fig. 3.27. The aberrations, from the highest contribution to the lowest, are T_{126}, T_{146}, T_{122}, T_{166}, T_{124} and T_{144} for σ_x^* and T_{326}, T_{346}, T_{322}, T_{366}, T_{324} and T_{344} for σ_y^*. Here the 2nd order knobs contructed use strength variations of the 6 normal sextupoles of the FFS. As discussed in Section 2.8.2 (see Eq. (2.95)), only the T_{122}, T_{126}, T_{144}, T_{166}, T_{324} and T_{346} aberrations can be corrected using the FFS normal sextupoles. Among the 6 possible 2nd order knobs, 5 were constructed: T_{122}, T_{126}, T_{166}, T_{324} and T_{346}. The T_{144} knob was not constructed as this aberration has a negligeable contribution to the beam size growth.

Table 3.8: Errors applied to the CLIC 3 TeV FFS lattice for the tuning simulations

σ_{offset} (Quadrupoles, Sextupoles and BPMs)	10 μm
BPM resolution	10 nm
σ_{roll} (Quadrupoles, Sextupoles and BPMs)	300 μrad
Strength error (Quadrupoles and Sextupoles)	0.01 %

The Figure 3.28 shows the quasi-orthogonality of the constructed 2nd order knobs.

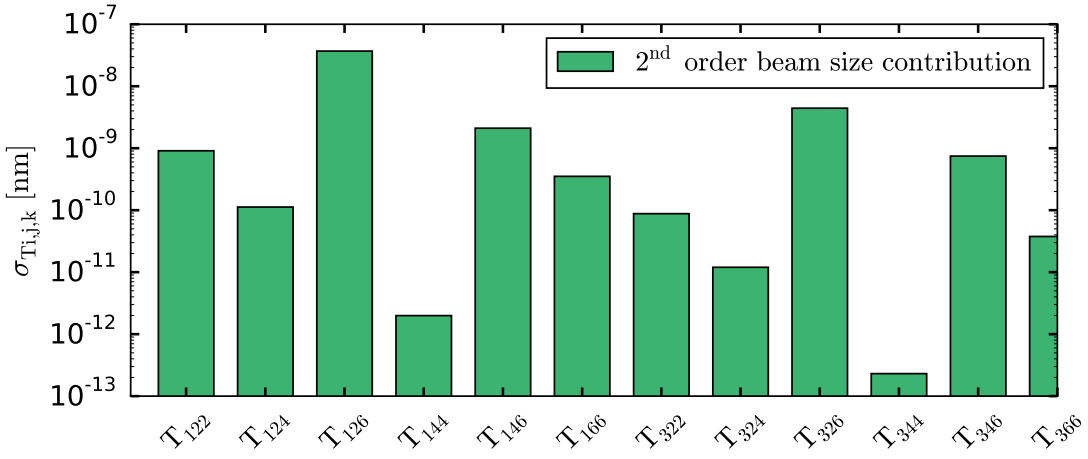

Figure 3.27: Average beam size contribution of the 2nd order aberrations over the 100 machines simulated after applying the errors of Table 3.8.

3.7.3.2 Results

The tuning procedure has been applied as follows: one iteration of BBA, then iterations of linear knobs until convergence is reached. When the effect of the linear knobs on the luminosity of each machine becomes negligeable, the 2nd order knobs are applied in combination with the linear knobs. The tuning performance converged after 12 iterations of linear knobs where 72% of the machines reach at least 110% of $\mathcal{L}_0$. When 2 additional iterations of linear and nonlinear sextupole knobs are applied the tuning performance has been improved to 85% of the machines reaching more than 110% of $\mathcal{L}_0$, falling very close to the tuning goal. The luminosity obtained for 90% of the machines is $\geq$97% of $\mathcal{L}_0$. The tuning time and efficiency can be further improved by inserting 4 skew sextupoles in the lattice, as performed in the ATF2 final focus beam line, in order to correct the remaining 2nd order aberrations T_{146}, T_{326}, T_{322} and T_{366} [54].

This study has shown the efficiency of the nonlinear correction technique applied in the tuning procedure and demonstrated the tunability of the L* = 6 m lattice under realistic static imperfections. The overall performance of the L* = 6 m FFS presented in this

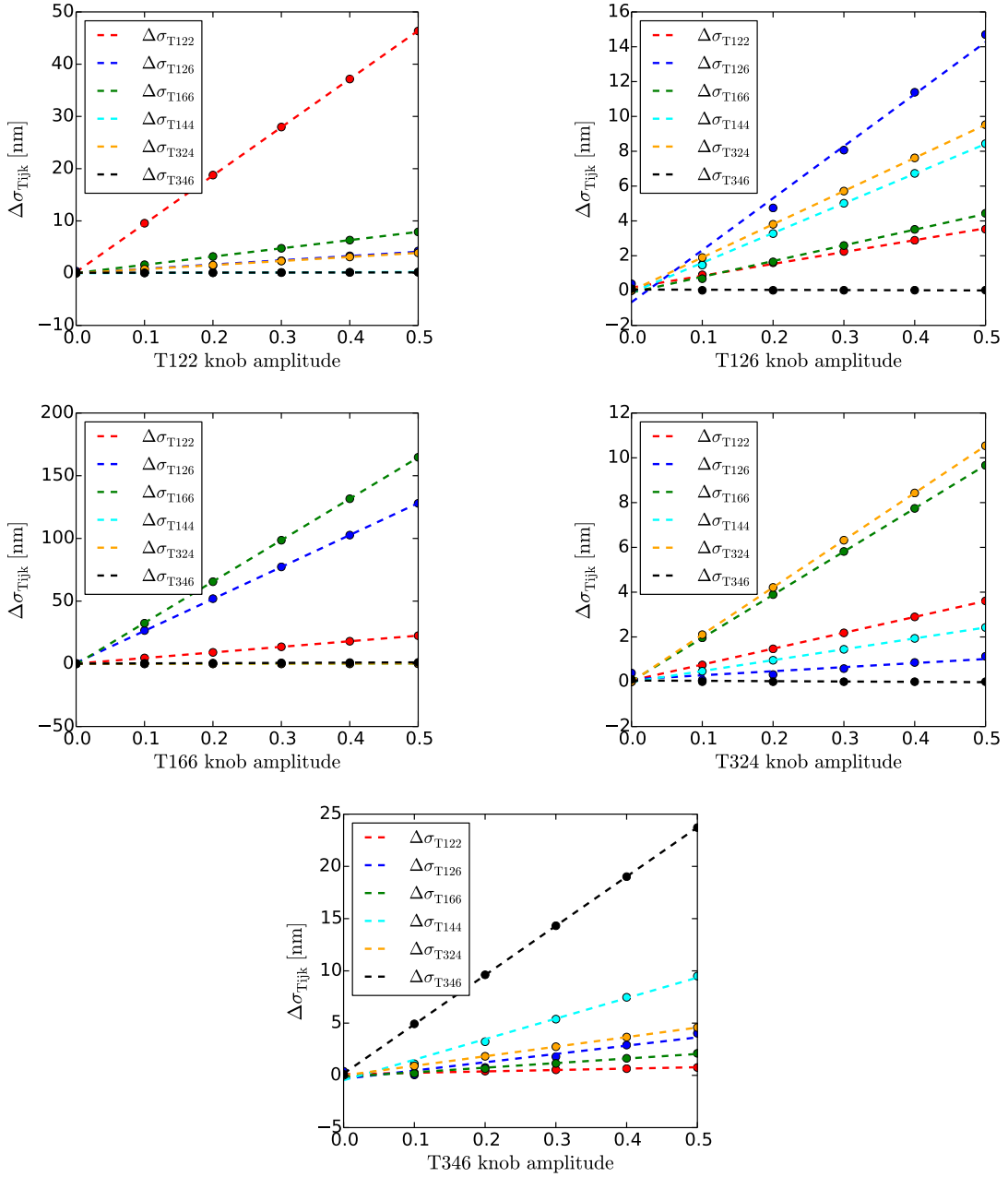

Figure 3.28: Simulation result showing the orthogonality of the second order knobs, T_{122}, T_{126}, T_{166}, T_{324} and T_{346} constructed using strength variation of the normal sextupoles of the FFS.

Chapter, makes this alternative design a realistic and robust candidate for the future CLIC BDS. However, in the present simulations, the luminosity is computed assuming that both the electron and positron FFS are identical, so the same beam distribution at the IP is assigned for both e^- and e^+ beam lines. In order to fully establish the

tunability of the CLIC FFS, tuning simulations have to include the impact of the 2-beam tuning as well as dynamic imperfections. These studies are beyond the scope of this thesis. However, 2-beam tuning tuning simulations on the CLIC 3 TeV FFS with L* = 3.5 m assuming realistic static imperfections has been performed in [80,81], showing results very close to the goal with 90% of the machines reaching ≥97% of $\mathcal{L}_0$ in ≈ 15000 luminosity measurements, due to the 2 independent systems to be tuned. These tuning results are encouraging towards fully demonstrating the tunability of the CLIC FFS with L* = 6 m.

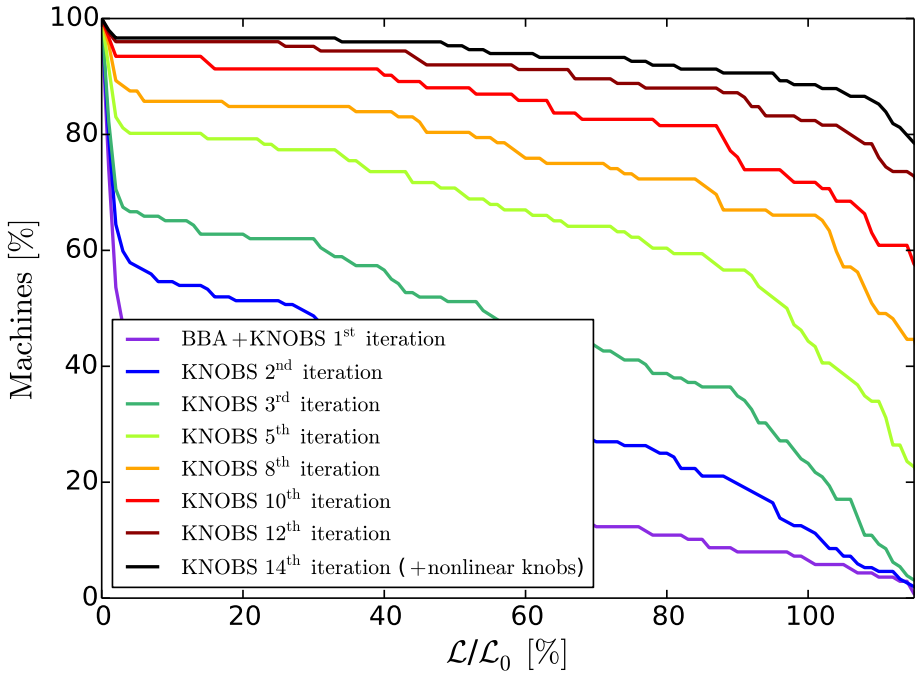

Figure 3.29: Tuning performances of the CLIC 3 TeV with L* = 6 m under realistic static error conditions. The 2 last knobs iterations includes the five 2nd order knobs constructed from the normal sextupoles of the FFS. There is 89% and 85% of the machines reaching $\geq \mathcal{L}_0$ and $\geq 110\%\mathcal{L}_0$ after ≈ 7200 luminosity measurements.

3.7.4 Executive summary

An optimized BDS with a longer L*, simplifying the MDI layout, has been addressed for the CLIC at 3 TeV c.o.m. The scaled in length FFS with L* = 6 m, w.r.t the increase of L* from the CDR design, ensure the preservation of the chromaticity compensation properties along the system. The design IP vertical β-function, β_y^*, has been changed from $\beta_y^* = 0.068$ mm (CDR) to $\beta_y^* = 0.12$ mm (L* = 6 m), in order to maximize both the luminosity and the tuning efficiency. The dispersion level along the FFS has been optimized by finding the right balance between the impact of synchrotron radiation and chromaticity correction efficiency on the luminosity. The nature of the remaining higher

order aberrations contributing the most to the vertical beam size growth at the IP were identified and corrected by adding the appropriate multipoles in the FFS beamline. The peak luminosity $\mathcal{L}_{1\%}$ of the L* = 6 m design exceeds by 15% the design value and is 5% lower than the $\mathcal{L}_{1\%}$ of the L* = 3.5 m BDS design. It is worth mentioning that this luminosity comparison, between the nominal and the long L* designs, does not take into account the impact of the new MDI layout on the luminosity (no stray field interplay, QD0 vibration reduction and larger detector acceptance). The FD tolerances to multipole field errors have been evaluated. The larger $\beta_{x,y}$ at the FD location for the L* = 6 m design makes the lattice more sensitive to higher multipole field errors compared to the nominal design. The results of the collimation depth study suggest that no tightening of the collimation depth is required for the scaled in length L* = 6 m FFS compared to the nominal design (beam collimated to $15\sigma_x$ and $55\sigma_y$). Finally, the results of the 1-beam tuning study of the L* = 6 m FFS, under realistic static imperfections applied to the quadrupoles, sextupoles and BPMs, are very close to the tuning goal with 85% of the machines simulated reaching above 110% of the design luminosity. The MADX and PLACET lattice models optimized in this Chapter are available in [82].

Chapter 4

Alternative FFS length optimization with L* = 6 m and L* = 3.5 m for CLIC 3 TeV

This Chapter presents the optimization and tuning study performed on various FFS lengths for CLIC at 3 TeV. The impact of shorter and longer lattices for the L* = 6 m and L* = 3.5 m options, on luminosity and tuning performances are compared. The MADX and PLACET lattice model optimized in this Chapter are available in [83].

4.1 Shorter FFS with L* = 6 m for tunnel cost reduction

The optimized FFS with L* = 6 m, presented in Chapter 3, features a total length of 770 m, so 320 m longer than the nominal FFS design with L* = 3.5 m. In the interest of tunnel cost reduction, 5 shorter designs have been fully optimized for FFS lengths reduced down to 495.7 m, comparable to the length of the nominal FFS design. The lattices have been designed by shortening drifts, bending magnets and quadrupole magnets proportionally while keeping the last drift L* at constant length. The design optimization procedure applied to these lattices, their performances and the impact on tuning are discussed in this Section.

4.1.1 Chromaticity correction preservation for shorter designs

The change in the FFS length, referred to as L_{FFS}, is obtained by scaling the length of the drifts, dipoles and quadrupoles while keeping the last drift L* = 6m. With such changes in the lattices design, the chromatic correction conditions, discussed in Section 2.3, through the FFS to the IP are no longer satisfied. In order to understand the impact of the changes applied to the shorter lattices on the beam size at the IP, let's recall the local chromaticity correction concept. This scheme uses 2 pairs of sextupoles for the horizontal and vertical aberration corrections. For each pair, one sextupole is located near the FD in high dispersion region and the other is located upstream of the bends in non dispersion region. They are separated by a -$\mathcal{I}$ matrix, in order to correct both the natural chromaticity and the geometrical aberrations proportional to $x^2 - y^2$ or xy, as shown in Eq. (2.59). The second order dispersion (terms proportional to δ_p^2), impacting the horizontal beam size σ_x^*, is fully cancelled by running the sextupoles twice stronger. The additional chromaticity generated by the sextupoles is compensated by producing once more the natural chromaticity upstream of the bends in non dispersion

region.

The nominal FFS design with L* = 3.5 m [8] fulfills these chromatic correction conditions, as well as for the L* = 6 m design presented in Chapter 3, as its length has been scaled from the nominal design with respect to the increase of L*. When L_{FFS} is shortened while keeping L* constant, the natural chromaticity upstream of the bends is reduced while the chromaticity generated by the FD is kept to the same level. As a consequence, the sextupoles will no longer simultaneously compensate the natural chromaticity and the 2nd order dispersion. When the sextupoles are optimized to minimize the 2nd order beam size contributions, using PTC and the MAPCLASS codes, their strengths converge to values that compensate the contribution from the natural chromaticity, leading to remaining contribution from the horizontal 2nd order dispersion. Figure 4.1 shows the horizontal beam sizes, taking into account aberrations up to the 2nd order, calculated for various shorter L_{FFS}. The tracking of a monochromatic beam, $\delta_p = 0$, shows that the impact of L_{FFS} reduction on the second order horizontal beam size $\sigma^*_{x,2^{\mathrm{nd}}\mathrm{order}}$ is fully chromatic. As the natural chromaticity generated upstream of the bends reduces when

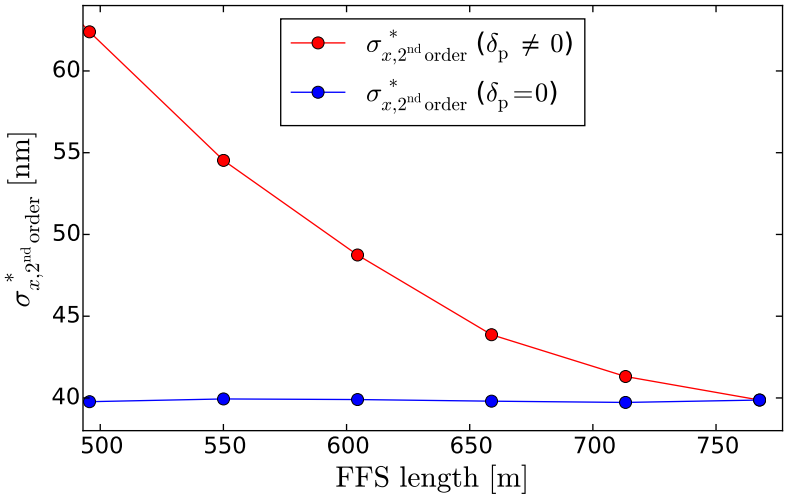

Figure 4.1: Horizontal beam size σ^*_x including only second order aberrations, simulated before $L_{\mathrm{QF1-QD0}}$ optimization, as function of the FFS length.

the FFS is shortened, the chromaticity generated by the FD has to be reduced in order to re-balance the chromatic compensation and therefore minimize second order chromatic aberration contributions to the horizontal beam size. This was performed by reducing the distance between QF1 and the IP. As L* is constant, this is equivalent to reducing the distance between QF1 and QD0, referred to as $L_{\mathrm{QF1-QD0}}$. Figure 4.2 shows an example of $L_{\mathrm{QF1-QD0}}$ scan for $\sigma^*_{x,2^{\mathrm{nd}}\mathrm{order}}$ minimization applied to a lattice length reduced down to 658.9 m and 495.7 m. The quadrupoles and sextupoles have been re-optimized after each change of the distance $L_{\mathrm{QF1-QD0}}$. The optimal FD position fitted from the $L_{\mathrm{QF1-QD0}}$ scan allows to bring the horizontal beam size back to its nominal value of 40 nm for all the

shorter designs. For the shortest FFS design optimized here, with $L_{\mathrm{FFS}} = 495.7$ m, the contribution of each 2nd order aberration to the horizontal beam size has been calculated before and after the $L_{\mathrm{QF1-QD0}}$ optimization and the results are shown in Fig. 4.3. After

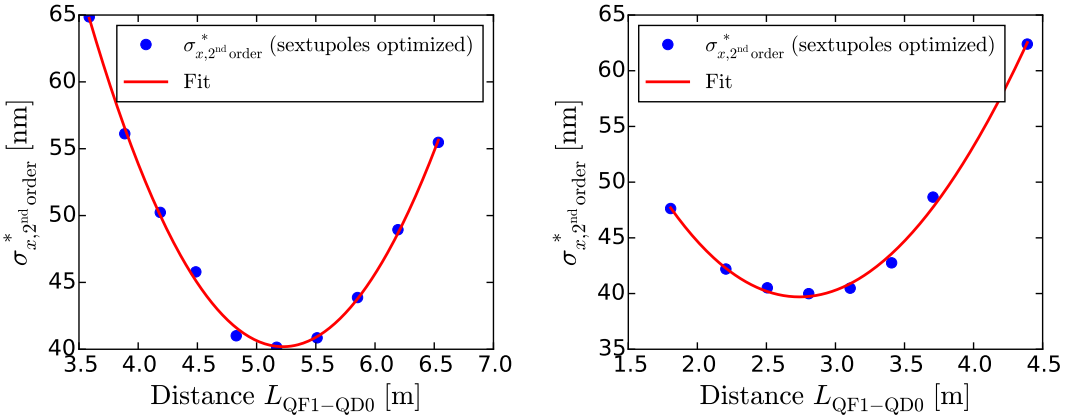

Figure 4.2: Example of $L_{\mathrm{QF1-QD0}}$ scan for $\sigma^*_{x,2^{\mathrm{nd}}\mathrm{order}}$ minimization applied on the $L_{\mathrm{FFS}} = 658.9$ m (left plot) and $L_{\mathrm{FFS}} = 495.7$ m lattice (right plot). Original distance $L_{\mathrm{QF1-QD0}}$ after FFS length reduction was 5.8 m for $L_{\mathrm{FFS}} = 658.9$ m and 4.4 m for $L_{\mathrm{FFS}} = 495.7$ m.

scaling the FFS length down to 495.7 m and sextupoles optimization, the horizontal beam size was approximately 63 nm. Figure 4.3 shows that before $L_{\mathrm{QF1-QD0}}$ optimization, the beam size contribution from the horizontal 2nd order dispersion, noted σ_{T166}, is around 22 nm. Therefore, σ_{T166} is almost fully responsible for the horizontal beam size growth from its nominal value of 40 nm. This chromaticity design correction has been

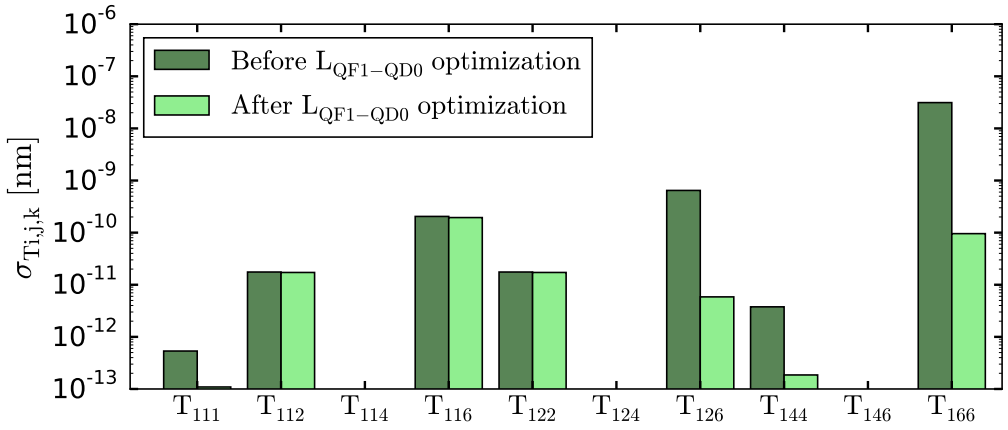

Figure 4.3: Horizontal beam size contribution from the 2nd order aberrations before and after $L_{\mathrm{QF1-QD0}}$ optimization for the $L_{\mathrm{FFS}} = 495.7$ m lattice.

performed on the 5 shorter lattices with lengths of 713.3 m, 658.9 m, 604.5 m, 550 m

and 495.7 m. The fits of the $L_{\mathrm{QF1-QD0}}$ scans for all designs is shown in Figure 4.4. The optimal $L_{\mathrm{QF1-QD0}}$ distance needed to preserve the chromaticity correction properties of the local scheme is linearly proportional to the FFS length as shown in Fig. 4.5. Finally, the sextupoles of each shorter design, after $L_{\mathrm{QF1-QD0}}$ optimization, are optimized to reduce the contributions from higher order aberrations to the vertical and horizontal beam sizes. The final beam sizes, for which the synchrotron radiation is not included, gives comparable values for all lattices, as shown in Fig. 4.6.

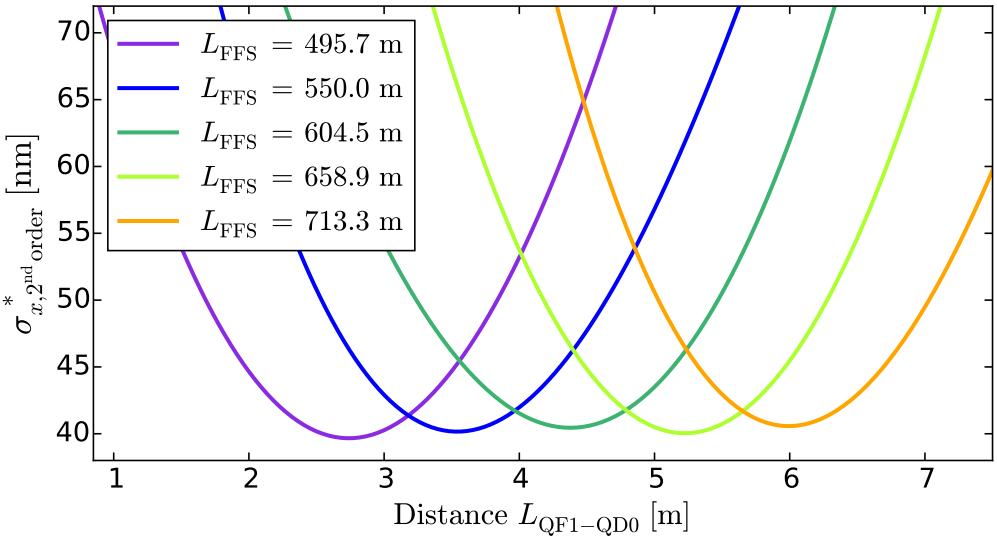

Figure 4.4: Parabolic fits of the $L_{\mathrm{QF1-QD0}}$ scan for different FFS lengths.

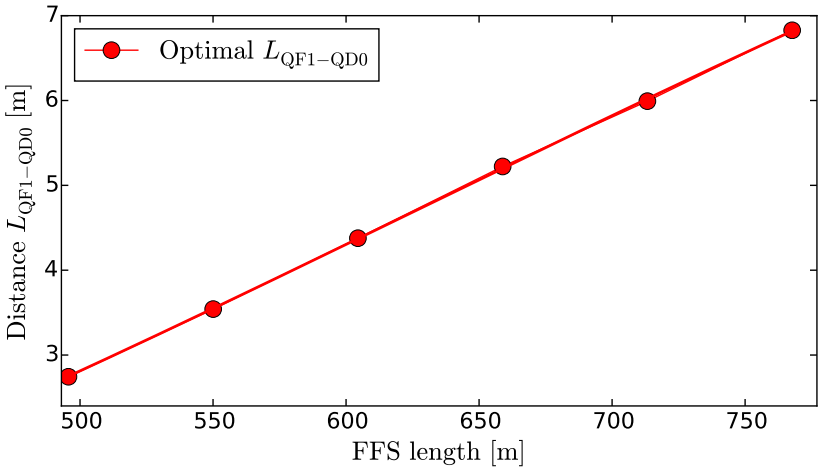

Figure 4.5: Optimal distance $L_{\mathrm{QF1-QD0}}$ for $\sigma^*_{x,2^{\mathrm{nd}}\mathrm{order}}$ minimization as function of the FFS length.

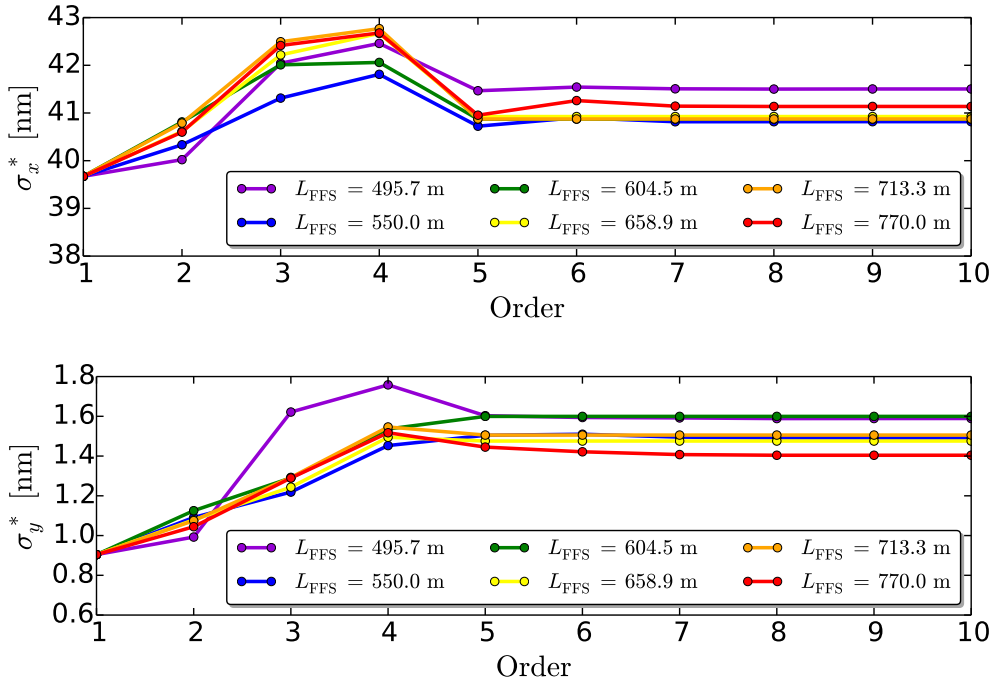

Figure 4.6: High order optimization of the horizontal (top plot) and vertical (lower plot) beam sizes for CLIC 3 TeV with L* = 6 m and for different lengths L_{FFS}.

4.1.2 Luminosity performances

The luminosity has been optimized by scanning the angles of the FFS bending magnets while taking into account the impact of synchrotron radiation, as performed on the L* = 6 m BDS described in Section 3.2.1. This scan has been performed on each shorter design and the results are shown in Fig. 4.7. The final performance of each lattice is presented in Table 4.1. Except for the shortest design simulated with L_{FFS} = 496.7 m, for which the peak luminosity is 1.5% below the design, all lattices reach or exceed the required luminosity. By shortening the bending magnets of the FFS, the observed impact of synchrotron radiation on the horizontal beam size σ_x^* is slightly reduced. However, as the quadrupole lengths are scaled, the synchrotron radiation inside the FD becomes important for shorter lattices. The shorter and stronger QD0 for shorter designs increases the vertical beam size contribution from the Oide effect [43, 44]. Finally, the impact of synchrotron radiation on the peak luminosity increases when the length of the system is reduced.

The energy bandwidth has been simulated and compared for all lattices (see Fig. 4.8). The results show similar bandwidths for all shorter designs after full optics optimization. Simulations have shown that shorter FFS with L* = 6 m can achieve the luminosity requirement for CLIC 3 TeV. However, as QF1 and QD0 are stronger for shorter designs with constant L*, their maximum apertures are smaller and therefore collimation depth may be a concern. Also, the larger FFS sextupole strength, caused by the reduction of

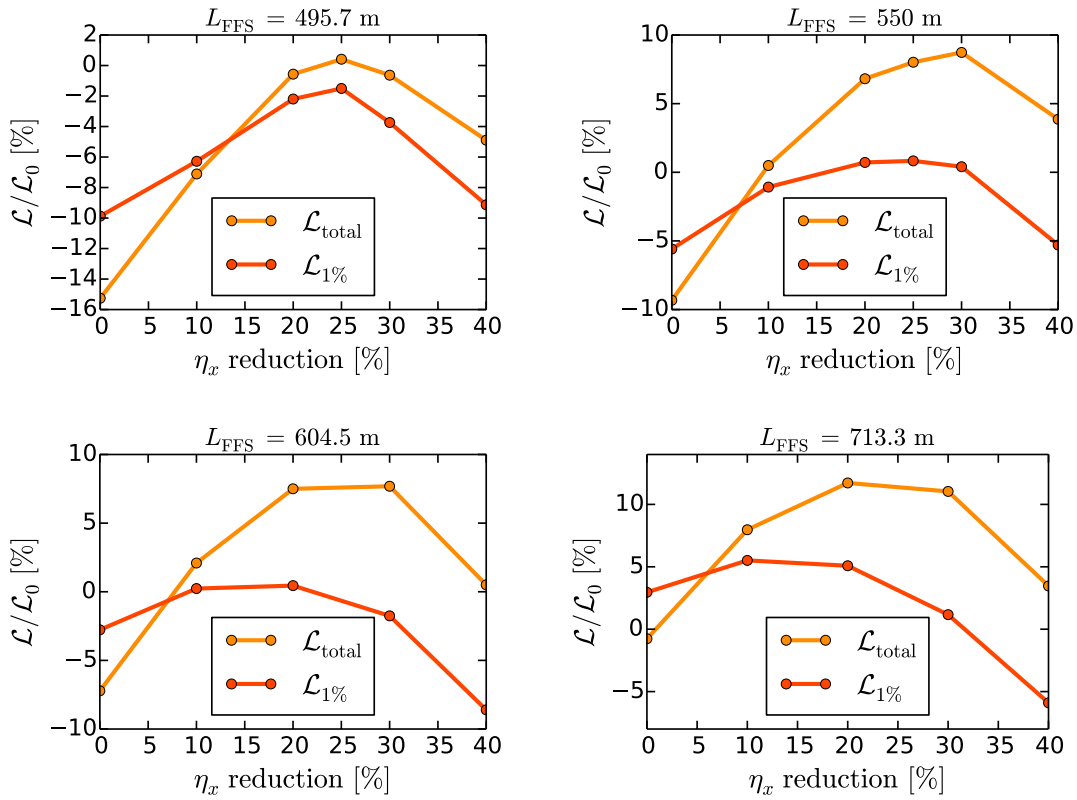

Figure 4.7: Scans of the FFS bending magnet angles for $\mathcal{L}_{\mathrm{total}}$ and $\mathcal{L}_{1\%}$ luminosities maximization, for different shorter FFS length with L* = 6 m. $\mathcal{L}_0$ is the design peak or total luminosity.

the dispersion level along the FFS for shorter lattices impacts the tuning efficiency as discussed in the next Section.

4.1.3 Impact on tuning efficiency

The tuning efficiency is expected to be reduced for shorter lattices because of the stronger sextupoles in the beamline. When the sextupoles are displaced horizontally and vertically, feed-down to normal and skew quadrupole and dipole kicks are generated:

$$\Delta B_x = B\rho\, k_2 \big[y\Delta x + x\Delta y + \Delta x \Delta y \big], \tag{4.1}$$

$$\Delta B_y = B\rho\, k_2 \left[(x\Delta x - y\Delta y) + \frac{1}{2}\left(\Delta x^2 - \Delta y^2\right) \right], \tag{4.2}$$

$$\Delta k_{1\mathrm{n}} = k_2 \Delta x \quad , \quad \Delta k_{1\mathrm{s}} = k_2 \Delta y, \tag{4.3}$$

$$\Delta k_{0\mathrm{n}} = \frac{1}{2} k_2 (\Delta x^2 - \Delta y^2) \quad , \quad \Delta k_{0\mathrm{s}} = k_2 \Delta x \Delta y, \tag{4.4}$$

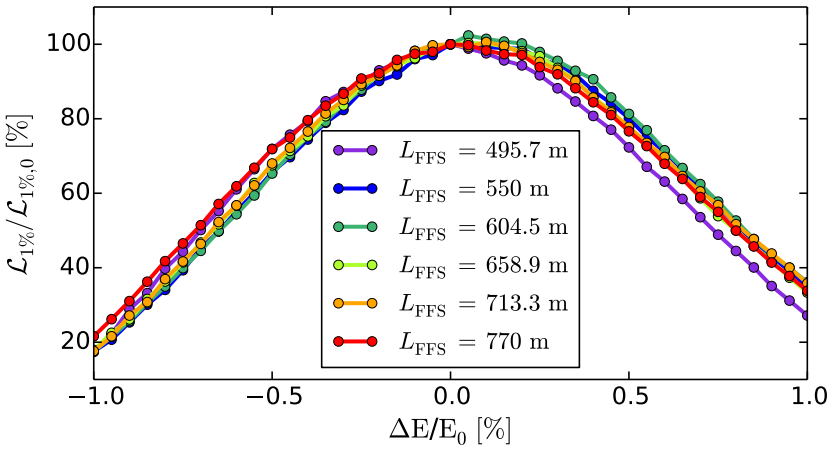

Figure 4.8: Energy bandwidth comparison between shorter $L_{\rm FFS}$ with L* = 6 m. $\mathcal{L}_{1\%}$ is normalized to their respective maximum peak luminosity $\mathcal{L}_{1\%,0}$ (see Table 4.1).

Table 4.1: Luminosity performance, synchrotron radiation impact and QD0 parameters comparison for different FFS length with L* = 6 m (no octupoles and decapoles added to the FFS beamline).

$L_{\rm FFS}$ [m]	$\frac{\sigma_x^*}{\sigma_x^{*\rm noSR}}$	$\frac{\sigma_y^*}{\sigma_y^{*\rm noSR}}$	$\mathcal{L}_{\rm total}$ [10^{34}cm^{-2}s^{-1}]	$\mathcal{L}_{1\%}$ [10^{34}cm^{-2}s^{-1}]	$\frac{\mathcal{L}_{1\%}}{\mathcal{L}_{1\%}^{\rm noSR}}$	$k_{\rm QD0}$ [m^{-2}]	$l_{\rm QD0}$ [m]	$\sigma_{y,\rm Oide}$ [nm]
770	1.21	1.35	6.5	2.14	0.88	-0.0394	4.7	0.45
713.3	1.185	1.44	6.51	2.12	0.855	-0.0441	4.4	0.50
658.9	1.176	1.56	6.6	2.11	0.85	-0.0474	4.16	0.53
604.5	1.173	1.59	6.34	2.01	0.84	-0.0555	3.75	0.63
550	1.155	1.75	6.37	2.00	0.80	-0.0663	3.35	0.76
495.7	1.15	1.82	5.93	1.97	0.79	-0.0788	3.0	0.93

where $B\rho$ is the magnetic rigidity, k_2 is the normalized sextupole strength, $k_{1\rm n}$, $k_{1\rm s}$, $k_{0\rm n}$ and $k_{0\rm s}$ are the normalized normal and skew quadrupole and dipole strengths, respectively. Assuming a $\frac{\pi}{2}$ betatron phase advance between the sextupoles and the IP, the corresponding changes in the IP vertical spot size due to the feed-down to normal and skew quadrupole kicks are evaluated in [51] by:

$$\Delta\sigma_y^* = k_2 l_s \Delta x \beta_{y,s} \sigma_{y0}^* , \tag{4.5}$$

$$\Delta\sigma_y^* = k_2 l_s \Delta y \sigma_{x,s} \left| R_{34}^{s\rightarrow *} \right| , \tag{4.6}$$

where $\beta_{x,s}$ and $\beta_{y,s}$ are the β-functions at the sextupole locations, $\sigma_{x,s}$ is the horizontal beam size at the sextupole locations, l_s is the sextupole length and $R_{34}^{s\rightarrow *}$ is the matrix element from the sextupole to the IP. Lowering $\beta_{y,s}$ or k_2 makes the beamline more tolerant to transverse misalignment of the sextupoles. When the length of the FFS is reduced, the dispersion profile is shrunk accordingly as shown in Fig. 4.9, resulting in

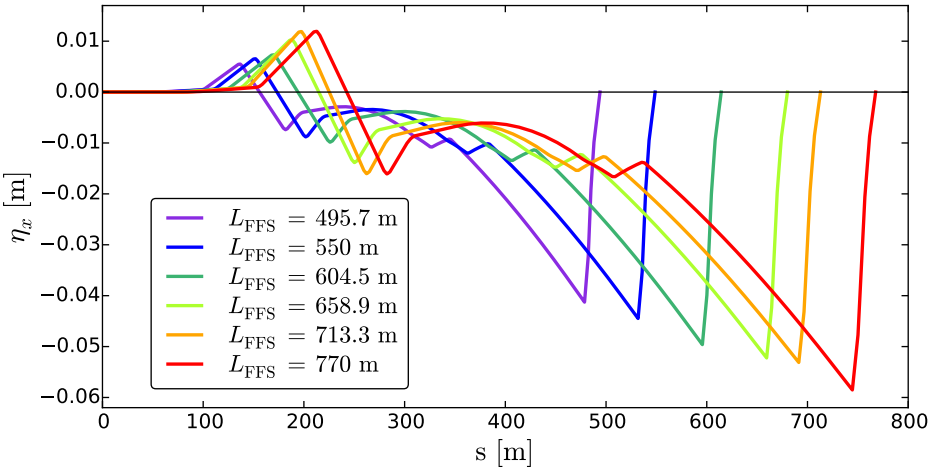

Figure 4.9: Dispersion profile for different FFS length with L* = 6 m.

higher sextupole gradients. Figure 4.10 shows the average dispersion reduction $\eta_{x,s}$ at the sextupole locations and the corresponding increase of the average sextupole strength k_s for shorter lattices. When L_{FFS} is reduced from 770 meters to 495.7 meters the average dispersion is reduced by 31% and the average sextupole strength is increased by 160%.

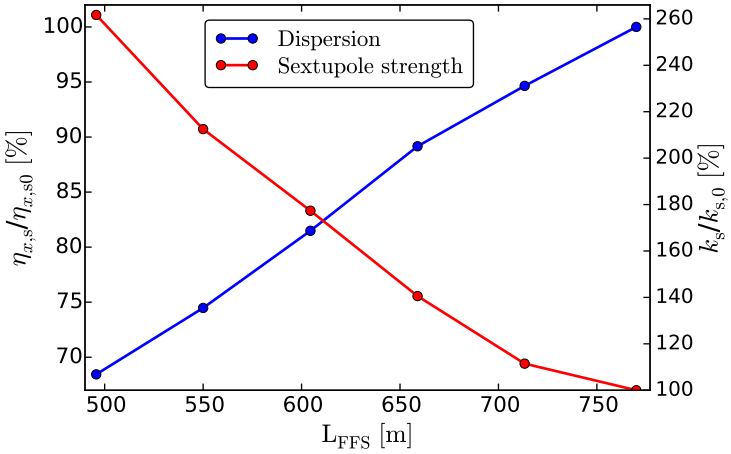

Figure 4.10: Average sextupole strength and dispersion at the sextupole locations as function of the FFS length.

The impact of shorter FFS designs on the tuning efficiency, taking into account only the transverse misalignment of the quadrupole, sextupoles and BPMs with $\sigma_{\mathrm{RMS}} = 10$ μm, has been checked by applying one iteration of BBA (1-1 correction + DFS) and one iteration of sextupole knobs. The average luminosity over the 100 machines simulated after BBA and linear knobs for different shorter designs are shown in Fig. 4.11. The results clearly show that longer systems with weaker FFS sextupoles give better tuning

performances under transverse misalignment of the FFS optics.

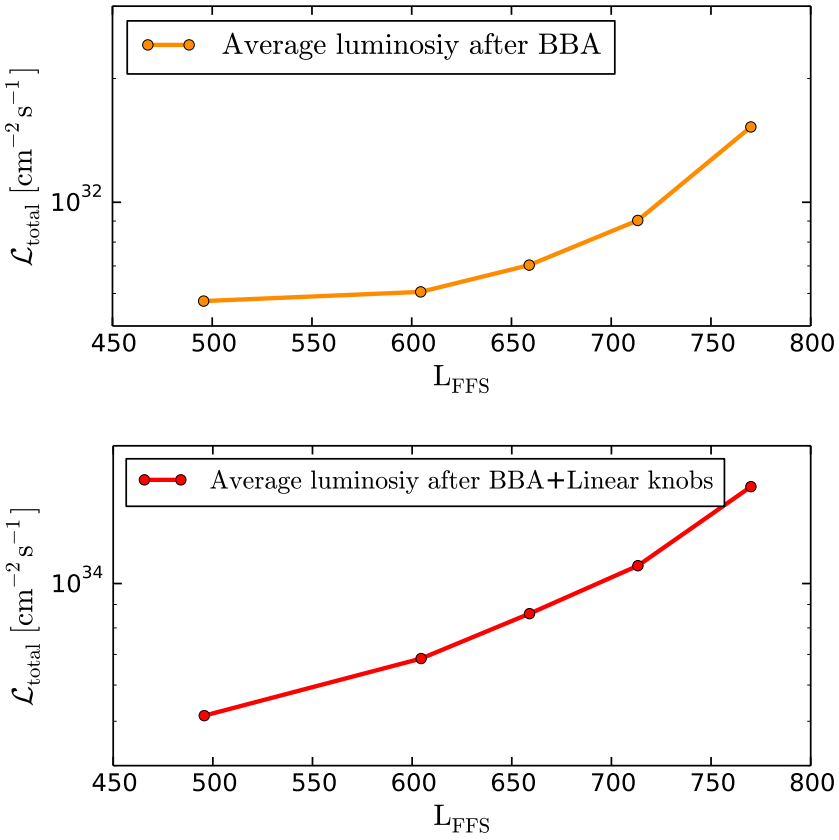

Figure 4.11: Average luminosity over the 100 machines tuned for the different shorter FFS lattices after BBA (top plot) and linear knobs (bottom plot).

Figure 4.12 shows the tuning results comparison after one iteration of BBA and three iterations of the linear knobs, for the shortest and longest FFS lengths optimized here, with L* = 6 m. For L_{FFS} = 495.7 m, 16% of the machines reach ≥90% of $\mathcal{L}_0$ while 71% of the machines reach ≥90% of $\mathcal{L}_0$ for L_{FFS} = 770 m. While the maximum luminosity achievable differs slightly for shorter L_{FFS} when the beamline is fully optimized (see Table 4.1), one should expect longer tuning time to reach it.

4.2 Longer FFS with L* = 3.5 m to ease the tuning

Tuning efficiency dependence on L_{FFS} for systems with L* = 3.5 m is discussed in this Section. As shown in [70, 79], tuning the nominal FFS design for the local scheme requires longer tuning time to recover the luminosity. A tuning-based design optimization has been performed on the nominal lattice. The tuning performance is thus promoted as figure of merit, along with the luminosity of the error-free system, for the optimization of the FFS design. The strategy is to reduce the sextupole strength k_2 along the

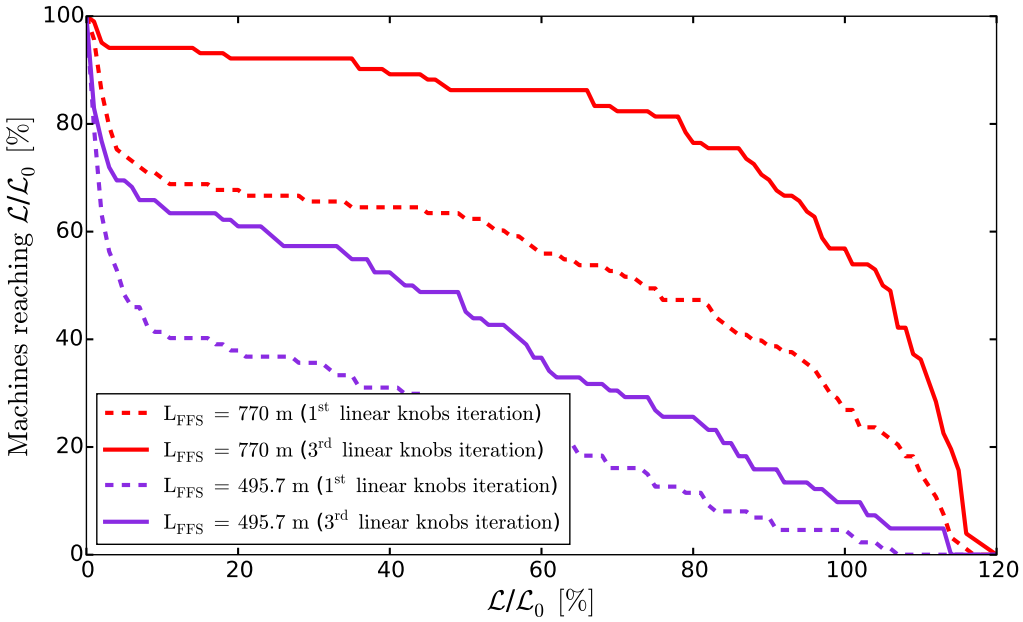

Figure 4.12: Tuning efficiency comparison after one iteration of BBA and three iterations of linear knobs for L_{FFS} = 495.7 m and L_{FFS} = 770 m with L* = 6 m.

FFS in order to improve the tuning efficiency while preserving the maximum luminosity achievable. Increasing the bending magnet angles is strongly limited by the synchrotron radiation emitted at 3 TeV and the available range of dispersion increase for which the luminosity stays within the design requirements is too small to significantly reduce k_2. Therefore, the dispersion has been increased with the length of the FFS. The bending magnets are lengthened and weakened accordingly in order to minimize the additional energy spread generated by the synchrotron radiation. The same optimization process described for the shorter FFS designs with L* = 6 m has been applied for the longer designs with L* = 3.5 m: matching of the linear optics for the lengthened FFS with scaled drift, bend and quadrupole lengths, $L_{\mathrm{QF1-QD0}}$ optimization for the second order chromaticity compensation and dispersion optimization.

4.2.1 Chromaticity correction preservation for longer designs

The design optimization of longer FFS with L* = 3.5 m consisted in lengthening the drifts, dipoles and quadrupoles of the CDR nominal FFS for CLIC 3 TeV [8] (with β_y^* = 0.068 mm). The FFS length has been increased up to 773 m, which is comparable to the baseline L_{FFS} of the L* = 6 m design. As discussed in Section 4.1, changes in the FFS length while keeping the L* constant require to re-balance the chromatic compensation in order to avoid remaining horizontal beam size contribution from 2nd order dispersion (see Fig. 4.13). When the length of the FFS is increased, the natural chromaticity generated upstream of the bending magnets becomes larger than the natural chromaticity generated by the FD. In order to fully cancel the chromatic aberrations

after the lengthening of the FFS, the distance $L_{\mathrm{QF1-QD0}}$ was increased accordingly. The $L_{\mathrm{QF1-QD0}}$ optimization has been performed for each longer system and their respective optimal $L_{\mathrm{QF1-QD0}}$ is shown in Fig. 4.14.

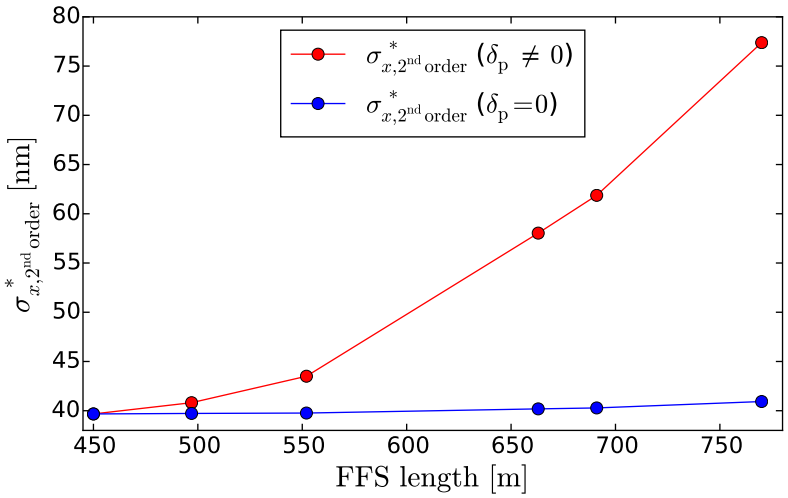

Figure 4.13: Horizontal beam size σ^*_x including only second order aberrations, simulated before $L_{\mathrm{QF1-QD0}}$ optimization, as function of the FFS length (L* = 3.5 m).

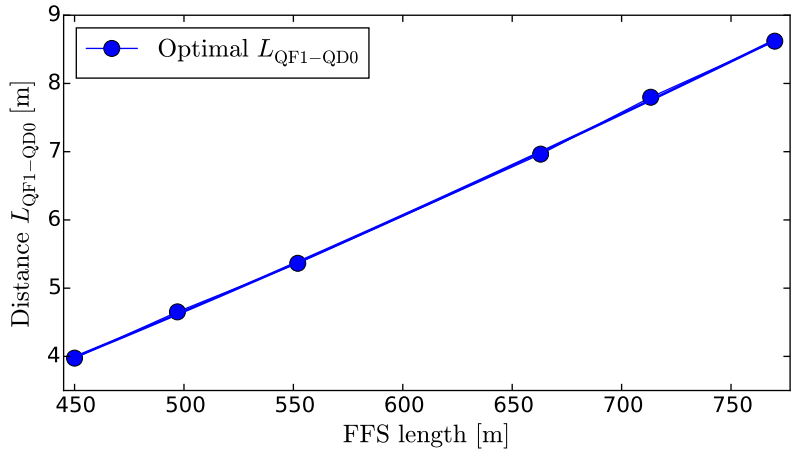

Figure 4.14: Optimal distance $L_{\mathrm{QF1-QD0}}$ for $\sigma^*_{x,2^{\mathrm{nd}}\mathrm{order}}$ minimization as function of the FFS length (L* = 3.5 m).

4.2.2 Luminosity performances

The luminosity has been optimized by scanning the angles of the FFS bending magnets while taking into account the impact of synchrotron radiation, as performed for shorter FFS with L* = 6 m described in Section 4.1. This procedure has been applied on 5

Table 4.2: Luminosity performance and synchrotron radiation impact comparison for different FFS length with L* = 3.5 m (no octupoles or decapoles added to the FFS beamline).

L_{FFS} [m]	$\frac{\sigma_x^*}{\sigma_x^{*\mathrm{noSR}}}$	$\frac{\sigma_y^*}{\sigma_y^{*\mathrm{noSR}}}$	$\mathcal{L}_{\mathrm{total}}$ [$10^{34}\mathrm{cm}^{-2}\mathrm{s}^{-1}$]	$\mathcal{L}_{1\%}$ [$10^{34}\mathrm{cm}^{-2}\mathrm{s}^{-1}$]	$\frac{\mathcal{L}_{1\%}}{\mathcal{L}_{1\%}^{\mathrm{noSR}}}$	k_{QD0} [m^{-2}]	l_{QD0} [m]	$\sigma_{y,\mathrm{Oide}}$ [nm]
773	1.22	1.21	7.02	2.34	0.894	-0.053	4.7	0.50
691	1.20	1.25	7.06	2.38	0.892	-0.062	4.2	0.54
663	1.188	1.43	7.2	2.38	0.86	-0.066	4.0	0.58
552	1.185	1.58	7.2	2.34	0.85	-0.086	3.35	0.71
497	1.183	1.59	7.1	2.33	0.84	-0.10	3.0	0.80
450	1.18	1.86	7.04	2.3	0.81	-0.11	2.73	0.92

longer systems, with lengths of 497 m, 552 m, 663 m, 691 m and 770 m, and their performances after full optimization are shown in Table 4.2. For all designs, the total and peak luminosity achieved are above the design requirements with at least by 15% of the luminosity budget. A similar dependence between synchrotron radiation influence and FFS length is observed for the nominal and the long L* designs. The impact of the synchrotron radiation on the horizontal beam size σ_x^* increases with the length of the system while the impact on the vertical beam size and luminosity is reduced. The quadrupole gradient k_{QD0} is reduced and its length l_{QD0} increased with L_{FFS}, resulting in a reduction of the vertical beam size contribution from the Oide effect. The energy bandwidth has been simulated and compared between each lattices (see Fig. 4.15). The results show similar bandwidth for all FFS designs.

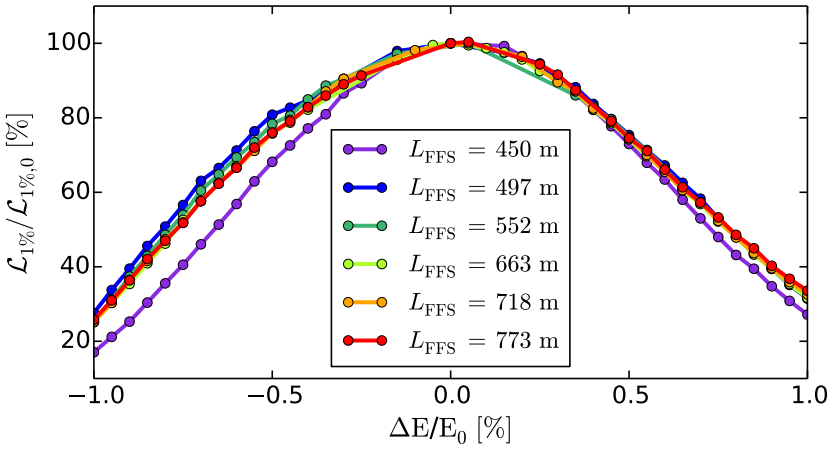

Figure 4.15: Energy bandwidth comparison between longer L_{FFS} with L* = 3.5 m. $\mathcal{L}_{1\%}$ is normalized to their respective maximum peak luminosity $\mathcal{L}_{1\%,0}$ (see Table 4.2).

4.2.3 Impact on tuning efficiency

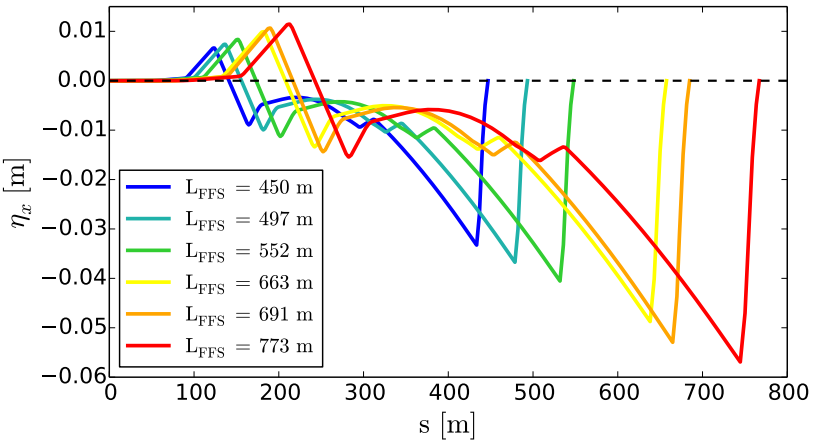

Figure 4.16: Dispersion profile for different FFS length with L* = 3.5 m.

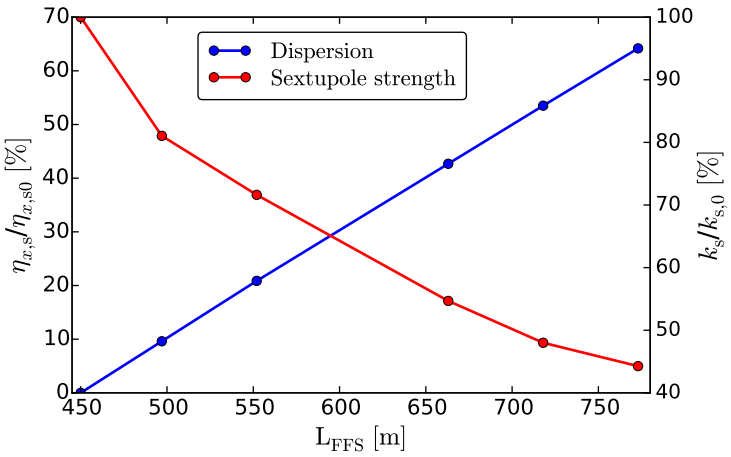

Figure 4.17: Average sextupole strength and dispersion at the sextupole locations as function of the FFS length (L* = 3.5 m).

The lengthening of the FFS lattice modifies the dispersion profile along the system as shown in Fig. 4.16. Figure 4.17 shows the average dispersion level at the sextupole locations and the average strength of the sextupoles, as function of the FFS length. The larger dispersion level at the sextupole location allows to reduce the average strength of the FFS sextupoles by more than a factor 2 for $L_{\rm FFS}$ = 773 m. The sextupole strength reduction of these new longer lattices should make the FFS more tolerant to sextupole transverse misalignments and thus give better tuning efficiency than the nominal CDR design. First, the impact of $L_{\rm FFS}$ on the tuning efficiency under $\sigma_{\rm RMS} = 10$ μm transverse misalignment of the optics, has been checked on various longer designs after one iteration

of BBA followed by one iteration of linear sextupole knobs. The average luminosity achieved over the 100 different machines simulated as function of L_{FFS} is shown in Fig. 4.18. As expected, a clear improvement of the tuning efficiency for longer FFS is observed, which is consistent with the tuning simulations performed on different L_{FFS} with L* = 6 m (see Section 4.1). In Fig. 4.19, the tuning efficiency is compared for the L_{FFS} = 450 m and L_{FFS} = 770 m design options after one iteration of BBA and three iterations of linear knobs applied to 100 machines. For the nominal design with L_{FFS} = 450 m, 35% of the machines reach ≥90% of $\mathcal{L}_0$ while for L_{FFS} = 770 m, 78% of the machines reach ≥90% of $\mathcal{L}_0$.

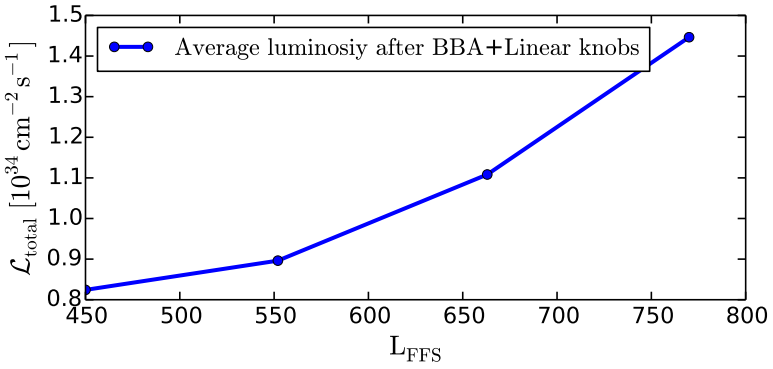

Figure 4.18: Average luminosity over the 100 machines tuned for the different longer FFS lattices with L* = 3.5 m after BBA (top plot) and linear knobs (bottom plot).

4.2.4 Executive summary

In this Section, the luminosity and tuning performances of the FFS for different lengths have been compared. This study has been repeated for the two L* options proposed for CLIC 3 TeV. The long L* design presented in Chapter 3 is 320 meters longer than the nominal FFS lattice with L* = 3.5 m requiring an extension of the CLIC tunnel. Shorter FFS designs have been optimized with L* = 6 m in the interest of cost reduction, while longer systems were optimized with L* = 3.5 m with the aim of improving the tuning efficiency while preserving the maximum luminosity achievable.
The uncompensated chromaticity generated by the shortened or lengthened FFS with constant L*, results in a large horizontal beam size contribution from the second order dispersion aberration referred to as T_{166}. The correction applied consisted in recovering the chromaticity compensation properties of the Local scheme in the FFS, by reducing (in the case of the shorter FFS with L* = 6 m) or increasing (for the longer FFS with L* = 3.5 m) the chromaticity generated by the FD. The dispersion function along the FFS has been re-optimized for all lattices of the two L* options. The optics optimization procedure applied has allowed to propose various length for the FFS that achieve the CLIC design luminosity. The performances for both L* options are given in Table 4.1 and 4.2.

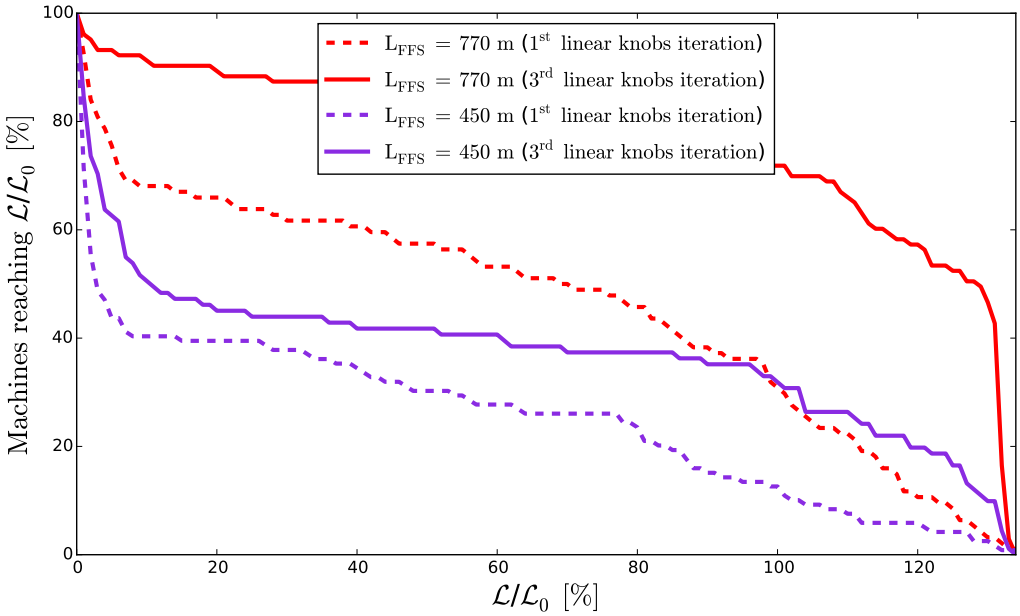

Figure 4.19: Tuning efficiency comparison after one iteration of BBA and three iterations of linear knobs for $L_{\mathrm{FFS}} = 450$ m and $L_{\mathrm{FFS}} = 773$ m with $\mathrm{L}^* = 3.5$ m.

Reducing the length of the FFS results in lower dispersion at the sextupole locations. In order to provide the required chromaticity correction, the strength of the sextupoles is increased accordingly. When misaligned, the stronger sextupoles generate larger linear aberrations via feed-down to normal and skew quadrupole fields. Tuning efficiency dependence on L_{FFS} has been observed for the lattices with $\mathrm{L}^* = 3.5$ m and $\mathrm{L}^* = 6$ m. Simulations shows that, under transverse misalignments, longer systems allow to improve the tuning efficiency. In the case of $\mathrm{L}^* = 6$ m, the longer lattice with $L_{\mathrm{FFS}} = 770$ m offers the best overall performances in terms of maximum luminosity achievable and tuning. The tunability of this lattice under realistic static imperfections (adding strength and roll errors) has been addressed in Chapter 3. Moreover, the required collimation depth is unchanged compared to the nominal (CDR) FFS design with $\mathrm{L}^* = 3.5$ m (see Chapter 3), while it may be a concern for the shorter designs with $\mathrm{L}^* = 6$ m, due to the stronger FD (see Table 4.1). Longer lattices with $\mathrm{L}^* = 3.5$ m ease the tuning, under transverse misalignments, while keeping the maximum luminosity achievable to similar values (see Table 4.2). It is worth pointing out that the larger dispersion level along the FFS, required to weaken the sextupole strengths, may amplify second order chromatic aberrations generated by the sextupole roll and strength errors, such as T_{166} and T_{366}, that increase quadratically with dispersion (see Eqs.(2.97 and 2.103)). Further comparative tuning simulations, including additional roll and strength errors to the lattice imperfections, would allow to precisely quantify the tuning efficiency improvement for the longer FFS designs with $\mathrm{L}^* = 3.5$ m.

Chapter 5

CLIC BDS optimization at $\sqrt{s} = 380$ GeV: $L^* = 4.3$ m vs $L^* = 6$ m

The CLIC rebaselining foresees a staged machine with an initial centre-of-mass energy of 380 GeV [27], for which the design optimization and tuning of the FFS is presented in this Chapter. The nominal BDS layout was based on the $\sqrt{s} = 500$ GeV design, with $L^* = 4.3$ m, planned in the old energy staging strategy [84]. Unlike the CLIC BDS at $\sqrt{s} = 3$ TeV, the nominal design has not been re-optimized in the past for this updated initial center of mass energy. Throughout this Chapter, the performances of two L^* options for CLIC 380 GeV are compared: the nominal BDS design with $L^* = 4.3$ m, with the last quadrupole QD0 partially inside the detector and the $L^* = 6$ m design, with QD0 in entirely supported by the tunnel ground.

5.1 BDS optics design optimization

For the nominal CLIC 380 GeV BDS with $L^* = 4.3$ m, the quadrupoles and sextupoles have been re-matched, from the previously optimized BDS lattice for the CLIC 500 GeV [85], with respect to the design beam parameters optimized for the new initial energy stage [27]. The total length of the nominal BDS is 1728 m with a length $L_{\mathrm{FFS}} = 550$ m. The design parameters are summarized in Table 5.1. The design normalized horizontal and vertical emittances at the exit of the linacs are $\varepsilon_x = 920$ nm and $\varepsilon_y = 20$ nm, respectively. The normalized emittances, for the BDS lattice optimization and luminosity computation presented throughout this Chapter, are $\varepsilon_x = 950$ nm and $\varepsilon_y = 30$ nm. This increase of horizontal and vertical emittances results in a reduction of luminosity of more than 20% compared to the design parameters at the end of the linacs, which corresponds to the luminosity budget assumed for the statics and dynamics imperfections of the lattice. After optics matching and nonlinear corrrection of the nominal lattice, the beam sizes were calculated using the MAPCLASS code. While the vertical beam size at the IP σ_y^* achieves closely the design beam size, the horizontal beam size σ_x^* cannot reach a value below 150 nm, so approximately 7 nm above the design. When computing the beam sizes order by order, it is observed that the large contributions to σ_x^* are from 2^{nd} order aberrations. When an achromatic beam is assumed ($\delta_p = 0$), these contributions are removed, showing that 2^{nd} order chromatic aberrations are almost entirely responsible for the larger σ_x^*. As performed on the CLIC 3 TeV FFS in

Table 5.1: CLIC 380 GeV design parameters

L* [m]	4.3	6
FFS length [m]	550	770
Norm. emittance (end of linacs) $\gamma\varepsilon_x/\gamma\varepsilon_y$ [nm]	920 / 20	920 / 20
Norm. emittance (IP) $\gamma\varepsilon_x/\gamma\varepsilon_y$ [nm]	950 / 30	950 / 30
Beta function (IP) β_x^*/β_y^* [mm]	8 / 0.1	8 / 0.1
IP beam size σ_x^*/σ_y^* [nm]	144 / 2.9	144 / 2.9
Bunch length σ_z [μm]	70	70
rms energy spread δ_p [%]	0.3	0.3
Bunch population N_e [10^9]	5.2	5.2
Number of bunches n_b	352	352
Repetition rate f_rep [Hz]	50	50
Luminosity $\mathcal{L}_\mathrm{total}$ [$10^{34}\mathrm{cm}^{-2}\mathrm{s}^{-1}$]	1.5	1.5
Peak luminosity $\mathcal{L}_{1\%}$ [$10^{34}\mathrm{cm}^{-2}\mathrm{s}^{-1}$]	0.9	0.9

Chapter 4, these additional 2nd order chromatic contributions are minimized by optimizing the length $L_{\mathrm{QF1-QD0}}$ between QF1 and QD0. The beam sizes, calculated order by order, before and after corrections, are shown in Fig. 5.1. After $L_{\mathrm{QF1-QD0}}$ optimization, both σ_x^* and σ_y^* closely reach the design beam sizes as shown in Fig. 5.2.

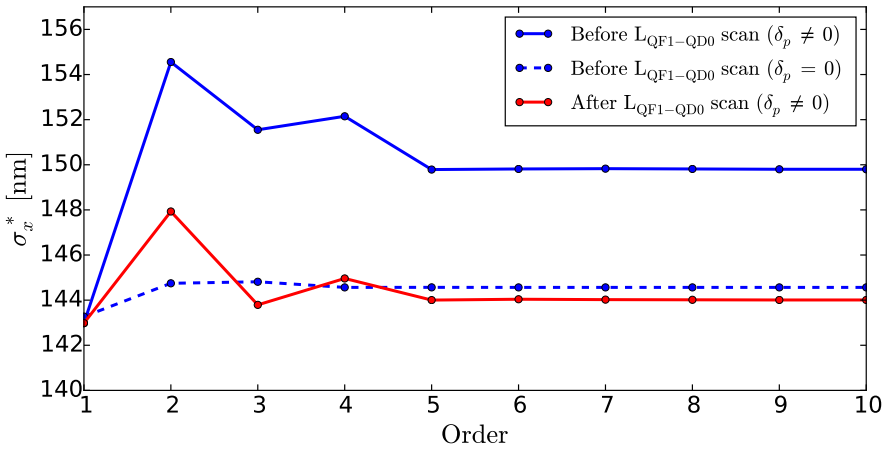

Figure 5.1: Horizontal beam sizes at the IP calculated up to the maximum order considered, before and after $L_{\mathrm{QF1-QD0}}$ optimization, for L* = 4.3 m.

The drifts and quadrupoles of the L* = 6 m FFS have been scaled in length according to the increase of L* from the optimized lattice with L* = 4.3 m. Hence, the length of the L* = 6 m design has been increased by 40%. The optical functions comparison between both L* options after optimization are shown in Fig. 5.3. After nonlinear optimization of the FFS sextupoles, the beam sizes were calculated order by order using the MAPCLASS code. While the horizontal beam size achieves the design value of 143 nm,

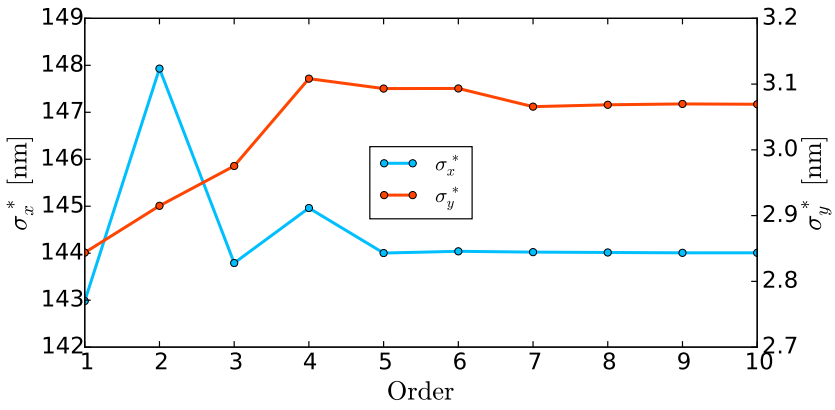

Figure 5.2: Horizontal and vertical beam sizes at the IP calculated up to the maximum order considered, after $L_{\mathrm{QF1-QD0}}$ optimization, for L* = 4.3 m.

the vertical beam size experiences large 3$^{\mathrm{rd}}$ contributions leading to $\sigma_y^* = 5.8$ nm, so a factor 2 larger than the design value. Figure 5.4 shows that 3$^{\mathrm{rd}}$ aberrations contribute to 2.3 nm of the σ_y^* beam size growth. The vertical beam size contributions calculated for an achromatic beam ($\delta_p = 0$) shows that the beam size growth is mainly coming from geometrical 3$^{\mathrm{rd}}$ aberrations. In order to remove these contributions to the vertical beam size, a pair of octupoles has been inserted in the FFS line. The geometrical 3$^{\mathrm{rd}}$ aberrations are compensated by the octupole located in high-β_y and low dispersion region (*OCTUPOLE 2*) as shown in Fig. 5.5. The residual 3$^{\mathrm{rd}}$ chromatic contributions are removed by the *OCTUPOLE 1*, located at the entrance of the FD in high dispersion region. As the 3$^{\mathrm{rd}}$ chromatic contributions are small, the impact of *OCTUPOLE 1* is weak. The comparison of the impact of *OCTUPOLE 1* and *OCTUPOLE 2* on σ_y^* is shown in Fig. 5.6. After octupoles optimization, σ_y^* was reduced down to 3.6 nm for this lattice. In Fig. 5.7 each 3$^{\mathrm{rd}}$ aberration contributions to the vertical beam size were computed using the nonlinear map coefficient provided by MAPCLASS. It shows that before the integration of the octupoles, the major contribution to σ_y^* is the geometrical aberration U_{3224}, which was reduced from 2 nm to 0.2 nm after octupole optimization.

For both L* options, the dispersion level of the FFS has been optimized with the goal of maximizing the luminosity. In the case of the CLIC 380 GeV, the small impact of synchrotron radiation on the luminosity allows large increase of the dispersion along the FFS compare to the CLIC at 3 TeV (see Chapter 3). Different lattices have been re-optimized with a peak of dispersion increased up to factor 2 with steps of 20% increase for L* = 4.3 m and L* = 6 m as shown in Fig. 5.8. For L* = 6 m, the octupoles have been re-optimized for each lattice. The impact of dispersion increase on the horizontal and vertical beam sizes, taking into account synchrotron radiation, are shown in Fig. 5.9. The increase of horizontal dispersion η_x results in a similar increase of the horizontal beam size σ_x^* due to synchrotron radiation. However, the vertical beam size tends to decrease with dispersion, due to better chromaticity correction, especially for

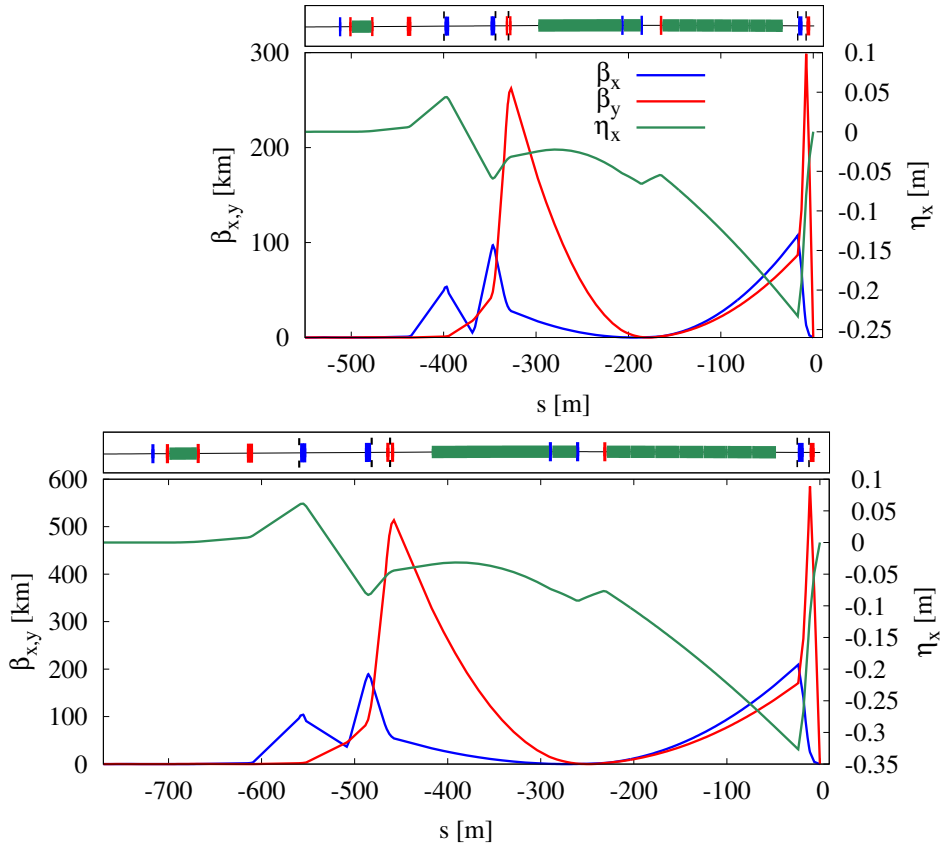

Figure 5.3: Optical functions through the Local correction scheme of the FFS for L* = 4.3 m (top plot) and L* = 6 m (bottom plot), where η_x is the dispersion function. The lattice for L* = 6 m has been lengthened with respect to the increase of L* from the nominal design.

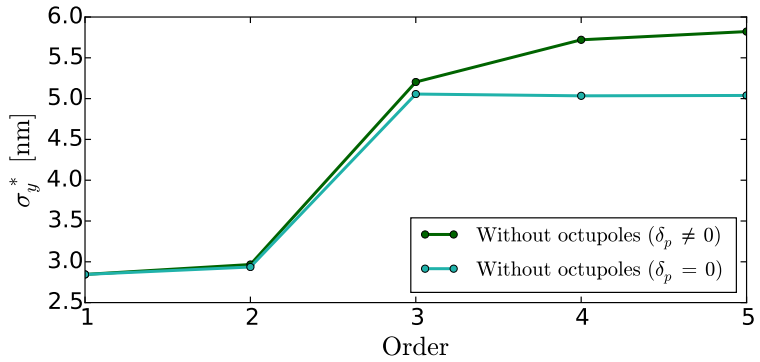

Figure 5.4: Vertical beam sizes at the IP calculated up to the 5$^{\text{th}}$ order, for a chromatic and achromatic beam simulated, showing the large impact of the 3$^{\text{rd}}$ order geometrical contributions for the L* = 6 m case.

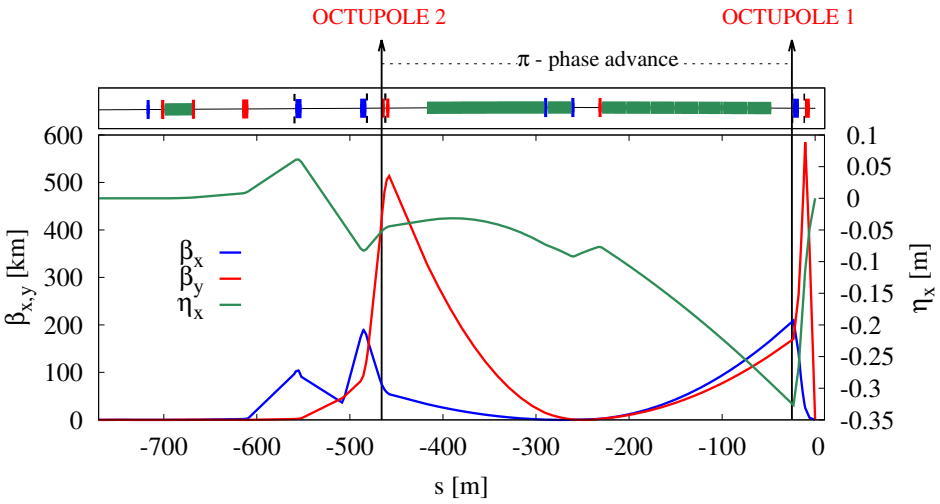

Figure 5.5: Location of the two octupoles inserted in the FFS with L* = 6 m.

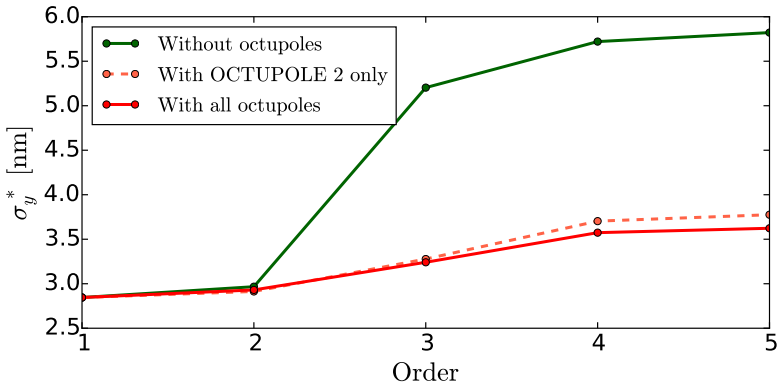

Figure 5.6: Comparison of the vertical beam sizes at the IP, with and without octupoles in the FFS with L* = 6 m.

the L* = 6 m. In order to find the optimal dispersion level in the FFS that balances between σ_y^* reduction resulting from better chromaticity correction and σ_x^* growth due to synchrotron radiation, one has to look at the lattice that provides the maximum total ($\mathcal{L}_{\text{total}}$) and peak ($\mathcal{L}_{1\%}$) luminosities. Figure 5.10 shows the corresponding luminosities simulated with PLACET and GUINEA-PIG codes, normalized to the design total and peak luminositites $\mathcal{L}_0$ (see Table 5.1). For the nominal design with L* = 4.3 m, increasing the dispersion η_x tends to decrease the luminosity and thus no changes has been applied to the bending magnet angles. However, for the L* = 6 m lattice, the peak luminosity passes by a maximum for a peak dispersion increased by 60% and is thus chosen as the new baseline for the long L* lattice. Figure 5.10 shows also the relative decrease of the average FFS sextupole strength as function of the dispersion level. For the updated lattice with L* = 6 m and dispersion increased by 60%, the average FFS sextupole strength has been reduced by approximately 40%. The impact of the octupoles for this updated

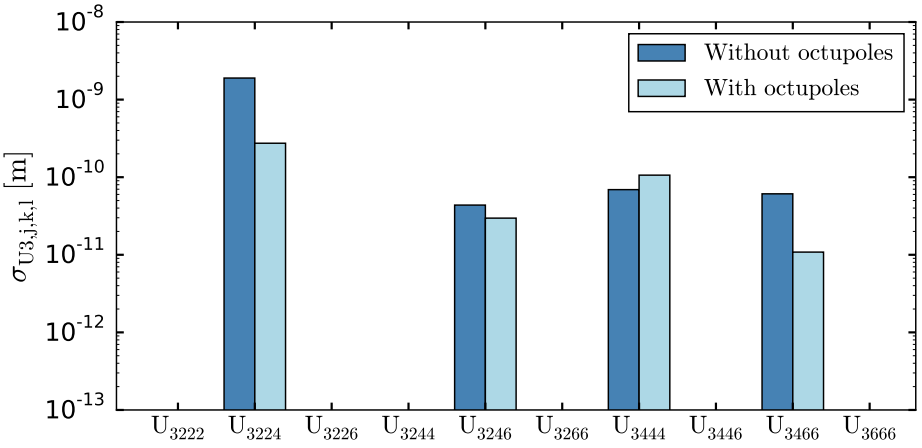

Figure 5.7: 3rd order contributions to the vertical beam size at the IP, before and after inserting the pair of octupoles.

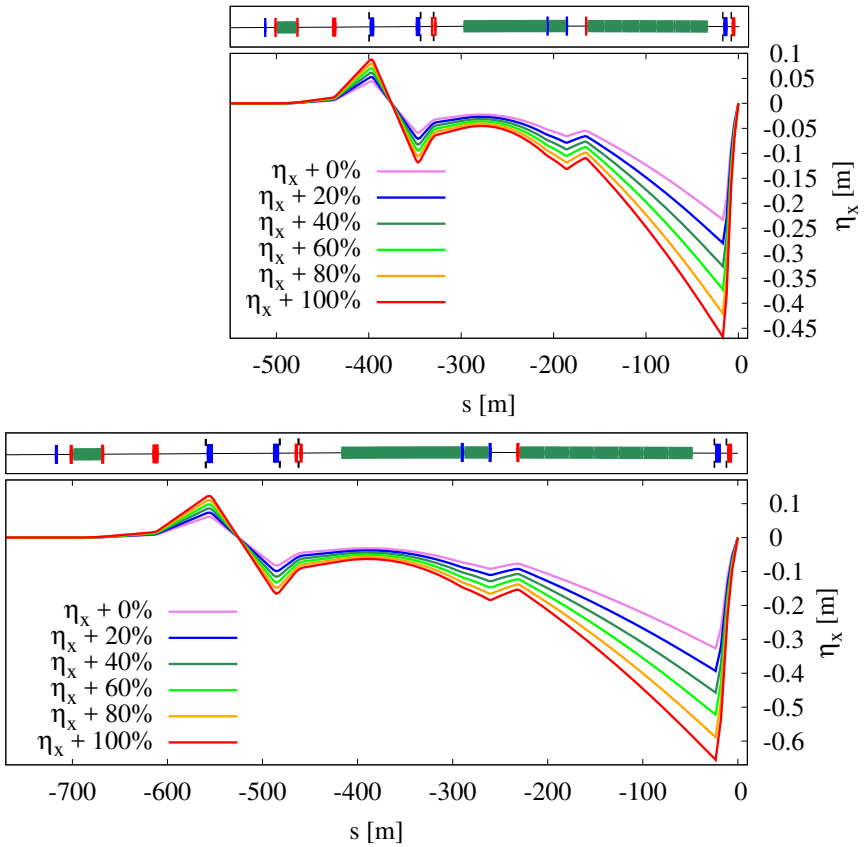

Figure 5.8: Dispersion profile along the FFS changed by changing the bending magnet angles up to a factor 2 for L* = 4.3 m (upper plot) and L* = 6 m (bottom plot).

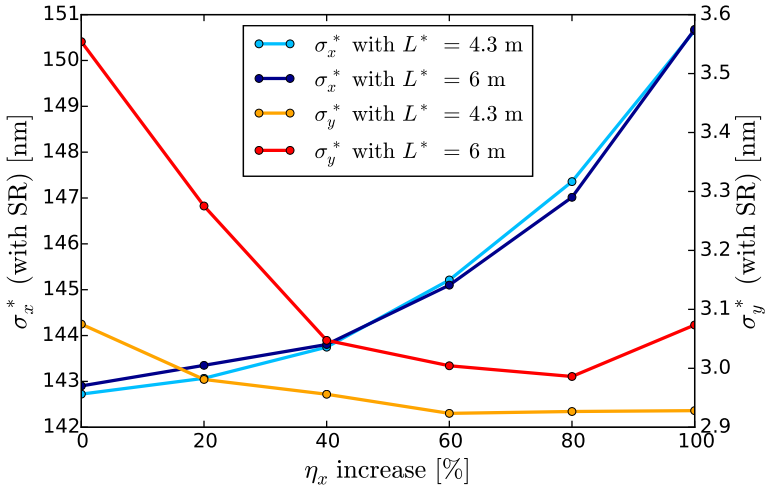

Figure 5.9: Horizontal and vertical beam sizes at the IP, taking into account synchrotron radiation, as function of the increase of dispersion η_x along the FFS for L* = 4.3 m and L* = 6 m.

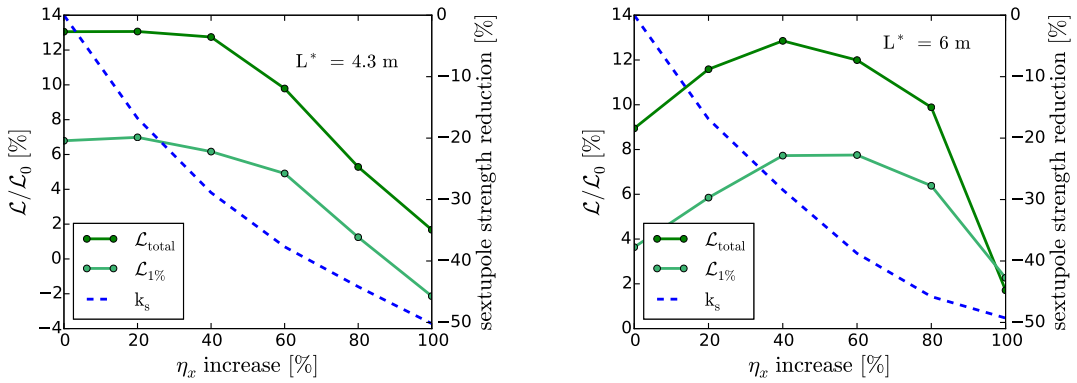

Figure 5.10: Luminosity and average sextupole strength in the FFS, as function of the increase of dispersion η_x. The total ($\mathcal{L}_{\text{total}}$) and peak ($\mathcal{L}_{1\%}$) luminosities are normalized to their respective design luminosity $\mathcal{L}_0$ given in Table 5.1.

lattice with L* = 6 m is shown in Fig. 5.11. As observed in the previous design with no increase of dispersion, the vertical beam size growth is mainly caused by geometrical 3rd order aberrations that are almost entirely removed by the *OCTUPOLE 2*, located in low-η_x region. Figure 5.12 confirms the large contribution from U_{3224} aberration before octupoles optimization.

Both L* options have been fully optimized and their respective performances are encapsulated in Table 5.2. The chromaticity generated by the FFS was computed using the second order map coefficients provided by PTC and Eq. (2.56). While the chromatic-

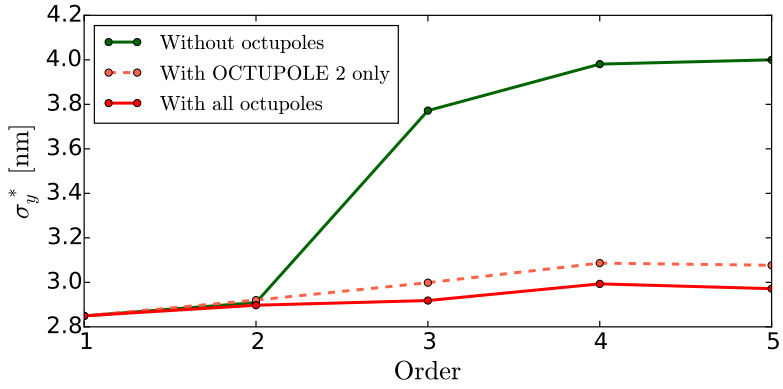

Figure 5.11: Comparison of the vertical beam sizes at the IP, with and without octupoles in the FFS with L* = 6 m after dispersion optimization.

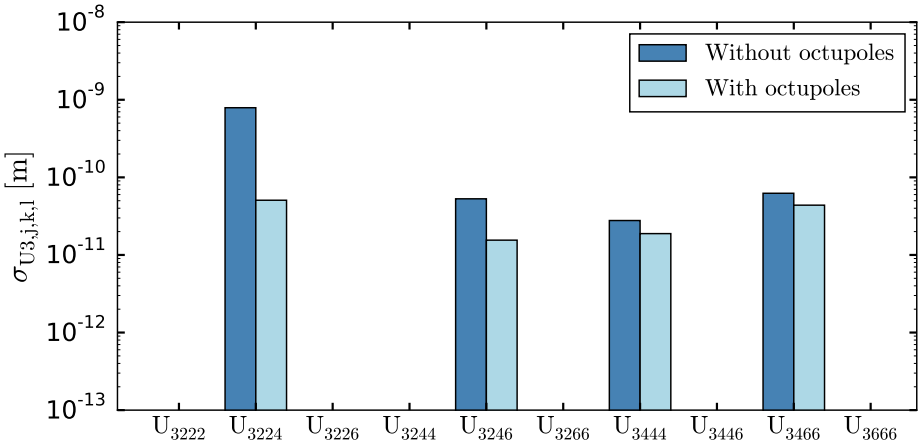

Figure 5.12: 3rd order contributions to the vertical beam size at the IP, before and after inserting the pair of octupoles, for the FFS with L* = 6 m after dispersion optimization.

ity for the L* = 6 m FFS is, as expected, larger than the nominal design, their final performances after optimization are very similar. This is mainly due to the octupolar corrections that were perfomed only on the long L* FFS to bring σ_y^* very close to the design. The larger dispersion applied to the L* = 6 m FFS increases the impact of synchrotron radiation on the peak luminosity compared to the L* = 4.3 m design. Both lattices exceed the design peak luminosity by approximately 8%. It is worth recalling that the 20% luminosity budget for static and dynamic imperfections is already included in the larger assumed vertical emittance ($\gamma\varepsilon_y$ = 30 nm). The energy bandwidths are comparable for both L* designs, as shown in Fig. 5.13.

The total and peak luminosities reported in Table 5.2 were calculated assuming a beam with a full width 1% energy spread at the exit of the main linac as shown in left plot of Fig. 5.14. In Table 5.3 the luminosities were simulated assuming a more realistic energy

Table 5.2: Simulated performance of both L* options when the beam is tracked through the entire BDS. Comparison of chromaticity, horizontal and vertical beam sizes, total and peak luminosities and impact of synchrotron radiation at the IP.

Design	ξ_y^*	σ_x^* [nm]	σ_y^* [nm]	$\mathcal{L}_{\text{total}}$ [$10^{34}\text{cm}^{-2}\text{s}^{-1}$]	$\mathcal{L}_{1\%}$ [$10^{34}\text{cm}^{-2}\text{s}^{-1}$]	$\frac{\mathcal{L}_{1\%}}{\mathcal{L}_{1\%}^{\text{noSR}}}$	$\sigma_{y,\text{Oide}}$ [nm]
L* = 4.3 m	63365	143	3.07	1.7	0.96	0.03	0.135
L* = 6 m	95388	145.1	3.00	1.64	0.94	1	0.133

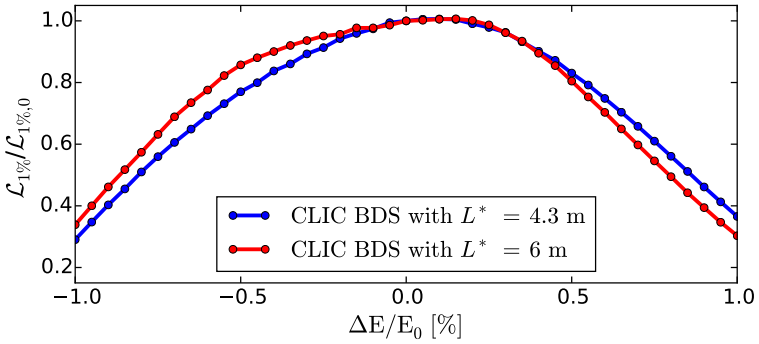

Figure 5.13: Comparison of the CLIC 380 GeV BDS energy bandwidth for both L* options.

spread shape coming from the main linac and taking into account uncorrelated energy spread of 0.1% of the post linac beam energy and 1.6% of the pre-linac beam energy with a gaussian distribution. The energy distribution along the bunch is shown in the right plot of Fig. 5.14. The energy spread shape coming from the main linac causes a luminosity loss of approximately 9% in total and peak luminosities for both L* designs. The FFS designs with L* = 4.3 m and L* = 6 m achieve both above the design total and peak luminosities.

Table 5.3: Simulated performance of both L* options when the beam is tracked through the entire BDS assuming a realistic energy spread shape coming from the Main Linac.

Design	σ_x^* [nm]	σ_y^* [nm]	$\mathcal{L}_{\text{total}}$ [$10^{34}\text{cm}^{-2}\text{s}^{-1}$]	$\mathcal{L}_{1\%}$ [$10^{34}\text{cm}^{-2}\text{s}^{-1}$]
L* = 4.3 m	148.2	3.22	1.55	0.93
L* = 6 m	151.2	3.20	1.52	0.91

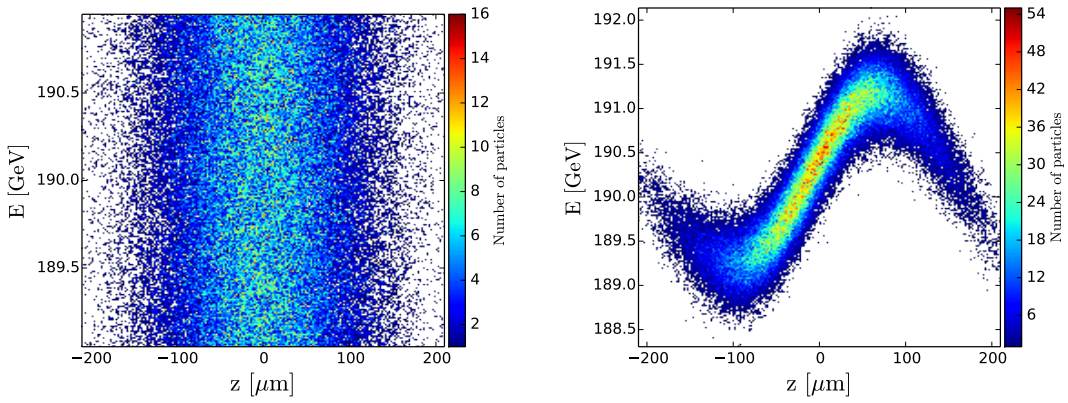

Figure 5.14: Energy distribution along the bunch at the entrance of the BDS assuming a 1% full width energy spread (left plot) and assuming a realistic energy spread coming from the Main Linac (right plot).

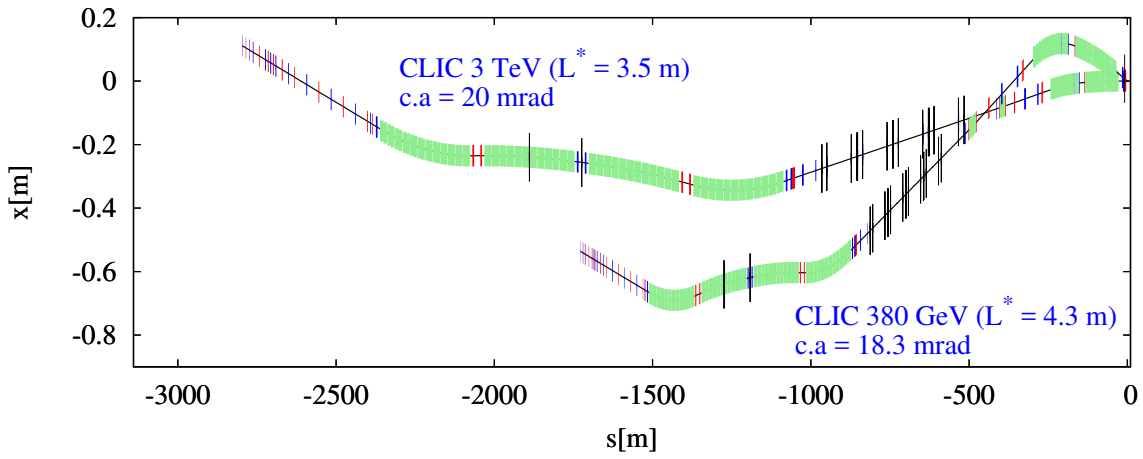

Figure 5.15: CLIC 3 TeV BDS, with L* = 3.5 m, and 380 GeV BDS, with L* = 4.3 m, footprints after linacs alignment.

5.2 Design optimization for the CLIC energy upgrade

The intitial and final energy stages of the CLIC BDS will be hosted inside the 4.5 m diameter CLIC tunnel [8]. In order to allow the energy upgrade inside the CLIC tunnel, the 380 GeV and 3 TeV Main Linacs must be aligned. The linacs alignment requires changes in the IP crossing angles and slight increase of the first bending magnets of the collimation section for the CLIC BDS at 380 GeV. The two L* options were studied for the energy upgrade and the performances reported in this Chapter were computed after applying these changes. The CLIC 380 GeV BDS with L* = 4.3 m must be aligned with the CLIC 3 TeV BDS with L* = 3.5 m and similarly for the first and final energy stages with L* = 6 m. The crossing angle for the CLIC 3 TeV is 20 mrad. The footprint of the

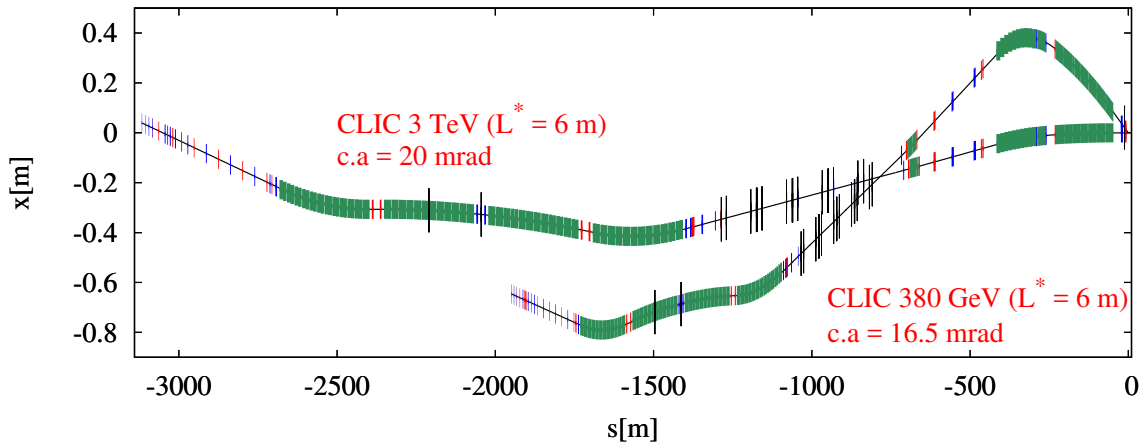

Figure 5.16: CLIC 3 TeV BDS and 380 GeV BDS, with L* = 6 m, footprints after linacs alignment.

Table 5.4: Errors applied to the lattice

σ_{offset} (Quadrupoles, Sextupoles and BPMs)	10μm
BPM resolution	10 nm
σ_{roll} (Quadrupoles, Sextupoles and BPMs)	300μrad
Strength error (Quadrupoles and Sextupoles)	0.01%

BDS is shown in Fig. 5.16 for the short L* option and in Fig. 5.17 for L* = 6 m. For the L* = 4.3 m design, the crossing angle has been reduced down to 18.3 mrad and the angle of the first bending magnets of the collimation section has been increased by 8%. For the L* = 6 m design, due to the large FFS dipole angles increase (+ 60%) applied for the dispersion optimization (see Section 5.1), the crossing angle at the IP has been reduced down to 16.5 mrad for the linacs alignment. The angle of the first bending magnets of the collimation section has been increased by 12%.

5.3 Tuning of the Final Focus System

One crucial step towards proving the feasibility of the FFS is the demonstration of its tunability under realistic imperfection conditions. As performed in Chapter 3, the tunability of the FFS is studied under static errors and does not take into account dynamic imperfections. The errors applied to the different machines for tuning simulations are shown in Table 5.4. The tuning goal, for both L* designs, is to show that 90% of the tuned machines can reach at least the design total luminosity reffered to as $\mathcal{L}_0$. The tuning procedure is the same as for the CLIC 3 TeV FFS. It consists of one iteration of BBA (1-1 correction + DFS), followed by iterations of sextupoles knobs for aberration corrections at the IP. In order to remove the remaining 2^{nd} order aberrations generated by strength and roll errors of the FFS sextupoles, 2^{nd} order knobs have been constructed using pre-computed strength variation of the normal sextupoles. The quasi

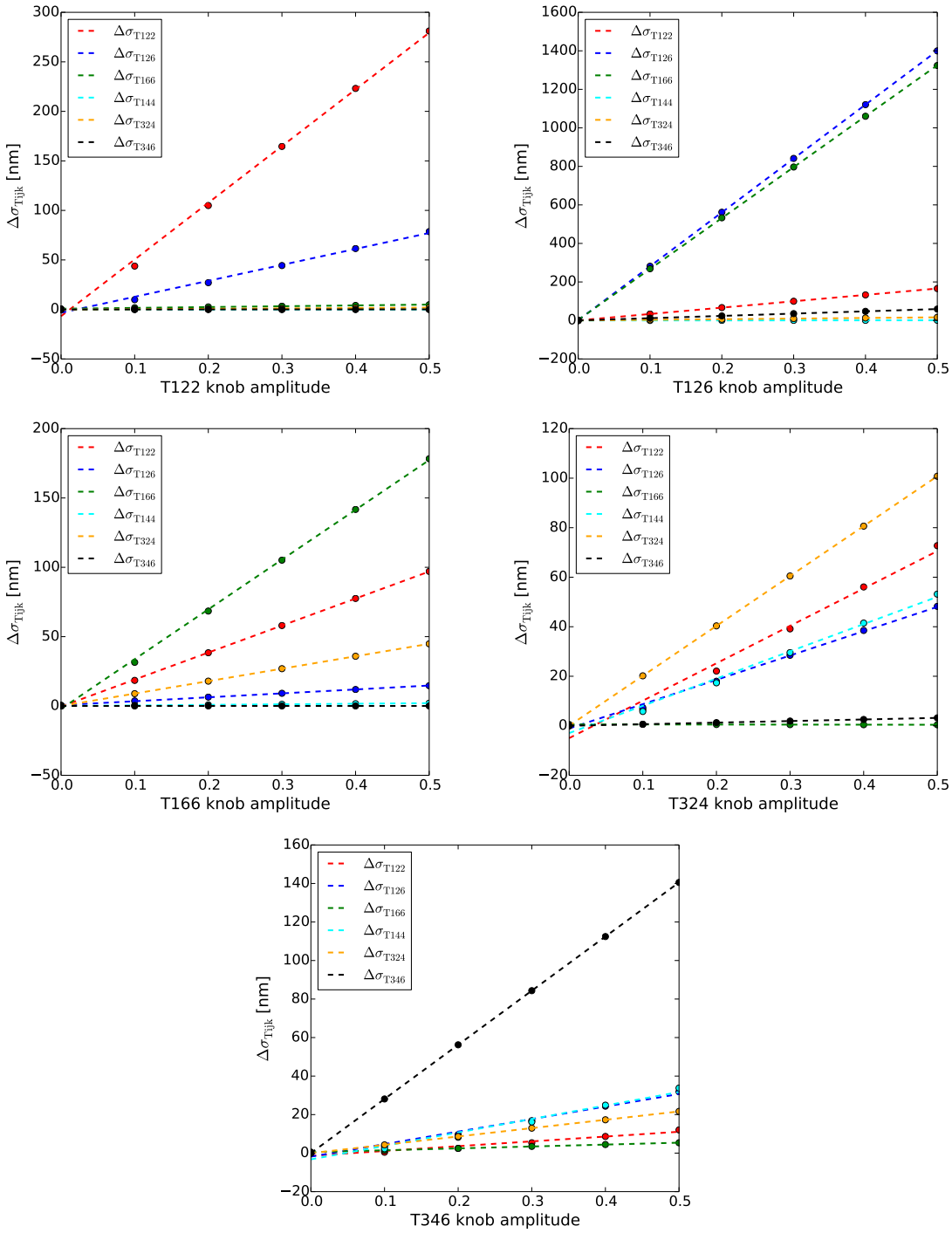

Figure 5.17: Simulation results showing the orthogonality of the second order knobs, T_{122}, T_{126}, T_{166}, T_{324} and T_{346} constructed using strength variation of the normal sextupoles of the FFS with $L^* = 4.3$ m

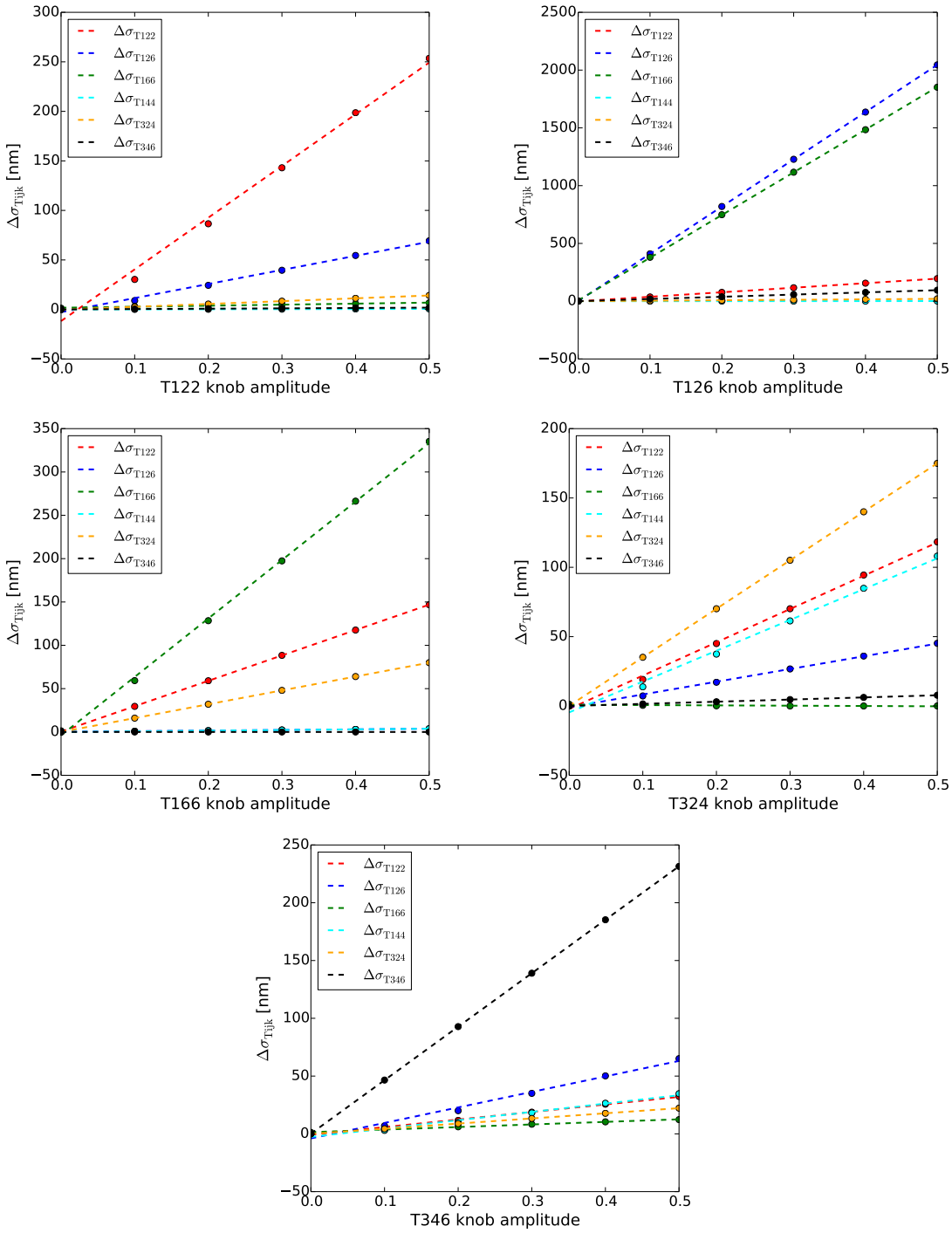

Figure 5.18: Simulation result showing the orthogonality of the second order knobs, T_{122}, T_{126}, T_{166}, T_{324} and T_{346} constructed using strength variation of the normal sextupoles of the FFS with L* = 6 m

orthogonality of these nonlinear knobs are shown in Fig. 5.17 for the L* = 4.3 m design and in Fig. 5.18 for L* = 6 m. Linear and nonlinear sextupole knobs are applied iteratively. Here, one iteration consists in scanning the linear and 2nd order knobs twice. The beam tracking simulations and luminosity calculations are performed using PLACET and GUINEA-PIG, assuming a 1% full width energy spread at the entrance of the FFS. The luminosity is computed assuming that both systems are identical, and therefore the same beam distribution at the IP is assigned for both e^+ and e^- beamlines.
The achieved luminosity distribution of the tuned machines are shown in Figs. 5.19 and 5.20 for L* = 4.3 m and L* = 6 m, respectively. The results show that after 12 iterations, corresponding here to approximately 6300 luminosity measurements, both L* designs fall closely to the tuning goal and show very similar tuning performances. For the L* = 4.3 m lattice, there is 84% of the machines that reach $\mathcal{L}_0$ and 85% of the machines reaching $\mathcal{L}_0$ for L* = 6 m. The luminosity obtained for 90% of the machines is ≥92% and ≥96% for L* = 4.3 m and L* = 6 m, respectively. The small luminosity gap needed to reach the tuning goal can be achieved with additional knob scans.

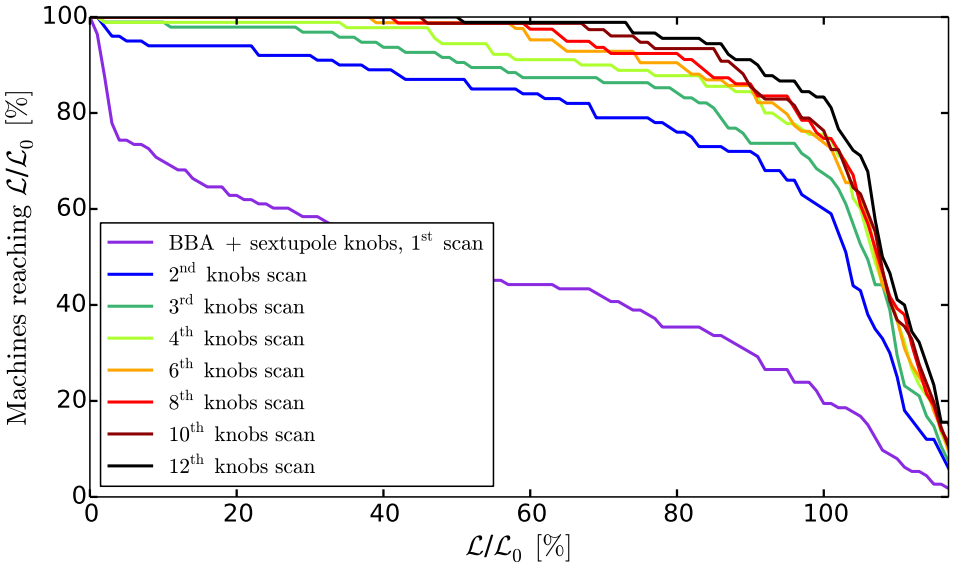

Figure 5.19: Tuning performances of the CLIC 380 GeV with L* = 4.3 m under realistic static error conditions. There is 85% of the machines reaching ≥ $\mathcal{L}_0$ after ≈ 6300 luminosity measurements.

5.4 Dispersion impact on tuning under transverse misalignment

Mitigating the impact of transverse misalignment of the FFS optics is imperative to preserve and recover the design luminosity. The quadrupole offsets, generating undesired dispersive orbit, are minimized using the DFS technique. The FFS sextupole misalign-

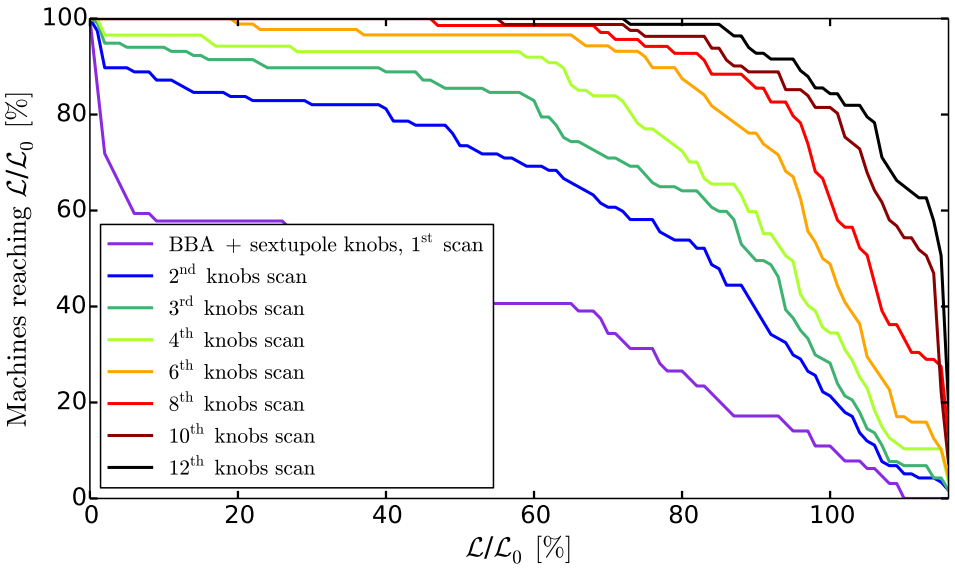

Figure 5.20: Tuning performances of the CLIC 380 GeV with L* = 6 m under realistic static error conditions. There is 87% of the machines reaching $\geq \mathcal{L}_0$ after $\approx$ 6300 luminosity measurements.

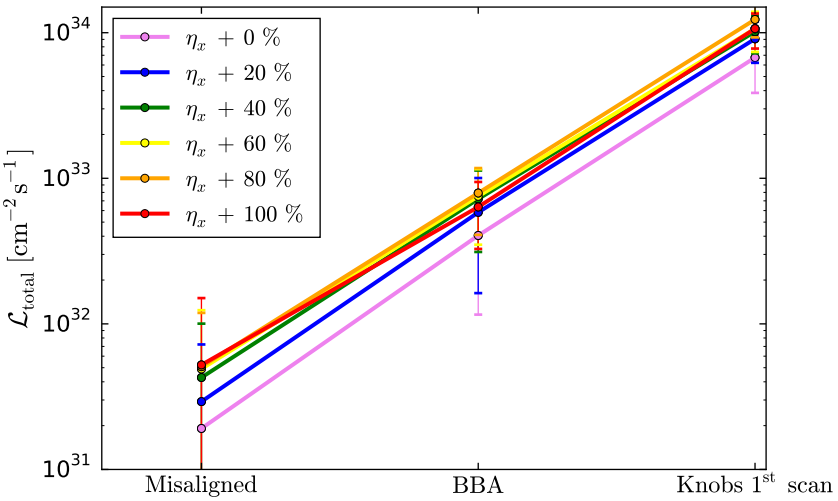

Figure 5.21: Average luminosity over 100 randomly misaliged machines after applying errors (see Table 5.5), BBA and sextupole knobs on the L* = 4.3 m lattice for different dispersion profile.

ments generates linear aberrations that cause large beam size dilution at the IP. It has been shown in Chapter 3 and 4 that either reducing β-fucntions or increasing dispersion at the sextupole locations makes the FFS less sensitive to sextupole offsets. This study aims to check the impact of weaker FFS sextupoles on tuning performances, only

Table 5.5: Errors applied to the lattice

σ_{offset} (Quadrupole, Sextupole and BPMs)	10 μm
BPM resolution	10 nm

under static transverse misalignments, and to propose possible alternative designs that could speed up the tuning of the FFS. Several FFS optics have been fully optimized previously for a peak dispersion increase up to a factor 2, for both L^* options. Here the tuning performance of 6 FFS designs with different dispersion level are compared for L^* = 4.3 m. For each lattice, one iteration of BBA (1-1 correction + DFS) and one iteration of linear knobs using sextupoles (each knob is scanned twice) have been applied to 100 machines randomly misaligned by σ_{offset} = 10 μm. The imperfection conditions for the tuning simulations are summarized in Table 5.5. Figure 5.21 shows the evolution of the average luminosity, over the 100 machines simulated, during each step of the tuning procedure. Except for the lattice with dispersion increased by +100%, where the maximum luminosity achievable is notably reduced (see Fig. 5.10), the average luminosity is larger for larger dispersion level after misalignment at every tuning step. Figure 5.22 shows that the luminosity for lattices with larger dispersion is less impacted by transverse misalignment and therefore the average luminosity recovered after BBA and sextupole knobs increases. For a lattice with no increase in dispersion there is approximately 30% of the machines that achieve the design luminosity $\mathcal{L}_0$ after BBA and one iteration of linear knobs, compare to 85% of the machines reaching $\mathcal{L}_0$ for a lattice with dispersion increased by a factor 2. The number of machines that reach $\mathcal{L}_0$ increases with dispersion as shown in Fig. 5.23.

It is worth noting that the tuning performance dependance with dispersion may not be

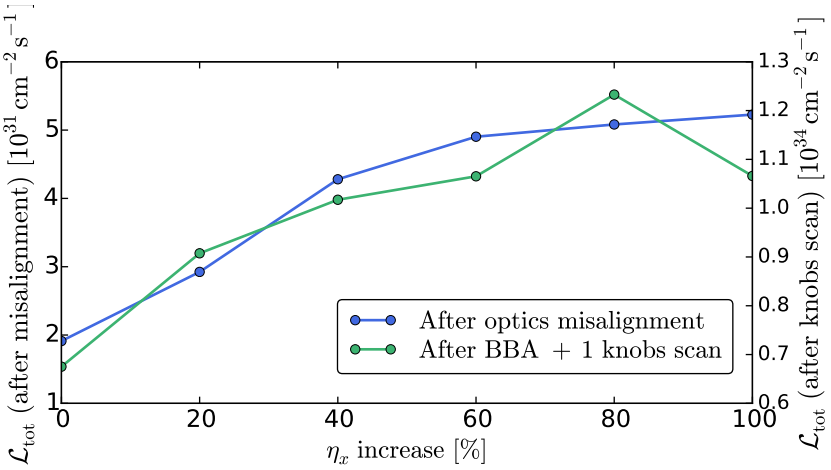

Figure 5.22: Average luminosity, over 100 randomly misaligned machines (see Table 5.5), after applying errors and after one tuning iteration, as function of FFS dispersion increase.

as strong when roll and strength errors are taken into account. Indeed, these additional

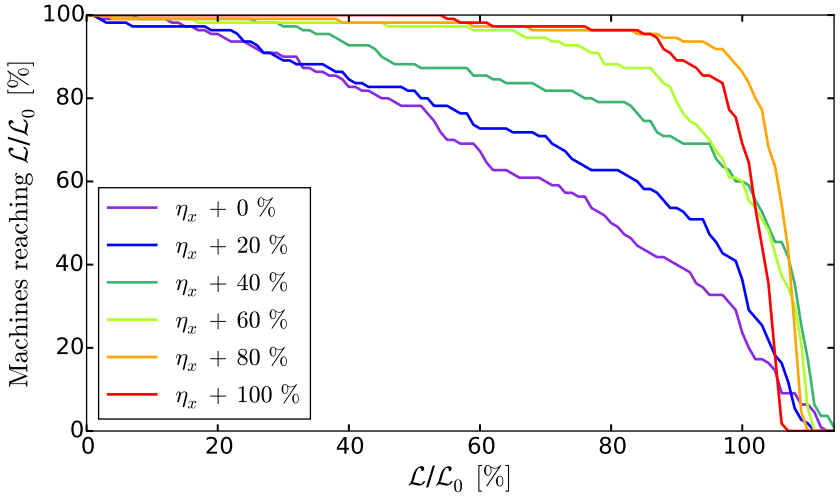

Figure 5.23: Luminosity distribution after one iteration of BBA + sextupole knobs, applied on the L* = 4.3 m lattice for different dispersion profile.

errors introduce normal and skew sextupole field errors and among them, some 2nd order dispersion aberrations that will be amplified with larger dispersion (see Eq.(2.97) and Eq.(2.103)). The impact of these residual 2nd order dispersion contributions on the tuning performance must be included in order to draw conclusions on the optimal lattice for tuning. The lattices optimized in Section 5.1, providing the required luminosity and tuning efficiency, remain the baseline lattices for the future CLIC 380 GeV FFS with L* = 4.3 m or L* = 6 m. The lattice models, for both L* options and their alternative designs optimized in this Chapter, are available in [86].

5.5 Alternative optics for beamstrahlung minimization

As discussed in Section 2.6, the choice of the horizontal beam size is driven by the emission of beamstrahlung that causes deterioration of the luminosity spectrum. The spectrum quality is evaluated by the ratio of the peak luminosity $\mathcal{L}_{1\%}$ and the total luminosity $\mathcal{L}_{\text{total}}$ for which the target is 60% for CLIC 380 GeV. It has been proposed by the detector community to study the impact of alternative optics, where the horizontal beam size varies and all other parameters are left constant, on the luminosity spectrum quality and hence on the resolution of physics analysis. Here, various lattices have been re-optimized with horizontal beta functions increased from $\beta_x^* = 4$ mm to $\beta_x^* = 20$ mm for the L* = 4.3 m and L* = 6 m designs. These designs have been optimized to allow further studies on the optimal beamstrahlung level for the resolution of the main physics process analysis, which is not covered in this thesis.

The horizontal and vertical beam sizes after optimization, as function of β_x^*, is shown in Fig. 5.24. Larger β_x^* tends to improve vertical beam size σ_y^* correction up to $\beta_x^* = 12$ mm

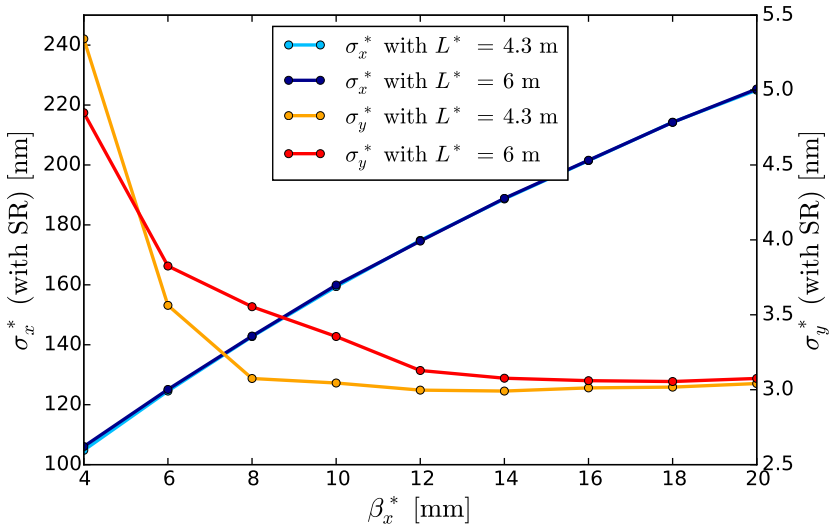

Figure 5.24: Horizontal and vertical beam sizes at the IP as function of the horizontal beta function β_x^*.

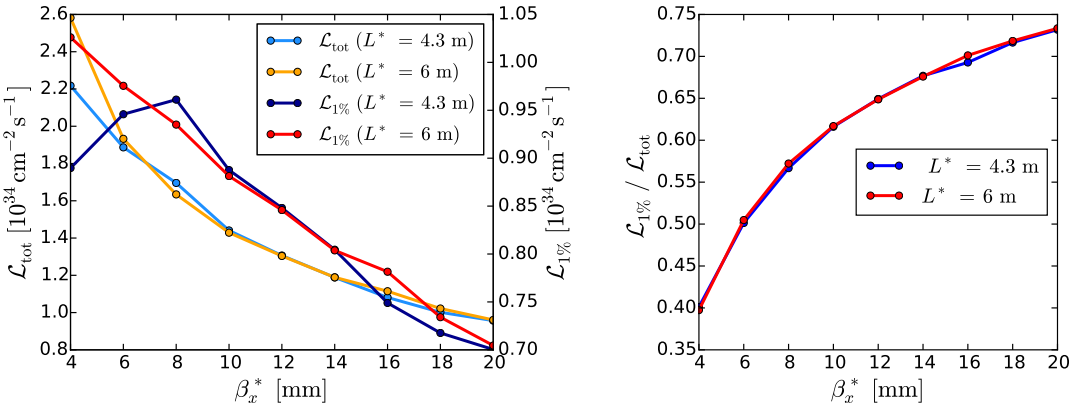

Figure 5.25: Total and peak luminosities (left plot) and luminosity spectrum quality (right plot) as function of the horizontal beta function for L* = 4.3 m and L* = 6 m.

for both L* options. The corresponding total and peak luminosities are shown in the left plot of Fig. 5.25. For both L* designs, the total luminosity increases more rapidly than the peak luminosity for lower β_x^* which leads to a large reduction of the ratio $\frac{\mathcal{L}_{1\%}}{\mathcal{L}_{\text{total}}}$, as shown in the right plot of Fig. 5.25. The luminosity spectrum quality improves with larger β_x^* but implies lower total and peak luminosities. Further studies on the optimum beam parameter choice will decide the best exploitation strategy for future linear colliders.

Table 5.6: Performance summary for the $L^* = 4.3$ m and $L^* = 6$ m options. Beam sizes and luminosities calculated assuming a realistic energy spread shape coming from the Main Linac. Tuning simulations assuming realistic transverse misalignements, roll and strength errors applied to the quadrupoles, sextupoles and BPMs.

FFS design	σ_x^* / σ_y^* [nm]	$\mathcal{L}_{\text{total}}$ / $\mathcal{L}_{1\%}$ [$10^{34}\text{cm}^{-2}\text{s}^{-1}$]	$\mathcal{L}_{\text{total}}$ achieved by 90% of the machines	Nbr. of $\mathcal{L}$ measurements
$L^* = 6$ m	152.0 / 4.25	1.36 / 0.82	-	-
$L^* = 6$ m*	151.2 / 3.20	1.52 / 0.91	96% $\mathcal{L}_0$	∼6300
$L^* = 4.3$ m	148.2 / 3.22	1.55 / 0.93	92% $\mathcal{L}_0$	∼7000

*with octupoles

5.6 Executive summary

Two L^* options for the BDS of the new initial CLIC energy stage ($\sqrt{s} = 380$ GeV) have been fully optimized and their tuning performances under realistic static imperfections have been addressed. The Final Focus lattice for $L^* = 6$ m has been lengthened by a factor 6/4.3 from the previous $\sqrt{s} = 500$ GeV design [84]. In order to allow the energy upgrade inside the CLIC tunnel, the 380 GeV and 3 TeV Main Linacs have been aligned. The crossing angle for the CLIC 3 TeV (with $L^* = 3.5$ m and $L^* = 6$ m) is 20 mrad and the required crossing angles for the CLIC 380 GeV BDS are 16.5 mrad for the $L^* = 6$ m BDS and 18.3 mrad for the $L^* = 4.3$ m. In the case of the $L^* = 6$ m FFS, a pair of octupoles has been introduced in the lattice to correct the remaining 3^{rd} order chromatic and geometric aberrations (especially the large contribution from the geometrical aberration referred to as U_{3224}) bringing the IP beam size very close to the design value. The luminosity achieved by the BDS, for both L^* options, fulfill the CLIC requirements. These simulations use the IP emittances from Table 5.1 to account for static and dynamic imperfections in the BDS. The tuning simulations have been performed assuming a 1% full width energy spread at the exit of the Main Linac. The effect of ground motion is not included into the simulations and the tuning performance goal is to obtain 90% of the machines simulated reaching a luminosity above the design luminosity $\mathcal{L}_0$. The luminosity and tuning performances compared with the shorter L^* option for the CLIC BDS are shown in Table 5.6. The goal is well surpassed when taking into account that the emittance used in simulations has about a 20% margin for static and dynamic imperfections.

Chapter 6

The Accelerator Test Facility 2 (ATF2)

The Accelerator Test Facility 2 is an international project to build and operate a test facility for the final focus system that is envisaged at ILC and CLIC [87]. A schematic layout of the ATF2 section is shown in Fig. 6.1. The main project goals are to establish the feasibility of the beam handling technologies related to transverse focussing of the electron beams to nearly 40 nm for the ILC-like FFS optics and 20 nm for the CLIC-like FFS optics and to demonstrate the beam stabilisation to the nanometer level using the intra-train feedback systems [88–90]. Other crucial studies for the future linear colliders are currently conducted at ATF2, such as the demonstration of the ground motion feedforward system [91,92], the development and test of a non-invasive transverse profile station based on Optical Diffraction Radiation Interference (ODRI) [93] and the development of diamond sensors for beam halo and Compton spectrum diagnostics after the ATF2 interation point [94, 95]. This Chapter presents the work conducted in the framework of the CLIC FFS feasibility, on the optics optimization of the ATF2 beamline, referred to as ultra-low β_y^* optics [96, 97]. A special emphasis will be given on the experimental work performed on the ATF2 beamline at KEK in 2017 for the tuning of the ultra-low β_y^* optics with the use of a recently installed pair of octupole magnets. This work follow past experimental studies on optics with β_y^* reduced by a factor 2 from the nominal value. In Sections 6.1 and 6.2 the motivations for the ultra-low β_y^* project at ATF2, the expected performances from our nonlinear optimization of the final focus (FF) beamline and tuning simulations are discussed. Section 6.3 gives a brief introduction on the instrumentations and correction techniques used for the FF beamline tuning then present the experimental tuning results measured at ATF2 between December 2017 and February 2018.

6.1 Motivations for ultra-low β_y^* study at ATF2

The nominal beam optics of ATF2 is a scaled down design of the ILC FFS based on the local chromaticity correction scheme, with equivalent beam energy spread, natural chromaticity and tolerances of magnetic field errors. The vertical beam size was focused to 41±2 nm at the bunch population of 0.7×10^9 at the virtual IP [98]. The achieved beam size is close to the ATF2 target value of 37 nm. The bunch population at the recent ATF2 beam operation is much smaller than ILC due to the strong intensity dependence of vertical beam size at the IP. The candidate of the intensity dependence source is IP angle jitter via wakefield. The IP horizontal and vertical beta-functions (β_x^*, β_y^*) of ATF2

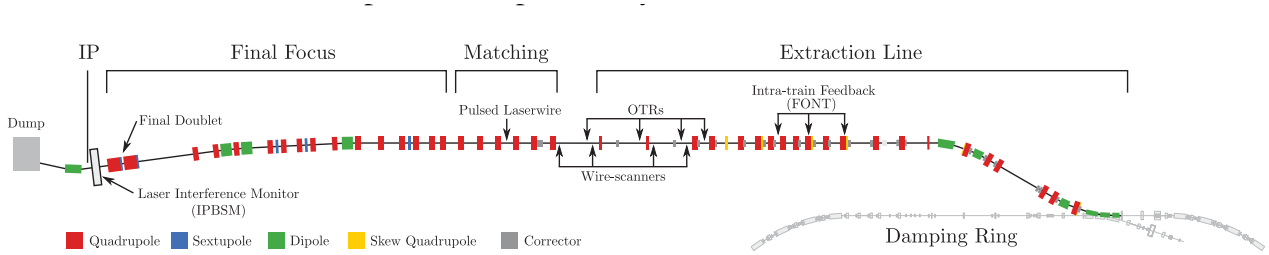

Figure 6.1: Schematic layout of the ATF2 section [23].

Table 6.1: Beam and optics parameters for the ILC, CLIC and ATF2 Final Focus

	ILC	CLIC	ATF2 ($10\beta_x^* \times 1\beta_y^*$)	($10\beta_x^* \times 0.25\beta_y^*$)
Beam energy [GeV]	500	3000	1.3	1.3
L^* [m]	4.1	6	1	1
ε_y [pm]	0.07	0.003	12	12
β_x^* / β_y^* [mm]	11 / 0.48	4 / 0.07	40 / 0.1	40 / 0.025
σ_x^* [μm] / σ_y^* [nm]	0.47 / 5.9	0.04 / 1	8.9 / 37	8.9 / 20
Energy spread δ_p [%]	≈0.1	0.3	0.08	0.08
Chromaticity ($\frac{L^*}{\beta_y^*}$)	8542	50000	10000	40000

were originally designed to generate the same horizontal and vertical chromaticities as ILC, referred to as $1\beta_x^* \times 1\beta_y^*$ optics. However, since the ATF2 beam energy is much smaller than ILC, the effect of the multipole errors are also larger. Therefore, in recent ATF2 beam operation, the ATF2 beamline was operated with a 10 times larger horizontal IP beta-function than that of original optics ($10\beta_x^* \times 1\beta_y^*$ optics) in order to reduce the sensitivity to the multipole errors (see Table 6.1). The local chromaticity correction scheme is considered as a baseline for ILC and a strong candidate for CLIC. However, for CLIC the expected level of chromaticity is higher by about a factor 5. The ATF2 ultra-low β_y^* lattice is a proposal [96] to test the feasibility for an even larger chromaticity lattice as the CLIC 3 TeV BDS. The ultra-low β_y^* design features a value of β_y^* =25 μm, which represents a quarter of the ATF2 nominal value. The expected minimum beam size achievable, after high order optimization of the ultra-low β_y^* FFS design, is 20 nm when optimized with a pair of octupoles. These simulations will be detailed in Section 6.1. Operating the ATF2 FFS with lower β_y^* optics would also allow to study the FFS tuning difficulty as function of the IP beam spot size, the impact of the measured multipolar errors, the impact on intensity dependence via wakefield and the compatibility of the IP beam size monitor (Shintake monitor) with a probably enlarged halo. Both the ILC and CLIC projects will benefit from the ATF2 experience at these ultra-low IP betas. The ILC project will benefit from this test by gaining experience in exploring larger chromaticities and facing increased tuning difficulties for smaller beam size.

6.2 Simulation studies of the ATF2 ultra-low β_y^* optics

Simulations for the optimization of the half ($\beta_y^* = 50$ μm) and the ultra-low β_y^* ($\beta_y^* = 25$ μm) lattices for ATF2 has been extensively studied in [17, 25, 42, 96, 99, 100]. This Section presents the updated optimized ultra-low β_y^* optics that will be applied and tested at ATF2. The identification of the 3$^{\text{rd}}$ order vertical beam size contributions has been carried out as well as the optimization of the octupoles needed to bring the vertical beam size down to 20 nm. The ultra-low β_y^* optics has been re-optimized for the nominal and larger horizontal beta-function at the IP. These optics are referred to as $1\beta_x^* \times 0.25\beta_y^*$ ($\beta_x^* = 4$ mm), $10\beta_x^* \times 0.25\beta_y^*$ ($\beta_x^* = 40$ mm) and $25\beta_x^* \times 0.25\beta_y^*$ ($\beta_x^* = 100$ mm). Tuning simulations have been performed on these lattices, assuming realistic error conditions at ATF2 and taking into account the magnetic fringe fields, the measured multipolar errors of the FF magnets, as well as realistic tuning time allocated for the ultra-low β_y^* optics during ATF2 operations. The impact of the octupoles and larger β_x^* on the tuning performance is also presented.

6.2.1 Optics design and higher order correction

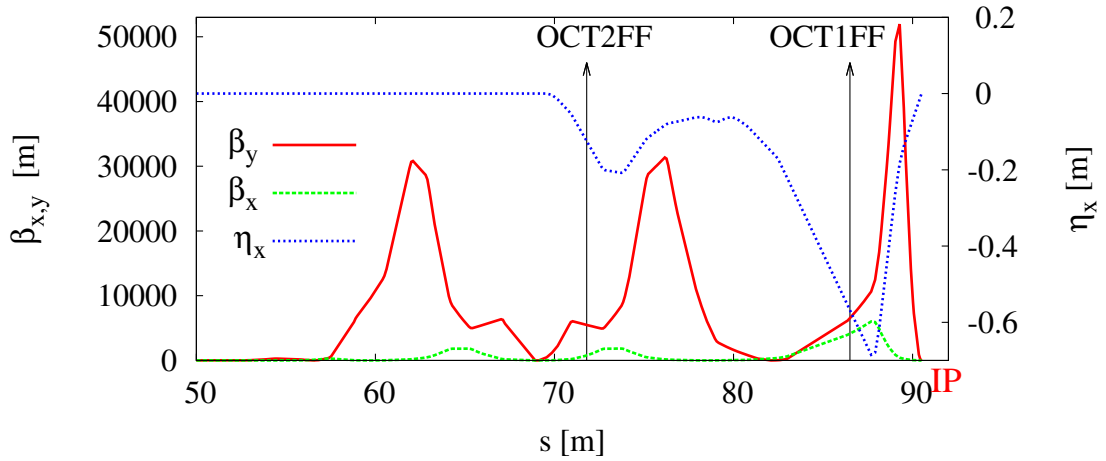

Figure 6.2: Optical functions of the $1\beta_x^* \times 0.25\beta_y^*$ lattice along the Final Focus beamline and location of the pair of octupoles installed at ATF2.

The linear optics has been rematched for $\beta_y^* = 25$ μm by varying 2 quadrupoles in the extraction line named QF21X and QD20X, 5 quadrupoles in the matching section named QM16FF, QM15FF, QM14FF, QM13FF, QM12FF and QM11FF, and the FD quadrupoles QF1FF and QD0FF. The quadrupoles located upstream in the extraction line and between the matching section and the FD are kept unchanged in order to preserve the phase-advance constraints between the kickers for the beam orbit feedback and the IP. The $\beta_{x,y}$ fucntions and horizontal dispersion η_x along the ATF2 FF beamline (from QM16FF to the IP) after matching the $1\beta_x^* \times 0.25\beta_y^*$ optics, are shown in Figure 6.2.

The chromaticity and higher order aberration corrections were first performed using only the 5 normal sextupole magnets named SF6FF, SF5FF, SD4FF, SF1FF and SD0FF and the 4 skew sextupoles SK1FF, SK2FF, SK3FF and SK4FF. The use of the skew sextupoles is needed when the measured high order field terms are included. Data on the multipole components of the ATF2 magnets can be found in [101]. This data was obtained after a careful cross-check between two different magnet measurement campaigns conducted at IHEP and KEK [102].

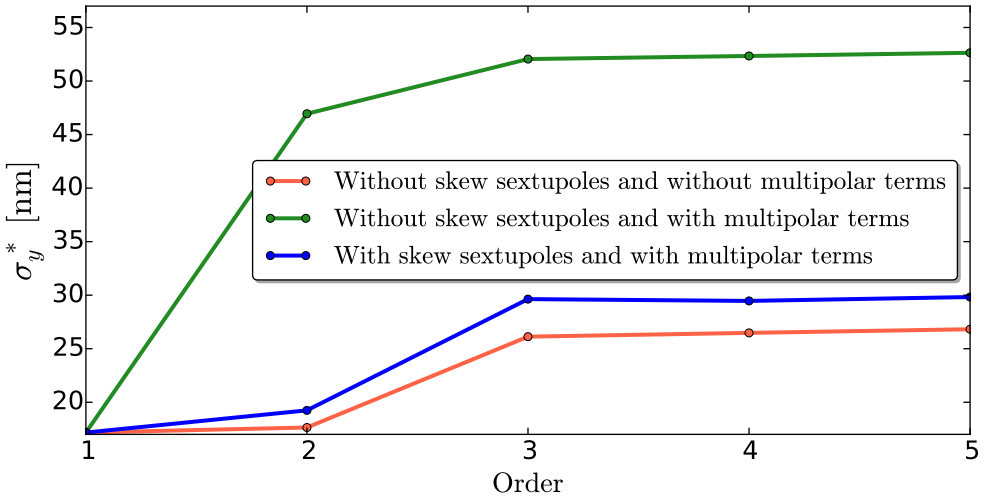

Figure 6.3: Vertical beam size σ_y^* calculated order by order for the $1\beta_x^* \times 0.25\beta_y^*$ optics with and without the ATF2 skew sextupoles and with and without the magnets higher order field terms.

The magnet multipolar errors have a large impact on the vertical beam size of the ultra-low β_y^* optics as shown in Fig. 6.3. When only the 5 normal sextupoles are used for beam size optimization, the minimum σ_y^* achievable is 52 nm, where the 2^{nd} order aberrations contribute to 30 nm of the vertical beam size increase. Without these multipolar errors, the skew sextupoles are not needed to fully correct the 2^{nd} order contributions to the vertical beam size. The nonlinear optimization of the FF beamline, including the measured magnet multipolar components and using the 4 skew sextupoles, brings the vertical beam size down to 30 nm, where the 3^{rd} order aberrations contribute to 11 nm of σ_y^*. Figure 6.3 also shows that the 3^{rd} order contributions are substantial with or without magnet multipolar errors. These observations are consistent with the results presented in [100, 103], showing that the main sources of 3^{rd} order aberrations for the ultra-low β_y^* optics are the nonlinear fringe field components increasing σ_y^* by 47%. Figure 6.4 shows the main 2^{nd} order contributions to σ_y^* with and without using the skew sextupoles. This study shows that the T_{344} aberration, introduced by the magnet multipolar errors, dominates the vertical beam size for ultra-low β_y^* optics, with a contribution of 27 nm. The T_{326} aberration contributes to approximately 1 nm to σ_y^*. These aberrations are

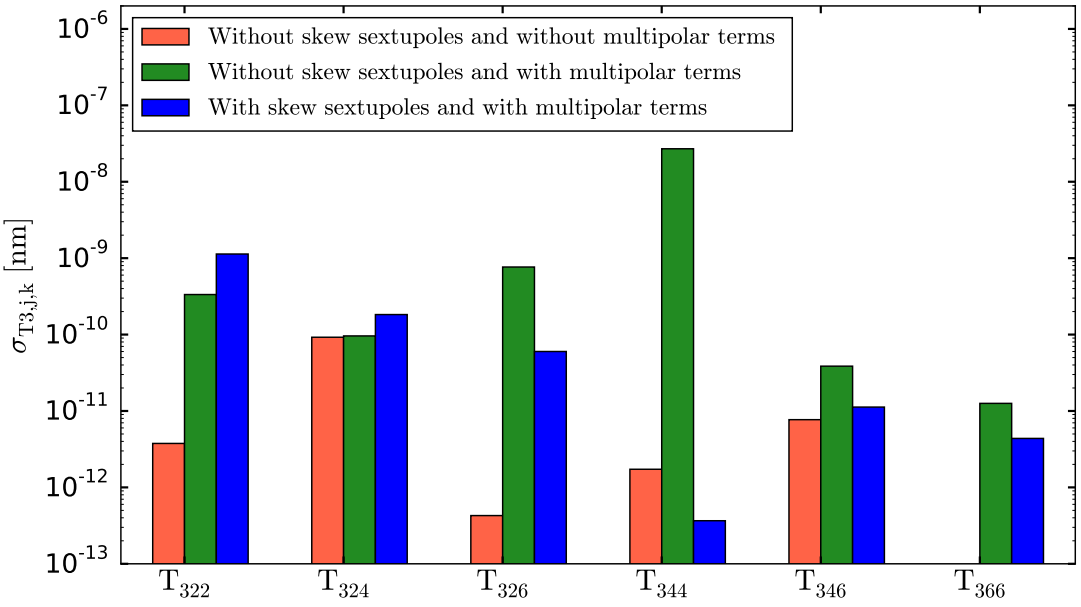

Figure 6.4: 2^{nd} order contributions to the vertical beam size with and without the ATF2 skew sextupoles and with and without the magnets higher order field terms.

corrected by using skew sextupoles (see Eq.(2.103)). Figure 6.5 compares the impact of the multipolar errors between the ultra-low β_y^* optics ($1\beta_x^* \times 0.25\beta_y^*$) and the nominal optics ($1\beta_x^* \times 1\beta_y^*$) on σ_y^*. The impact is considerably reduced for the nominal optics due to the smaller β_y along the FF beamline. Another way to reduce the contributions from the multipolar errors is to increase β_x^*. For the $10\beta_x^* \times 1\beta_y^*$ optics, no skew sextupoles are needed to achieve the design σ_y^*, while for the $10\beta_x^* \times 0.25\beta_y^*$ optics, the contributions from T_{344} is still very important with $\sigma_{T_{344}} = 18$ nm.

For the $1\beta_x^* \times 0.25\beta_y^*$ optics, after optimization of the normal and skew sextupoles, the minimum vertical beam size is 30 nm, where the 3^{rd} order aberrations being responsible for 11 nm of σ_y^* increase. The left plot of Fig. 6.6 shows that these 3^{rd} order components are partially chromatic and geometric. The right plot of Fig. 6.6 shows the beam size contribution from the main 3^{rd} order aberrations. The chromatic aberration U_{3246} contributes to 7.2 nm to σ_y^* and the geometric aberration U_{3224} contributes to approximately 2.5 nm. These aberrations can be corrected using normal octupoles as shown in Eq.(2.111). In order to reduce the impact of the main source of σ_y^* increase, U_{3246} and U_{3224}, two normal octupoles have been inserted in the FF beamline. One octupole, named OCT1FF, is located in high-η_x region, between QD2FF and SF1FF magnets, and aims to correct 3^{rd} order chromatic aberrations. The second octupole, OCT2FF, is located upstream of OCT1FF, in low-η_x region, between QD6FF and SK3FF magnets, and aims to correct 3^{rd} order geometrical aberrations. The left plot of Fig. 6.7 shows the

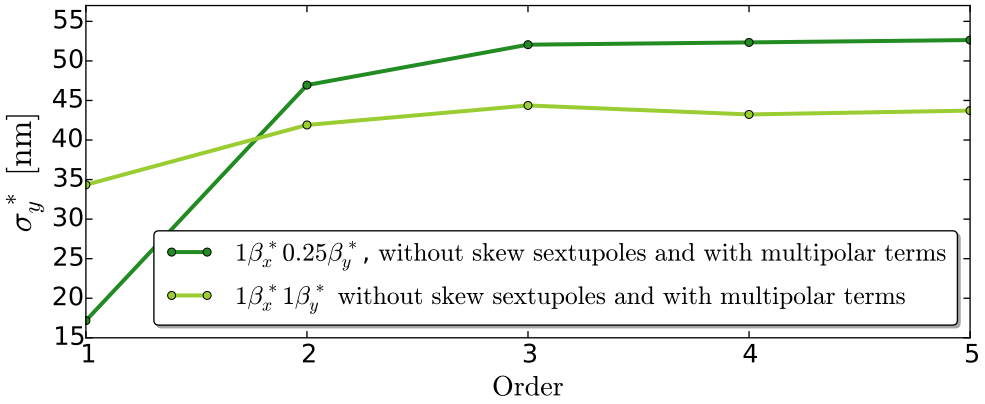

Figure 6.5: Vertical beam size σ_y^* calculated order by order for the $1\beta_x^* \times 0.25\beta_y^*$ and the $1\beta_x^* \times 1\beta_y^*$ optics without the ATF2 skew sextupoles and by taking into account the magnets higher order field terms.

final vertical beam size after optimization of the pair of octupoles. The beam size has been reduced from 30 nm down to 20 nm. In the right plot of Fig. 6.7 one can observe that σ_{U3246} has been reduced from 7.2 nm down to 0.1 nm and σ_{U3224} has been reduced from 2.5 nm down to 0.04 nm. All other 3$^{\mathrm{rd}}$ order contributions are below the nanometer level. As discussed in [103], one possiblity for the fringe field effect mitigation is the

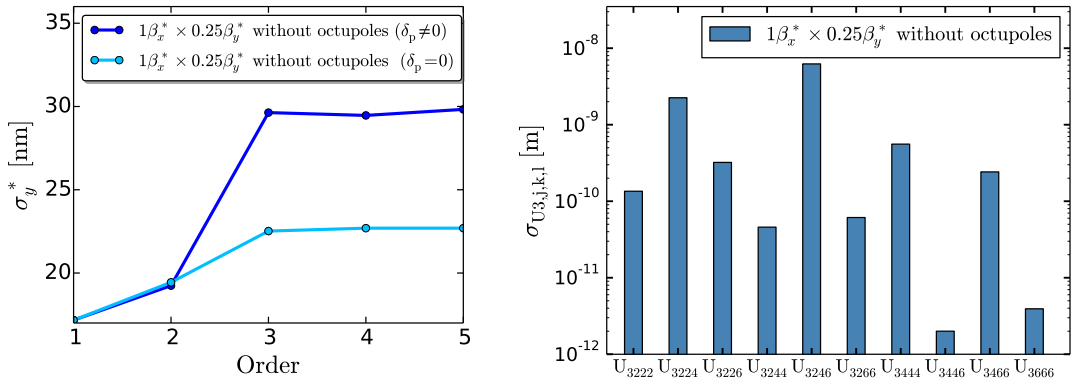

Figure 6.6: Left: Vertical beam size σ_y^* calculated order by order for the $1\beta_x^* \times 0.25\beta_y^*$ optics without octupoles. Right: 3$^{\mathrm{rd}}$ order contributions to the vertical beam size growth before octupoles optimization.

increase of β_x^*. This option reduces β_x at the FD location therefore makes the fringe field effect weaker, hence the 3$^{\mathrm{rd}}$ order contributions to σ_y^* smaller. Figure 6.8 shows the smaller impact of larger β_x^* on the 3$^{\mathrm{rd}}$ order beam size contributions, compare to the nominal β_x^*. For the $10\beta_x^* \times 0.25\beta_y^*$ optics, $\sigma_{\mathrm{U3246}} = 1.5$ nm and $\sigma_{\mathrm{U3224}} = 1$ nm. The octupoles parameters, for the $1\beta_x^* \times 0.25\beta_y^*$ and $10\beta_x^* \times 0.25\beta_y^*$ optics are summarized in Table 6.2.

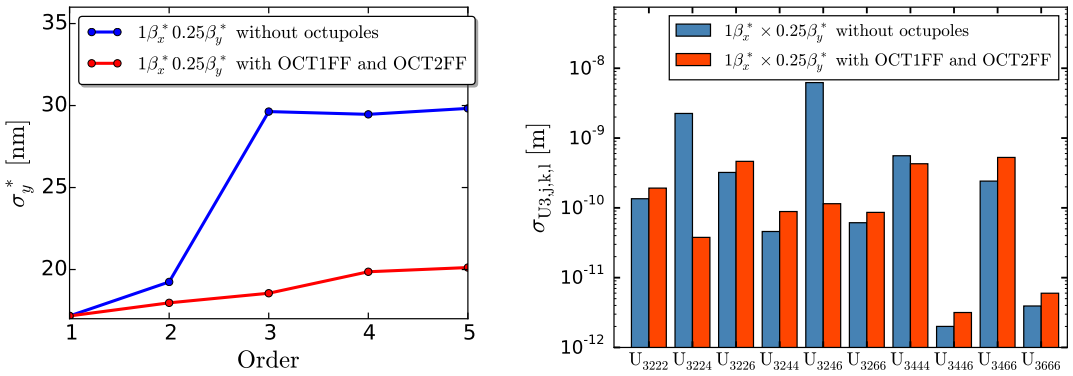

Figure 6.7: Left: Vertical beam size σ_y^* calculated order by order for the $1\beta_x^* \times 0.25\beta_y^*$ optics with and without octupoles. Right: 3rd order contributions to the vertical beam size growth before and after octupoles optimization.

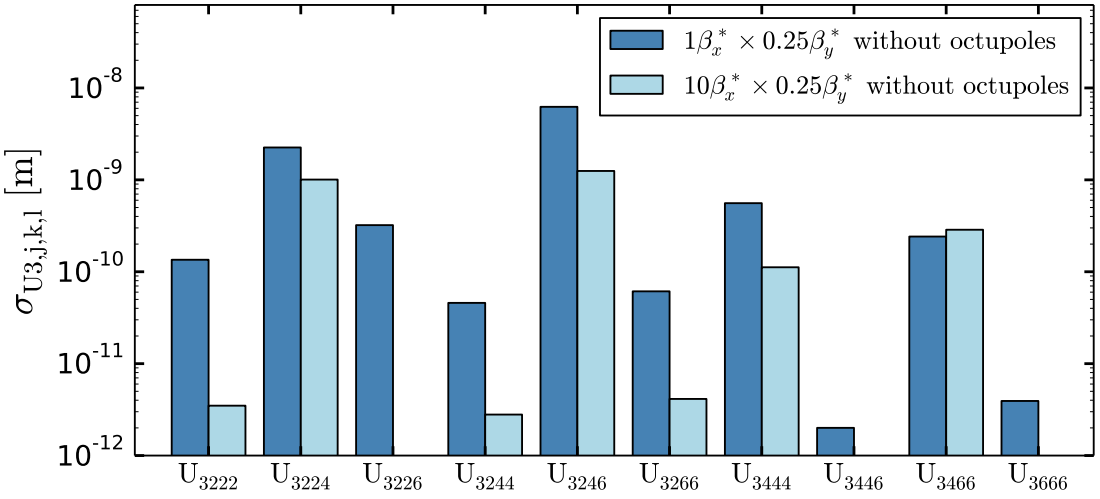

Figure 6.8: 3rd order contributions to the vertical beam size growth before octupoles optimization for $\beta_x^* = 40$ mm and $\beta_x^* = 4$ mm ($\beta_y^* = 25$ μm).

6.2.2 Tuning of the FFS for lower β_y^* optics

This Section presents the tuning simulations of the ultra-low β_y^* lattice under realistic static imperfections assumed for the ATF2 FF beamline. This study prepares the experimental tuning of the ATF2 ultra-low β_y^* optics performed at KEK, which will be discussed in Section 6.3. The tuning simulations were done by using numerical tools based on MAD-X environment. The machine errors applied to the ATF2 beamline, see Table 6.3, concern the transverse misalignment, roll angle and strength of the quadrupoles, sextupoles and octupoles of the FFS. These errors are randomly allocated to the ATF2 magnets following a Gaussian distribution. The statistical analysis of the tuning perfor-

Table 6.2: Octupoles parameters for the ultra-low β_y^* optics

	$1\beta_x^* \times 0.25\beta_y^*$	$10\beta_x^* \times 0.25\beta_y^*$
OCT1FF k_3L [m^{-3}]	-36.6	-24.1
OCT2FF k_3L [m^{-3}]	191.4	98

Table 6.3: Errors applied to the ATF2 FF lattice

σ_{offset} (Quadrupoles, Sextupoles and octupoles)	100μm
σ_{roll}	200μrad
Strength error	0.1%

mance was performed using 100 random seeds. The simultions also include the fringe field and the measured multipolar components of the magnets.
The applied imperfections generate large linear aberrations that dominates the beam size. As performed for the tuning of the ATF2 machine at KEK, only the 3 main linear aberration contributions, impacting the vertical beam size, are corrected during the tuning process. These aberrations are the vertical beam waist shift α_y^*, vertical dispersion η_y^* and <x',y> coupling at the IP. They are corrected using pre-computed combination of sextupole horizontal displacements, for α_y^* correction, and vertical displacements, for η_y^* and <x',y> coupling corrections.
Nonlinear knobs are also constructed in order to correct the residual 2$^{\text{nd}}$ and 3$^{\text{rd}}$ order aberrations at the IP. The T_{324} and T_{346} knobs are constructed using strength variations of the 5 normal sextupoles. The T_{322}, T_{326}, T_{344} and T_{366} knobs are constructed using strength variation of the 4 skew sextupoles. Finally, 2 additional knobs based on strength variations of the 2 octupoles target the U_{3224} and U_{3466} aberrations. It is worth noticing that it is possible to create up to four 2$^{\text{nd}}$ order knobs by using the feed-down to normal and skew sextupole fields created by horizontal and vertical displacements, respectively, of the octupoles. However, due to the poor orthogonality of these knobs, it was preferred to use only the 2$^{\text{nd}}$ order knobs already constructed from the normal and skew sextupoles.
The experimental tuning study at ATF2 is limited by the number of shifts allocated for this study, where one shift corresponds to 8 hours of operation. For the tuning simulations presented here, one takes into account realistic number of knob scans that can be applied within the allocated tuning time. The number of knobs applied has been calculated assuming one week of tuning (12 shifts) and 30 minutes to perform one knob scan (3 minutes per beam size measurement with the Shintake monitor). The tuning of the 1 $\beta_x^* \times 0.25\ \beta_y^*$ optics, when using the octupoles, shows poor performance with only 10% of the machines that reach σ_y^* below 30 nm. The average σ_y^* after tuning is 75 $\pm$ 20 nm over the 100 machines simulated. However, the tuning performance is significantly improved for larger β_x^* optics. For the tuning of the 10 $\beta_x^* \times 0.25\ \beta_y^*$ optics under the same conditions, 63% of the machines reach $\sigma_y^* \leq 30$ nm and the average beam size after tuning is 35 $\pm$ 10 nm. The tuning performance comparison between these two optics is shown in Fig 6.9. The impact of the octupoles for the tuning of the

10 β_x^* × 0.25 β_y^* optics is noticeable as shown in Fig. 6.10. When the octupoles are turned off, the number of machines reaching $\sigma_y^* \leq 30$ nm is reduced down to 41 %, where the average σ_y^* is equal to 44.2 ± 13 nm.

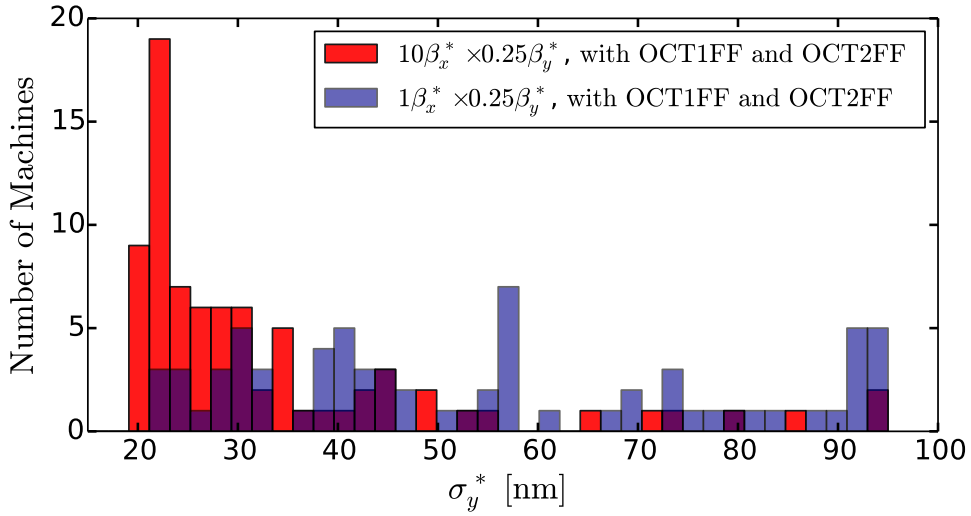

Figure 6.9: Tuning performance comparison between the 1 β_x^* × 0.25 β_y^* and the 10 β_x^* × 0.25 β_y^* optics.

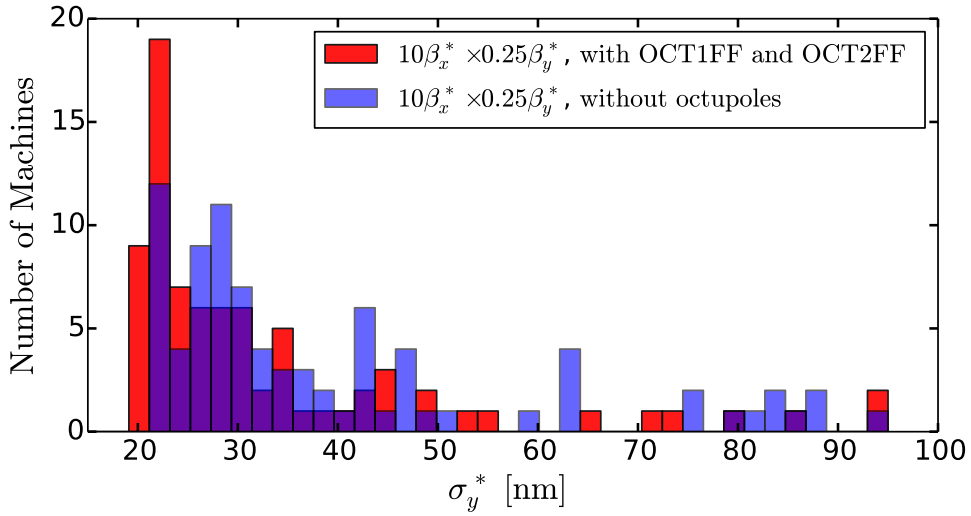

Figure 6.10: Tuning performance comparison for the 10 β_x^* × 0.25 β_y^* optics lattice, with and without the use of OCT1FF and OCT2FF during the tuning procedure.

6.3 Experimental study of the ultra-low β_y^* optics tuning

Following the tuning measurement campaign at the ATF2 performed on the half-β_y^* optics ($\beta_y^* = 50$ μm) during the February 2016 operation, reported in [104], the optics has been pushed towards ultra-β_y^* and the first tuning attempts of this optics were done between December 2017 and February 2018. These tuning measurements paved the way towards exploring the lower beam size limit of the CLIC-like optics and helped to highlight the possible limitations on beam focusing that the future linear colliders will face. A description of the indispensable instrumentations, correction and measurement techniques, that are used for the beam tuning, are detailed in Section 6.3.1. A special emphasis on the recently installed octupoles and their alignment in the ATF2 beamline will be given in Section 6.3.2. Finally, the Section 6.3.3 presents the path taken towards the first implementation and probing of the ultra-low β_y^* optics at ATF2.

6.3.1 Diagnostics and correction techniques used for beam size tuning

6.3.1.1 Shintake monitor

As mentioned previously, the nominal ATF2 FF design aims to focus the vertical e^- beam size down to 37 nm and down to 20 nm when using the ultra-low β_y^* optics. By now the only existing device capable of measuring such beam sizes is an interference monitor called Shintake monitor installed at the virtual IP of the ATF2. The ATF2 Shintake monitor is an upgraded version of the one used at FFTB [105] and is capable of measuring beam size from 6 μm down to 25 nm. This instrument is therefore crucial during beam tuning operations, hence to demonstrate ILC and CLIC FFS feasibilities.

The Shintake monitor system consists of laser optics and a gamma detector. The laser, located outside the accelerator tunnel, generates laser pulses of wavelength $\lambda = 532$ nm, which are transported to an upright standing optical table located at the IP. The laser beam is there split into upper and lower paths. The two laser beams are focused at the IP where they cross in the plane transverse to the e^- beam to form interference fringes. The schematic layout of the beam size monitor is shown in Fig. 6.11. As the e^- beam interacts with the laser interference fringes, the fringe pattern is modified by changing the phase of one laser path using the optical delay line. The beam size is inferred from the modulation of the resulting Compton scattered photon signal detected by a downstream photon detector. After collision, the beam is bent by a dipole magnet safely into a dump. The smaller σ_y^* is with respect to the fringe pitch, the larger the observed modulation will be (see Fig. 6.11). The number of signal photons (N) is calculated by Eq.(6.4) as the convolution of a Gaussian beam distribution and the laser fringe intensity:

$$M = \frac{N_+ - N_-}{N_+ + N_-} \tag{6.1}$$

$$= |\cos\theta| \exp\left[-2(k_y\sigma_y)^2\right] \tag{6.2}$$

$$\Rightarrow \sigma_y = \frac{d}{2\pi}\sqrt{2\ln\left(\frac{|\cos\theta|}{M}\right)}, \tag{6.3}$$

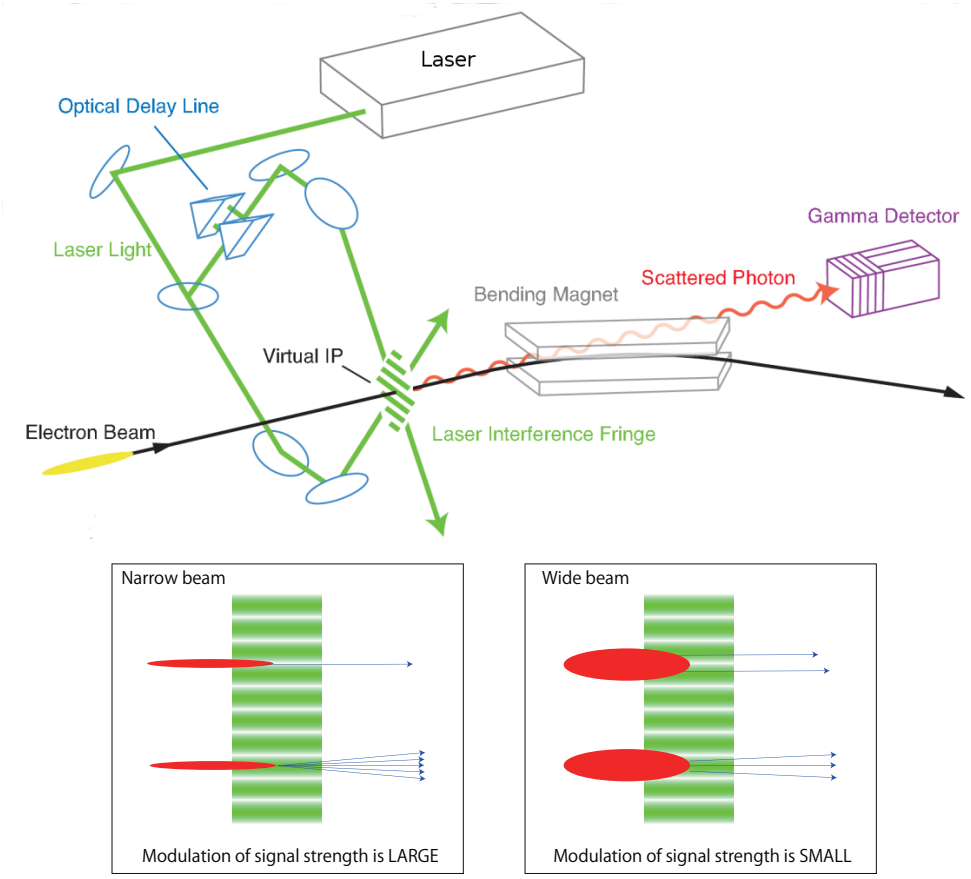

Figure 6.11: Schematic layout of Shintake Monitor [106].

where $k_y = \frac{\pi}{d}$, the fringe pitch $d = \frac{\lambda}{2\sin(\theta/2)}$, N_+ and N_- are the maximum and minimum signal intensity, respectively, and θ is the laser crossing angle. The Shintake monitor has three crossing angle modes, 6.4, 30 and 174 degree, and the corresponding measurable σ_y range are summarized in Table 6.4. An example of modulation measurement taken at ATF2 during beam tuning, using the crossing angle mode $\theta = 30$ deg, is shown in Fig 6.12. Beam size measurements with the Shintake monitor experience various types of systematic errors that lead to an over-evaluation of the observed beam size. The overall effect of the systematic errors are represented by the modulation reduction factor C where $M_{\text{measured}} = CM_{\text{ideal}}$. The systematic errors related to the laser imperfections (alignment accuracy, polarization, temporal coherence, phase jitter, tilt of the fringe pattern and spherical wave front) were evaluated in [106, 107]. One important systematic error to be evaluated for the ultra-low β_y^* optics is related to the beam size growth within the fringe pattern. Due to the stronger focusing of the ultra-low β_y^* optics compare to the nominal one, the laser sport size at the IP in the longitudinal direction $\sigma_{z,laser}$, where $\sigma_{z,\text{laser}} \approx 15$ μm at 174 deg mode, becomes influencial on the measured modulation (see Fig. 6.13). The modulation reduction factor due to beam size growth within the fringes

Table 6.4: Observable beam sizes for the different laser crossing angle modes.

Crossing angle θ [deg]	6.4	30	174
Fringe pitch d [μm]	4.77	1.028	0.266
Measurable σ_y [nm]	424 $\sim$ 1700	90 $\sim$ 400	25 $\sim$ 100

($C_{\sigma_y \mathrm{growth}}$) is given by [107]:

$$M_{\mathrm{meas.}} = \left(1 + 4k_y^2 \sigma_{z,\mathrm{laser}}^2 \frac{\varepsilon_y}{\beta_y^*}\right)^{-\frac{1}{2}} M_{\mathrm{ideal}}. \tag{6.4}$$

$$\tag{6.5}$$

For $\beta_y^* = 25$ μm and $\varepsilon = 12$ pm, $C_{\sigma_y \mathrm{growth}} = 97.1$ % at 174 deg mode while for the nominal optics ($\beta_y^* = 100$ μm) $C_{\sigma_y \mathrm{growth}}$ =99.7 %.

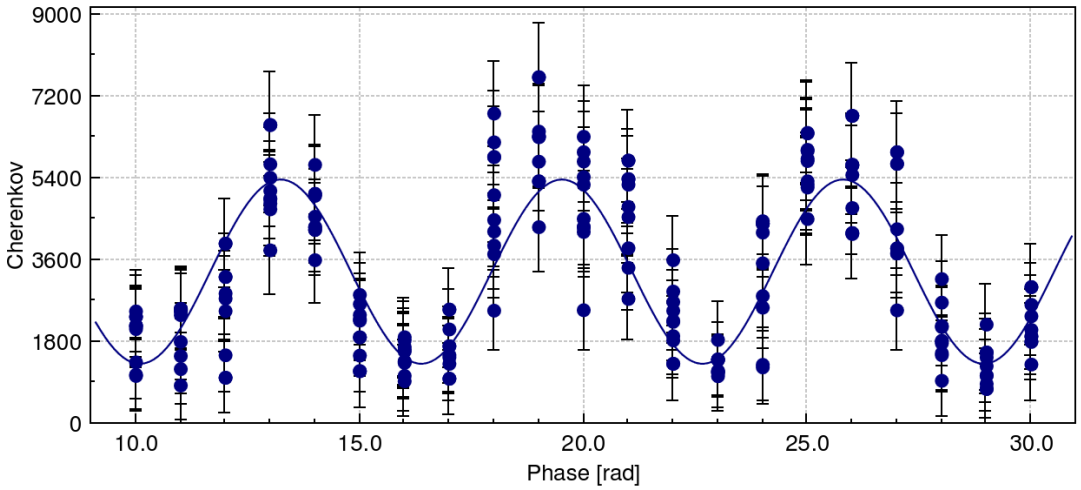

Figure 6.12: Example of an interference scan for vertical beam size measurement using the Shintake monitor at 30 degree mode (M = 0.6 $\Rightarrow \sigma_y^* = 130$ nm).

6.3.1.2 Orbit and dispersion correction

The orbit is corrected using horizontal and vertical steering dipoles to minimize the beam offset at the BPMs located along the FF beamline. After flattening the orbit, the dispersion along the FF beamline is evaluated by observing the orbit change at the BPMs $\Delta x, y_{\mathrm{BPM}}$ when changing the beam energy in the damping ring ($f_{\mathrm{DR}} = 714$ MHz). The dispersion is given by:

$$D_{x,y} = \frac{\Delta x, y_{\mathrm{BPM}}}{\Delta p/p}, \tag{6.6}$$

where $\Delta p/p$ is the momentum shift related to the frequency change Δf by

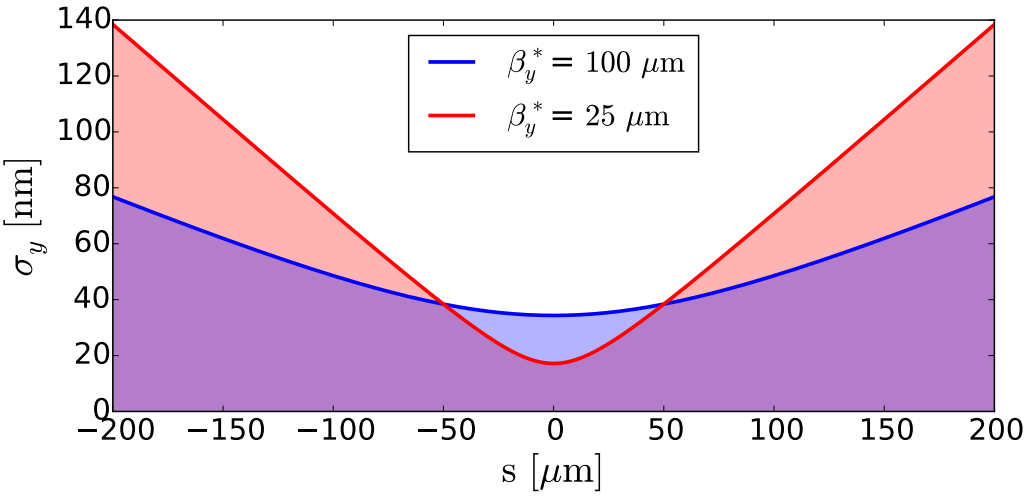

Figure 6.13: Verticl beam size comparison around the virtual IP for $\beta_y^* = 100$ μm and $\beta_y^* = 25$ μm.

$$\frac{\Delta p}{p} = \frac{\Delta f}{f_{\mathrm{DR}}} \frac{1}{\alpha}, \tag{6.7}$$

where $\alpha = 0.00214$ is the ATF DR momentum compaction factor. During dispersion measurement the damping ring frequency is changed by ± 2 kHz leading to a relative beam energy change of about ±1.3%. The dispersion correction procedure at ATF2 uses quadrupole strength variations. In order to correct the dispersion along the FFS while not affecting too much other parameters with minimum strength variations, the quadrupoles used for the correction are located at the dispersion peaks in the extraction line. The vertical dispersion is corrected using a pair of skew quadrupoles QS1X and QS2X that generates vertical dispersion via coupling from the horizontal dispersion. Their locations are shown in Fig. 6.14. The same strength variations of QS1X and QS2X are applied during correction. The $< x, y >$ coupling generated by QS1X is cancelled by QS2X thanks to their transfer matrix relation. The horizontal dispersion is corrected using 2 normal quadrupoles QF1X (located close to QS1X) and QF6X (located close to QS2X). Their strengths are varied independently until matching the design horizontal dispersion.

6.3.1.3 $\beta_{x,y}^*$ measurement

The measurements of the $\beta_{x,y}^*$ values are crucial to verify that the desired optics was correctly implemented. The quadrupole scan method is used at ATF2 for the evaluation of the transverse beam parameters. The strengths of the FD quadrupoles QF1FF and QD0FF are scanned while the horizontal and vertical beam size, respectively, are measured using the IP wire scanner [108]. In the vincinity of the IP, σ_x and σ_y depend on the beam divergence and waist longitudinal displacement $\Delta f_{x,y}$ according to [37]

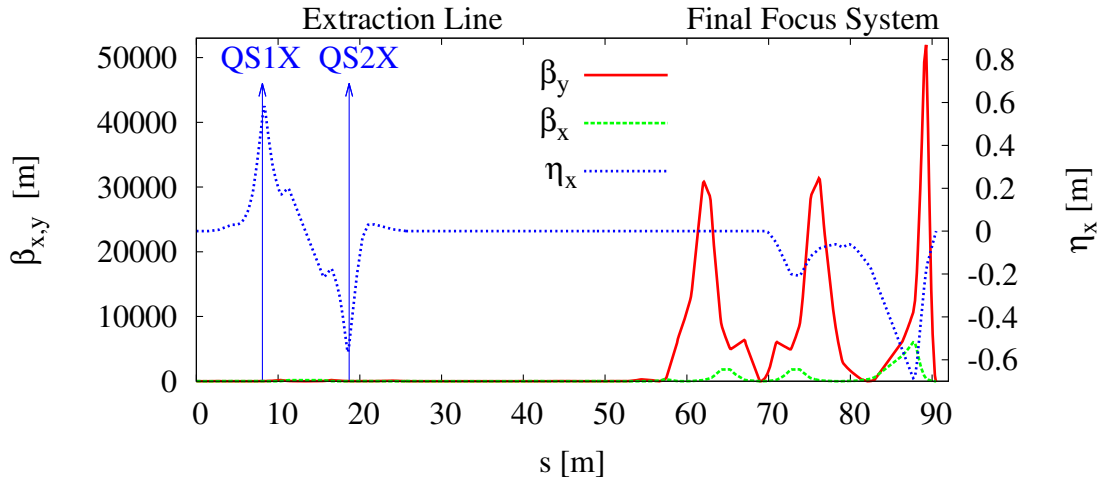

Figure 6.14: Optical functions along the extraction and the FF beamline with the location of the pair of skew quadrupoles used to correct horizontal dispersion and $< x , y >$ coupling.

$$\sigma^2_{x,y} = \varepsilon_{x,y}\beta^*_{x,y} + \frac{\varepsilon_{x,y}}{\beta^*_{x,y}}\Delta f^2_{x,y}, \tag{6.8}$$

where the measured beam size has to be corrected for residual dispersion at the IP and for the geometric properties of the cabon wire as

$$\sigma^2_{x,y} = \sigma^2_{x,y,\text{measured}} - \left(\frac{\delta p}{p}\right)^2 \eta^2_{x,y} - \left(\frac{\mathrm{d}}{4}\right)^2. \tag{6.9}$$

The ATF2 energy spread $\delta p/p = 0.0006$ for low beam intensity of 10^9 e^-/bunch and the carbon wire diameter is d = 5 μm. By fitting parabolic curves to the measured data as a function of the quadrupole magnet current, both emittance and β function can be determines simultaneously if one can resolve the minimum beam size at the waist. This is the case for the horizontal beam size for which the usual values vary from 6 μm to 10 μm. However, the vertical beam size is expected to be smaller than 1 μm at the start of the tuning and therefore cannot be precisely measured at waist with the carbon wire. Only the beam divergence can be resolved using

$$\sigma^2_y \approx \frac{\varepsilon_y}{\beta^*_y}\Delta f^2_y. \tag{6.10}$$

The quadrupole scan method cannot be applied to resolve both the vertical emittance ε_y and β^*_y since the waist is too small to be measured by the wire scanner. The vertical waist could be measured by the Shintake monitor using the appropriate laser crossing

Table 6.5: OCT1FF and OCT2FF main parameters

	OCT1FF	OCT2FF
Maximum gradient [T/m^3]	10312.1	1237.5
Magnetic length [mm]	300	300
Aperture radius [mm]	52	52
Ampere-turns [A] (per coil)	1800	180
Number of turns (per coil)	50	6
Max. current [A]	50	50
Total magnet mass [kg]	330	90

angle mode. However, the narrow dynamic range, of the beam size measurement using the 30 or 174 degree modes of the Shintake monitor, requires very fine control of the beam waist that cannot be achieved by varying QD0FF strength. A novel method using the vertical waist position α_y^* knob instead of QD0FF scan to measure both ε_y and β_y^* has been proposed and tested at ATF2 [100, 104] using more relaxed optics (matching target was $\beta_y^* = 2.5$ mm). This method requires precise beam size measurements, good knowledge of the systematic errors and good orthogonality of the α_y^* knob in order to ensure that the scan is not bias by other linear aberrations generated by the offset sextupoles. This method has not been applied during the ultra-low β_y^*, instead the divergence has been precisely measured by the traditional QD0FF scan, and the vertical emittance was measured upstream of the FFS. For the evaluation of the β_y^* the emittance is assumed to be close to the emittance measured by the multi-OTR [109] located at the matching section of the FFS or, as assumed during December 2017 and February 2018 (see Section 6.3.3), to the emittance measured in the damping ring.

6.3.2 The ATF2 octupoles

6.3.2.1 Technical description and installation at ATF2

The two octupoles, OCT1FF and OCT2FF, were manufactured at CERN according to the specifications given in [110]. The parameters of the octupoles are shown in Table 6.5. The magnetic measurement team in the MSC group of CERN's technology department measured the magnetic properties of the two octupole magnets, by means of both the rotating-coil (see Fig. 6.15) and the stretched/vibrating wire techniques, for the measurement of the field quality and magnetic center.
The higher-order multipole errors are expressed at a reference radius R_{ref} of 20 mm and the magnetic multipoles measured at 50 A are shown in Table 6.6. The measured multipolar terms of the octupoles have been included in the ultra-low β_y^* optics optimization and tuning simulations discussed in this Chapter. The maximum possible magnet current of 50 A was determined by means of a thermal camera, fixing the maximum working temperature at 65 degree Celsius on the external part of the coils. A demagnetization cycle was performed, before and after the magnetic measurement, in order to guarantee the repeatability conditions for the measurements and for the final usage in the machine. The octupole strengths allow the correction of the 3rd order aberrations

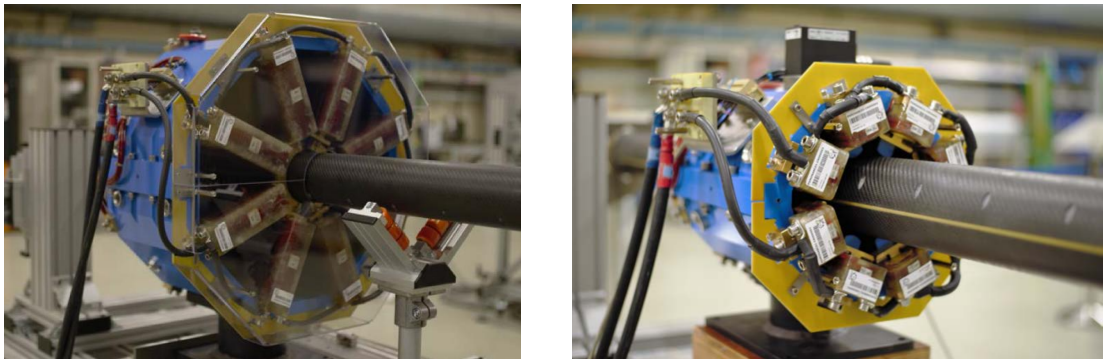

Figure 6.15: Octupoles on magnetic measurement bench at CERN. Left: OCT1FF ; Right: OCT2FF

and the measured multipolar components are within the tolerances summarized in [110]. A detail report on the magnetic measurements of the octupoles carried out at CERN can be found in [111, 112]. The two octupoles were shipped to KEK (Japan) and installed in November 2016 (see Fig. 6.16) in the ATF2 FF beamline at the locations indicated in Fig. 6.2. Both magnets are mounted on micrometric tables with dynamic range of $\pm$ 1 mm.

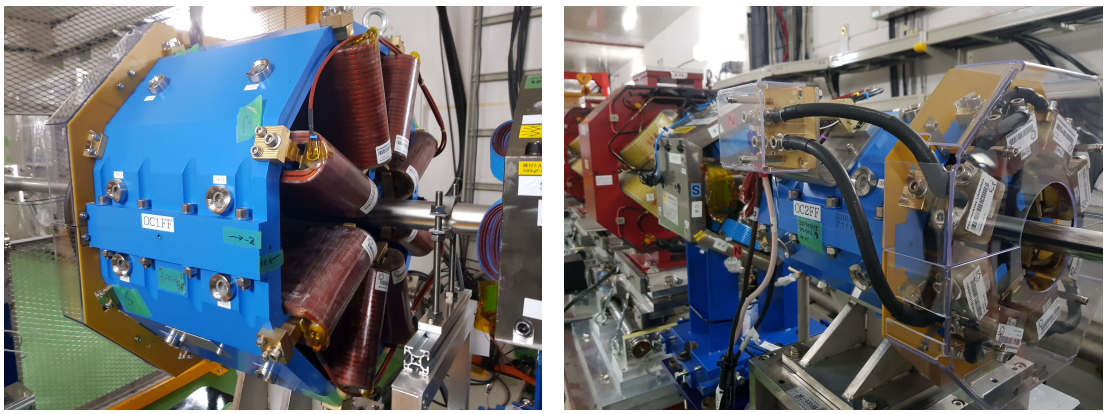

Figure 6.16: Octupoles installed in ATF2 FF beamline in November 2016. Left: OCT1FF ; Right: OCT2FF

6.3.2.2 Beam-based alignment of the octupoles using IPBPMs

In order to minimize the undesired beam size contributions coming from the feed-down magnetic fields of the offset octupoles, it is necessary to align their magnetic centers with respect to the beam. The transverse offset tolerances of both octupoles were calculated by simulation and are defined as the offsets which result in a vertical beam size increase of $\Delta\sigma_y^* = 2\%$. The tolerances are shown in Table 6.7. The BBA is performed by measuring the beam position change induced by the horizontal and vertical offset of the octupole. Both octupoles are mounted on micro-metric movers with a dynamic range

Table 6.6: OCT1FF and OCT2FF multipoles measured at 50 A at 20 mm reference radius

OCT1FF		OCT2FF	
R_{ref} = 20 mm	[10^{-4}]	R_{ref} = 20 mm	[10^{-4}]
b_5	2.20	b_5	-0.93
a_5	-1.11	a_5	-0.53
b_6	1.06	b_6	0.37
a_6	-0.35	a_6	-0.41
b_7	-0.15	b_7	-0.17
a_7	0.01	a_7	0.04
b_8	-0.04	b_8	-0.02
a_8	-0.02	a_8	-0.12
b_9	0.02	b_9	-0.01
a_9	-0.03	a_9	0.01
b_{10}	0.02	b_{10}	0.01
a_{10}	0.00	a_{10}	0.01
b_{11}	0.00	b_{11}	0.02
a_{11}	0.01	a_{11}	-0.06
b_{12}	-0.27	b_{12}	-0.27
a_{12}	0.00	a_{12}	0.00

of ± 1 mm. The low maximum strength of OCT2FF and the limited dynamic range of its mover induce a beam position change smaller than the resolution of the downstream BPMs. Therefore, the BBA measurements were performed only on OCT1FF, which has tighter transverse tolerances than OCT2FF. For OCT1FF BBA, the beam position change, when OCT1FF is set to its maximum current of 50 A and moved from - 1 mm to + 1 mm, is of the order of few micrometers and therefore was measured by the IPBPMs, which provide the best position resolution of all available downstream BPMs [90]. The beam position around the virtual IP is measured by three cavities IPBPM-A, IPBPM-B and IPBPM-C. IPBPM-A and B are located at 167.9 mm and 87.1 mm upstream the IP, respectively. The IPBPM-C is located 87.1 mm downstream the IP. These three cavities are used to measure the beam trajectory in the IP region, providing enough information to reconstruct the bunch position and angle at the IP. The horizontal (vertical) beam position change, induced by the feed-down horizontal (vertical) dipole kick of the horizontally (vertically) offset octupole, is proportional to Δx^3 (Δy^3) as shown in Eqs. (2.105, 2.107). When OCT1FF is set 50 A and displaced only along the horizontal or vetical axis, the expected beam position change at the IP is shown in Fig. 6.17. The sub-micrometer vertical position change makes the evaluation of the vertical magnetic center challenging even when using the IPBPM. In addition, during the BBA at ATF2, due to a large horizontal beam jitter, the x position resolution was estimated to ≈ 2 μm after calibration, while the y position resolution was approximately 200 nm. In order to accurately evaluate the x and y magnetic center by looking only at the y beam position measured by the IPBPMs, the horizontal and vertical scans of the octupole were per-

Table 6.7: OCT1FF and OCT2FF transverse offset tolerances

Magnet	x [μm]	x [μm]
OCT1FF	130	23
OCT2FF	250	90

formed with a constant offset Δy and Δx, respectively, of +1 mm. When the normal

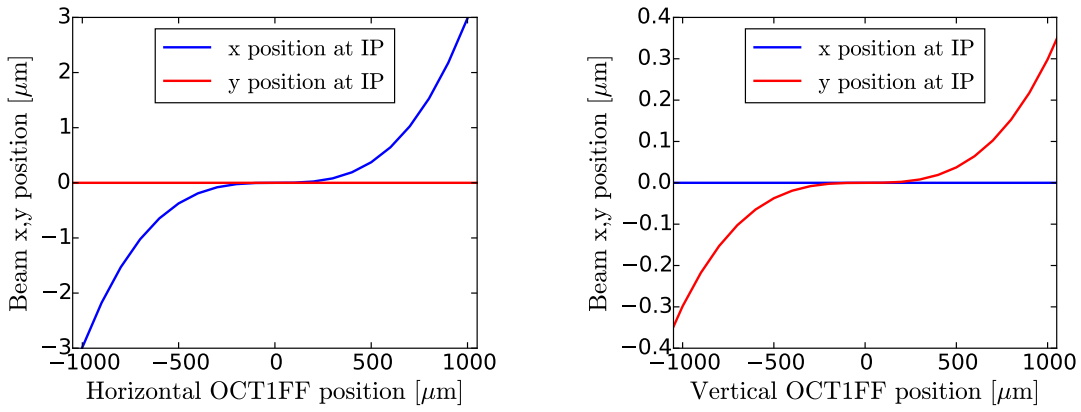

Figure 6.17: Left: simulations of the horizontal beam position at the IP when OCT1FF is set to 50 A and is horizontally displaced; Right: simulations of the vertical beam position at the IP when OCT1FF is set to 50 A and is vertically displaced.

octupole is moved both horizontally and vertically the deflection of the particles is given by:

$$\Delta x'_{\text{octupole}} = \frac{K_{3N}}{6}\left[3(x+\Delta x)(y+\Delta y)^2-(x+\Delta x)^3\right] \tag{6.11}$$

$$= \overbrace{\frac{K_{3N}}{6}(3xy^2-x^3)}^{\text{Normal octupole}} - \overbrace{\frac{K_{3N}}{6}(x^2-y^2)\Delta x}^{\text{Normal sextupole}} + \overbrace{K_{3N}y\Delta x\Delta y}^{\text{Skew quadrupole}} + \overbrace{\frac{K_{3N}}{2}\Delta y^2\Delta x}^{\text{Dipole}}$$

$$+ \overbrace{K_{3N}xy\Delta y}^{\text{Skew sextupole}} + \overbrace{\frac{K_{3N}}{2}x\Delta x^2}^{\text{Normal quadrupole}} + \overbrace{\frac{K_{3N}}{2}x\Delta y^2}^{\text{Normal quadrupole}} - \overbrace{\frac{K_{3N}}{6}\Delta x^3}^{\text{Dipole}}$$

$$\Delta y'_{\text{octupole}} = \frac{K_{3N}}{6}\left[3(x+\Delta x)^2(y+\Delta y)-(y+\Delta y)^3\right] \tag{6.12}$$

$$= \overbrace{\frac{K_{3N}}{6}(3x^2y-y^3)}^{\text{Normal octupole}} + \overbrace{\frac{K_{3N}}{6}(x^2-y^2)\Delta y}^{\text{Skew sextupole}} + \overbrace{K_{3N}xy\Delta x}^{\text{Normal sextupole}} + \overbrace{K_{3N}x\Delta x\Delta y}^{\text{Skew quadrupole}}$$

$$+ \overbrace{\frac{K_{3N}}{2}y\Delta x^2}^{\text{Normal quadrupole}} + \overbrace{\frac{K_{3N}}{2}\Delta x^2\Delta y}^{\text{Dipole}} - \overbrace{\frac{K_{3N}}{2}y\Delta y^2}^{\text{Normal quadrupole}} - \overbrace{\frac{K_{3N}}{6}\Delta y^3}^{\text{Dipole}}$$

Table 6.8: Horizontal OCT1FF magnetic center measured by the IPBPMs

Cavity	OCT1FF x position [μm]
IPBPM-A	227 ± 93
IPBPM-B	326 ± 150
IPBPM-C	83 ± 96

Table 6.9: Vertical OCT1FF magnetic center measured by the IPBPMs

Cavity	OCT1FF y position [μm]
IPBPM-A	-157.5 ± 14
IPBPM-B	-176.7 ± 23
IPBPM-C	-156.5 ± 22

The beam position at the IPBPMs caused by the offset octupole is given by:

$$\Delta x^{\text{IPBPMs}} = \text{R}_{12}^{\text{octupole}\rightarrow\text{IPBPMs}}\Delta x'_{\text{octupole}} \quad (6.13)$$

$$\Delta y^{\text{IPBPMs}} = \text{R}_{34}^{\text{octupole}\rightarrow\text{IPBPMs}}\Delta y'_{\text{octupole}} \quad (6.14)$$

The expected vertical beam position change at each IPBPM from simulation is shown in the left plot of Fig. 6.18. In this simulation, as performed during the BBA measurements at ATF2, the vertical waist has been placed at equal distance from IPBPM-A and IPBPM-C. The right plot of Fig. 6.18 shows the position measurements. The fitted magnetic centers of the BBA measurements from the three IPBPMs are summarized in Table 6.8. The OCT1FF was moved by 185 μm, the horizontal magnetic center calculated as the weighted mean position given by the measurements of the 3 IPBPMs. The left plot of Fig. 6.19 shows the expected vertical beam position change at each IPBPM from simulations and the right plot shows the measured positions. The results are encapsulated in Table 6.9. The OCT1FF was moved to its calculated vertical magnetic center by -161 μm.

6.3.3 $25\beta_x^* \times 0.25\beta_y^*$ optics tuning measurements at ATF2

6.3.3.1 Choice of the β_x^* for the ultra-low β_y^*

The experimental tuning work on the ultra-low β_y^* performed in 2017 in the framework of this thesis, follow previous studies performed in 2016 [100, 104] on optics that provide a β_y^* reduced by a factor two from the nominal value. In February 2016, a week of beam operation has been dedicated for the first time to explore the potential of lower β_y^* optics at ATF2. The so-called "half β_y^*" optics ($\beta_y^* = 50$ μm) has been applied in the machine for which two β_x^* has been tested, the $10\beta_x^* \times 0.5\beta_y^*$ ($\beta_x^* = 40$ mm) and $25\beta_x^* \times 0.5\beta_y^*$ ($\beta_x^* = 100$ mm) optics. Both tuning simulations and experimental tuning results of the half β_y^* optics agree on the better tuning performance of the FFS for the $25\beta_x^*$ option compared to the $10\beta_x^*$ one. The minimum beam size achieved at ATF2 for

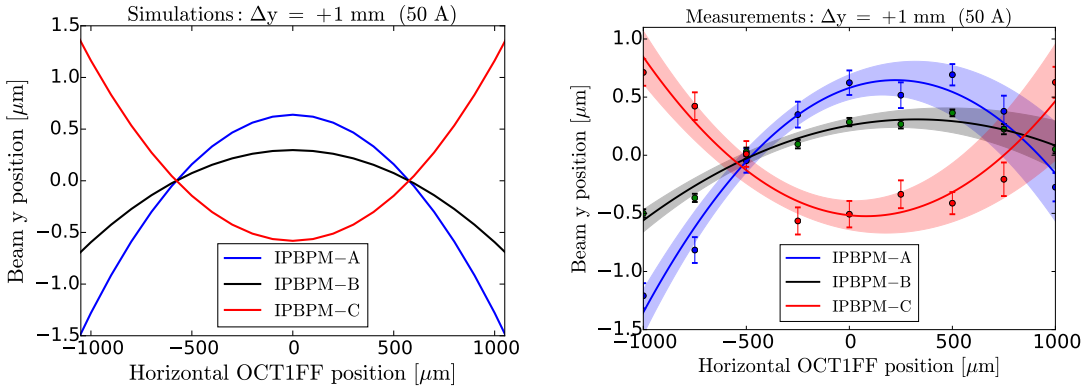

Figure 6.18: Left: Simulations of the vertical beam position at IPBPMs A,B and C when OCT1FF is set to 50 A and is horizontally displaced with a constant vertical offset $\Delta y = +1$ mm; Right: Measurements at ATF2 for the same configuration.

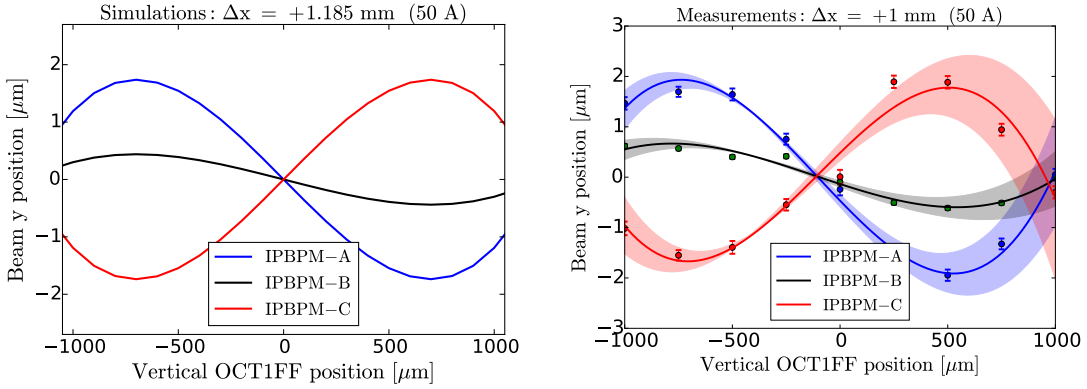

Figure 6.19: Left: Simulations of the vertical beam position at IPBPMs A,B and C when OCT1FF is set to 50 A and is vertically displaced with a constant horizontal offset $\Delta x = +1$ mm; Right: Measurements at ATF2 for the same configuration.

the $10\beta_x^* \times 0.5\beta_y^*$ optics is 58 ± 5 nm and 51 ± 6 nm for the $25\beta_x^* \times 0.5\beta_y^*$ optics. The complete study performed on this optics is described in [100, 104]. The amplified magnetic imperfections such as multipolar errors [42] and fringe field [103] in high-β regions, together with orbit deviations, are the main suspected IP beam size limitations for lower β_y^*. The linear approximation of the vertical beam size along the ATF2 FF beamline for lower β_y^* optics is shown in Fig. 6.20. As discussed in Section 6.2, the nominal optics for ATF2 operates with $10\beta_x^*$ to reduce the effect of multipole field errors to be comparable to the tolerances of the ILC FFS. The study on the multipolar field tolerances comparison between the $1\beta_x^* \times 1\beta_y^*$, $10\beta_x^* \times 1\beta_y^*$ and ILC is given in [54]. For the ultra-low β_y^* optics, the FD multipolar field error tolerances are much tighter

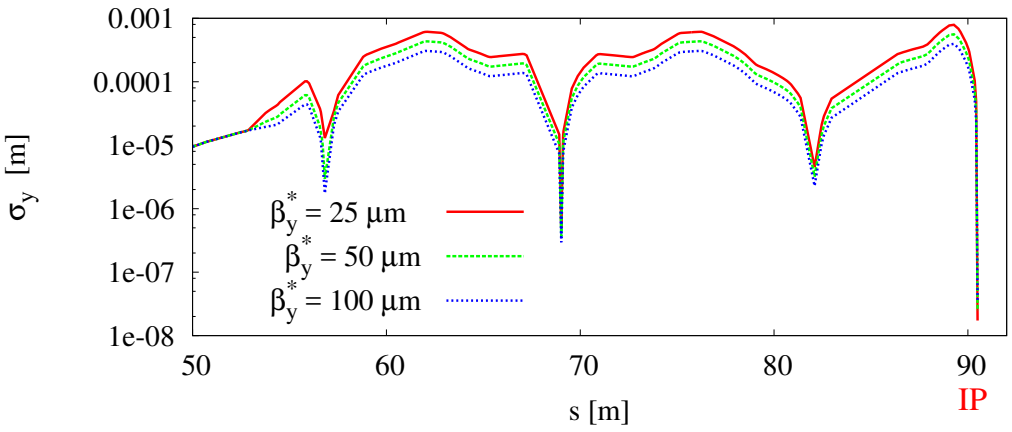

Figure 6.20: Vertical beam size along the FF beamline for $\beta_y^* = 100$, 50 and 25 μm.

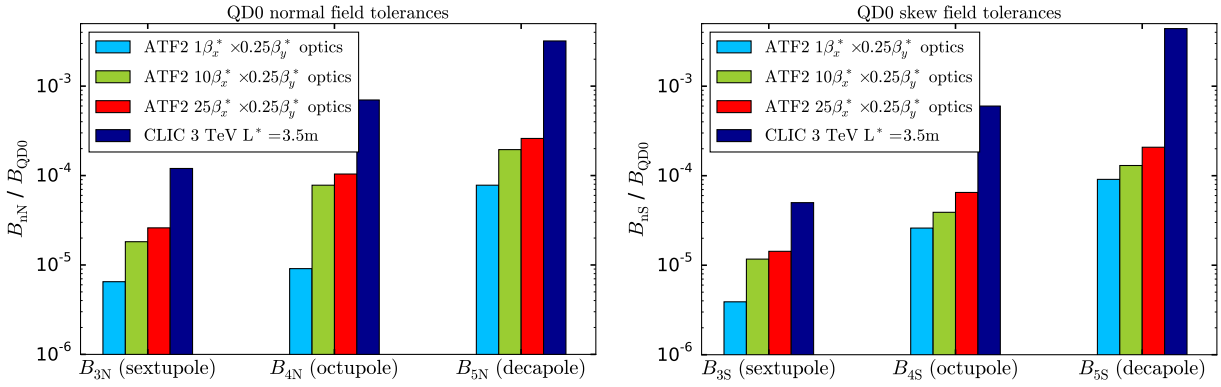

Figure 6.21: QD0 normal (left) and skew (right) sextupole, octupole and decapole field error tolerances for different β_x^* options of the ultra-low β_y^* optics

than for the $10\beta_x^*$ nominal optics, ILC or even CLIC. The optics chosen for tuning at ATF2, during December 2017 and February 2018 operations, is the $25\beta_x^* \times 0.25\beta_y^*$ in order to bring the FD multipolar tolerances of the system closer to the CLIC ones as shown in Fig. 6.21 and Fig. 6.22. The tolerances are defined as the error required to induce a 2% IP vertical beam size growth, measured at a bore radius of 1 cm for ATF2 lattices. Even for the β_x^* option of 100 mm, the FD tolerances are tighter than for CLIC for most of the multipole terms. However, increasing the horizontal beam size at the IP is limited as it becomes comparable or greater than the Shintake laser Rayleigh range, leading to undesired interactions of the divergent laser beam with the e^- and therefore compromising the measurement of the vertical beam size [23]. Also, the very flat beam at the IP with larger σ_x^* and $\beta_y^* = 0.25$ μm, makes the measurement of the vertical beam size more sensitive to couplings at the IP.

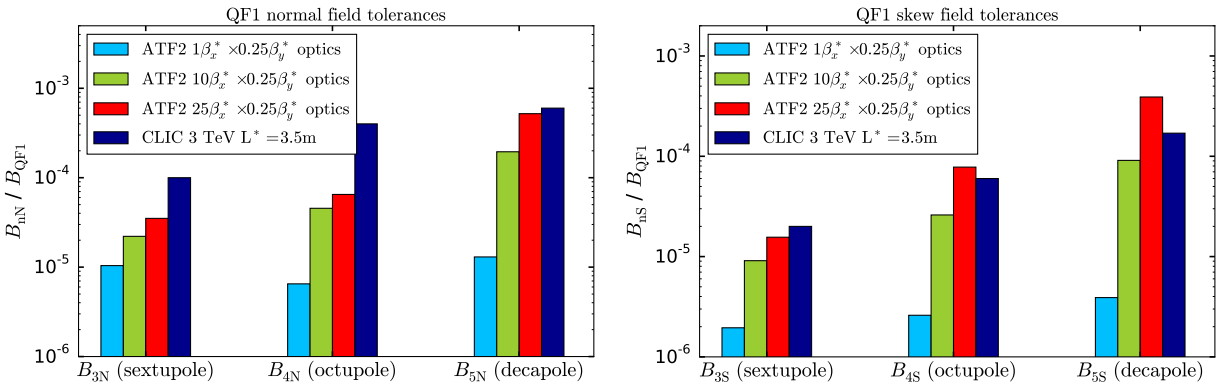

Figure 6.22: QF1 normal (left) and skew (right) sextupole, octupole and decapole field error tolerances for different β_x^* options of the ultra-low β_y^* optics

During the last week of operation in December 2017, 8 consecutive shifts (64 hours in total) were dedicated to the tuning of the $25\beta_x^* \times 0.25\beta_y^*$ optics. Despite the long beam tuning, allowing multiple iterations of linear and nonlinear knobs, the vertical beam size could not be reduced enough to observe clear modulation at 174 degree mode with the Shintake monitor ($\sigma_y^* \sim$ 90-100 nm). From the lessons learnt about the applied optics during December 2017 operation, new optics have been optimized for a second tuning attempt in February 2018. A detailed description of the experimental tuning results performed during these two tuning campaigns is given in the following sections.

6.3.3.2 Machine tuning: December 2017

The ultra-low β_y^* optics applied in December 2017 was calculated the same way as for the calculation of the half-β_y^* optics tuned in February 2016 [100] by using the optics matching tool available in the ATF2 control room. The matching quadrupoles from QM16FF to QM11FF, the 2 upstream quadrupoles QF21X and QD20X and the FD strengths are varied to match the constraints on $\beta_{x,y}^*$, $\alpha_{x,y}^*$ and $\eta_{x,y}^*$. For the initial $25\beta_x^* \times 0.25\beta_y^*$ optics, the calculated current needed for the QM14FF magnet was too large to be set. Therefore two more upstream magnets in the extraction line QF18X and QD19X were used to match the ultra-low β_y^* optics. Several iterations of optics changes were needed due to discrepencies between the target $\beta_{x,y}^*$ set in the optics matching calculator and the measurements. After each optics change, the horizontal and vertical dispersions are corrected using QF1X-QF6X knobs and the QS1X-QS2X knob respectively (see Section 6.3.1). The multi-OTR used in previous operations to measure and correct the vertical emittance ε_y in the matching section of the FF beamline could not be used during both ultra-low β_y^* tuning operations because 2 of the 4 OTRs were broken. The vertical emittance was thus measured upstream in the damping ring but could not be corrected at the entrance of the FFS. The measured emittance in the DR of $\varepsilon_y = 12.9$ pm was assumed for the evaluation of the β_y^* value. The measured β_y^* obtained from the

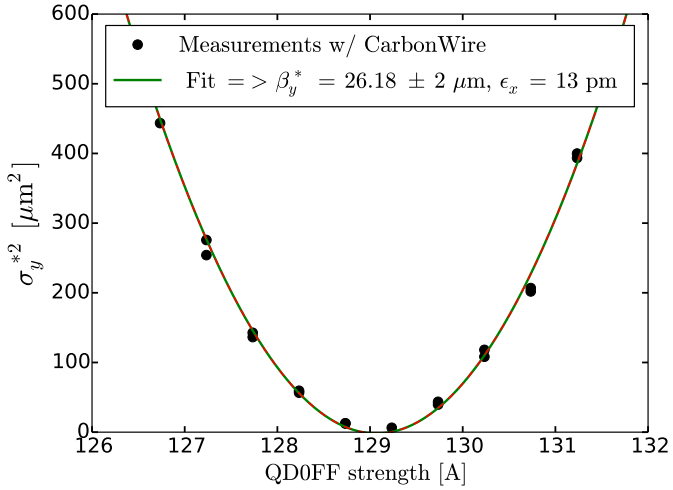

Figure 6.23: QD0FF strength scan for β_y^* measurement using the ATF2 carbon wire at the IP. β_y^* measured in December 2017.

fit of the QD0FF strength scan is shown in Fig 6.23. The measured squared divergence was $\varepsilon_y/\beta_y^* = (4.98 \pm 0.05).10^{-7}$ which gives $\beta_y^* = 26 \pm 2$ μm. The horizontal β could not be matched as well as for the vertical one. The measured β_x^* by scanning QF1FF was approximately 80 mm. Large residual horizontal dispersion was measured at the IP with $\eta_x^* = 34.5$ mm. The residual η_x^* strongly bias the horizontal emittance ε_x^* and β_x^* evaluated by the QF1FF scan. Due to time constraints, no further corrections on ε_x^* and β_x^* has been applied to match the design value.

After optics matching and dispersion correction, linear and 2$^{\text{nd}}$ order knobs are applied

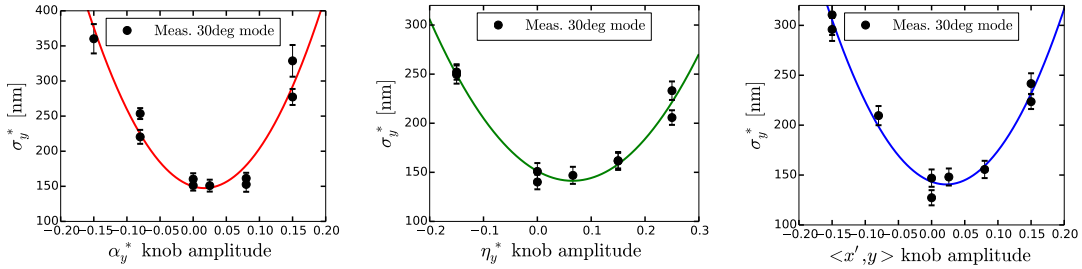

Figure 6.24: Examples of linear knob scans (vetical waist α_y^*, dispersion η_y^* and coupling $< x', y >$) performed during the ultra-low β_y^* tuning (Dec.17) at 30 degree mode with the Shintake monitor.

iteratively and the beam sizes are measured by the Shintake monitor starting from the 6.4 degree mode up to 174 degree mode. The strength of the normal and skew sextupoles optimized for the $25\beta_x^* \times 0.25\beta_y^*$ optics using PTC and MAPCLASS codes, were implemented in the machine before the tuning. Examples of the linear knobs correcting α_y^*, η_y^* and coupling $< x', y >$ are shown in Fig. 6.24. Examples of the 2$^{\text{nd}}$ order knobs

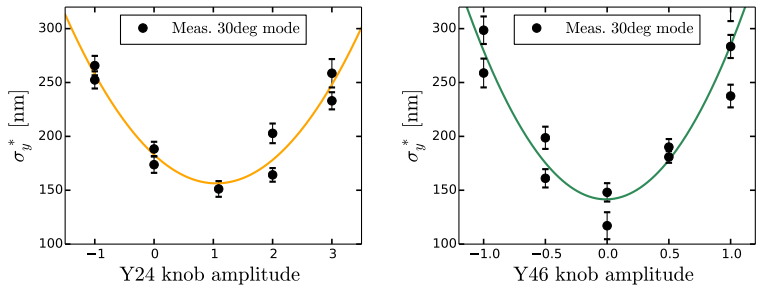

Figure 6.25: Examples of 2nd order knob scans (using the 5 normal sextupoles) performed during the ultra-low β_y^* tuning (Dec.17) at 30 degree mode with the Shintake monitor, where Y_{24} corresponds to $T_{yx'y'}$ and Y_{46} corresponds to $T_{yy'\delta}$

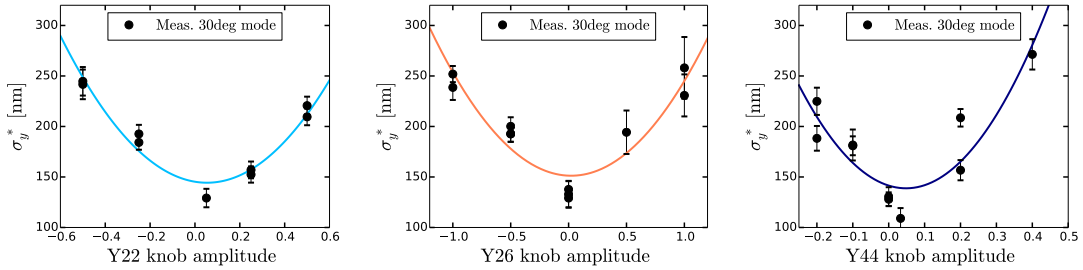

Figure 6.26: Examples of 2nd order knob scans (using the 4 skew sextupoles) where Y_{22} corresponds to $T_{yx'x'}$, Y_{26} corresponds to $T_{yx'\delta}$ and Y_{44} corresponds to $T_{yy'y'}$

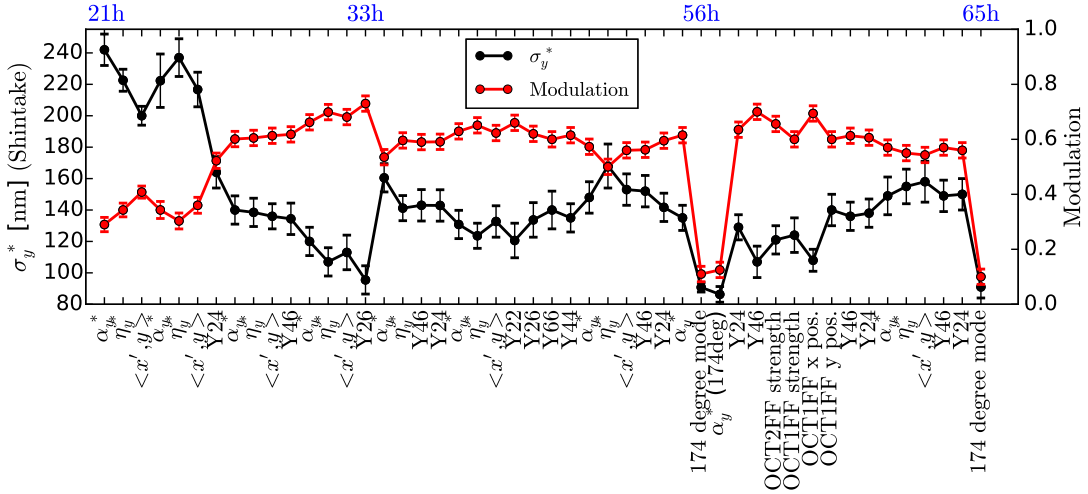

Figure 6.27: Vertical beam size σ_y^* and modulation after each knob scan, measured at 30 and 174 degree mode during the last 5 shifts of tuning operation.

constructed from the normal sextupoles (for $T_{yx'y'}$ and $T_{yy'\delta}$ aberration correction) and from the skew sextupoles (for $T_{yx'x'}$, $T_{yx'\delta}$, $T_{yy'y'}$ and $T_{y\delta\delta}$ aberration correction) applied during the tuning are shown in Fig. 6.25 and Fig. 6.26. The evolution of the vertical beam size after each knob is applied during the last 5 shifts of machine tuning is shown in Fig. 6.27. Most of the knobs were applied by measuring beam size at 30 degree mode. There were two unsuccessful attempts to observe modulation at 174 degree mode with $M \geq 0.1$. The modulation at 174 degree mode was too small to perform linear or nonlinear corrections. The octupoles were switched on when observing beam sizes at 30 degree mode. However the expected impact of the octupoles on the vertical beam size, from simulation, is comparable to the resolution of the beam size measurement at 30 degree mode and therefore should be used for 3$^{\text{rd}}$ order aberration correction only when measuring beam size at 174 degree mode. The minimum beam size observed at 30 degree mode was $\sigma_y^* = 97 \pm 6$ nm, but the average vertical beam size during the tuning at 30 degree mode was $\sim$135 nm.

6.3.3.3 Discussion on the measurements of December 2017

The large beam size observed during the tuning of the $0.25\beta_y^*$ optics can come from various machine imperfections: bad orbit control, larger contribution from wakefields combined with orbit jitter, larger contributions from the multipolar field, nonlinear aberrations and magnet alignment error. The absence of the multi-OTR for the emittance correction at the entrance of the FFS can also strongly limit the tuning performance. The misalignment of the sextupoles does not explain such vertical beam size growth as the beam based alignment of the normal and skew sextupoles was done the week before, reducing the impact of the feed-down quadrupole field. However, as shown in the simulation discussed in Section 6.2, the impact of the 2$^{\text{nd}}$ order aberrations, for $\beta_y^* = 25$ μm, is much stronger than for the nominal optics. It is therefore important to match the normal and skew sextupole strengths with the applied optics to avoid large 2$^{\text{nd}}$ order beam size contributions.

Although it was not possible to perform 3$^{\text{rd}}$ order correction using the octupoles at 30 degree mode, the OCT1FF still brought out important informations about the applied optics. The OCT1FF was set to its maximum current of 50 A and scanned horizontally and vertically around their respective reference position measured during the octupole BBA (see Section 6.3.2.2). The beam sizes recorded by the Shintake monitor at 30 degree mode while scanning the OCT1FF are shown in Fig. 6.28. For the horizontal scan (left plot), despite the spread of the measurements, one can observe that the beam size tends to decrease for very large positive OCT1FF offset and the range of the mover was not large enough to fit the position of the minimum beam size. On the other hand, the vertical scan (right plot), shows minimum beam size for an OCT1FF offset of 235 $\pm$44 μm. When a horizontal or vertical offset is applied to OCT1FF, it generates feed-down to normal or skew sextupole field, respectively, propagated to the IP. OCT1FF is located in high-β, high-η_x regions and separated from the IP by a $\frac{\pi}{2}$ phase advance. The horizontal scan of Fig. 6.28 suggests that important contributions from $T_{yx'y'}$ and/or $T_{yy'\delta}$ are being

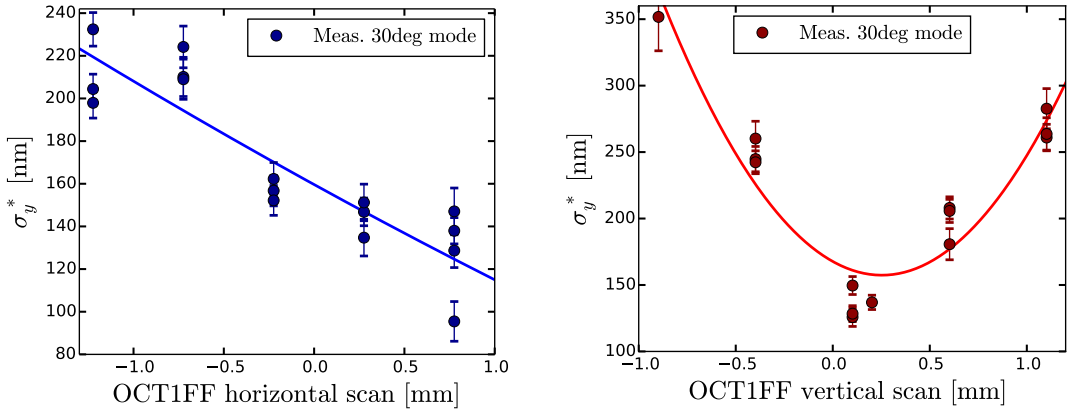

Figure 6.28: Left: OCT1FF horizontal position scan at maximum current (50 A) versus σ_y^*; Right: OCT1FF vertical position scan at 50 A. Measurement taken at 30 degree mode at ultra-low β_y^* optics (Dec. 17).

corrected by the offset octupole. The vertical scan suggests smaller contributions from $T_{yx'x'}$, $T_{yx'\delta}$, $T_{yy'y'}$ and/or $T_{y\delta\delta}$. This study tends to indicate that the normal sextupole strengths calculated for the $25\beta_x^* \times 0.25\beta_y^*$ lattice do not match the applied optics.

In June 2017, a very similar study with OCT1FF has been performed on the $10\beta_x^*$

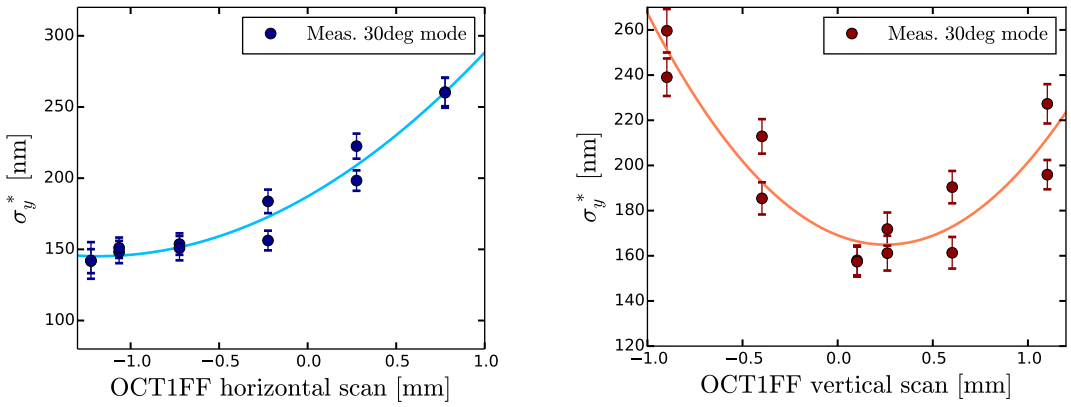

Figure 6.29: Left: OCT1FF horizontal position scan at maximum current (50 A) versus σ_y^*; Right: OCT1FF vertical position scan at 50 A. Measurement taken at 30 degree mode at $10\beta_x^* \times 1\beta_y^*$ optics (Jun. 2017).

$\times 1\beta_y^*$ lattice. At this time, no modulation at 174 degree mode could be observed with the nominal optics. The horizontal and vertical scans taken when measuring beam size at 30 degree mode are shown in Fig. 6.29. The minimum beam size was found for an horizontal offset of OCT1FF of -1.11±0.24 mm. For the vertical scan, the minimum beam size was found for an offset of 262±67 μm. From these measurements, the same conclusion as for the $25\beta_x^* \times 0.25\beta_y^*$ lattice about the optics mismatched have been drawn.

Therefore, during the next operation in November 2017, the ATF2 team in charge of the tuning of the nominal optics, performed corrections on the $10\beta_x^* \times 1\beta_y^*$ lattice in order to have a better match of the sextupoles with the applied optics. After the optics change, modulations could be observed at 174 degree mode, with beam sizes around 60 nm, and the OCT1FF scan has been reiterated. In order to have a better resolution on the beam size measured at 174 degree mode and observe the effect of transverse offset of the octupoles, OCT1FF was set to 10 A during the scan. The strength scan performed on the OCT1FF (see left plot of Fig. 6.30), shows the important impact of this strong octupole on the beam size. In contrary, OCT2FF has very small impact on the beam size even when set to its maximum current of 50 A (see right plot of Fig. 6.30). Both octupole strength scans suggest beam size reduction for negative current. As the polarity of the octupoles cannot be reversed remotely from the control room and due to time constraints, the octupole strength were not scanned during this shift for negative currents. The results of the transverse offset scans for OCT1FF are presented in Fig. 6.31 and show smaller 2$^{\text{nd}}$ order corrections. For the horizontal OCT1FF scan on the $10\beta_x^* \times 1\beta_y^*$ lattice, the minimum beam size was found for a smaller offset of 250 $\pm$60 μm. The minimum beam size for the vertical scan was observed at the magnetic center. These results suggest a better matching between the linear optics and the applied sextupole strengths than during June 2017 operation.

From the observations made after the octupole studies performed in June, November

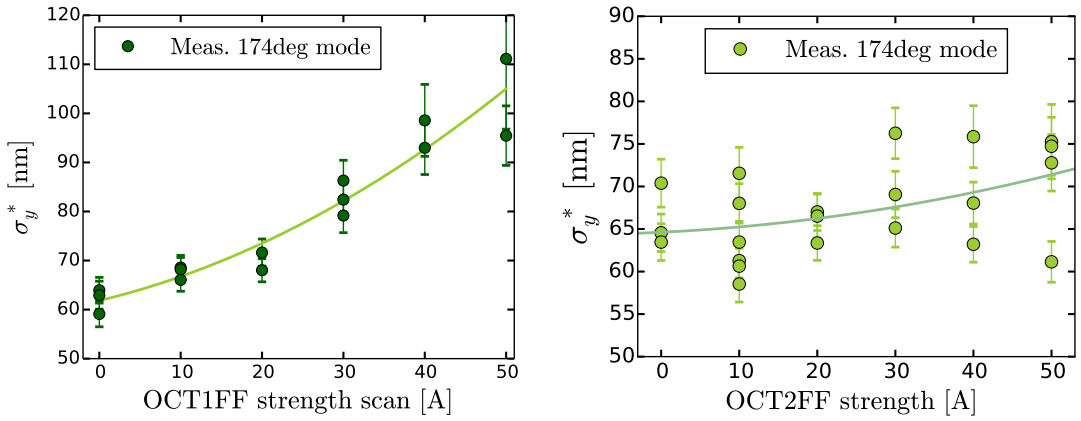

Figure 6.30: Strength scan of OCT1FF performed on the $10\beta_x^* \times 1\beta_y^*$ lattice at 174 degree mode (Nov. 2017).

and December 2017, it has been decided to re-optimize the $25\beta_x^* \times 0.25\beta_y^*$ optics, using the MADX code and taking into account the matching quadrupole strength constraints of the machine. The newly optimized optics has been applied to the ATF2 machine for the 2$^{\text{nd}}$ low-β_y^* tuning attempt in February 2018.

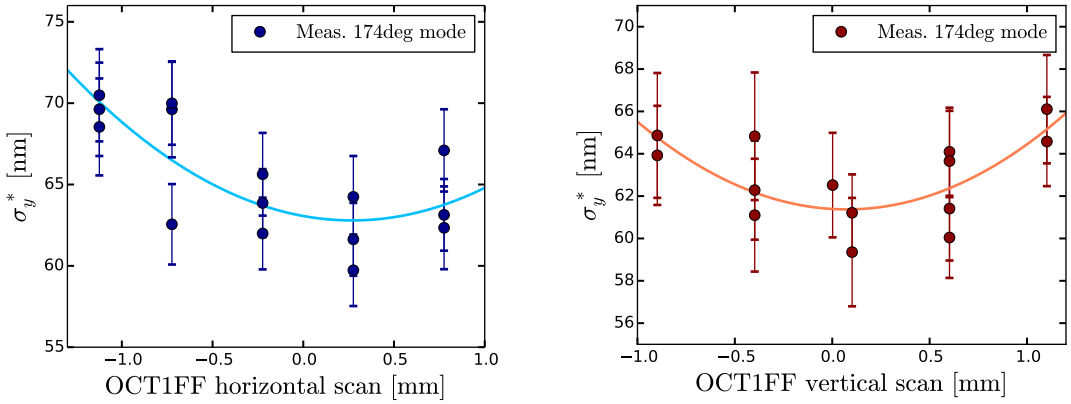

Figure 6.31: Left: OCT1FF horizontal position scan at 10 A versus σ_y^*; Right: OCT1FF vertical position scan at 10 A. Measurement taken at 174 degree mode at $10\beta_x^* \times 1\beta_y^*$ optics after optics correction (Nov. 17).

6.3.3.4 Machine tuning: February 2018

In order to assure a better 2$^{\text{nd}}$ order correction of the ultra-low β_y^* optics at ATF2, all the quadrupole and sextupole strengths coming from the updated MADX model of the $25\beta_x^* \times 0.25\beta_y^*$ optics have been applied in the machine. This lattice model is available in [113]. As the multi-OTR was still not working, the emittance could not be corrected in the matching section and was measured in the DR with $\varepsilon_y = 12.7$ pm. After applying the $25\beta_x^* \times 0.25\beta_y^*$ optics in the machine, the horizontal and vertical dispersion were corrected as shown in Figs. 6.32 and 6.33, respectively. In order to check that the QD0FF scan for the vertical divergence measurement was not biased by <x,y> coupling which would lead to an over estimation of the measured divergence, a quick scan of the QS1X-QS2X difference knob was performed. When QS1X and QS2X are powered with equal amplitude and opposite polarity, referred to as the QS difference knob, they generate pure <x,y> coupling without vertical dispersion [114]. The QS difference knob scan applied on the ultra-low β_y^* optics is shown in Fig. 6.34. The minimum squared vertical divergence was $\varepsilon_y/\beta_y^* = (5.13 \pm 0.05)\ 10^{-7}$ which corresponds to $\beta_y^* = 25.3 \pm 2\ \mu$m (see left plot of Fig. 6.35). For the QF1FF scan, the residual horizontal dispersion has been measured and removed from the the measured beam sizes. The residual dispersion at the IP was $\eta_x^* = 3$ mm. The measured β_x^* was 103 $\pm$4 mm and the horizontal emittance $\varepsilon_x^* = 1.7 \pm 0.2$ nm (see right plot of Fig. 6.35).

Multiple issues appeared during the tuning programme, such as very large background to be corrected using the ATF2 collimators (due to the larger beam size along the beamline with the low β_y^* optics), charge drift coming from temperature variation caused by the cooling system and Shintake laser stability and timing tuning. Finally after mathcing the optics, there were only 1.5 shifts left for beam size tuning using the Shintake monitor. Only linear knobs were applied and were sufficient to reduce the beam size enough to

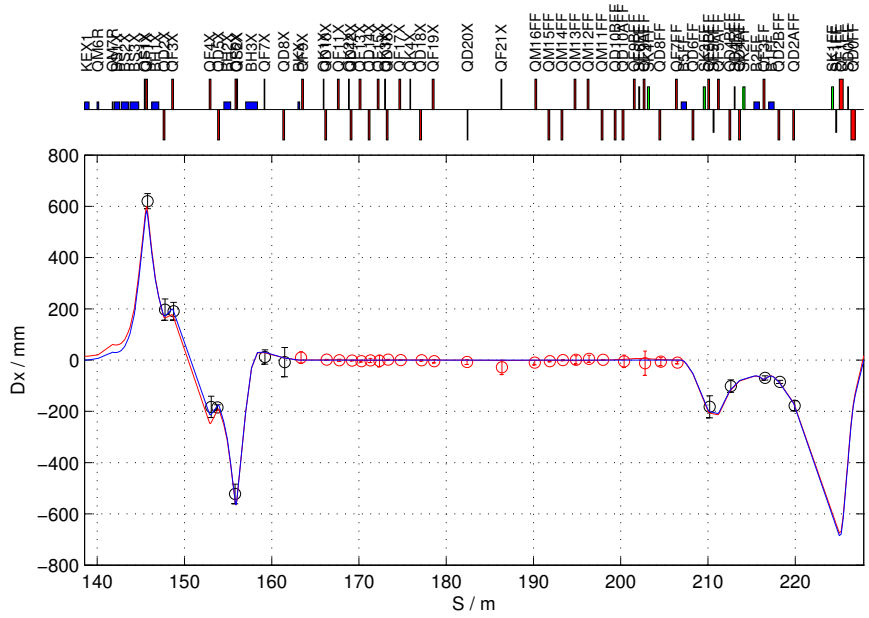

Figure 6.32: Horizontal dispersion measurement after correction, using QF1X and QF6X strength scan, on the 25 β_x^* × 0.25 β_y^* optics.

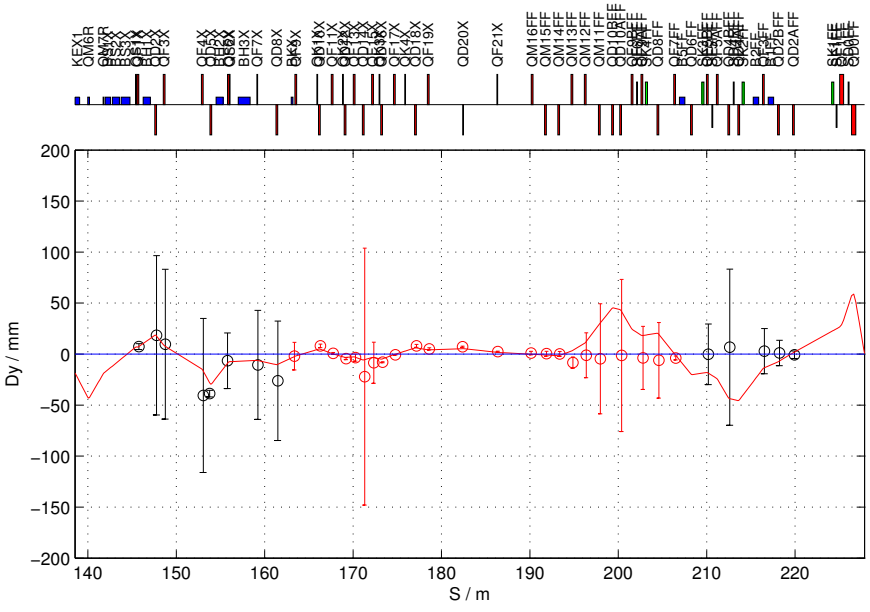

Figure 6.33: Vertical dispersion measurement after correction, using QS1X-QS2X knob, on the 25 β_x^* × 0.25 β_y^* optics.

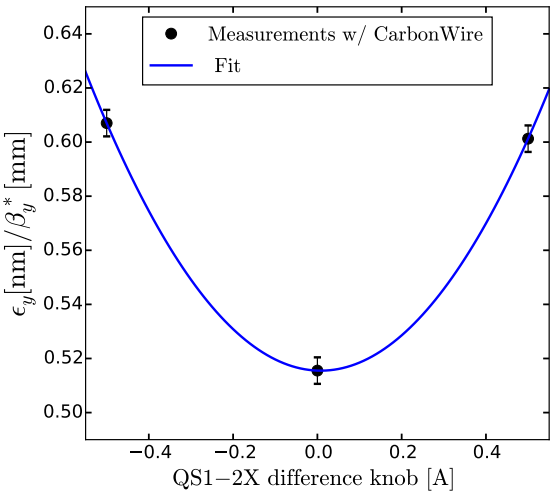

Figure 6.34: Divergence squared, measured after QD0FF scan, versus QS1X-QS2X difference knob (February 2018).

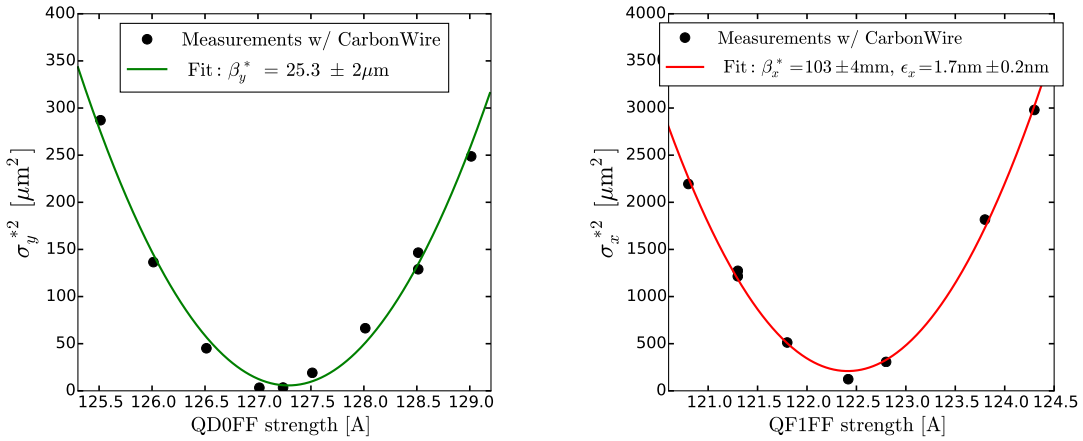

Figure 6.35: QD0FF and QF1FF strength scan for $\beta^*_{x,y}$ measurement using the ATF2 carbon wire at the IP. (February 2018).

observe clear modulation at 174 degree mode. The modulation and corresponding beam size after each knob applied during the tuning programme is shown in Fig. 6.36. The average vertical beam size observed, without octupoles and 2$^{\text{nd}}$ order knobs applied, was σ^*_y = 70 ±6 nm and the beam size was stable around this value when tuning at at 174 degree mode.

6.3.4 Discussion on the measurements of February 2018

During the second tuning attempt of the 25 β^*_x × 0.25 β^*_y FF lattice, the performance of the system in terms of beam size achieved was improved despite the shorter tuning

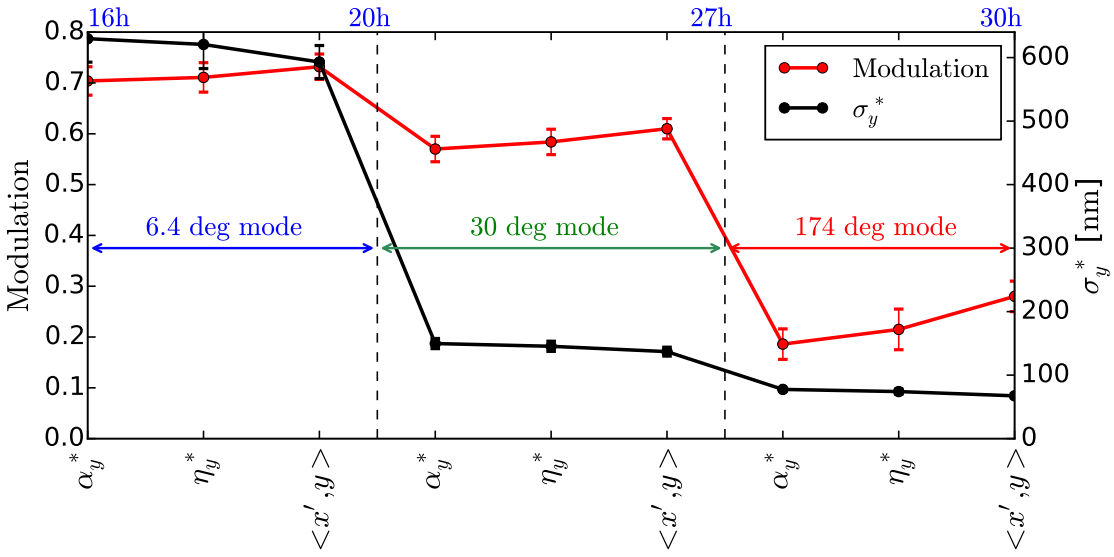

Figure 6.36: Vertical beam size σ_y^* and modulation after each knob scan, measured at 6.4, 30 and 174 degree mode during the last 1.5 shifts of the tuning operation (February 2018).

time and the fact that no octupoles were used and no nonlinear knobs were applied. These results highlight the supicions raised during the last operations about the applied optics. The tuning performance of the updated lattice optimized for the February run could be further improved if more tuning time is allocated on this optics. The use of all the 2$^{\text{nd}}$ order sextupole knobs are needed to achieve beam sizes below 30 nm (see Section 6.2). Furthermore, as it has been demonstrated that modulation can be observed at 174 degree mode with this optics, it will be possible during future operations, to use and optimize the octupoles for 3$^{\text{rd}}$ order correction on the IP beam size. In to expand and ease the 3$^{\text{rd}}$ order aberration corrections of the octupoles, their polarities should be controllable remotely for future tuning operations. Regarding the octupoles locations, simulations on the lower β_y^* optics show that for correcting the dominant 3$^{\text{rd}}$ order aberrations U_{3224} and U_{3246}, the most upstream octupole from the IP is the strongest. In the present situation at ATF2, OCT1FF is the strongest octupole but is located closer to the IP, where the required octupole field is weaker. This situation was kept unchanged during ultra-low β_y^* tuning operations as the design octupole strengths could be applied, but with OCT2FF set close to its maximum current. In order to allow a wider tuning range for the most upstream octupole and to be more consistent with the design model, OCT2FF and OCT1FF locations should be swapped.

The last tuning session ends on an incomplete tuning study for the exploration of the ultra-low β_y^* performance. Nevertheless, these studies have opened the path towards measuring smaller beam size using the ultra-low β_y^* optics at ATF2 for future opera-

Table 6.10: Summary of the run operations for different optics between 2016 and 2018 at ATF2. Beam size measured with a charge of $\sim 1 \times 10^9$.

Optics	run date	Minimum σ_y^* [nm]	Comments
10 β_x^* × 1 β_y^*	16/02/05	47±6	-
10 β_x^* × 0.5 β_y^*	16/02/22	58±5	-
25 β_x^* × 0.5 β_y^*	16/02/25	55±6	-
10 β_x^* × 1 β_y^*	16/03/10	41±2	2 bunch mode
10 β_x^* × 1 β_y^*	16/05/20	75±10	-
10 β_x^* × 1 β_y^*	16/06/16	69±5	-
10 β_x^* × 1 β_y^*	16/11/24	60±5	-
10 β_x^* × 1 β_y^*	16/12/01	74±9	-
10 β_x^* × 1 β_y^*	17/02/15	82±14	-
10 β_x^* × 1 β_y^*	17/06/15	89±14	mOTR non-operational
10 β_x^* × 1 β_y^*	17/12/08	63±4	mOTR non-operational + correction of the matching optics
25 β_x^* × 0.25 β_y^*	17/12/14	97±6	mOTR non-operational + bad optics matching
25 β_x^* × 0.25 β_y^*	18/02/22	70±6	mOTR non-operational + correction of the matching optics w/o 2nd order knobs and octupoles

tions. Tuning the ATF2 final focus beamline is a time consuming process. Indeed, each vertical beam size measured by the Shintake monitor takes approximately 3 minutes and many data points are needed when applying linear and nonlinear knobs in order to minimize the beam size errors and to apply the right knob amplitude for the correction. The tuning of the Shintake monitor (changing between various modes, laser paths, timings, waist, etc.), especially for the 174 degree mode, also takes a good fraction of the tuning time allocated. The tuning time is critical for a dynamic system such as ATF2. The multi-OTR is a key ingredient for the tuning and it is being fixed and will be available from the next run. It will allow the minimization of coupling and emittance correction at the entrance of the FFS. The twiss parameters can be reconstructed at the OTR locations which allows fine tuning of the extraction and matching quadrupole to bring the system closer to the design optics if needed. A complete tuning session on the $0.25\beta_y^*$ optics, by applying all available correctors, is necessary to quantify the contributions of the 3rd order aberrations with a proper study of the octupoles at 174 degree mode. The Table 6.10 summarizes the experimental results obtained at ATF2 for various optics during the past two years. The standard tuning procedure (optics matching, dispersion correction, emittance and coupling correction using the multi-OTR, linear and nonlinear

corrections using the normal and skew sextupoles), has been proven to be efficient for beam size reduction. The larger beam size observed for the nominal β_y^* optics seems to be correlated with absence of the multi-OTR, as the jitter conditions were similar during past and recent operations [115]. The tuning of ultra-low β_y^* in February 2018 may have suffered from the non-correction of the emittance and couplings in the matching section in addition to a lack of nonlinear corrections (2^{nd} order sextupole knobs and octupoles). Tuning the ultra-low β_y^* optics is a very challenging task that requires long dedicated operation time and a more collaborative effort on this special optics in order to maintain optimal beam conditions in and upstream of the FFS and to keep the required diagnotics operational. Addressing other beam size limitations related to this optics, such as impact of wakefields, multipolar fields, orbit stabilization, magnet alignment errors and resolution limit of the Shintake monitor, are crucial to achieve the ATF2 goals and for the future linear colliders. A summary on the experimental results of the ultra-low β_y^* lattice tuning and the use of the octupoles for the ATF2 FFS, as well as recommandations for the future tuning sessions, based on the observations and experience gain during these tuning operations, are also given in Chapter 7.

Chapter 7

Conclusions

In this thesis, Final Focus System lattices for CLIC and for its test facility, ATF2, have been designed and optimized, based on local chromaticity correction scheme. Alternative FFS designs have been investigated for the first stage of CLIC at 380 GeV center of mass energy and for its top energy stage at 3 TeV c.o.m. Experimental work has been conducted on the ATF2 machine, at KEK, with the aim of validating and probing highly reduced β_y^* optics, already optimized in simulation. The comissioning and first tests in situ of the new pair of octupoles, manufactured at CERN and installed at ATF2, were performed and the main issues related to these magnets, for the improvement of future operations at ultra-low β_y^*, have been addressed.

The primary goal of this thesis was to optimize and address the expected performances, in simulation, of the CLIC 3 TeV FFS with a longer final focal length L*, allowing the removal of the strong final focusing quadrupole, QD0, from the CLIC experiment, thus simplifying the machine detector interface design. For this purpose, the CLIC FFS was re-optimized with a L* of 6 m based on the new proposed design for the CLIC detector named CLICdet. The larger chromaticity generated by the longer L^* design makes the goal of achieving luminosities above $\mathcal{L}_{\text{total}} = 5.9\times10^{34}\text{cm}^{-2}\text{s}^{-1}$ and $\mathcal{L}_{1\%} = 2\times10^{34}\text{cm}^{-2}\text{s}^{-1}$, more challenging than for the nominal design with $L^* = 3.5$ m. The luminosity performance of this lattice was maximized by optimizing β_y^* and the dispersion level along the FFS, identifying the main residual higher order aberrations responsible for the vertical beam size growth and correcting them by introducing the corresponding multipoles in the beamline. The maximum performance of the BDS after optimization is $\mathcal{L}_{\text{total}} = 6.4\times10^{34}\text{cm}^{-2}\text{s}^{-1}$ and $\mathcal{L}_{1\%} = 2.3\times10^{34}\text{cm}^{-2}\text{s}^{-1}$. The peak luminosity allows a comfortable budget of 15% for static and dynamic imperfections and is only 5% lower than for the nominal L^* design. Beam tracking simulations suggest that no tightening of the collimation depth is required for L* = 6 m FFS when the sytem is scaled in length w.r.t the increased L^*. The 1-beam tuning performance of the FFS with $L^* = 6$ m has been studied under realistic static error conditions. The main beam size contributions from the linear and 2$^{\text{nd}}$ order aberrations generated by the lattice imperfections have been identified and the corresponding correction knobs have been constructed. The results obtained are very close to the tuning goal and show that 85% of the machines simulated reach a total luminosity above 110% of the design luminosity after approximately 6300 luminosity measurements. By comparison with current tuning studies on the nominal design with L* = 3.5 m, no larger tuning difficulties are observed for the longer L* design. The 2-beam tuning performances including dynamic imperfections still need to be addressed.

In the interest of tunnel cost reduction, a set of shorter designs, for CLIC at 3 TeV with $L^* = 6$ m , have been fully optimized for FFS lengths reduced down to 495.7 m, comparable to the length of the nominal L^* FFS design. Additional changes on the FFS layout were needed to preserve the chromatic correction conditions of the Local scheme. While shorter FFS can achieve the required luminosity, their stronger sexupoles generates larger linear aberrations when misaligned and therefore degrade their tuning performances. The sextupoles could be weakened by increasing the dispersion along the FFS, however increasing the dipole strength is strongly limited by the synchrotron radiation emitted at 3 TeV. In addition, the stronger FD required for the shorter designs impose smaller apertures and therefore collimation depth may be a concern. From these observations, the longer FFS option, scaled in length w.r.t the increased of L^* from 3.5 m to 6 m ($L_{FFS} = 770$ m), remains the best candidate for the $L^* = 6$ m design.
A tuning-based design optimization for the FFS with $L^* = 3.5$ m has also been performed. The strategy was to reduce the sextupole strengths of the FFS by optimizing a set of longer systems, up to 770 m, in order to improve their tuning efficiency. The longer systems show comparable luminosity performanced after optimization. Tuning simulations have shown improved performances for longer designs when the FFS experiences transverse misalignment of its optics. Further tuning simulations, including roll and strength errors of the optics as well as dynamic imperfections, are still needed to more precisely quantify the benefit of longer FFS.

For the initial energy stage of CLIC at 380 GeV, two L^* options, of 4.3 m and 6 m for the BDS have been fully optimized and their tuning performances have been adressed. The luminosity performances for both L^* options fulfill the design requirements including 20% luminosity budget for static and dynamic imperfections. For $L^* = 4.3$ m, the achieved performances are $\mathcal{L}_{\text{total}} = 1.55\times10^{34}\text{cm}^{-2}\text{s}^{-1}$ and $\mathcal{L}_{1\%} = 0.93\times10^{34}\text{cm}^{-2}\text{s}^{-1}$. For $L^* = 6$ m, $\mathcal{L}_{\text{total}} = 1.52\times10^{34}\text{cm}^{-2}\text{s}^{-1}$ and $\mathcal{L}_{1\%} = 0.91\times10^{34}\text{cm}^{-2}\text{s}^{-1}$. The very comparable luminosities between the two L^* options comes from the additional pair of octupoles optimized for the $L^* = 6$ m lattice, that were not needed in the case of the $L^* = 4.3$ m design. The optics of the two L^* options were optimized to have their respective Main Linacs aligned with the CLIC 3 TeV ML in the CLIC tunnel. Both L^* designs fall closely to the tuning goal and show very similar tuning performances. For the $L^* = 4.3$ m lattice, there is 84% of the machines that reach design total luminosity and 85% for $L^* = 6$ m. The luminosity obtained for 90% of the machines is $\geq$92% and $\geq$96% of the design the luminosity, for $L^* = 4.3$ m and $L^* = 6$ m, respectively. The small luminosity gap needed to reach the tuning goal can be achieved with additional knob scans.

The performances of the long L^* option of 6 m, compared with the nominal designs with $L^* =$3.5 m or $L^* =$4.3 m, makes it a realistic candidate for CLIC. The luminosity performance comparisons between the two L^* options do not take into account the benefits of having QD0 outside of the experiment, such as QD0 vibration reduction, no field interplay between the solenoid of the detector and QD0 and increased detector forward acceptance. The proposed quadrupole-free detector FFS design is now strongly consid-

ered as the new baseline for CLIC 380 GeV and its upgrade to 3 TeV. The decision of moving to the long L* option has been based on the promissing performances of the new detector, CLICdet, and on the performances of the BDS with L* =6 m.

The ultra-low β_y^* optics study, conducted in the framework of the CLIC-like FFS feasibility tests, first consisted of simulations aiming to optimize and estimate the expected tuning performances of such reduced β_y^* optics ($\beta_y^* = 25$ μm) when using the new pair of octupoles, that were manufacted at CERN and installed in the ATF2 beamline. Experimental work was then carried out at KEK, with the aim of comissioning the newly installed octupoles, performing the first tests of their impact during the FFS tuning procedure, and to experimentally check the validity and beam size tuning limitations, of the optimized model for the ultra-low β_y^* optics.
For the design optimization of the ulra-low β_y^* lattice, the main nonlinear aberration contributions to σ_y^* were identified and corrected using the corresponding sextupole and octupole magnets. These simulations included the measured multipolar errors of the ATF2 magnets as well as fringe field effects. The simulation results highlight the strong impact of the multipolar errors and the need of skew sextupole corrections for the ulra-low β_y^* lattice. In design, for the $1\beta_x^*\times0.25\beta_y^*$ optics, the minimum vertical beam size achievable is 29 nm when using only normal and skew sextupoles, and is reduced down to 20 nm when octupoles are included. The amplified 2$^{\text{nd}}$ and 3$^{\text{rd}}$ order aberration contributions for the lower β_y^* optics can be reduced by applying larger IP horizontal β function. Tuning simulations, assuming realistic optics imperfections and tuning time, have shown significant improvement in the performance when tuning the $10\beta_x^*\times0.25\beta_y^*$ optics compared to $1\beta_x^*\times0.25\beta_y^*$, where the number of machines reaching vertical beam sizes below 30 nm was multiplied by a factor 6 for the larger β_x^* option. Tuning simulations have shown also the benefit of using the octupoles during the tuning process even for 10 times larger β_x^* optics, where the number of machines simulated achieving $\sigma_y^* \leq 30$ nm is 41% when octupoles are switched off and 63% when used for tuning.

After installation of the octupoles at ATF2, the alignment of OCT1FF was performed, based on the beam positions measured at the virtual IP by the IPBPMs. The use of the IPBPMs for the BBA required the expertise of the FONT group, who are currently developing this instrument, for the calibration and position data analysis. The OCT1FF, located closer to the IP and having tighter transverse tolerances than OCT2FF, is strong enough to generate beam position offset measureable by the IPBPMs. For OCT2FF, the lower maximum strength and the limited dynamic range of its mover induce a beam position change smaller than the resolution of the downstream BPMs, therefore the BBA could be performed only for the OCT1FF magnet.
The octupoles were used for the first time during the tuning process of the nominal β_y^* optics ($10\beta_x^*\times1\beta_y^*$) in June 2017. During this tuning session, the beam size could not be reduced enough to observe modulation at 174 degree mode with the Shintake monitor. The use of the octupoles brought to light the optics mismatched of the applied quadrupole and normal sextupole strengths for the 2$^{\text{nd}}$ order corrections, as the feed-down to normal sextupole fields, generated by the large amplitude horizontal offset of

OCT1FF, induced visible beam size reduction. The same measurements using OCT1FF offset was repeated in November 2017 after optics correction, where finally modulation could be observed at 174 degree mode with beam size measured around 60 nm. The minimum beam size observed during OCT1FF position scans was measured closer to the magnetic center, indicating smaller residual 2^{nd} order aberrations than observed in June operation. OCT1FF was also used for the ultra-low β_y^* optics to indicate whether the quadrupole strengths applied for $\beta_{x,y}^*$ matching are in agreement with the normal and skew sextupole settings.
During the first attempt of tuning the ultra-low β_y^* lattice in December 2017, the vertical beam size, σ_y^*, after iterations of linear and nonlinear knobs using the FF sextupoles and octupoles, could not be reduced below ≈100 nm and therefore could not be measured precisely at 174 degree mode with the Shintake monitor. The target β_x^* was 25 times larger than the nominal setting ($25\beta_x^*\times 0.25\beta_y^*$ optics). The OCT1FF horizontal position scan, revealed the presence of residual 2^{nd} order aberrations, as they were partially corrected by the feed-down to normal sextupole field of the octupole. From these observations, the optics model was re-optimized in simulation and tested during the second tuning attempt of the $25\beta_x^*\times 0.25\beta_y^*$ lattice in February 2018. The sextupole strengths were optimized in simulation w.r.t the quadrupole strengths applied in the machine that matches the target optics. Due to time constraints, no nonlinear knobs could be applied during the tuning operation and the octupoles were not switched on. Despite the lack of higher order aberration corrections, the average beam size at the end of the tuning session was reduced down to 70±6 nm, measured at 174 degree mode. The improved ultra-low β_y^* optics optimized for the February 2018 operation shows better performances than for the previous operation. Longer tuning time and nonlinear knob corrections will be needed during future operations to quantify the minimum beam size achievable with this optics.

From experience gained during ATF2 tuning operations, one can draw up a list of required actions to improve the corrections applied on the beam for the ultra-low β_y^* as well as for other optics.

- First, regarding the octuples, higher order optimization of the ultra-low β_y^* optics shows that for correcting the dominant 3^{rd} order aberrations U_{3224} and U_{3246}, the most upstream octupole from the IP is the strongest. In the present situation at ATF2, OCT1FF is the strongest octupole but is located closer to the IP, where the required octupole field is weaker. This situation was kept unchanged during low β_y^* tuning operations as the design octupole strengths could be applied, but with OCT2FF set close to its maximum current. In order to allow a wider tuning range for the most upstream octupole and to be more consistent with the design model, OCT2FF and OCT1FF locations should be swapped. However, this new configuration makes the BBA of the closest octupole from the IP, OCT2FF, more challenging even with the IPBPMs, due to its strength more than 8 times weaker than OCT1FF.

- A good knowledge of the beam conditions in the FFS is of prime importance to apply the required corrections. During ultra-low β_y^* tuning sessions, the mulit-OTR, which provide fast measurement of the beam emittance and coupling conditions at the entrance of the FFS, was inoperable. This was an important limitation for tuning the beam as emittance and couplings at the matching section were unknown and could not be corrected. The Multi-OTR should be fixed for future tuning operations.

- Improving the existing orbit control in the ATF2 should strongly help in lowering the IP beam size. Orbit drift propagates undesired linear and nonlinear aberrations to the IP, that are amplified for lower β_y^* optics. The orbit is flatten w.r.t the BPMs center at the begining of tuning operations and then is controlled by orbit feedbacks in the extraction and FF beamlines. The quality of the orbit control is therefore limited by the BPMs resolution and calibration, that should be checked regularly.

- In order to reduce the vertical beam position jitter and to improve the beam size measurements with the Shintake monitor, it was proposed to operate the machine in 2 bunches mode during the tuning to allow the use of the IP feedback system. The IP feedback system uses IPBPMs informations and fast kickers to correct the vertical position of the second incoming bunch. The stabilization of the beam at the IP should reduce the measured beam size and improve the Shintake monitor resolution, which ultimately allow more precise corrections when scanning the knobs.

- The performance of the tuning stongly depends on the quality of the knobs applied for IP beam size corrections. It has been shown that it is very difficult to observe beam sizes below 100 nm for the nominal and ultra-low β_y^* optics, when the linear optics does not match correctly with the applied sextupole strengths. This degrades the chromaticity correction along the FFS, and also biases the orthogonality of the pre-computed linear and nonlinear knobs. The orthogonality of the knobs can also be strongly altered by the initial transverse misaligment of the sextupoles. It is therefore necessary for the quality of the tuning, to perform regularly normal and skew sextupoles BBA and to ensure that the applied lattice matches the design model.

- Finally, the tuning process requires many knob scans, and their quality depend also on the number of beam size measurements used for the fit, where each of them requires approximately 3 minutes. The two ultra-low β_y^* optics tuning sessions and also previous tuning operations have shown that the time allocated for tuning is crucial to be able to apply all the needed linear and nonlinear corrections and to have a chance measure the lowest e^- beam size at ATF2.

List of publications

- F. Plassard, A. Latina, E. Marin, R. Tomás and P. Bambade
  Quadrupole-free detector optics design for the CLIC FFS at 3 TeV, Phys. Rev. Accel. Beams **21**, 011002, Published 17 January 2018 [116]

- F. Plassard, A. Latina, E. Marin and R. Tomás
  Beam Delivery System Optimization for CLIC 380 GeV, Proceedings of IPAC2017, Copenhagen, Denmark MOPIK100 (2017) [117]

- F. Plassard, A. Latina, E. Marin and R. Tomás
  Tuning-Based Design Optimization of CLIC Final Focus System at 3 TeV, Proceedings of IPAC2017, Copenhagen, Denmark MOPIK099 (2017) [118]

- F. Plassard, A. Latina, E. Marin and R. Tomás
  Comparative Study of the Tuning Performances of the Nominal and Long L CLIC Final Focus System at 380GeV*, Proceedings of the CERN-BINP Workshop for Young Scientists in e+e- colliders, CERN Proceedings, Vol. 1/2017 [119]

- F. Plassard, A. Latina, E. Marin and R. Tomás
  CLIC Beam Delivery System Rebaselining and Long L Lattice Optimization*, THPMR045 Proceedings of IPAC2016, Busan, Korea (2016) [120]

Co-author in:

- M. Patecki, D. Bett, E. Marin, F. Plassard (co-author), R. Tomás, K. Kubo, S. Kuroda, T. Naito, T. Okugi, T. Tauchi, and N. Terunuma
  Probing half β_y^* optics in the Accelerator Test Facility 2, Phys. Rev. Accel. Beams **19**, 101001, Published 5 October 2016 [104]

- *Updated baseline for a staged Compact Linear Collider*,
  Published 12 August 2016, CERN-2016-004 [28]

- *Intra-beam IP Feedback Studies for the 380 GeV CLIC Beam Delivery System*,
  Proceedings of IPAC2016, Busan, Korea WEPOR009 [121]

- *Progress in Ultra-Low β^* Study at ATF2*,
  Proceedings of IPAC2016, Busan, Korea THPMB043 [122]

- *Tuning simulations for the CLIC Traditional Beam Delivery System*
  Proceedings of IPAC2017, Copenhagen, Denmark MOPIK108 [123]

- *CLIC tuning performances under realistic error conditions*,
  Proceedings of IPAC2017, Copenhagen, Denmark TUPVA130 [81]

List of Figures

1.1 General scheme of the Accelerator Test Facility 5
1.2 CLIC potential energy staging concepts for 380 GeV, 1.5 TeV and 3 TeV c.o.m. In this solution, the modules at the beginning of the previous main linac are moved to the new beginning during the upgrade.(Figure taken from [8]) 6
1.3 General scheme of the CLIC 380 GeV (Figure taken from [8]) 7
1.4 General scheme of the CLIC 3 TeV (Figure taken from [8]) 7
1.5 Optics (top) and layout (bottom) of the CLIC 3 TeV Beam Delivery System ($L^* = 6$ m FFS). 8
1.6 Layout of the CLIC 3 TeV collimation system. 8
1.7 Simplified layout of the Traditional FFS scheme (upper plot) versus the Local chromaticity correction scheme (bottom plot). The blue lines represents the horizontal dispersion η_x along the system. The sextupoles are represented by green hexagons. 9

2.1 Coordinate system used to describe the motion of particles. Figure comes from [38] 11
2.2 Graphical representation of the Twiss parameters 14
2.3 From left to right: magnetic fields of pure normal quadrupole, sextupole and octupole. 17
2.4 Scheme of the chromatic effect produced by the final quadrupole QD0 approximated as a thin lens of focal length L^*. The blue, green and red lines represent the trajectory of particles arriving at the quadrupole with the same y coordinate but with larger, equal and smaller momentum respectively than p_0. 18

3.1 Left: Vertical cut through the SiD experiment. QD0 is located inside the detector and partially supported by the pre-insulator (green block) in the tunnel. Right: simplified MDI layout view showing a representation of part of the final-focus quadrupole, QD0, integrated into the CLIC SiD detector and shielded by an anti-solenoid. Figure comes from [8]. 30
3.2 Schematic overview of the SiD interaction region layout from the last 12 meters of the FFS (upper plot). Simulation of the longitudinal and radial fields (bottom plot). QD0 overlaps with the SiD solenoid field for $L^* = 3.5$ m. 31
3.3 Left: Vertical cut through the new detector model CLICdet allowing QD0 to be located outside of the experiment. No pre-insulator or QD0 shielding are needed as opposed to the short L^* design in Fig. 3.1 [63]. Right: Forward region of the CLICdet experiment [63]. 31

3.4 Schematic overview of the new detector (CLICdet) interaction region layout from the last 12 meters of the FFS (upper plot). Simulation of the longitudinal and radial fields (bottom plot). No overlapping between QD0 and the new detector field with L* = 6 m. 32
3.5 Optical functions through the Local correction scheme of the FFS for L* = 3.5 m (top plot) and L* = 6 m (bottom plot), where η_x is the dispersion function. The lattice for L* = 6 m has been lengthened with respect to the increase of L* from the nominal design. 34
3.6 High order optimization of the vertical beam size for CLIC 3 TeV with L* = 6m and for different β_y^*. σ_y^* calculated for $\delta_p = 0$ (upper plot) and for $\delta_p \neq 0$ (lower plot). 35
3.7 Impact of the dispersion level in the FFS on the horizontal and vertical beam sizes $\sigma_{x,y}^*$ (top plot), luminosity and sextupole strength k_2 (bottom plot) when η_x is reduced up to 40%. 36
3.8 Peak luminosity maximization versus β_y^* for L* = 6 m. 37
3.9 Energy bandwidth comparison between L* = 3.5 m and L* = 6 m. $\mathcal{L}_{1\%}$ is normalized to their respective maximum peak luminosity $\mathcal{L}_{1\%,0}$. 38
3.10 Main 3rd order contributions to the vertical beam size at the IP before the optimization of the octupoles and decapoles. 38
3.11 Main 4th order chromatic contributions to the vertical beam size at the IP before the optimization of the octupoles and decapoles. 39
3.12 Locations along the FFS of the pair of octupoles (OCT1 and OCT2) and the decapole (DEC1). 39
3.13 Vertical beam sizes at the IP calculated up to the 5th order, with and without octupoles and decapoles. 40
3.14 Energy distribution along the bunch at the entrance of the 3 TeV BDS assuming a realistic energy spread coming from the Main Linac. 40
3.15 QD0 vertical offset scan as function of the relative peak luminosity loss for L* = 6 m and L* = 3.5 m designs. 42
3.16 Scan of normal octupole field error applied on QD0 at R = 1 mm for L* = 3.5 m and L* = 6 m. 43
3.17 Normal (left) and skew (right) sextupole, octupole and decapole field error tolerances for QD0. 43
3.18 Normal (left) and skew (right) sextupole, octupole and decapole field error tolerances for QF1. 44
3.19 Left plot: Beam distribution at the entrance of the FFS collimated to $15\sigma_x$ and $55\sigma_y$. Right plot: resulting beam distribution at the entrance of QF1, when tracked with 1.4% flat distribution energy spread and synchrotron radiation for the L* = 6 m design. 44
3.20 Horizontal position of the emitted photons through the FD and CLIC detector for L* = 3.5 m (top plot) and L* = 6 m (bottom plot). 45
3.21 Vertical position of the emitted photons through the FD and CLIC detector for L* = 3.5 m (top plot) and L* = 6 m (bottom plot). 46

3.22 Simulation results showing the orthogonality of the linear knobs, constructed using transverse displacements of the normal sextupoles of the FFS. The plots shows the relative change of each aberration w.r.t the error-free lattice design value when the knobs are scanned. 48
3.23 Example of the average beam sizes $\sigma^*_{x,y}$ and total luminosity $\mathcal{L}_{\text{total}}$ after one iteration of BBA and 1 iteration of sextupole knobs (all linear knobs are scaned 2 times) applied on the L* = 6 m FFS lattice with $\beta^*_y = 0.12$ mm. 49
3.24 Vertical β-functions along the FFS for different β^*_y values. 49
3.25 Left plot: tuning performance comparison for different β^*_y values after one iteration of BBA and 1 iteration of sextupole knobs. Right plot: tuning performance comparison between $\beta^*_y = 0.1$ mm and $\beta^*_y = 0.12$ mm, after one iteration of BBA and 5 iterations of sextupole knobs. 50
3.26 Tuning performance results for the optimized L* = 6 m design with $\beta^*_y = 0.12$ mm under transverse misalignment of the optics. 87% of the machines achieve at least 110% of the design luminosity after 12 iterations of linear knobs, corresponding to approximately 5000 luminosity measurements. 51
3.27 Average beam size contribution of the 2$^{\text{nd}}$ order aberrations over the 100 machines simulated after applying the errors of Table 3.8. 52
3.28 Simulation result showing the orthogonality of the second order knobs, T_{122}, T_{126}, T_{166}, T_{324} and T_{346} constructed using strength variation of the normal sextupoles of the FFS. 53
3.29 Tuning performances of the CLIC 3 TeV with L* = 6 m under realistic static error conditions. The 2 last knobs iterations includes the five 2$^{\text{nd}}$ order knobs constructed from the normal sextupoles of the FFS. There is 89% and 85% of the machines reaching $\geq \mathcal{L}_0$ and $\geq 110\%\mathcal{L}_0$ after $\approx$ 7200 luminosity measurements. 54

4.1 Horizontal beam size σ^*_x including only second order aberrations, simulated before $L_{\text{QF1}-\text{QD0}}$ optimization, as function of the FFS length. 58
4.2 Example of $L_{\text{QF1}-\text{QD0}}$ scan for $\sigma^*_{x,2^{\text{nd}}\text{order}}$ minimization applied on the $L_{\text{FFS}} = 658.9$ m (left plot) and $L_{\text{FFS}} = 495.7$ m lattice (right plot). Original distance $L_{\text{QF1}-\text{QD0}}$ after FFS length reduction was 5.8 m for $L_{\text{FFS}} = 658.9$ m and 4.4 m for $L_{\text{FFS}} = 495.7$ m. 59
4.3 Horizontal beam size contribution from the 2$^{\text{nd}}$ order aberrations before and after $L_{\text{QF1}-\text{QD0}}$ optimization for the $L_{\text{FFS}} = 495.7$ m lattice. 59
4.4 Parabolic fits of the $L_{\text{QF1}-\text{QD0}}$ scan for different FFS lengths. 60
4.5 Optimal distance $L_{\text{QF1}-\text{QD0}}$ for $\sigma^*_{x,2^{\text{nd}}\text{order}}$ minimization as function of the FFS length. 60
4.6 High order optimization of the horizontal (top plot) and vertical (lower plot) beam sizes for CLIC 3 TeV with L* = 6 m and for different lengths L_{FFS}. 61

4.7 Scans of the FFS bending magnet angles for $\mathcal{L}_{\text{total}}$ and $\mathcal{L}_{1\%}$ luminosities maximization, for different shorter FFS length with L* = 6 m. $\mathcal{L}_0$ is the design peak or total luminosity. 62
4.8 Energy bandwidth comparison between shorter L_{FFS} with L* = 6 m. $\mathcal{L}_{1\%}$ is normalized to their respective maximum peak luminosity $\mathcal{L}_{1\%,0}$ (see Table 4.1). 63
4.9 Dispersion profile for different FFS length with L* = 6 m. 64
4.10 Average sextupole strength and dispersion at the sextupole locations as function of the FFS length. 64
4.11 Average luminosity over the 100 machines tuned for the different shorter FFS lattices after BBA (top plot) and linear knobs (bottom plot). 65
4.12 Tuning efficiency comparison after one iteration of BBA and three iterations of linear knobs for L_{FFS} = 495.7 m and L_{FFS} = 770 m with L* = 6 m. 66
4.13 Horizontal beam size σ_x^* including only second order aberrations, simulated before $L_{\text{QF1}-\text{QD0}}$ optimization, as function of the FFS length (L* = 3.5 m). 67
4.14 Optimal distance $L_{\text{QF1}-\text{QD0}}$ for $\sigma^*_{x,2^{\text{nd}}\text{order}}$ minimization as function of the FFS length (L* = 3.5 m). 67
4.15 Energy bandwidth comparison between longer L_{FFS} with L* = 3.5 m. $\mathcal{L}_{1\%}$ is normalized to their respective maximum peak luminosity $\mathcal{L}_{1\%,0}$ (see Table 4.2). 68
4.16 Dispersion profile for different FFS length with L* = 3.5 m. 69
4.17 Average sextupole strength and dispersion at the sextupole locations as function of the FFS length (L* = 3.5 m). 69
4.18 Average luminosity over the 100 machines tuned for the different longer FFS lattices with L* = 3.5 m after BBA (top plot) and linear knobs (bottom plot). 70
4.19 Tuning efficiency comparison after one iteration of BBA and three iterations of linear knobs for L_{FFS} = 450 m and L_{FFS} = 773 m with L* = 3.5 m. 71

5.1 Horizontal beam sizes at the IP calculated up to the maximum order considered, before and after $L_{\text{QF1}-\text{QD0}}$ optimization, for L* = 4.3 m. . . . 74
5.2 Horizontal and vertical beam sizes at the IP calculated up to the maximum order considered, after $L_{\text{QF1}-\text{QD0}}$ optimization, for L* = 4.3 m. 75
5.3 Optical functions through the Local correction scheme of the FFS for L* = 4.3 m (top plot) and L* = 6 m (bottom plot), where η_x is the dispersion function. The lattice for L* = 6 m has been lengthened with respect to the increase of L* from the nominal design. 76
5.4 Vertical beam sizes at the IP calculated up to the 5$^{\text{th}}$ order, for a chromatic and achromatic beam simulated, showing the large impact of the 3$^{\text{rd}}$ order geometrical contributions for the L* = 6 m case. 76
5.5 Location of the two octupoles inserted in the FFS with L* = 6 m. 77
5.6 Comparison of the vertical beam sizes at the IP, with and without octupoles in the FFS with L* = 6 m. 77

5.7 3rd order contributions to the vertical beam size at the IP, before and after inserting the pair of octupoles. 78
5.8 Dispersion profile along the FFS changed by changing the bending magnet angles up to a factor 2 for L* = 4.3 m (upper plot) and L* = 6 m (bottom plot). 78
5.9 Horizontal and vertical beam sizes at the IP, taking into account synchrotron radiation, as function of the increase of dispersion η_x along the FFS for L* = 4.3 m and L* = 6 m. 79
5.10 Luminosity and average sextupole strength in the FFS, as function of the increase of dispersion η_x. The total ($\mathcal{L}_{\text{total}}$) and peak ($\mathcal{L}_{1\%}$) luminosities are normalized to their respective design luminosity $\mathcal{L}_0$ given in Table 5.1. 79
5.11 Comparison of the vertical beam sizes at the IP, with and without octupoles in the FFS with L* = 6 m after dispersion optimization. 80
5.12 3rd order contributions to the vertical beam size at the IP, before and after inserting the pair of octupoles, for the FFS with L* = 6 m after dispersion optimization. 80
5.13 Comparison of the CLIC 380 GeV BDS energy bandwidth for both L* options. 81
5.14 Energy distribution along the bunch at the entrance of the BDS assuming a 1% full width energy spread (left plot) and assuming a realistic energy spread coming from the Main Linac (right plot). 82
5.15 CLIC 3 TeV BDS, with L* = 3.5 m, and 380 GeV BDS, with L* = 4.3 m, footprints after linacs alignment. 82
5.16 CLIC 3 TeV BDS and 380 GeV BDS, with L* = 6 m, footprints after linacs alignment. 83
5.17 Simulation results showing the orthogonality of the second order knobs, T_{122}, T_{126}, T_{166}, T_{324} and T_{346} constructed using strength variation of the normal sextupoles of the FFS with L* = 4.3 m 84
5.18 Simulation result showing the orthogonality of the second order knobs, T_{122}, T_{126}, T_{166}, T_{324} and T_{346} constructed using strength variation of the normal sextupoles of the FFS with L* = 6 m 85
5.19 Tuning performances of the CLIC 380 GeV with L* = 4.3 m under realistic static error conditions. There is 85% of the machines reaching $\geq \mathcal{L}_0$ after $\approx$ 6300 luminosity measurements. 86
5.20 Tuning performances of the CLIC 380 GeV with L* = 6 m under realistic static error conditions. There is 87% of the machines reaching $\geq \mathcal{L}_0$ after $\approx$ 6300 luminosity measurements. 87
5.21 Average luminosity over 100 randomly misaliged machines after applying errors (see Table 5.5), BBA and sextupole knobs on the L* = 4.3 m lattice for different dispersion profile. 87
5.22 Average luminosity, over 100 randomly misaligned machines (see Table 5.5), after applying errors and after one tuning iteration, as function of FFS dispersion increase. 88

5.23 Luminosity distribution after one iteration of BBA + sextupole knobs, applied on the L* = 4.3 m lattice for different dispersion profile. 89
5.24 Horizontal and vertical beam sizes at the IP as function of the horizontal beta function β_x^*. 90
5.25 Total and peak luminosities (left plot) and luminosity spectrum quality (right plot) as function of the horizontal beta function for L* = 4.3 m and L* = 6 m. 90

6.1 Schematic layout of the ATF2 section [23]. 94
6.2 Optical functions of the $1\beta_x^* \times 0.25\beta_y^*$ lattice along the Final Focus beamline and location of the pair of octupoles installed at ATF2. 95
6.3 Vertical beam size σ_y^* calculated order by order for the $1\beta_x^* \times 0.25\beta_y^*$ optics with and without the ATF2 skew sextupoles and with and without the magnets higher order field terms. 96
6.4 2nd order contributions to the vertical beam size with and without the ATF2 skew sextupoles and with and without the magnets higher order field terms. 97
6.5 Vertical beam size σ_y^* calculated order by order for the $1\beta_x^* \times 0.25\beta_y^*$ and the $1\beta_x^* \times 1\beta_y^*$ optics without the ATF2 skew sextupoles and by taking into account the magnets higher order field terms. 98
6.6 Left: Vertical beam size σ_y^* calculated order by order for the $1\beta_x^* \times 0.25\beta_y^*$ optics without octupoles. Right: 3rd order contributions to the vertical beam size growth before octupoles optimization. 98
6.7 Left: Vertical beam size σ_y^* calculated order by order for the $1\beta_x^* \times 0.25\beta_y^*$ optics with and without octupoles. Right: 3rd order contributions to the vertical beam size growth before and after octupoles optimization. 99
6.8 3rd order contributions to the vertical beam size growth before octupoles optimization for $\beta_x^* = 40$ mm and $\beta_x^* = 4$ mm ($\beta_y^* = 25$ μm). 99
6.9 Tuning performance comparison between the 1 $\beta_x^* \times 0.25$ β_y^* and the 10 $\beta_x^* \times 0.25$ β_y^* optics. 101
6.10 Tuning performance comparison for the 10 $\beta_x^* \times 0.25$ β_y^* optics lattice, with and without the use of OCT1FF and OCT2FF during the tuning procedure. 101
6.11 Schematic layout of Shintake Monitor [106]. 103
6.12 Example of an interference scan for vertical beam size measurement using the Shintake monitor at 30 degree mode (M = 0.6 $\Rightarrow \sigma_y^* = 130$ nm). . . . 104
6.13 Verticl beam size comparison around the virtual IP for $\beta_y^* = 100$ μm and $\beta_y^* = 25$ μm. 105
6.14 Optical functions along the extraction and the FF beamline with the location of the pair of skew quadrupoles used to correct horizontal dispersion and $< x , y >$ coupling. 106
6.15 Octupoles on magnetic measurement bench at CERN. Left: OCT1FF ; Right: OCT2FF 108

6.16 Octupoles installed in ATF2 FF beamline in November 2016. Left: OCT1FF ; Right: OCT2FF . . . 108
6.17 Left: simulations of the horizontal beam position at the IP when OCT1FF is set to 50 A and is horizontally displaced; Right: simulations of the vertical beam position at the IP when OCT1FF is set to 50 A and is vertically displaced. . . . 110
6.18 Left: Simulations of the vertical beam position at IPBPMs A,B and C when OCT1FF is set to 50 A and is horizontally displaced with a constant vertical offset $\Delta y = +1$ mm; Right: Measurements at ATF2 for the same configuration. . . . 112
6.19 Left: Simulations of the vertical beam position at IPBPMs A,B and C when OCT1FF is set to 50 A and is vertically displaced with a constant horizontal offset $\Delta x = +1$ mm; Right: Measurements at ATF2 for the same configuration. . . . 112
6.20 Vertical beam size along the FF beamline for $\beta_y^* = 100$, 50 and 25 μm. . . . 113
6.21 QD0 normal (left) and skew (right) sextupole, octupole and decapole field error tolerances for different β_x^* options of the ultra-low β_y^* optics 113
6.22 QF1 normal (left) and skew (right) sextupole, octupole and decapole field error tolerances for different β_x^* options of the ultra-low β_y^* optics 114
6.23 QD0FF strength scan for β_y^* measurement using the ATF2 carbon wire at the IP. β_y^* measured in December 2017. . . . 115
6.24 Examples of linear knob scans (vetical waist α_y^*, dispersion η_y^* and coupling $< x', y >$) performed during the ultra-low β_y^* tuning (Dec.17) at 30 degree mode with the Shintake monitor. . . . 115
6.25 Examples of 2$^{\text{nd}}$ order knob scans (using the 5 normal sextupoles) performed during the ultra-low β_y^* tuning (Dec.17) at 30 degree mode with the Shintake monitor, where Y_{24} corresponds to $T_{yx'y'}$ and Y_{46} corresponds to $T_{yy'\delta}$ . . . 116
6.26 Examples of 2$^{\text{nd}}$ order knob scans (using the 4 skew sextupoles) where Y_{22} corresponds to $T_{yx'x'}$, Y_{26} corresponds to $T_{yx'\delta}$ and Y_{44} corresponds to $T_{yy'y'}$ . . . 116
6.27 Vertical beam size σ_y^* and modulation after each knob scan, measured at 30 and 174 degree mode during the last 5 shifts of tuning operation. . . . 116
6.28 Left: OCT1FF horizontal position scan at maximum current (50 A) versus σ_y^*; Right: OCT1FF vertical position scan at 50 A. Measurement taken at 30 degree mode at ultra-low β_y^* optics (Dec. 17). . . . 118
6.29 Left: OCT1FF horizontal position scan at maximum current (50 A) versus σ_y^*; Right: OCT1FF vertical position scan at 50 A. Measurement taken at 30 degree mode at $10\beta_x^* \times 1\beta_y^*$ optics (Jun. 2017). . . . 118
6.30 Strength scan of OCT1FF performed on the $10\beta_x^* \times 1\beta_y^*$ lattice at 174 degree mode (Nov. 2017). . . . 119
6.31 Left: OCT1FF horizontal position scan at 10 A versus σ_y^*; Right: OCT1FF vertical position scan at 10 A. Measurement taken at 174 degree mode at $10\beta_x^* \times 1\beta_y^*$ optics after optics correction (Nov. 17). . . . 120

6.32 Horizontal dispersion measurement after correction, using QF1X and QF6X strength scan, on the 25 β_x^* $\times$ 0.25 β_y^* optics. 121
6.33 Vertical dispersion measurement after correction, using QS1X-QS2X knob, on the 25 β_x^* $\times$ 0.25 β_y^* optics. 121
6.34 Divergence squared, measured after QD0FF scan, versus QS1X-QS2X difference knob (February 2018). 122
6.35 QD0FF and QF1FF strength scan for $\beta_{x,y}^*$ measurement using the ATF2 carbon wire at the IP. (February 2018). 122
6.36 Vertical beam size σ_y^* and modulation after each knob scan, measured at 6.4, 30 and 174 degree mode during the last 1.5 shifts of the tuning operation (February 2018). 123

List of Tables

1.1 CLIC and ILC design parameters . . . 3
1.2 Beam and optics parameters for the ILC, CLIC and ATF2 Final Focus . . 5

3.1 CLIC 3 TeV design parameters . . . 33
3.2 Simulated performance of both L* options when the beam is tracked through the entire BDS (for L* = 6 m, β_y^* = 0.12 mm). Comparison of vertical chromaticity, total and peak luminosities and impact of synchrotron radiation at the IP. . . . 37
3.3 Simulated performance of both L* options when the beam is tracked through the entire 3 TeV BDS assuming a realistic energy spread shape coming from the Main Linac. . . . 41
3.4 Integrated sextupole strengths k_2, dispersion η_x^s and horizontal β-function β_x^s at the sextupole locations of the FFS for both optimized L* options. . 41
3.5 Final Doublet gradient and aperture radius comparison. . . . 41
3.6 Vertical offset tolerances (in nanometer) for the last quadrupole magnets in the CLIC FFS for a relative peak luminosity loss of 2% . . . 42
3.7 Errors applied to the CLIC 3 TeV FFS lattice for the tuning simulations . 47
3.8 Errors applied to the CLIC 3 TeV FFS lattice for the tuning simulations . 52

4.1 Luminosity performance, synchrotron radiation impact and QD0 parameters comparison for different FFS length with L* = 6 m (no octupoles and decapoles added to the FFS beamline). . . . 63
4.2 Luminosity performance and synchrotron radiation impact comparison for different FFS length with L* = 3.5 m (no octupoles or decapoles added to the FFS beamline). . . . 68

5.1 CLIC 380 GeV design parameters . . . 74
5.2 Simulated performance of both L* options when the beam is tracked through the entire BDS. Comparison of chromaticity, horizontal and vertical beam sizes, total and peak luminosities and impact of synchrotron radiation at the IP. . . . 81
5.3 Simulated performance of both L* options when the beam is tracked through the entire BDS assuming a realistic energy spread shape coming from the Main Linac. . . . 81
5.4 Errors applied to the lattice . . . 83
5.5 Errors applied to the lattice . . . 88

5.6 Performance summary for the L* = 4.3 m and L* = 6 m options. Beam sizes and luminosities calculated assuming a realistic energy spread shape coming from the Main Linac. Tuning simulations assuming realistic transverse misalignements, roll and strength errors applied to the quadrupoles, sextupoles and BPMs. 91

6.1 Beam and optics parameters for the ILC, CLIC and ATF2 Final Focus . . 94
6.2 Octupoles parameters for the ultra-low β_y^* optics 100
6.3 Errors applied to the ATF2 FF lattice 100
6.4 Observable beam sizes for the different laser crossing angle modes. 104
6.5 OCT1FF and OCT2FF main parameters 107
6.6 OCT1FF and OCT2FF multipoles measured at 50 A at 20 mm reference radius 109
6.7 OCT1FF and OCT2FF transverse offset tolerances 110
6.8 Horizontal OCT1FF magnetic center measured by the IPBPMs 111
6.9 Vertical OCT1FF magnetic center measured by the IPBPMs 111
6.10 Summary of the run operations for different optics between 2016 and 2018 at ATF2. Beam size measured with a charge of $\sim 1\times10^9$. 124

Bibliography

[1] CERN, "LHC Design Report," *CERN-2004-003*, 2004. [Online]. Available: https://cds.cern.ch/record/782076?ln=fr (Cited on page 1.)

[2] ——, "HL-LHC Preliminary Design Report," *CERN-ACC-2014-0300*, 2014. [Online]. Available: https://cds.cern.ch/record/1972604/files/CERN-ACC-2014-0300.pdf (Cited on page 1.)

[3] H. Murayama and M. Peskin, "Physics Opportunities of e+e- Linear Colliders," *Annual Review of Nuclear and Particle Science. 1996. **46**:533-608*, 1996. [Online]. Available: http://www.annualreviews.org/doi/abs/10.1146/annurev.nucl.46.1.533 (Cited on page 1.)

[4] J. Feng, "Physics at e-e- Colliders," *IASSNS-HEP-00-10*, 1999. [Online]. Available: https://cds.cern.ch/record/425684/files/0002055.pdf (Cited on page 1.)

[5] ECFA/DESY LC Physics Working Group, "Physics with e+e- linear colliders," *DESY 97-100*, 1997. [Online]. Available: https://arxiv.org/abs/hep-ph/9705442 (Cited on page 1.)

[6] FCC-ee website. [Online]. Available: https://tlep.web.cern.ch/ (Cited on page 2.)

[7] "ILC TDR Volume 3, Accelerator R&D ," 2013. [Online]. Available: https://www.linearcollider.org/ILC/Publications/Technical-Design-Report (Cited on pages 2 and 29.)

[8] "CLIC Conpectual Design Report Vol. 1,2,3," *CERN-2012-007*, 2012. [Online]. Available: http://clic-study.web.cern.ch/content/conceptual-design-report (Cited on pages 2, 6, 7, 22, 30, 46, 50, 58, 66, 82 and 133.)

[9] L. Rinolfi et al., "The CLIC electron and positron polarized sources," *CERN-OPEN-2010-017, CLIC-Note-817*, 2010. [Online]. Available: http://inspirehep.net/record/1509665/files/ (Cited on page 2.)

[10] Y. Papaphilippou et al., "Conceptual Design of the CLIC Damping Rings," *CERN-ATS-2012-176 ; CLIC-Note-965*, 2012. [Online]. Available: https://cds.cern.ch/record/1464093 (Cited on page 2.)

[11] W. Singer et al., "Production of superconducting 1.3 GHz cavities for the European X-ray Free Electron Laser," *Phys. Rev. Accel. Beams 19, 092001*, 2016. [Online]. Available: https://journals.aps.org/prab/abstract/10.1103/PhysRevAccelBeams.19.092001 (Cited on page 2.)

[12] H. Zha and A. Grudiev, "Design and optimization of Compact Linear Collider main linac accelerating structure," *Phys. Rev. Accel. Beams 19, 111003*, 2016. [Online].

Available: link.aps.org/pdf/10.1103/PhysRevAccelBeams.19.111003 (Cited on page 3.)

[13] F. Tecker et al., "CTF3 Combiner Ring Commissioning," *CERN-AB-2007-056; CLIC Note -718*, 2007. [Online]. Available: https://cds.cern.ch/record/1055561/files/ab-2007-056.pdf (Cited on page 3.)

[14] R. Corsini, "Commissioning Status of the CTF3 Delay Loop," 2006. [Online]. Available: cern.ch/accelconf/e06/Pre-Press/MOPLS093.pdf (Cited on page 3.)

[15] ——, "Final Results From the CLIC Test Facility (CTF3)," *IPAC talk*, 2017. [Online]. Available: accelconf.web.cern.ch/AccelConf/ipac2017/talks/tuzb1_talk.pdf (Cited on page 4.)

[16] V. Balakin et al, "Focusing of submicron beams for TeV scale e+e- linear colliders," *Physical Review Letters, American Physical Society, 1995, 74, pp.2479-2482*, 1995. [Online]. Available: https://www.researchgate.net/publication/13232391_Focusing_of_Submicron_Beams_for_TeV-Scale_e_e_-_Linear_Colliders (Cited on pages 4 and 10.)

[17] ATF2 group, "ATF2 Proposal," *CERN-AB-2006-004*, 2006. [Online]. Available: https://arxiv.org/pdf/physics/0606194 (Cited on pages 4 and 95.)

[18] G. White et al., "Experimental Validation of a Novel Compact Focusing Scheme for Future Energy Frontier Linear Lepton Colliders," *Phys. Rev. Lett. 112, 034802*, 2014. [Online]. Available: https://link.aps.org/doi/10.1103/PhysRevLett.112.034802 (Cited on page 4.)

[19] P. Raimondi and A. Seryi, "Novel Final Focus Design for Future Linear Colliders," *Phys. Rev. Accel. Beams 86 3779-3782*, 2003. [Online]. Available: link.aps.org/pdf/10.1103/PhysRevLett.86.3779 (Cited on pages 4, 10 and 32.)

[20] K. Kubo et al, "Measurement of a small vertical emittance with a laser wire beam profile monitor," *Phys. Rev. Accel. Beams 5, 122801*, 2002. [Online]. Available: link.aps.org/pdf/10.1103/PhysRevSTAB.5.122801 (Cited on page 4.)

[21] Y. Honda et al, "Achievement of Ultralow Emittance Beam in the Accelerator Test Facility Damping Ring," *Phys. Rev. Accel. Beams 92, 054802*, 2004. [Online]. Available: https://journals.aps.org/prl/abstract/10.1103/PhysRevLett.92.054802 (Cited on page 4.)

[22] Jacqueline Yan et al, "Shintake Monitor Nanometer Beam Size Measurement and Beam Tuning," *TIPP 2011 - Technology and Instrumentation for Particle Physics*, 2012. [Online]. Available: http://www.sciencedirect.com/science/article/pii/S1875389212019177 (Cited on page 4.)

[23] L. Nevay et al, "Laserwire at the Accelerator Test Facility 2 with submicrometer resolution," *Phys. Rev. Accel. Beams 17, 072802*, 2014. [Online]. Available: https://link.aps.org/doi/10.1103/PhysRevSTAB.17.072802 (Cited on pages 4, 94, 113 and 138.)

[24] T. Okugi, "Achievement of small beam size at ATF2," *Proceedings of LINAC2016, East Lansing MO3A02*, 2016. [Online]. Available: accelconf.web.cern.ch/AccelConf/linac2016/papers/mo3a02.pdf (Cited on page 4.)

[25] M. Patecki, "Towards Ultra-Low beta* in ATF2," *Proceedings of IPAC2015, Richmond MOBC1*, 2015. [Online]. Available: accelconf.web.cern.ch/AccelConf/IPAC2015/papers/mobc1.pdf (Cited on pages 4 and 95.)

[26] M. Modena, "Procurement, Measurement and Installation of 2 Octupoles for ATF2," *LCWS16, Morioka, Japan*, 2016. [Online]. Available: https://agenda.linearcollider.org/event/7371/sessions/4305 (Cited on page 4.)

[27] "Updated baseline for a staged Compact Linear Collider," *CERN-2016-004 ; arXiv:1608.07537*, 2017. [Online]. Available: https://cds.cern.ch/record/2210892 (Cited on pages 6 and 73.)

[28] W. Alasdair, "Physics Potential of CLIC Operation at 380 GeV," *CLICdp-Conf-2017-009*, 2017. [Online]. Available: https://cds.cern.ch/record/2263676 (Cited on pages 6 and 132.)

[29] R. Tomás, "Overview of the compact linear collider," *Phys. Rev. Accel. Beams **13** 014801*, 2010. [Online]. Available: https://journals.aps.org/prab/abstract/10.1103/PhysRevSTAB.13.014801 (Cited on page 6.)

[30] J. Resta-Lopez, "Status report of the baseline collimation system of CLIC," 2011. [Online]. Available: https://arxiv.org/abs/1104.2431 (Cited on pages 9 and 44.)

[31] G. Blair, "Simulation of the CLIC Beam Delivery System Using BDSIM," *CERN-OPEN-2002-057*, 2002. [Online]. Available: https://cds.cern.ch/record/582181/files/?ln=fr (Cited on page 9.)

[32] T. Raubenheimer and F. Zimmermann, "Final-focus systems in linear colliders," *Rev. Mod. Phys. 72, 95*, 2000. [Online]. Available: https://journals.aps.org/rmp/abstract/10.1103/RevModPhys.72.95 (Cited on page 10.)

[33] H. Garcia Morales, "Traditional final focus system for clic," *Phys. Rev. Accel. Beams **13** 014801*, 2012. [Online]. Available: https://cds.cern.ch/record/1464102/files/?ln=fr (Cited on page 10.)

[34] K. Wille, "The physics of particle accelerators, an introduction," 1996. (Cited on page 11.)

[35] S Y. Lee, "Accelerator physics," 2012. (Cited on page 11.)

[36] A. Wu Chao, K. Mess, M. Tigner, F, Zimmermann, "Handbook of accelerator physics and engineering," 2012. (Cited on page 11.)

[37] H. Wiedemann, "Particle accelerator physics," 2007. (Cited on pages 11 and 105.)

[38] L. Deniau, "The mad-x program, users reference manual," 2017. [Online]. Available: http://mad.web.cern.ch/mad/ (Cited on pages 11 and 133.)

[39] R. Tomás, "Direct measurement of resonance driving terms in the super proton synchrotron (sps) of cern using beam position monitors," *CERN-THESIS-2003-010*, 2003. [Online]. Available: https://cds.cern.ch/record/615164?ln=en (Cited on page 16.)

[40] E. Maclean and R. Tomás, "Modelling and correction of the non-linear transverse dynamics of the lhc from beam-based measurements," *CERN-THESIS-2014-135*, 2014. [Online]. Available: https://cds.cern.ch/record/1951379?ln=en (Cited on page 16.)

[41] R. Tomás, "Nonlinear optimization of beam lines," *Phys. Rev. Accel. Beams **9** 081001*, 2006. [Online]. Available: https://journals.aps.org/prab/abstract/10.1103/PhysRevSTAB.9.081001 (Cited on page 18.)

[42] E. Marin Lacoma, "Design and high order optimization of final focus systems for linear colliders," *CERN-THESIS-2012-218*, 2012. [Online]. Available: https://cds.cern.ch/record/1504285?ln=zh_CN (Cited on pages 19, 31, 95 and 112.)

[43] K. Oide, "Synchrotron-radiation limit on the focusing of electron beams," *Phys. Rev. Accel. Beams **61** 15*, 1988. [Online]. Available: link.aps.org/doi/10.1103/PhysRevLett.61.1713 (Cited on pages 20 and 61.)

[44] O. Blanco , R. Tomás , P. Bambade, "Beam focusing limitation from synchrotron radiation in two dimensions," *Phys. Rev. Accel. Beams **19** 021002*, 2016. [Online]. Available: link.aps.org/pdf/10.1103/PhysRevAccelBeams.19.021002 (Cited on pages 20 and 61.)

[45] D. Schulte, "Beam-beam effects in linear colliders," *School Proceedings, Vol. 3/2017, CERN-2017-006-SP*, 2017. [Online]. Available: https://e-publishing.cern.ch/index.php/CYRSP/article/view/267/309 (Cited on page 21.)

[46] Y. Nosochkov and A. Seryi, "Compensation of detector solenoid effects on the beam size in a linear collider," *Phys. Rev. Accel. Beams **8** 021001*, 2005. [Online]. Available: link.aps.org/pdf/10.1103/PhysRevSTAB.8.021001 (Cited on pages 22 and 23.)

[47] Y. Nosochkov, A. Seryi, "First beam waist measurements in the final focus beam line at the kek accelerator test facility 2," *Phys. Rev. ST Accel. Beams 8, 021001*, 2005. [Online]. Available: https://journals.aps.org/prab/references/10.1103/PhysRevSTAB.8.021001 (Cited on page 23.)

[48] B. Parker and A. Seryi, "Compensation of the effects of a detector solenoid on the vertical beam orbit in a linear collider," *Phys. Rev. Accel. Beams* ***8****, 041001*, 2005. [Online]. Available: link.aps.org/pdf/10.1103/PhysRevSTAB.8.041001 (Cited on pages 23 and 30.)

[49] Y. Inntjore Levinsen et al, "Impact of detector solenoid on the compact linear collider luminosity performance," *Phys. Rev. Accel. Beams* ***17*** *051002*, 2014. [Online]. Available: link.aps.org/pdf/10.1103/PhysRevSTAB.17.051002 (Cited on page 23.)

[50] A. Latina et al, "Experimental demonstration of a global dispersion-free steering correction at the new linac test facility at slac," *Phys. Rev. Accel. Beams* ***17*** *042803*, 2014. [Online]. Available: link.aps.org/pdf/10.1103/PhysRevSTAB.17.042803 (Cited on pages 23 and 24.)

[51] F. Zimmermann, "Lecture notes for: Accelerator physics and technologies for linear colliders," 2002. [Online]. Available: https://hep.uchicago.edu/~kwangje/LectureNotes_Zimmermann.pdf (Cited on pages 23 and 63.)

[52] J. Pfingstner et al, "Recent improvements in the orbit feedback and ground motion mitigation techniques for clic," *CERN-ATS-2012-207 ; CLIC-Note-959*, 2012. [Online]. Available: https://cds.cern.ch/record/1470344?ln=fr (Cited on page 23.)

[53] Y. Nosochkov, P. Raimondi, T. Raubenheimer, A. Seryi, "Tuning knobs for the nlc final focus," *SLAC-PUB-9255*, 2002. [Online]. Available: http://inspirehep.net/record/588085/ (Cited on pages 24 and 25.)

[54] T. Okugi, "Linear and second order optics corrections for the kek accelerator test facility final focus beam line," *Phys. Rev. Accel. Beams* ***17*** *023501*, 2014. [Online]. Available: link.aps.org/pdf/10.1103/PhysRevSTAB.17.023501 (Cited on pages 25, 52 and 112.)

[55] T. Abe, et al., "The international large detector: Letter of intent," *Fermilab-Pub-09-682-E, arXiv:1006.3396*, 2010. [Online]. Available: https://arxiv.org/abs/1006.3396 (Cited on page 29.)

[56] H. Aihara, et al., "Sid letter of intent," *arXiv:0911.0006*, 2009. [Online]. Available: https://arxiv.org/abs/0911.0006 (Cited on page 29.)

[57] F. Simon, "Detector systems at clic," *TIPP 2011 - Technology and Instrumentation for Particle Physics*, 2011. [Online]. Available: http://www.sciencedirect.com/science/article/pii/S1875389212016665 (Cited on page 29.)

[58] R. Tomás, H. Braun, M. Jorgensen and D. Schulte, "Optimizing the clic beam delivery system," *Proceedings of EPAC08, Genoa, Italy MOPP038*, 2008. [Online]. Available: https://accelconf.web.cern.ch/accelconf/e08/papers/mopp038.pdf (Cited on pages 29, 33 and 35.)

[59] K. Artoos et al., "Ground vibration and coherence length measurements for the clic nano-stabilization studies," *Proceedings of PAC09, Vancouver, BC, Canada TH5RFP081*, 2009. [Online]. Available: accelconf.web.cern.ch/accelconf/PAC2009/papers/th5rfp081.pdf (Cited on page 30.)

[60] Lau Gatignon, "Clic mdi overview," *CLIC-Note-937*, 2012. [Online]. Available: https://cds.cern.ch/record/1448256/files/CERN-OPEN-2012-010.pdf (Cited on page 30.)

[61] B. Dalena et al., "Solenoid and synchrotron radiation effects in clic," *Proceedings of PAC09, Vancouver, BC, Canada TH6PFP074*, 2009. [Online]. Available: https://accelconf.web.cern.ch/accelconf/pac2009/papers/th6pfp074.pdf (Cited on page 30.)

[62] B. Dalena, D. Schulte and R. Tomás, "Impact of the experiment solenoid on the clic luminosity," *Proceedings of IPAC'10, Kyoto, Japan WEPE029*, 2010. [Online]. Available: https://accelconf.web.cern.ch/accelconf/IPAC10/papers/wepe029.pdf (Cited on page 30.)

[63] CLICdp collaboration, "The post-cdr clic detector model," *CLICdp-Note-2017-001*, 2017. [Online]. Available: https://cds.cern.ch/record/2254048?ln=fr (Cited on pages 31, 32 and 133.)

[64] A. Seryi, "Near ir ff design including fd and longer l* issues," *CLIC'08 Workshop*, 2008. (Cited on pages 30 and 32.)

[65] ——, "Summary of the bds and mdi clic08 working group," *CLIC Note-776*, 2008. [Online]. Available: cds.cern.ch/record/1216866/files/CERN-OPEN-2009-018.pdf (Cited on pages 30 and 32.)

[66] R. Tomás et al., "The clic bds towards the conceptual design report," *CERN-ATS-2010-088*, 2010. [Online]. Available: https://accelconf.web.cern.ch/accelconf/IPAC10/html/sessi0n.htm (Cited on page 31.)

[67] G. Zamudio and R. Tomás, "Optimization of the clic 500 gev final focus system and design if a new 3 tev final focus system with l*=6.0 m," *CLIC-Note-882*, 2010. [Online]. Available: https://cds.cern.ch/record/1368480 (Cited on page 31.)

[68] L. Gatignon, "Mdi status and plans," *CLIC Workshop 2016*, 2016. [Online]. Available: https://indico.cern.ch/event/449801/timetable/?view=standard_inline_minutes (Cited on page 32.)

[69] H. Grote, F. Schmidt, L. Deniau, G. Roy, "The mad-x program," *User's Reference Manual*, 2015. [Online]. Available: mad.web.cern.ch/mad/madx.old/madx_manual.pdf (Cited on page 32.)

[70] H. Garcia Morales and R. Tomás, "Final-focus systems for multi-tev linear colliders," *Phys. Rev. Accel. Beams* ***17*** *101001*, 2014. [Online]. Available:

link.aps.org/pdf/10.1103/PhysRevSTAB.17.101001 (Cited on pages 33, 36, 37 and 65.)

[71] R. Tomás, "Mapclass: a code to optimize high order aberrations," *Report No. CERN-AB-Note-017, ABP*, 2006. [Online]. Available: https://cds.cern.ch/record/944769/files/ab-note-2006-017.pdf (Cited on page 33.)

[72] ——, "Nonlinear optimization of beam lines," *Phys. Rev. Accel. Beams* ***9*** *081001*, 2006. [Online]. Available: https://journals.aps.org/prab/references/10.1103/PhysRevSTAB.9.081001 (Cited on page 33.)

[73] D. Martínez, A. Rosam, R. Tomás and R. de Maria, "Mapclass2: a code to aid the optimisation of lattice," *CERN-ATS-Note-2012-087 TECH*, 2012. [Online]. Available: https://cds.cern.ch/record/1491228?ln=fr (Cited on page 33.)

[74] E. Forest, F. Schmidt, E. McIntosh, "Introduction to the polymorphic tracking code," *CERN-SL-2002-044 (AP)*, 2002. [Online]. Available: https://cds.cern.ch/record/573082/files/sl-2002-044.pdf (Cited on page 33.)

[75] E. D'Amico, G. Guignard, N. Leros and D. Schulte, "Simulation package based on placet," *CERN/PS 2001/028*, 2001. [Online]. Available: http://inspirehep.net/record/560785 (Cited on page 34.)

[76] D. Schulte, "Beam-beam simulations with guinea-pig," *Report No. CERN-PS-99-014-LP; Report No. CLIC-Note-387*, 2009. [Online]. Available: https://cds.cern.ch/record/382453?ln=fr (Cited on page 34.)

[77] ——, "Beam-beam effects in linear colliders," *9th International School for Linear Colliders*, 2015. [Online]. Available: https://cds.cern.ch/record/2264414/files/ICFA69_237-245.pdf (Cited on page 35.)

[78] J. Snuverink, J. Barranco, H.Garcia, Y. Levinsen, R. Tomás and D. Schulte, "Clic final focus system alignment and magnet tolerances," *Proceedings of IPAC13, TUPME051*, 2013. [Online]. Available: accelconf.web.cern.ch/accelconf/ipac2013/papers/tupme051.pdf (Cited on page 42.)

[79] B. Dalena and R. Tomás, "Beam delivery system tuning and luminosity monitoring in the compact linear collider," *Phys. Rev. Accel. Beams* ***15*** *051006*, 2012. [Online]. Available: https://journals.aps.org/prab/abstract/10.1103/PhysRevSTAB.15.051006 (Cited on pages 46 and 65.)

[80] E. Marin, A. Latina, R. Tomás, and D. Schulte, "Final focus system tuning studies towards compact linear collider feasibility," *Phys. Rev. Accel. Beams 21, 011003*, 2018. [Online]. Available: https://journals.aps.org/prab/abstract/10.1103/PhysRevAccelBeams.21.011003 (Cited on page 54.)

[81] E. Marin, A. Latina, F. Plassard, D. Schulte, R. Tomás , "Clic tuning performances under realistic error conditions," *Proceedings of IPAC2017, Copenhagen, Denmark*

TUPVA130, 2017. [Online]. Available: accelconf.web.cern.ch/AccelConf/ipac2017/papers/tupva130.pdf (Cited on pages 54 and 132.)

[82] F. Plassard, "Clic 3 tev l*=6m lattice repository." [Online]. Available: http://clicr.web.cern.ch/CLICr/MainBeam/BDS/BDS_3TeV_l*6m_v11_01_18/ (Cited on page 55.)

[83] ——, "Clic 3 tev longer ffs lattice repository." [Online]. Available: http://clicr.web.cern.ch/CLICr/MainBeam/BDS/BDS_3TeV_Longer-FFS_l*3.5m_v11_01_18/ (Cited on page 57.)

[84] P. Lebrun, L. Linssen, A. Lucaci-Timoce, D. Schulte, F. Simon, S. Stapnes, N. Toge, H. Weerts, J. Wells, "The clic programme: Towards a staged e+e- linear collider exploring the terascale : Clic conceptual design report," *CERN-2012-005*, 2012. [Online]. Available: https://arxiv.org/abs/1209.2543 (Cited on pages 73 and 91.)

[85] "Clic 500 gev lattice repository," 2012. [Online]. Available: http://clicr.web.cern.ch/CLICr/MainBeam/BDS_500GeV/ (Cited on page 73.)

[86] F. Plassard, "Clic 380 gev lattice repository." [Online]. Available: http://clicr.web.cern.ch/CLICr/MainBeam/BDS_380GeV/ (Cited on page 89.)

[87] G. R. White et al. (ATF2 Collaboration), "Experimental validation of a novel compact focusing scheme for future energy-frontier linear lepton colliders," *Physical Review Letters 112, 034802*, 2014. [Online]. Available: https://journals.aps.org/prl/abstract/10.1103/PhysRevLett.112.034802 (Cited on page 93.)

[88] D. Bett, "The development and implementation of a beam position monitoring system for use in the font feedback system at atf2," 2011. [Online]. Available: https://groups.physics.ox.ac.uk/font/thesis/thesisApsimon.pdf (Cited on page 93.)

[89] N. Blaskovic Kraljevic, "Development of a high-precision low-latency position feedback system for single-pass beamlines using stripline and cavity beam position monitors," 2015. [Online]. Available: https://groups.physics.ox.ac.uk/font/thesis.html (Cited on page 93.)

[90] R. Apsimon, D. Bett, N. Blaskovic Kraljevic, P. Burrows, G. Christian, C. Clarke, B. Constance, H. Dabiri Khah, M. Davis, C. Perry, J. Resta Lopez, and C. Swinson, "Design and performance of a high resolution, low latency stripline beam position monitor system," *Phys. Rev. ST Accel. Beams 18, 032803 - Published 19 March 2015*, 2015. [Online]. Available: https://journals.aps.org/prab/abstract/10.1103/PhysRevSTAB.18.032803 (Cited on pages 93 and 109.)

[91] J. Pfingstner, K. Artoos, C. Charrondiere, St. Janssens, M. Patecki, Y. Renier, D. Schulte, and R. Tomás, "Mitigation of ground motion effects in linear accelerators via feed-forward control," *Phys. Rev. ST Accel. Beams 17, 122801*, 2014. [Online]. Available: link.aps.org/pdf/10.1103/PhysRevSTAB.17.122801 (Cited on page 93.)

[92] D. Bett, C. CharrondiÃ¨re, M. Patecki, J. Pfingstner, D. Schulte and R. Tomás, "Ground motion compensation using feed-forward control at atf2," *WEPOR005 Proceedings of IPAC2016, Busan, Korea*, 2016. [Online]. Available: accelconf.web.cern.ch/accelconf/ipac2016/papers/wepor005.pdf (Cited on page 93.)

[93] M. Bergamaschi, "Odr emittance measurement system at atf2," *CLIC Workshop 2018*, 2018. [Online]. Available: https://indico.cern.ch/event/.../2018_01_22_CLICWorkshop.pdf (Cited on page 93.)

[94] S. Liu and P. Bambade, "Development of diamond sensors for beam halo and compton spectrum diagnostics after the interaction point of atf2," *PhD Thesis*, 2015. [Online]. Available: https://tel.archives-ouvertes.fr/tel-01206862/ (Cited on page 93.)

[95] Shan Liu, Frederic Bogard, Patrick Cornebise, Angeles Faus-Golfe et al., "In vacuum diamond sensor scanner for beam halo measurements in the beam line at the kek accelerator test facility," *Nuclear Instruments and Methods in Physics Research A 832 (2016) 231-242*, 2016. [Online]. Available: https://www.sciencedirect.com/science/article/pii/S0168900216306921 (Cited on page 93.)

[96] R. Tomás, P. Bambade, E. Marin et al. , "Atf2 ultra-low ip betas proposal," *CLIC-Note-792*, 2009. [Online]. Available: https://cds.cern.ch/record/1312198/files/CERN-ATS-2009-092.pdf (Cited on pages 93, 94 and 95.)

[97] R. Tomás, P. Bambade, E. Marin, T. Okugi, G. White, A. Seryi , "Scenarios for the atf2 ultra-low ip betas proposal," *BNL-93636-2010-CP*, 2010. [Online]. Available: https://www.bnl.gov/isd/documents/73783.pdf (Cited on page 93.)

[98] T. Okugi, "Achievement of small beam size at atf2 beamline," *Proceedings of LINAC16, MO3A02*, 2016. [Online]. Available: accelconf.web.cern.ch/AccelConf/linac2016/papers/mo3a02.pdf (Cited on page 93.)

[99] E. Marin, R. Tomás, T. Okugi, N. Terunuma, "Design and high order optimization of the accelerator test facility lattices," *Phys. Rev. ST Accel. Beams 17, 021002*, 2014. [Online]. Available: link.aps.org/pdf/10.1103/PhysRevSTAB.17.021002 (Cited on page 95.)

[100] M. Patecki, R. Tomás, "Optimisation analysis and improvement of the effective beam sizes in accelerator test facility 2," *CERN-THESIS-2016-304*, 2016. [Online]. Available: https://cds.cern.ch/record/2265996/files/CERN-THESIS-2016-304.pdf (Cited on pages 95, 96, 107, 111, 112 and 114.)

[101] M. Woodley, "Repository of the multipole component measurements of the atf2," 2011. [Online]. Available: http://www.slac.stanford.edu/~mdw/ATF2/v4.4 (Cited on page 96.)

[102] M. Masuzawa et al., "Qea magnet measurements at kek and comparison with ihep results," 2011. [Online]. Available: http://ilcagenda.linearcollider.org/conferenceDisplay.py?confId=4904 (Cited on page 96.)

[103] M. Patecki and R. Tomás, "Effects of quadrupole fringe fields in final focus systems for linear colliders," *Phys. Rev. ST Accel. Beams 17, 101002*, 2014. [Online]. Available: https://journals.aps.org/prab/abstract/10.1103/PhysRevSTAB.17.101002 (Cited on pages 96, 98 and 112.)

[104] M. Patecki, D. Bett, E. Marin, F. Plassard, R. Tomás, K. Kubo, S. Kuroda, T. Naito, T. Okugi, T. Tauchi, and N. Terunuma, "Probing half beta* optics in the accelerator test facility 2," *Phys. Rev. Accel. Beams 19, 101001*, 2016. [Online]. Available: https://journals.aps.org/prab/abstract/10.1103/PhysRevAccelBeams.19.101001 (Cited on pages 102, 107, 111, 112 and 132.)

[105] T. Shintake, "Measurement of small electron-beam spots," *Annu. Rev. Nucl. Part. Sci. 1999. 49:125-62*, 1999. [Online]. Available: https://www.jlab.org/accel/beam_diag/DOCS/annurev.nucl.49.1.125.pdf (Cited on page 102.)

[106] J. Yan, "Shintake monitor nanometer beam size measurement and beam tuning," *TIPP 2011 - Technology and Instrumentation for Particle Physics*, 2011. [Online]. Available: https://www.researchgate.net/publication/271879884_Shintake_Monitor_Nanometer_Beam_Size_Measurement_and_Beam_Tuning (Cited on pages 103 and 138.)

[107] Y. Yamaguchi, "Evaluation of expected performance of shintake beam size monitor for atf2," *MOPE023, Proceedings of IPAC10, Kyoto, Japan*, 2010. [Online]. Available: https://accelconf.web.cern.ch/accelconf/IPAC10/papers/mope023.pdf (Cited on pages 103 and 104.)

[108] S. Bai, A. Aryshev, P. Bambade, D. Mc Cormick, B. Bolzon, J. Gao, T. Tauchi and F. Zhou, "First beam waist measurements in the final focus beam line at the kek accelerator test facility 2," *Phys. Rev. ST Accel. Beams 13, 092804*, 2010. [Online]. Available: https://journals.aps.org/prab/abstract/10.1103/PhysRevSTAB.13.092804 (Cited on page 105.)

[109] A. Faus-Golfe, "Multi-otr system for atf2," *TIPP 2011, Physics Procedia 37 2072 - 2079*, 2011. [Online]. Available: https://www.sciencedirect.com/science/article/pii/S1875389212019219 (Cited on page 107.)

[110] E. Marin, M. Modena, T. Tauchi, N. Terunuma, R. Tomás, G. White, "Specifications of the octupole magnets required for the atf2 ultra-low beta lattice," *SLAC-TN-14-019*, 2014. [Online]. Available: www.slac.stanford.edu/cgi-wrap/getdoc/slac-tn-14-019.pdf (Cited on pages 107 and 108.)

[111] C. Petrone and M. Modena, "Magnetic measurement results of the octupole 1 pxmonbanac-cr000001," *CERN Internal Note 2016-19*, 2016. (Cited on page 108.)

[112] ——, "Magnetic measurement results of the octupole 1 pxmonbanac-cr000002," *CERN Internal Note 2016-19*, 2016. (Cited on page 108.)

[113] F. Plassard, "Atf2 lattice repository." [Online]. Available: http://clicr.web.cern.ch/CLICr/ATF2/ (Cited on page 120.)

[114] C.Rimbault, P. Bambade, S. Kuroda and G. White, "Coupling correction in atf2 extraction line," *Proceedings of IPAC'19 FR5PFP005*, 2009. [Online]. Available: https://accelconf.web.cern.ch/accelconf/PAC2009/.../fr5pfp005.pdf (Cited on page 120.)

[115] E. Marin Lacoma, "Diagnose of atf2 tuning experiences," *21st ATF2 project meeting, LAL, Orsay*, 2018. [Online]. Available: https://agenda.linearcollider.org/event/7869/sessions/4621/ (Cited on page 125.)

[116] F. Plassard, Andrea Latina, Eduardo Marin, and R. Tomás, "Quadrupole-free detector design for the compact linear collider final focus system at 3 tev," *Phys. Rev. ST Accel. Beams 21, 011002*, 2018. [Online]. Available: link.aps.org/pdf/10.1103/PhysRevAccelBeams.21.011002 (Cited on page 132.)

[117] F. Plassard, A. Latina, E. Marin and R. Tomás, "Beam delivery system optimization for clic 380 gev," *Proceedings of IPAC2017, Copenhagen, Denmark MOPIK100*, 2017. [Online]. Available: http://inspirehep.net/record/1626358/ (Cited on page 132.)

[118] ——, "Tuning-based design optimization of clic final focus system at 3 tev," *Proceedings of IPAC2017, Copenhagen, Denmark MOPIK099*, 2017. [Online]. Available: inspirehep.net/record/1626357/ (Cited on page 132.)

[119] ——, "Comparative study of the tuning performances of the nominal and long l* clic final focus system at 380gev," *Proceedings of the CERN-BINP Workshop for Young Scientists in e+e- colliders, CERN Proceedings, Vol. 1/2017*, 2016. [Online]. Available: inspirehep.net/record/1650318/ (Cited on page 132.)

[120] ——, "Clic beam delivery system rebaselining and long l* lattice optimization," *THPMR045 Proceedings of IPAC2016, Busan, Korea*, 2016. [Online]. Available: inspirehep.net/record/1470533/ (Cited on page 132.)

[121] R.M. Bodenstein, P. Burrows, J. Snuverink, F. Plassard, "Intra-beam ip feedback studies for the 380 gev clic beam delivery system," *Proceedings of IPAC2016, Busan, Korea WEPOR009*, 2017. [Online]. Available: inspirehep.net/record/1470296/ (Cited on page 132.)

[122] M. Patecki, D.R. Bett, F. Plassard, R. TomÃ¡s, K. Kubo, S. Kuroda, T. Naito, T. Okugi, T. Tauchi, N. Terunuma,T. Tauchi, N. Terunuma, "Progress in ultra-low

beta* study at atf2," *Proceedings of IPAC2016, Busan, Korea THPMB043*, 2017. [Online]. Available: inspirehep.net/record/1470486 (Cited on page 132.)

[123] R. M. Bodenstein, P. N. Burrows, E. Marin, F. Plassard, R. Tomás, "Tuning simulations for the clic traditional beam delivery system," *Proceedings of IPAC2017, Copenhagen, Denmark MOPIK108*, 2017. [Online]. Available: inspirehep.net/record/1626359/ (Cited on page 132.)

École Doctorale
PHENIICS
Doctoral School

Titre : *Optimisation de la ligne de faisceau du système de focalisation finale à long L* du collisionneur linéaire CLIC et études des optiques de focalisation de l'ATF2 à ultra-bas β* avec utilisation d'octupôles.*

Mots clés : Collisionneurs linéaires, Dynamique des Faisceaux, Lentilles (optique), Luminosité

Résumé : Un défis important pour les futures collisionneurs linéaires électron-positron est de pouvoir focaliser le faisceau à des tailles transverses de l'ordre du nanomètre au point d'interaction (IP), permettant d'atteindre la luminosité de conception. Le système délivrant les faisceaux d'e- et de e + de la sortie du Linac principal vers le point d'interaction, le Beam Delivery System (BDS), réalise les fonctions critiques requises pour atteindre l'objectif de luminosité, tel que la collimation et la focalisation du faisceau. Le faisceau est focalisé par le système de focalisation finale (FFS) tout en corrigeant les aberrations d'ordre supérieur propagées le long du système. Les effets chromatiques contribuant à l'élargissement de la taille du faisceau, sont amplifiés par la force de focalisation des deux derniers quadripôles QF1 et QD0, ou doublet final (FD), et par la longueur de la distance focale finale L* entre QD0 et l'IP. L'approche de correction de la chromaticité retenue pour les deux grands projets actuels de collisionneurs linéaires, CLIC et ILC, est fondée sur la correction locale de la chromaticité générée par le doublet final. Ce shéma est actuellement testé à l'ATF2 au KEK (Japon). Ce travail de thèse se concentre sur les problématiques liées au système de focalisation finale du projet CLIC re-optimisé avec un plus long L*, dans le cadre de la simplification de l'interface machine-détecteur (MDI), ainsi que sur le travail expérimental conduit à l'ATF2 pour l'optimisation et l'étude des optiques du système de focalisation finale à ultra-bas β* incluant les tout premiers est in situ des octupôles à l'ATF2.

Title : *Optics optimization of longer L* Beam Delivery System designs for CLIC and tuning of the ATF2 final focus at ultra-low β* using octupoles*

Keywords : Linear collider, Beam dynamics, Lens (optical), Luminosity

Abstract : The future machines considered to carry out high precision physics in the TeV energy regime are electron-positron (e+e−) linear colliders. Future linear colliders feature nanometer beam spot sizes at the Interaction Point. The Beam Delivery System (BDS) transports the e + and e− beams from the exit of the linacs to the IP by performing the critical functions required to meet the CLIC luminosity goal such as beam collimation and focusing. The beam is focused through the Final Focus System while correcting higher order transport aberrations in order to deliver the design IP beam sizes. The chromatic contributions are amplified by the focusing strength of the two last quadrupoles named QD0 and QF1, reffered to as the Final Doublet (FD), and by the length of the final focal distance L* between QD0 and the IP. The chromaticity correction approach chosen for the CLIC FFS is based on the Local chromaticity correction scheme which uses interleaved pairs of sextupole magnets in the FD region in order to locally and simultaneously correct horizontal and vertical chromaticity. The current linear collider projects, the Compact Linear Collider (CLIC) and the International Linear Collider (ILC) have FFS lattices based on the Local Chromaticity correction scheme. This scheme is being tested in the Accelerator Test Facility 2 (ATF2) at KEK (Japan). This thesis concentrates on problems related to the optimization of BDS lattices for the simplification of the CLIC Machine Detector Interface (MDI) and on the experimental work for the implementation and study of a CLIC-like FFS optics for the ATF2, referred to as ultra-low β* optics.

Université Paris-Saclay
Espace Technologique / Immeuble Discovery
Route de l'Orme aux Merisiers RD 128 / 91190 Saint-Aubin, France